



TECHNISCHE UNIVERSITÄT MÜNCHEN

Fakultät für Chemie, Lehrstuhl für Technische Chemie II

Transition Metal Phosphides Catalysts for the Hydroprocessing of Triglycerides to Green Fuel

Marco Peroni

Vollständiger Abdruck der von der Fakultät für Chemie der Technischen Universität München zur Erlangung des akademischen Grades eines

Doktor-Ingenieurs (Dr.-Ing.)

genehmigten Dissertation.

Vorsitzender: Univ.-Prof. Dr.-Ing. Kai-Olaf Hinrichsen

Prüfer der Dissertation:

1. Univ.-Prof. Dr. techn. Johannes A. Lercher
2. Univ.-Prof. Dr.-Ing. Dirk Weuster-Botz

Die Dissertation wurde am 09.02.2017 bei der Technischen Universität München eingereicht und durch die Fakultät für Chemie am 21.04.2017 angenommen.

Statutory Declaration

I declare that I have authored this thesis on my own, that I have not used other than the declared (re)sources, and I have explicitly marked all material which has been quoted either literally or by content from the used sources. Published content of this thesis is clearly marked at the beginning of each chapter with the publishing agreement of the publisher.

_____ , _____

Alla mia Famiglia. A Cristina.

“Choose a job you love, and you will never have to work a day in your life”

Confucius (551 BC - 479 BC)

Acknowledgements

The course of my doctoral studies has come to the end. I will never forget the good time I spent at the Chair of Technical Chemistry II at Technische Universität München. My sincere gratitude goes to all the members from our group.

First of all I want to thank Prof. Dr. Johannes A. Lercher for giving me the opportunity to be part of this prestigious group. Thanks for the trust, Johannes. You gave me a chance to prove my qualities and I really hope I paid you back for everything you were doing for me. It was not easy in the beginning, but you gave me the time to learn how to do science. I cannot forget your human and professional guidance.

Secondly, I am extremely grateful to my supervisor Dr. Oliver Y. Gutiérrez. I want to thank you for your efficient and productive guidance. Thank you for correcting my thesis and all of my papers and for all our scientific discussions. It was a big pleasure for me to work with you. I have to say that you are an excellent scientist. I learned many things from you and without your help I could never reach this goal.

I am also very thankful to my supervisor Dr. Eszter Baráth for your support and your patience. Your supervision was important for me.

I would like to acknowledge all the students who worked with me, namely Insu Lee, Xiaoyang Huang, Paola Alejandra Sáenz Cavazos, Robert Schober, Marc J. Kloberg, Aleksandra Koltowska, Jacob Sag and Roland Kietz. In particular, my greatest thanks go to Insu. I wish you all the best for your career.

During the initial period of my PhD I had the pleasure and honor to work with Dr. Gabriella Mancino. I am proud to share a scientific paper with you and I am proud to be your friend. Thank you.

Further, I would like to thank Manuel Wagenhofer and Moritz Schreiber for your scientific support and the nice discussions we had together.

From the side of my project partner I want to thank the German Federal Ministry of Food and Agriculture in the framework of the Advanced Biomass Value project for the financial support of my thesis.

I would like to acknowledge Xaver Hecht for solving our technical problems, and for the BET measurement. I am also very grateful to Yu Lou and Andreas Ehrmaier for your TPD measurement.

The technical and administrative staffs of TCII have been very important during the time I spent in our group. Thank you Martin Neukamm, Andreas Marx, Steffi Maier, Bettina Federmann, Ulrike Sanwald and Karen Schulz.

Thank you to our senior scientist, fundamental to guide our group, namely Prof. Dr. Andreas Jentys, Dr. Maricruz Sanchez-Sanchez, Dr. Erika Ember, Dr. Ricardo Bermejo-Deval, Dr. Yue Liu and once again Dr. Oliver Y. Gutiérrez and Dr. Eszter Baráth.

Furthermore, I would like to express my gratitude to the whole TCII team. You create a positive and fruitful atmosphere. Special thanks go to my office mates, namely Takaaki Ikuno, Dr. Stanislav Kasakov, Yang Song, Sebastian Foraita, Dr. Xianjong Sun, Dr. Eva Schachtl, Dr. Tobias Berto, and Christoph Denk.

Further I would like to thank separately Guoju Yang, Dr. Bruno Dalla Costa, Dr. Bo Peng, Dr. Navneet Kumar Gupta, Dr. Francisco Luis Pena Gonzalez, and once again Takaaki Ikuno, Stanislav Kasakov, Moritz Schreiber, Ricardo Bermejo-Deval, Yang Song, Sebastian Foraita, Yu Lou and Manuel Wagenhofer. Stan, Takaaki, Moritz, Ricardo you are not only colleagues but also my best friends, one of the greatest successes of my PhD.

Last but not least I would like to thank the most important persons in my life. Thank you Mamma and Babbo, thank you Moreno and Mirco. Thank you Cristina. Vi amo. Grazie.

Thanks to all of you,

Marco

Abbreviations

AlPO	Aluminophosphate
API	Density of the oil compared with the density of the water
BET	Brunauer-Emmett-Teller surface area
BJH	Barret-Joyner-Halenda
BTL	Biomass to Liquids
CA	Citric acid
CTL	Coal to Liquids
DCO	Decarboxylation/Decarbonylation
FAME	Fatty-Acid-Methyl-Esters
FT	Fischer-Tropsch
GC	Gas chromatography
GTL	Gas to Liquids
HDO	Hydrodeoxygenation
HDS	Hydrodesulfurization
IUPAC	International Union of Pure and Applied Chemistry
LHSV	Liquid hourly space velocity
LPG	Liquid petroleum gas
LT	Low temperature synthesis
MIX	Mechanical mixture
NA	Nitric acid
SAPO	Silicoaluminophosphates
TEM	Transmission electron microscopy
TMP	Transition metal phosphides
TOF	Turnover frequencies
TPD	Temperature programmed desorption
TPR	Temperature programmed reduction
ULSD	Ultra low sulphur diesel
USY	Ultrastable Zeolite Y (FAU)

VGO	Vacuum gas oil
vol. %	Volume percent
WHSV	Weight hour space velocity
wt. %	Weight percent
XRD	X-ray diffraction
ZSM	Zeolite Socony Mobil

Abstract

Transition metal phosphides have been studied for hydrodeoxygenation of oxygenated hydrocarbons and for hydrocracking of alkanes. The activities correlate with the concentration of exposed metal sites, whereas the available pathways towards O-free products depend on the nature of the transition metal. For alkane hydrocracking, the phosphide catalyzes (de)hydrogenation, whereas the zeolite enables acid-catalyzed steps. The product distribution is determined by the atomic ratio of metal/acid sites.

Kurzzusammenfassung

Übergangsmetallphosphide wurden für die Hydrodeoxygenierung von sauerstoffhaltigen Kohlenwasserstoffen und für das Hydrocracken von Alkanen untersucht. Die Aktivitäten korrelieren mit der Konzentration der zugänglichen Metallzentren, während die möglichen Reaktionspfade zu O-freien Produkten von der Art des Übergangsmetalls abhängen. Beim Hydrocracken von Alkanen katalysiert das Phosphid die (De)hydrierung, während der Zeolith die säurekatalysierten Schritte ermöglicht. Die Produktverteilung wird durch das atomare Verhältnis von Metall-/Säure-Zentren bestimmt.

Table of contents

Acknowledgements	i
Abbreviations	iii
Abstract	v
Kurzzusammenfassung	v
Table of contents	vi
Chapter 1 - Introduction	1
1.1 General background	2
1.2 Transport fuel production.....	3
1.3 Synthetic Fuels	5
1.3.1 Fischer-Tropsch process	5
1.3.2 Coal to Liquids (CTL).....	5
1.3.3 Gas to Liquids (GTL).....	5
1.3.4 Biomass to Liquids (BTL)	6
1.4 Generations of Biofuels.....	6
1.5 Triglyceride conversion.....	8
1.5.1 Transesterification.....	8
1.5.2 Hydroprocessing	9
1.6 Hydrodeoxygenation	10
1.6.1 Hydrodeoxygenation mechanism.....	11
1.6.2 Hydrodeoxygenation catalysts	12
1.7 Hydrocracking	13
1.7.1 Reactors and processes.....	13
1.7.2 Hydrocracking mechanism	16
1.7.3 Hydrocracking catalysts	20
1.8 Transition Metal Phosphides	24
1.8.1 Structure of Ni ₂ P, MoP and WP	26

1.9 Scope of the Thesis	26
1.10 References	28
Chapter 2 - Bulk and γ-Al₂O₃-supported Ni₂P and MoP for hydrodeoxygenation of palmitic acid.....	34
2.1 Introduction	35
2.2 Experimental	36
2.2.1 Synthesis of the catalysts: Temperature programmed reduction method (TPR)	36
2.2.2 Synthesis of the catalysts: Low temperature method (LT)	36
2.2.3 Synthesis of the catalysts: Citric acid method (CA)	37
2.2.4 Characterization of the catalysts	37
2.2.5 Catalytic test.....	38
2.3 Results and discussion.....	39
2.3.1 Exploratory studies	39
2.3.2 Physicochemical properties	39
2.3.3 Catalytic tests at constant temperature and reaction network	45
2.3.4 Catalytic tests at varying temperatures and kinetic parameters	49
2.3.5 On the role of support and phosphide phase in the hydrodeoxygenation of palmitic acid.....	52
2.4 Conclusions	55
2.5 Acknowledgements	56
2.6 References	56
2.7 Appendix	58
2.7.1 Ni ₂ P supported on AlPO	58
2.7.2 Preparation of MoP supported on Al ₂ O ₃	60
2.7.3 N ₂ physisorption isotherms and pore size distributions	61
2.7.4 X-ray diffractograms of selected Ni ₂ P catalysts	62
2.7.5 Catalytic HDO of palmitic acid at 573 K and WHSV 1 h ⁻¹	63
2.7.6 References.....	64

Chapter 3 - Deoxygenation of palmitic acid on unsupported WP, MoP, and Ni₂P.....	65
3.1 Introduction	66
3.2 Experimental	67
3.2.1 Synthesis of the catalysts: Temperature programmed reduction of precursors synthesized in the absence of citric acid (TPR-phosphides).....	67
3.2.2 Synthesis of the catalysts: Temperature programmed reduction of precursors synthesized in the presence of citric acid (CA-phosphides)	67
3.2.3 Characterization of the catalysts	68
3.2.4 Catalytic tests	68
3.3 Results and discussion.....	69
3.3.1 Physicochemical properties	69
3.3.2 Catalytic tests at varying temperatures and kinetic parameters	73
3.3.3 Reaction network	76
3.3.4 Mechanism and active sites	80
3.3.5 Role of acid sites	82
3.4 Conclusions	83
3.5 Acknowledgements	84
3.6 References	84
3.7 Appendix	88
3.7.1 Fatty acid composition in triglyceride mixture of microalgae oil.....	88
3.7.2 Characterization of oxide precursors	88
3.7.3 Characterization of CA-phosphide materials.....	89
3.7.4 Catalytic tests at constant temperature.....	91
3.7.5 Conversion of hexadecanol at varying temperatures	92
3.7.6 Conversion of hexadecanal at varying temperatures	93
3.7.7 Study of the carbon loss mechanism on Ni ₂ P-CA	94
3.7.8 Conversion of microalgae oil on MoP.....	94
3.7.9 References.....	95

Chapter 4 - Hydrocracking of paraffins on Ni- and W-based phosphide catalysts	96
4.1 Introduction	97
4.2 Experimental	97
4.2.1 Synthesis of the catalysts	97
4.2.2 Characterization of the catalysts	98
4.2.3 Catalytic tests	99
4.3 Results and discussion.....	99
4.3.1 Physicochemical properties	99
4.3.2 Catalytic tests at varying temperatures	101
4.3.3 Catalytic tests at constant temperature.....	103
4.4 Conclusions	105
4.5 Acknowledgements	106
4.6 References	106
Chapter 5 - Ni₂P/H-USY and Ni/H-USY catalysts for hydrocracking of <i>n</i>-hexadecane	107
5.1 Introduction	108
5.2 Experimental	109
5.2.1 Synthesis of the catalysts	109
5.2.2 Characterization of the catalysts	110
5.2.3 Catalytic tests	111
5.3 Results and discussion.....	112
5.3.1 Physicochemical properties	112
5.3.2 On the stability of Ni/H-USY and Ni ₂ P/H-USY.....	117
5.3.3 Effect of the metal phosphide loading on the hydrocracking of <i>n</i> -hexadecane	119
5.3.4 Comparative study of the hydrocracking of <i>n</i> -hexadecane on Ni and Ni ₂ P-based phosphides.....	128
5.4 Conclusions	132
5.5 Acknowledgements	133
5.6 References	133

5.7 Appendix	137
5.7.1 Experimental details of the kinetic tests	137
5.7.2 Characterization of the Ni/H-USY and Ni ₂ P/H-USY precursors	137
5.7.3 Study of the stability of H-USY during impregnation.....	138
5.7.4 Particle size distribution on Ni(15)/H-USY and Ni ₂ P(15)/H-USY	140
5.7.5 Temperature programmed desorption of NH ₃ and <i>n</i> -propylamine	140
5.7.6 Characterization of Ni(25)/SiO ₂ and Ni ₂ P(25)/SiO ₂	142
5.7.7 Coke deposition on the spent catalysts	142
5.7.8 Test of stability on Ni(25)/SiO ₂ at 400 °C	143
5.7.9 Study of the effect of Ni to P ratio in the precursor solutions on the properties of the Ni ₂ P/H-USY materials	143
5.7.10 Effect of citric (CA) and nitric (NA) acid on the physicochemical properties of the Ni ₂ P-based catalysts	152
5.7.11 Comparison of the yield % at 3 % conversion on H-USY, Ni-based and Ni ₂ P-based catalysts at 370 °C.....	155
5.7.12 References	155
Chapter 6 - Summary and Conclusions	157
Curriculum Vitae	162
List of publications	163
Journal Articles	163
Oral presentations	163
Poster presentations	163

Chapter 1

Introduction

1.1 General background

The continuous increase of the energy demand since the industrialization period of the second half of the 18th century has become one of the major issues in global research activities. Nowadays, the total global energy production relies strongly on fossil fuels.^[1] Oil, coal and natural gas represent more than the 80 % of the worldwide energy supply with nuclear power providing 4%. Renewable energy production as wind, solar and hydroelectric, is strongly increasing in the last years but its contribution is less than the 5 % of the total energy supply whereas only 10 % of the total energy production is generated from biomass (Figure 1-1).^[1, 2] Transportation constitutes today almost 30 % of the worldwide energy consumption and in particular 65 % of the oil supply is used to produce fuels.^[1]

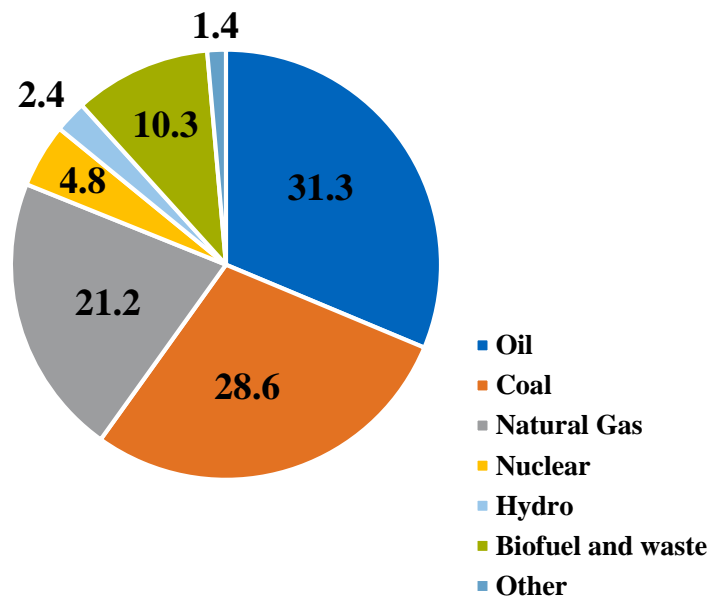


Figure 1-1. Total energy supply for the 2014.^[1]

However, oil reserves and conventional energy sources such as coal and natural gas have been estimated to last for decades to cover the worldwide energy consumption,^[2] whereas the energy demand is predicted to double in one decade.^[3] In particular, the usage of transportation fuels is forecasted to continue to grow in the future^[4] and the new technologies in petroleum extraction, oil refinery and automobile industry, that are considerably improving the fuel efficiency, are not enough to solve the problem for future energy resources. Moreover, the combustion of fossil fuels is strongly related to environmental problems as the global warming caused by the emission of the greenhouse gas CO₂ and the acid rain caused by NO_x and SO_x emissions.^[5] In particular, every year more than 30 gigatonnes of CO₂ are released in the atmosphere and the concentration of this greenhouse gas is increased in the last century from

290 ppm to 400 ppm.^[6] Therefore, due to the low supply of fossil fuels and the increase of political and environmental concerns about fossil fuels, nowadays research drives on the possibility to increase contribution of renewable energy supplies sources such as solar power, hydro power, biomass and waste energy to fuel production.^[2, 7] It is estimated that by 2050 the energy supply from biomass could be 30 times higher than now^[2] and in particular United States and the European Union fixed the goal to derive up to 20 % of liquid fuels from biomass in 5-10 years.^[8, 9, 10]

1.2 Transport fuel production

Nowadays, conventional transportation fuels are mainly produced through the distillation of crude oil. Crude oil is essentially a mixture of hydrocarbons as paraffins, olefins, naphthalenes and aromatics with different carbon number. The properties of the crude oil depend on the region where it is extracted and they are classified based on the API gravity (density of the oil compared with the density of the water), the content of asphaltenes, resins and oil and the concentration of impurities as sulfur and nitrogen.^[11] In refinery, the crude oil is converted to fuel through petroleum distillation, where the liquid fuels are separated into fraction based on their boiling points. Prior distillation, the crude oil is separated from the water, the salt and the sand that generally accompany the oil during the extraction and preheated up to 350 °C avoiding the thermal cracking before the distillation column.^[12] From the distillation column operating at atmosphere pressure and at temperatures between 400 °C in the bottom and 25 °C on the top of the column, heavy, middle and light distillates are obtained. For the bottom products a vacuum distillation is needed in order to get after thermal cracking, visbreaking and catalytic cracking, asphalt, wax, lubricating oil and heavy fuel oils. The gas and the light products formed on the top of the distillation column are processed in a gas plant to get liquid petroleum gas (LPG), light alkanes and sulfur. The middle fraction obtained from the atmospheric distillation is composed of naphtha, diesel, kerosene and jet fuel. After the hydrotreating unit, the light naphtha is further processed by isomerization, whereas the heavy naphtha needs to be treated in a catalytic reformer.^[13, 14] In general, between 30 and 70 % of all the crude oil processed may be converted to gasoline and diesel fuels.^[15]

An alternative way for producing fuel comes from the possibility to convert the syngas. Syngas is a mixture of carbon monoxide and hydrogen, obtained from the gasification of solid feedstocks such as coal or biomass or by reforming of natural gas.^[16, 17]

Figure 1-2 summarizes refinery applications for the production of high-quality transportation fuels.

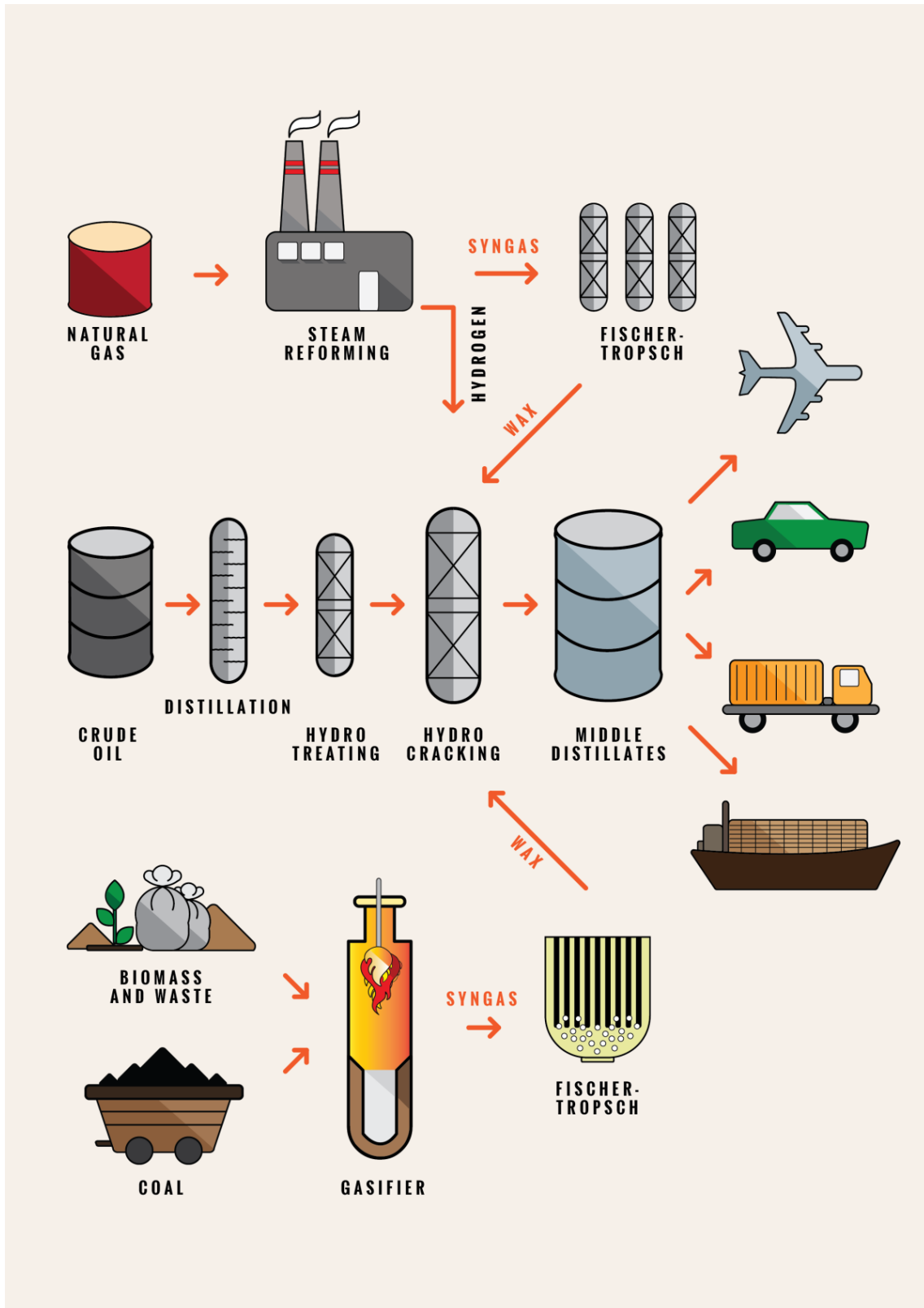


Figure 1-2. Refinery applications for the production of high-quality transportation fuels.

1.3 Synthetic Fuels

1.3.1 Fischer-Tropsch process

The Fischer-Tropsch synthesis is a catalytic process discovered by the German chemists Franz Fischer and Hans Tropsch in 1925. It consists of a catalytic hydrogenation of carbon monoxide to obtain hydrocarbons mainly in the diesel fuel range and water. It is a polymerization reaction taking place at 20-40 bar and 200-240 °C (low temperature Fischer-Tropsch process). In general, the catalyst used is based on cobalt, iron or ruthenium.^[18] In industry the Fischer-Tropsch process is mainly used to convert the syngas obtained from the gasification of coal, gas and biomass to transportation fuel.

1.3.2 Coal to Liquids (CTL)

The coal liquefaction technology has been used successfully to produce synthetic fuels in the last century and it can be direct and indirect. Direct liquefaction mainly involves the Bergius hydrogenation process where dry coal is mixed with heavy oil (recycled from the distillation process of the crude oil) and hydrogenated in presence of a catalyst at 400 °C and 20-70 bar in order to form alkanes.^[19] Indirect liquefaction processes involve gasification of coal to a mixture of carbon monoxide and hydrogen (syngas) that is converted through the Fischer-Tropsch process into liquid hydrocarbons. Due to the large coal reserves, this technology is highly applied especially in China. However, its application is limited by environmental concerns due to the high release of CO₂.

1.3.3 Gas to Liquids (GTL)

The GTL technology is a process to convert natural gas (or other gaseous waste products in refinery) into more valuable hydrocarbons, such as gasoline or diesel fuel. Natural gas consists in a gas mixture of light alkanes, containing mainly methane. The use of natural gas in the last years was encouraged by the many natural reserves situated throughout the globe that make the utilization of this feedstock available for centuries.^[20] During the GTL process the methane (or the light alkanes) is first converted to syngas by steam reforming or partial oxidation. The obtained syngas can be used to produce methanol that, in a Mobil process, can be further converted to gasoline on a zeolite catalyst^[21] or it can be in alternative used in the Fischer-

Tropsch synthesis to get high molecular weight paraffins as wax. The wax can be processed in a hydrocracker in order to produce more valuable fuel such as diesel, kerosene and gasoline.

1.3.4 Biomass to Liquids (BTL)

An alternative and renewable way to produce synthetic fuel is the BTL process.^[22] The entire biomass can be gasified to produce syngas that through the Fischer-Tropsch process polymerize into diesel-range hydrocarbons. Bio oil, char and gas can in alternative be produced by a flash pyrolysis at temperatures between 350-550 °C and residence times < 1 second. The use of biomass reduces significantly the impact of the production of fuel on the greenhouse effect but the low energy density of raw biomass together with the high costs of collection, transportation and pretreatment represent a considerable obstacle to the use of this technology.

1.4 Generations of Biofuels

In the European Union the most contribution to the renewable energy sources in the transport sector is given by the so called first generation of biofuels consisting in biodiesel, bioethanol and biogas.^[23, 24] Biodiesel, also called fatty-acid-methyl-esters (FAME), is made from vegetable oil or animal fat and it is synthesized via transesterification,^[24] whereas bioethanol is produced by fermentation of sugar, starch or cellulosic containing biomass such as wheat, sugar cane, barely, potato, corn, etc. Figure 1-3 shows the strategies for production of liquid fuels from biomass.^[25]

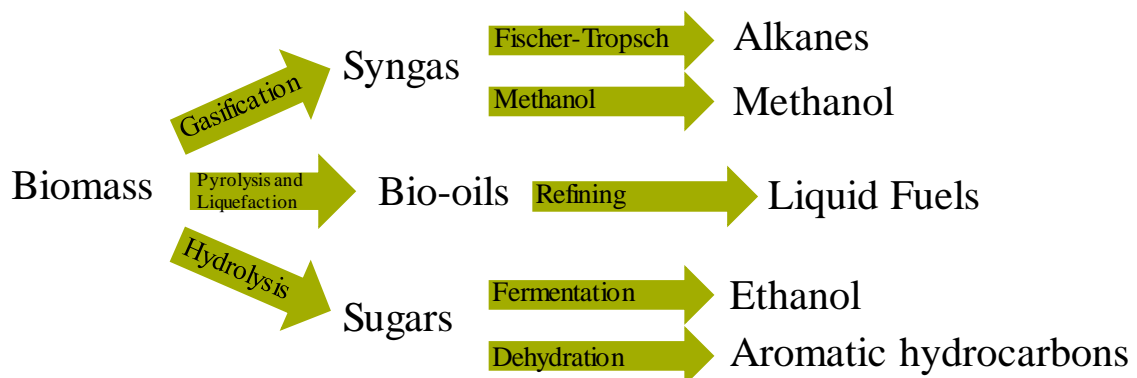


Figure 1-3. Strategies for production of liquid fuels from biomass.^[25]

However, first generations fuels have some disadvantages. Biodiesel and bioethanol are produced from food-crops, which are limited in their usage. Indeed, the production of first generation biofuel competes with the food production. Moreover, biofuels of the first generation

make use of fertilizers and pesticides and they release more carbon in their production than their feedstock's capture in their growth, reducing the environmental benefit of using biomass to fuel production.^[24]

In contrast to the first generation biofuels, the use of non-edible biomass such as forest and agricultural residues (straw, cellulose, etc.) or animal and oil wastes, represents a valid alternative feedstock for production of second generation biofuels, overcoming the main problems of the first generation biofuel.^[26-30] Second generation biofuels such as green diesel, differently to the first generation biofuels are not strictly competitive with food production and they have higher energy density compare to the latter. Table 1-1 shows that green diesel exhibits properties which surpasses biodiesel and even ULSD.^[24] For this reason, green diesel is the ideal candidate for blending biomass-derived oil with conventional fossil oil.

Table 1-1. Comparison between green diesel, biodiesel and petroleum (ULSD^a).

	Petroleum (ULSD)	Biodiesel (FAME)	Green diesel
% oxygen	0	11	0
Specific gravity	0.84	0.88	0.78
Sulphur	< 10	< 1	< 1
Heating value, MJ·kg ⁻¹	43	38	44
Cloud point	- 5	- 5 to 15	- 10 to 20
Distillation	40	50-60	70-90
Cetane	40	50-60	70-90
Stability	Good	Marginal	Good

^a ULSD: ultra low sulphur diesel.

Among the new biomass feedstocks, recently microalgae and yeast have been found to be ideal in order to produce a third generation biofuels in a large scale through hydroprocessing, reducing emissions of CO₂ and of S- and N-containing pollutants to alleviate environmental problems.^[31-33] Microalgae and yeast do not compete with edible biomass production and they need less land area to grow than other biomass.^[34] Generally, microalgae and yeast have high growth rates (in 24 h they can double their mass), high oil content (20 wt. % - 60 wt. %), high CO₂-fixation (1 kg of dry algae utilizes 1.83 kg of CO₂), low nutrition requirements and they do not need any herbicides or pesticides.^[33, 35-38] However, the direct application of this oil is limited due to the relatively high oxygen content that can reach 50 wt. %.^[39-41] This oxygen has to be removed in order to meet fuel requirements via hydrodeoxygenation (HDO).^[39] A following hydrocracking/hydroisomerization step would increase the value of the final fuel.

Nowadays, a fourth generation of biofuels is also realized using algal biomass through a metabolic engineering process where the algae is converted to fuel by oxygenic photosynthetic organisms.^[26]

1.5 Triglyceride conversion

Triglycerides make up the structure of all vegetable oils and animal fats found in nature. They are esters derived from glycerol and three long chains of fatty acid. The classification of triglycerides is made based on the length of the side chains that in nature normally can contain 16, 18, or 20 carbon atoms and that can be either saturated, monounsaturated or polyunsaturated.^[42] The use of triglycerides in diesel engines is limited due to the high viscosity and low volatility of this material that can cause several engine problems (carbon deposits, coking on the injector, oil ring sticking, etc.).^[43] In order to upgrade the triglycerides and make them suitable for fuel production, commercially transesterification and hydroprocessing are applied to the crude bio-oil.

1.5.1 Transesterification

Transesterification is a reaction between the triglyceride and an alcohol in the presence of an acid or base catalyst or an enzyme.^[44-46] It consists of three consecutive reversible reactions where the triglycerides convert first to diglycerides, followed by the conversion of the diglycerides to monoglycerides and finally to the production of fatty acid methyl esters (FAMES) and glycerol. The overall reaction is shown in Figure 1-4.

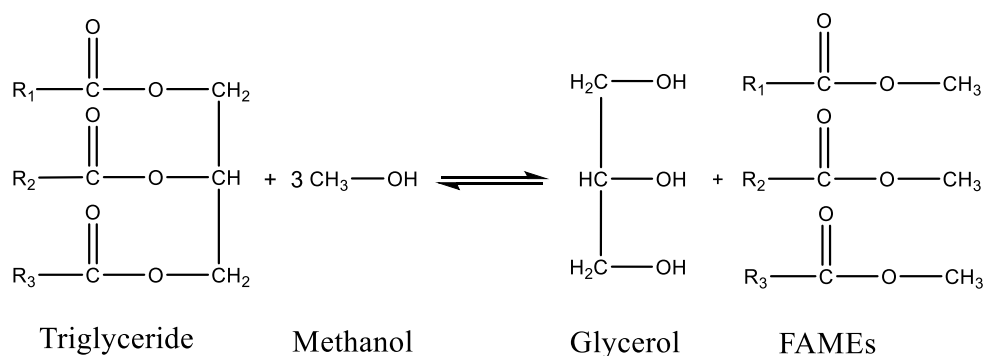


Figure 1-4. Transesterification reaction.

After a preliminary separation step, the alcohol phase is removed through flash evaporation or by distillation whereas the ester is purified to be used as biodiesel. In commercial biodiesel production plants high yield of ester formation are reached with homogeneous alkaline catalysts such as sodium or potassium hydroxide, at mild reaction conditions.^[47] However, the difficulty to separate the catalytic phase from the products and to recycle the catalyst after the reaction, makes the use of heterogeneous catalyst more desired for the transesterification reaction. More severe conditions (120-250 °C and high pressure) are required using the typical metal oxides

(ZrO₂, TiO₂), mixed metal oxides (e.g., tungstated zirconia, zirconia titania), or supported heteropolyacids.^[48, 49]

1.5.2 Hydroprocessing

An alternative process to convert triglyceride oil to green fuel is hydroprocessing. Hydroprocessing is used in refinery to convert a variety of petroleum distillates into clean transportation fuels and heating oil, in presence of hydrogen and through a bifunctional catalyst.^[50] This process, commercialized by Neste Oil to treat triglycerides, involves reactions that can be classified in two groups defined as hydrotreating and hydrocracking. Hydrotreating takes place on the metal active sites of a bifunctional catalyst (typically on sulfided NiMo or CoMo supported on γ -Al₂O₃) at 350-450 °C at 40-150 bar in presence of H₂. Hydrotreating of triglycerides allows to produce straight chain alkanes in the diesel hydrocarbons range (C12 to C18).^[51-54] In industry hydrotreating is also used to improve the quality of the petroleum distillates removing sulfur, nitrogen, and oxygen compounds undergo hydrogenolysis forming respectively hydrogen sulfide, ammonia, and water. Hydrotreating comprises the following steps: 1) hydrogenation of the double bonds of the side chains of the triglycerides; 2) hydrogenolysis of the saturated triglycerides with the formation of the corresponding fatty acids and propane; 3) hydrodeoxygenation of the formed fatty acids in order to remove oxygen leading to straight chain alkanes.^[54] The obtained alkanes can be further processed in a hydroisomerization/hydrocracking section in order to improve the properties of the final fuel. In general, hydroprocessing takes place in a two-step process where in the first reactor the oxygen is removed on a typical hydrotreating catalyst and in the second reactor hydrocracking/hydroisomerization of the deoxygenated products on a selective hydrocracking catalyst is needed in order to get lighter alkanes within the boiling range of naphtha, jet fuel and diesel.^[55] The complete hydroprocessing reaction network is shown in Figure 1-5.

Hydrocracking requires high temperature and high hydrogen pressures to avoid coke deposition^[56] and the presence of an acid support, ranging from amorphous supports (aluminosilicates) to silicoaluminophosphates (SAPO) and zeolites.^[51] Green naphtha is obtained using zeolites with strong acid sites.^[57] In contrast with the transesterification process, hydroprocessing allows to blend biomass-derived oil with conventional fossil oil. Indeed, the green diesel produced by hydroprocessing is compatible with existing engines and it does not cause additional pollution during its transportation since it can use the same pipelines that are currently used for distribution of petrodiesel.^[58]

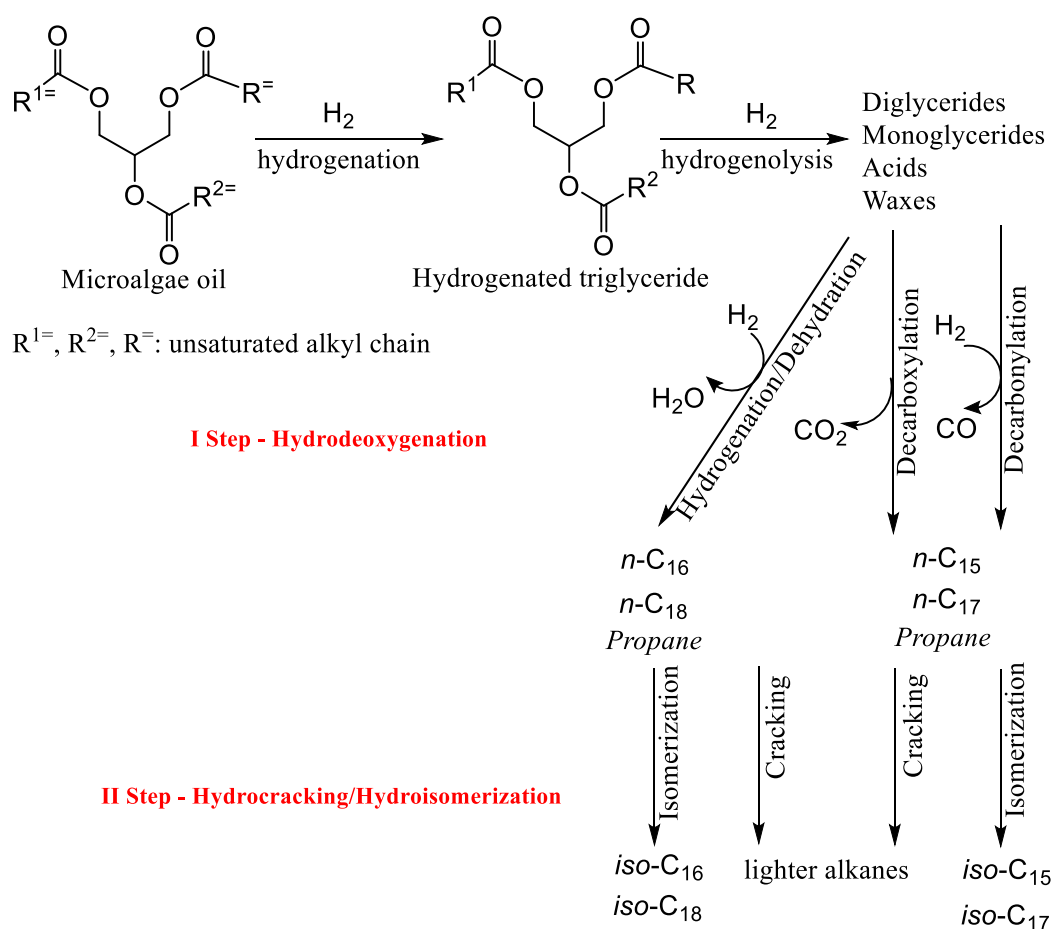


Figure 1-5. Hydroprocessing reaction network.

1.6 Hydrodeoxygenation

The high oxygen content and the low heating value of the FAMES produced by transesterification, limit their application as high grade fuels.^[53] Indeed, the presence of oxygenated compounds in the fuels can cause polymerization that could lead poor performance of fuel combustion. Oxygen in fuels can also damage the engines over time. In order to generate a more valuable biofuel, nowadays catalytic hydrodeoxygenation (HDO) is applied for converting fatty acids and triglycerides into diesel range hydrocarbons. This process consists in removal oxygen in presence of hydrogen. HDO is actually not used on conventional crudes, because they do not contain very high oxygen concentrations. However, in the last years due to environmental concerns, refineries have been forced to treat feedstocks with increasing concentrations of oxygen, which has to be removed in order to meet fuel requirements via

hydrodeoxygenation.^[39] Table 1-2 shows the content of oxygen compounds depending on the origin of the feed.

Table 1-2. Composition of feeds with different origin for possible HDO.^[39]

	Conventional crudes	Coal-derived naphta	Oil shale crude	Liquefied bio-oil	Pyrolysis bio-oil
Carbon	85.2	85.2	85.9	74.8	45.3
Hydrogen	12.8	9.6	11.0	8.0	7.5
H/C	1.8	1.4	1.5	1.3	2.0
Sulphur	1.8	0.1	0.5	< 0.1	< 0.1
Nitrogen	0.1	0.5	1.4	< 0.1	< 0.1
Oxygen	0.1	4.7	1.2	16.6	46.9

During hydrodeoxygenation the oxygen can be removed as CO (decarbonylation), CO₂ (decarboxylation) or H₂O (hydrodeoxygenation route) as reported in Figure 1-5.

1.6.1 Hydrodeoxygenation mechanism

The accepted hydrodeoxygenation mechanism of a bio-oil on a typical metal catalyst supported on zeolite consists in the hydrogenation of the double bonds of the side chains of the triglycerides on the metal sites of the catalyst, followed by hydrogenolysis of the formed saturated triglycerides producing the corresponding fatty acids and propane. In general, the side chains in the triglycerides contain mainly 18 carbon atoms. Therefore, the subsequent hydrogenation of the carboxylic group of fatty acids that mainly consists in stearic acid, leads to the corresponding octadecanal. This intermediate rapidly converts via hydrogenation to octadecanol, which yields *n*-octadecane via acid catalyzed alcohol dehydration followed by metal catalyzed alkene hydrogenation. *n*-Heptadecane can be produced either by decarbonylation of octadecanal or by direct decarboxylation of stearic acid.^[59]

Figure 1-6 shows the typical hydrodeoxygenation reaction network on a bifunctional catalyst.

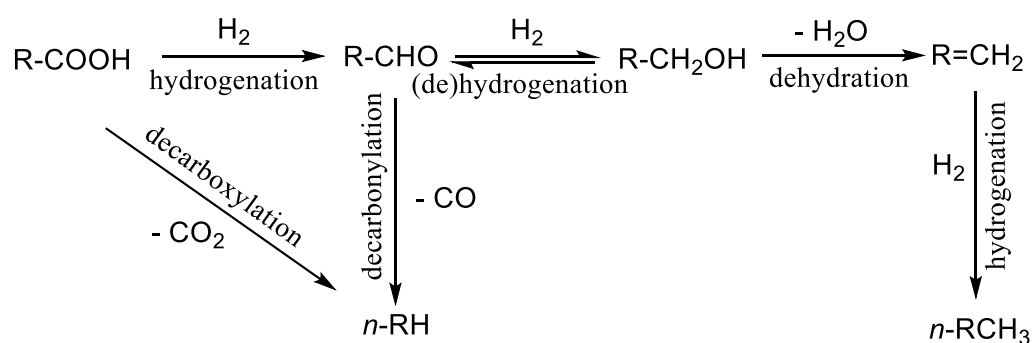


Figure 1-6. Hydrodeoxygenation reaction network.

1.6.2 Hydrodeoxygenation catalysts

The deoxygenation rates of various metals decrease in the sequence of Pd > Pt > Ni > Rh > Ir > Ru > Os.^[60] However, noble metals suffer from deactivation with high concentration of sulfur and nitrogen and their application in industry is economically infeasible due to their high prices and the difficulty of blending biomass-derived oil with conventional fossil oil. In particular, metals tend to decompose sulfur-containing molecules to sulfur atoms, which form a deactivating layer of sulfur on the metal surface.^[61] Conventional hydrodeoxygenation catalysts in industry are bimetallic CoMo/Al₂O₃ and NiMo/Al₂O₃.^[62] These catalysts have to be presulfided with H₂S before starting the reaction in order to increase the maximum catalytic activity.^[62, 63] CoMo/Al₂O₃ and NiMo/Al₂O₃ suffer from deactivation in presence of water which derived from the biomass compounds during HDO. Water changes the surface of the catalysts which results in deactivation of the active sites. However, the deactivation of these materials is reversible and the initial functionality of the catalyst can be restored adding sulfur compounds like dimethylsulfide into the feed to maintain a constant partial pressure of H₂S during the reaction.^[64] Another way of preventing catalytic deactivation is a constant increasing of the reaction temperature, but this method can lead to undesirable changes of selectivity.^[63] However, sulfide catalysts contaminate products through sulfur leaching and due to addition of the sulfiding agent to the feedstock, undesirable S-containing products can be formed. Carbides and nitrates were also tested in the hydrodeoxygenation of fatty acid. These two class of catalysts may be more active than conventional sulphide catalysts but they are thermodynamically not stable and they readily convert to the corresponding sulfides and oxides.^[52, 62, 65-67] As a consequence, the possibility to develop new kinds of hydrotreating catalysts is of primary importance. An interesting alternative to the materials mentioned before are phosphides of transition metals. Metal phosphides do not need any additives or presulfidation to maintain or increase their catalytic activity. These materials have been proven very active for hydrodefunctionalization of biomass derived molecules, intrinsically more active than sulfides and more poison tolerant than most base or noble metals.^[39, 68-71] Indeed, metal phosphides have been found stable under S- and O-containing conditions (although they may undergo surface modifications).^[72-75]

1.7 Hydrocracking

Hydrocracking is one of the most important and constant processes in modern petroleum refining.^[76, 77] In industry hydrocracking is used to convert heavy gasoil, vacuum gasoil and gasoil from coke into lighter and valuable transportation fuel or chemical raw materials by carbon-carbon bond breaking and simultaneous hydrogenation at high pressures in presence of hydrogen.^[76, 77] The hydrocracking process originates in Germany in the period between the two world wars. The large amount of coal and the very little reserves of crude oil drove the research activity on the liquefaction of coal and on the conception of the first hydrocracking plant, built in Leuna in 1927. The coal conversion to liquid fuels consisted of a catalytic process whose operating conditions were extremely high pressure (200-700 bar) and high temperatures (375-525 °C). One of the first hydrocracking processes designed to achieve the conversion of heavy oils into lighter fuels was born from the collaboration between the German I.G. Farbenindustrie and the American Standard Oil of New Jersey. Among the first catalytic systems, the most effective were based on tungsten sulfide, iron or nickel on a silica-alumina support. The hydrocracking of oil fractions became a commercial reality in 1959 with the California Research Company (Chevron).^[78] The auto industry contributed during the 60's to the rapid development of the hydrocracking, producing high-performance cars that required better quality gasoline.

1.7.1 Reactors and processes

Conventional hydrocracking is mainly used for the production of transportation fuels from heavy crude oil fractions or vacuum gas oil (VGO). It can also be used for the upgrading of products from other units in refinery. Typical catalysts used in conventional hydrocracking are nickel-molybdenum or nickel-tungsten supported on an amorphous silica-aluminate or zeolite. The reaction temperatures are in the range of 350-450 °C and the pressure between 100-200 bar. Nowadays mild hydrocracking conditions are applied in existing hydrotreating units in order to increase the production of middle distillates. In this case, the hydrocracking operates at less severe conditions (lower operating hydrogen partial pressure and lower temperatures) and the total cost of the process is moderate. However, mild hydrocracking leads to lower conversion (20-70%) and less quality of the final product.^[79] In areas where the coal is abundant and the crude oil reserves are limited, hydrocracking is applied at the Fischer-Tropsch process.^[80] Unlike the typical hydrocracker feeds in crude oil refineries that are usually rich in aromatics and olefins, the Fischer-Tropsch products are characterized by a high degree of

paraffinicity.^[81] FT wax hydrocracking leads to high quality fuel having no sulphur, nitrogen or aromatic compounds.^[82] The catalysts used in this hydrocracking process have to be selective to middle distillates minimizing overcracking. In addition, in the FT wax hydrocracking the catalyst should give high isomerization yields to improve the cold properties of the fuel.^[82, 83] In general, the hydrocracking of Fischer-Tropsch products can be performed at less severe conditions than those used for crude feeds with less acidic catalysts as reported in Table 1-3.

Table 1-3. Typical hydrocracking conditions.

	Conventional hydrocracking	Mild hydrocracking	FT wax hydrocracking
Temperature, °C	350-450	350-440	325-375
Pressure, bar	100-200	50-80	35-70
LHSV, h ⁻¹	0.2-2.5	0.2-2.0	0.5-3.0
H ₂ :feed, Nm ³ ·m ⁻³	800-2000	400-800	500-1800
Conversion, %	70-100	20-70	20-100
Metal	Ni/Mo; Ni/W	Ni/Mo; Co/Mo	Ni/W; Ni/Mo; Pt; Pd
Support	Si-Al; Zeolite	Alumina; Si-Al	Si-Al; Zeolite

The hydroprocessing units consist of one or more trickle fixed-bed reactors, where in most of the cases a simultaneous downward movement of liquid and hydrogen is ensured. Hydrocrackers can be configured in single-stage, single-stage in series or two-stage process, depending on the feedstock, the desired products and the used catalysts. In the single-stage process, the fractionating unit is situated after the hydrocracking unit (Figure 1-7). Reactions like hydrodesulfurization, hydrodenitrogenation and hydrocracking can take place in the same reactor. In alternative, in the single-stage in series process, at least two reactors are arranged in series.^[84] Single-stage hydrocracking process can be run with or without recycling (once-through process).^[84]

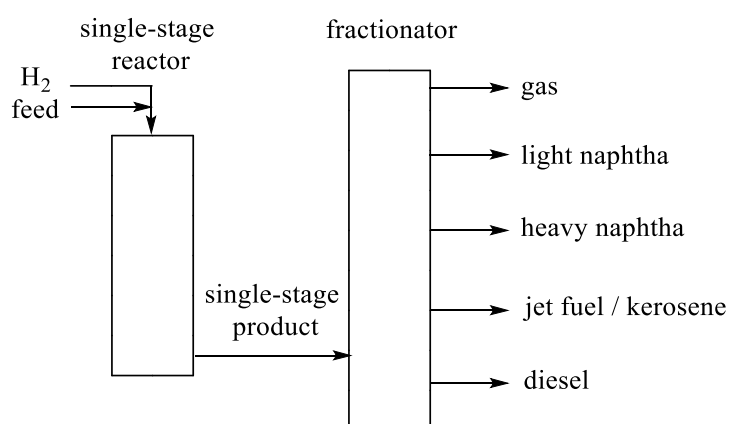


Figure 1-7. Scheme of single-stage hydrocracking process.^[84]

In the most common configuration, the two-stage process, the fractionating unit is located between two hydrocracking units (Figure 1-8).^[76, 84] In the first reactor hydrotreating reactions and aromatics saturation take place in order to remove sulphur, nitrogen, oxygen, metal compounds or aromatics by hydrogenation, while hydrocracking and hydroisomerization reactions occur primarily in the second-stage reactor.^[85] In this configuration base metal-sulfide catalysts such as NiMoS, NiWS or CoMoS are used in the first reactor while noble metals supported on zeolites are used for the hydrocracking stage as shown in Figure 1-8.^[85]

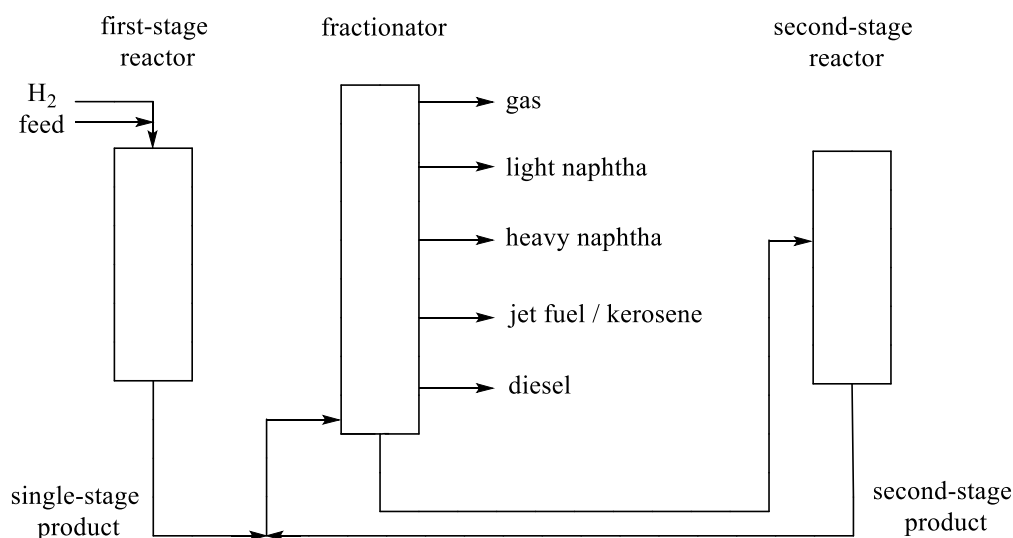


Figure 1-8. Scheme of two-stage hydrocracking process.^[76]

The different hydrocracking processes exhibit different key characteristics resulting in different properties: feedstock adaptabilities, LHSV, construction costs, etc. (Table 1-4).

Other reactor types are used such as moving bed, slurry-bed reactors and ebullating-bed reactor. The latter configuration allows for better heat control and continuous addition of fresh catalyst.^[86, 87]

Table 1-4. Different key characteristics of the single-stage, single-stage in series and two-stage hydrocracking process.^[84]

	Single-stage	Single-stage in series	Two-stage
Feedstock	Low N and S content	High N and S content	High N and S content
LHSV	High	High	Low
Hydrotreatment	No	Yes	Yes
Construction costs	Low	High	High
Yield target	Medium	High	High
Catalyst	Single catalyst	Several catalysts	Several catalysts
Operation flexibility	Low	High	High
Product quality	Average	Good	Good

1.7.2 Hydrocracking mechanism

The classical accepted hydrocracking mechanism is based on the paper by Coonradt and Garwood^[88] and Weisz^[89]. Hydrocracking occurs by a bifunctional mechanism in the presence of an acid catalytic function which catalyzes isomerization and cracking through carbenium-ion chemistry and a metal function responsible for hydrogenation/dehydrogenation reactions. The two functions have to be close enough in order to avoid the mass-transfer limitations during the diffusion of the intermediates between the two types of active sites.^[89] The mechanism is initiated via hydride extraction over the metal and the formation of an alkene. The olefin migrates to a Brønsted acid site, where it is protonated to form an alkylcarbenium ion.^[77] Alkylcarbenium ions are reactive intermediates, which undergo skeletal rearrangements and carbon-carbon bond rupture via β -scission (Figure 1-9). The heterolytic bond cleavage at the beta position forms an olefin and a carbenium ion of lower molecular weight. The primary carbenium ion is not energetically stable^[77] and in addition hydrocarbons such as methane, ethane or ethene are not formed, because also the intermediates CH_3^+ and C_2H_5^+ are energetically unfavoured. Therefore, a secondary carbenium ion that can be subsequently deprotonated is formed. Olefins diffuse back to a metal site, where they are hydrogenated to give saturated compounds. The formation of stable tertiary carbenium ions can only occur with starting molecules containing eight or more carbon atoms.^[82] Monobranched alkene, alkylcarbenium ion and small alkene are primary products, which can be observed at lower conversion. At higher conversion, consecutive reaction such as secondary rearrangement occurs at the acid sites, forming dibranched alkenes. Increasing the conversion a third step rearrangement can occur and tribranched alkylcarbenium ions are formed. The rate of β -scission increases with the degree of branching.^[77] When the products of the primary cracking are not desorbed fast enough the largest fragment undergoes secondary cracking and appears mainly as an alkane of the lighter fraction. With an active bifunctional catalyst olefinic intermediates, produced by dehydrogenation of paraffins on the metal function are consumed on the acid function shifting the dehydrogenation equilibrium and pushing the rate determining step on the acid sites.^[77] Moreover, in the presence of a strong metal function, unsaturated intermediates will more easily desorb from the acid sites, whereas with strong acid functionality, intermediates are more likely to react further on the acid sites, giving rise to further branching and secondary cracking. When hydrogenation activity is very low, the product distribution will resemble the one obtained by monofunctional acid cracking giving high selectivity of the catalyst to light alkanes.^[77]

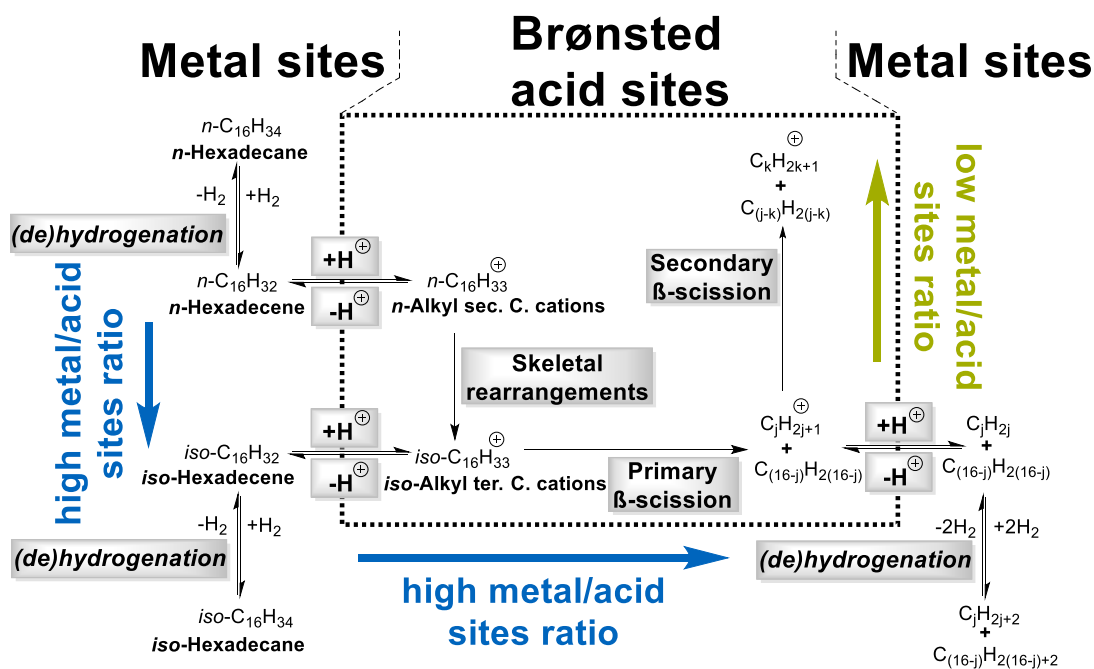


Figure 1-9. Classical mechanism of isomerization and hydrocracking of an *n*-alkane on a bifunctional catalyst comprising metal sites and Brønsted acid site.^[77]

At high temperatures and high pressure in presence of hydrogen other mechanisms might contribute to the C-C bond cleavage. Catalysts with strong metal function but limited in the concentration of acid sites can be selective to hydrogenolysis. Hydrogenolysis is a monofunctional hydrocracking mechanism, catalyzed by metals where the breaking of carbon-carbon bond followed by hydrogenation leads essentially to unbranched products. The reaction can be catalyzed by both noble and non-noble transition metals.^[77, 82, 90] In general, due to the instability of the intermediates CH_3^+ and $C_2H_5^+$ during bifunctional hydrocracking, the presence of methane and ethane is an indication of the hydrogenolysis selectivity.

At very high temperatures, the C-C bond can break by the thermal cracking that does not require the presence of a catalyst. This mechanism is observed at 500-600 °C and consists in reactions involving free radicals.^[77]

1.7.2.1 Classification of β -scission reactions

On bifunctional catalysts the hydrocracking follows the β -scission mechanism. β -scission of alkylcarbenium ions is classified into type A, type B1, type B2, type C and type D as shown in Figure 1-10. The rate of β -scission strongly increases from type D to type A. In general, the skeletal rearrangement may occur through type A and type B isomerization.

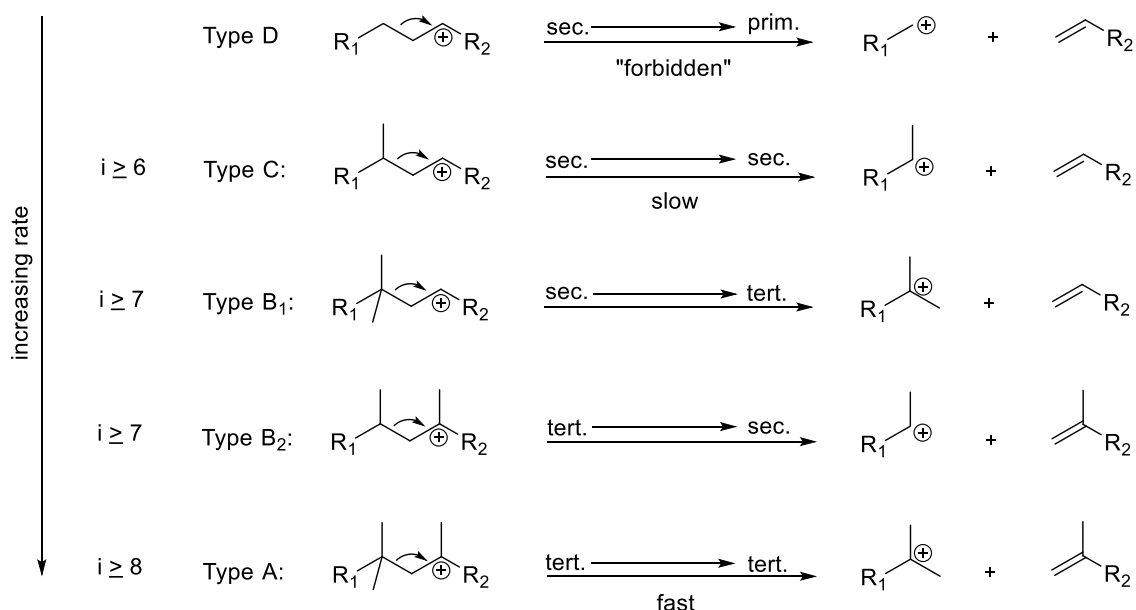


Figure 1-10. Classification of different β -scission reactions of alkylcarbenium ions.^[77]

In Type A rearrangement a hydride and an alkyl group shift their positions and the degree of branching remains unchanged. In Type B the formation of a cyclic carbonium ion intermediate increases or decreases the degree of branching (Figure 1-11).

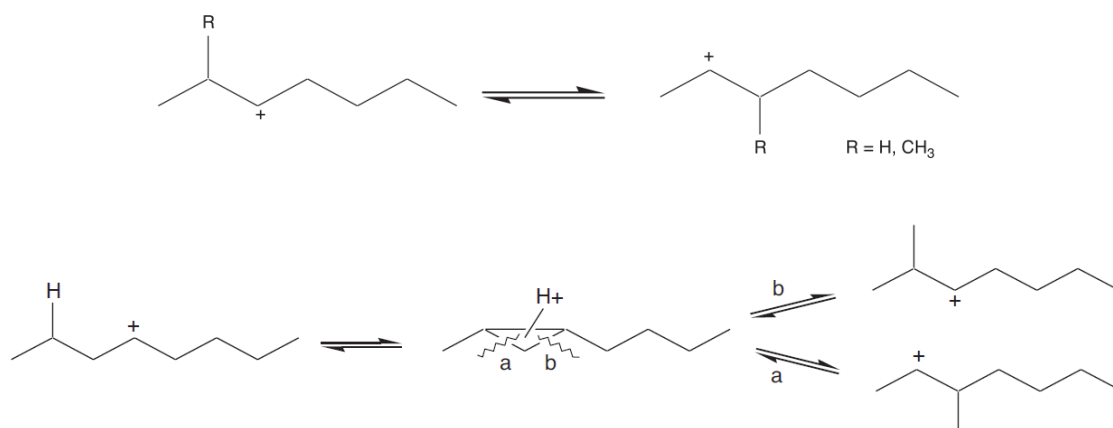


Figure 1-11. Type A and Type B rearrangement.^[82]

The rates of the β -scission typology depend on the stability of the formed alkylcarbenium ions. For this reason, the formation of a primary carbenium ion is forbidden whereas the most stable configuration is the tertiary carbenium ions.^[91] In general type A rearrangement which starts and ends with a tertiary carbenium ion is much faster than type B rearrangements. Indeed, based on the stability of the carbocations involved, the rate of rearrangement follows the order: Type A \gg Type B₁ \approx Type B₂ $>$ Type C $\gg \gg$ Type D.

1.7.2.2 Ideal hydrocracking

Ideal hydrocracking is a special case in hydrocracking on bifunctional catalysts. The term ideal hydrocracking was introduced by Weitkamp^[77] to indicate the case of bifunctional hydrocracking in which the dehydrogenation/hydrogenation reactions are at quasi-equilibrium and the rate determining step is the skeletal rearrangements and β -scissions on the acid sites. In this case an ideal balance between the two catalytic functions, hydrogenation/dehydrogenation and catalytic cracking, is necessary. Moreover, ideal hydrocracking depends on the nature, concentration and strength of the two catalytic functions, the intimacy between them, the reactants and the operating conditions. Under ideal hydrocracking conditions, the reaction may not be restricted by diffusion limitations of the olefinic species between metal sites and acid sites which should be in close proximity and the metal function is not rate limiting. In presence of a highly active hydrogenation/dehydrogenation function, the steady-state concentration of alkenes reaches the equilibrium value. This equilibrium value is considered to be high enough to displace an alkylcarbenium ion from the acid site by competitive adsorption/desorption, which highly favors hydroisomerization and primary cracking.^[77] In general, ideal hydrocracking is reached at lower reaction temperatures (250 °C) compared to the catalytic cracking. In the ideal hydrocracking, an *n*-alkane (C_n) is converted to a skeletal isomer (*iso*-C_n) at low conversion or to a mixture of shorter hydrocarbons with symmetric distribution of carbon numbers at high conversion with a pure primary hydrocracking selectivity and no secondary cracking.^[77] Therefore, ideal hydrocracking in contrast with fluid catalytic cracking allows to obtain a maximal product flexibility ranging from diesel fuel, jet fuel to gasoline.^[92]

1.7.2.2 Non-ideal hydrocracking

Non-ideal hydrocracking consists in a high selectivity to secondary cracking due to the weak hydrogenation/dehydrogenation function of the bifunctional catalyst. In this case the hydrogenation/dehydrogenation is the rate determining step and primary cracked products cannot desorb fast enough.^[77] In the case of not reaching quasi-equilibrium between hydrogenation/dehydrogenation and cracking function, product distribution shows a non-symmetrical carbon number distribution. Severe secondary cracking shifts the carbon number product distribution to lighter hydrocarbons (C₃-C₆). Other factors that can compromise the ideality of the hydrocracking are the decreasing of the total pressure leading to an increase of the carbenium ion concentration available for isomerization and cracking and an increase of the reaction temperature which leads to more severe cracking.

1.7.3 Hydrocracking catalysts

The catalysts used for the hydrocracking have to exhibit a strong dehydrogenation/hydrogenation function, provided by a metal, and an isomerization/cracking function in general provided by an acidic support. Based on the nature of the metal and the acidity of the support, the product distribution can be tuned as well as the cost of the process. Indeed, balancing this two functions hydrogenolysis and overcracking can be limited in order to optimize the product distribution and the properties of the final fuel. Both noble and non-noble metals are used for the dehydrogenation/hydrogenation function while the support can range from amorphous supports (alumino-silicates) to silicoaluminophosphates (SAPO) and zeolites as shown in Figure 1-12.^[93]

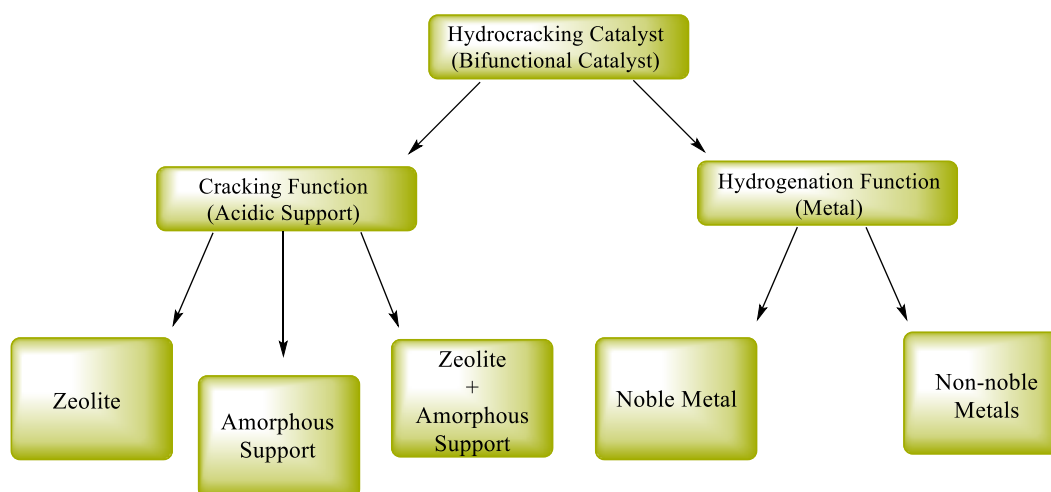


Figure 1-12. Composition of hydrocracking catalysts.

1.7.3.1 Metal component

The metal function is responsible for the dehydrogenation/hydrogenation of alkanes during hydrocracking. The hydrogenation function is determined by several factors as reported in Figure 1-13.^[79]

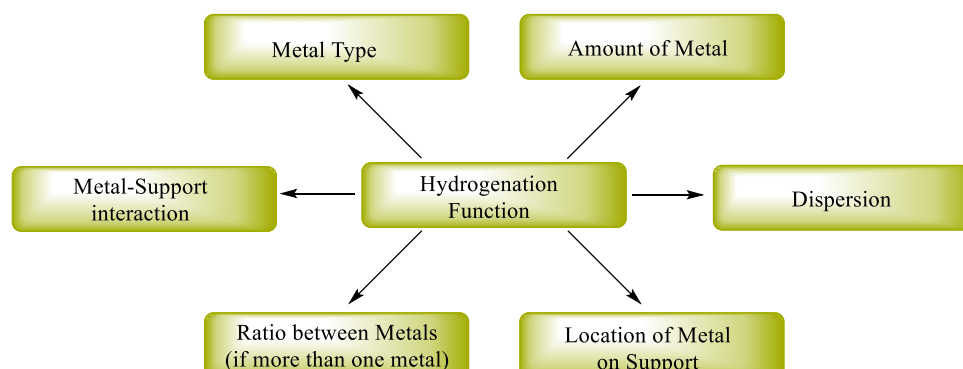


Figure 1-13. Influencing factors for hydrogenation activity of metals.

Various metals have been investigated for hydrocracking ranging from noble metals such as Pd or Pt to non-noble transition metals such as Mo, Ni, Co or W.^[76] Other metals such as Cr, V, Fe, Rh, Ru, Ir and Nb have been also investigated and recommended for hydrocracking.^[76, 94-96] The hydrogenation activity decreases in the following order: noble metal > sulfided transition metal > sulfided noble metals.^[76, 97] In two-stage hydrocracking or in Fischer-Tropsch wax hydroprocessing, where the sulfur concentration is extremely low, noble metals are preferred due to their higher hydrogenation activity.^[97] A strong hydrogenation function enhances the stability of the catalyst avoiding coke formation.^[82] Among the noble metals Pt has a higher hydrogenation activity than Pd^[82, 98] whereas the hydrogenation performance for metal sulfides decreases in the following order: Ni/W > Ni/Mo > Co/Mo.^[76] The metal amount of a hydrocracking catalyst is determined by the balance between cracking and hydrogenation function of the bifunctional catalyst and it depends on the intrinsic dehydrogenation/hydrogenation function of the metal. Therefore, noble metals need lower amount of metal loading compared to transition metals (Table 1-5).^[79]

In order to increase the activity of the dehydrogenation/hydrogenation function and decrease the price of the catalytic system, the metal has to be very well dispersed on the support. Dispersion of metal species can decrease with time on-stream due to agglomeration of metal particles (via sintering) or poisoning (e.g. sulfur). Agglomeration can be prevented by adding stabilizer metals such as ionic Fe or Cr.^[79]

Table 1-5. Metal loading in wt. % for the different metals used in hydrocracking.^[79]

Metal	wt. % of metal component
Pt; Pd	≤ 1
Co; Ni	3-8
Mo; W	10-30

When the metal function consists of more than one metal the performance of the catalyst can be tuned by the ratio between the metals. Hydrogenation of toluene has been performed on group VI (Mo, W) and VIII (Co, Ni) metals in presence of H₂S and it was found that an optimum in activity is reached at 25 wt. % loading of the metal from group VIII in the final metal mixture.^[79] Usual preparation methods for the synthesis of supported hydrocracking catalysts are impregnation and ion-exchange.^[79] Ion-exchange is limited by the concentration of available sites that can be exchanged. Therefore, this method is not suited for high loadings of metal as in the case of catalysts based on transition metals. In general, high loading of the metal

species is accomplished by impregnation methods. Metal species introduced via impregnation are preferably situated inside the pores of the acidic supports. On zeolitic supports during the preparation the metal can: 1) form clusters in the cage of the zeolite; 2) migrate from smaller cages into bigger cages; 3) agglomerate to form clusters in the supercages; 4) migrate outside of the pores and form bigger metal particles. The acidity of the support may influence the dispersion of the metal species on the support.^[99] A higher acidity of the support results in a higher dispersion of the metal and higher stability, which leads to a higher hydrogenation activity.^[99]

1.7.3.2 Zeolite as acidic support

The support used in hydrocracking application ranges from silicas, aluminas, amorphous silica-aluminas, tungstated or sulfated zirconia, to chlorinated alumina and zeolites. Weak or mild acid strength are preferred when increasing the selectivity to middle-distillate.^[81, 82, 97] However, in most of the recent industrial applications in oil refining and petrochemical industry, the use of different types of zeolite ensures a more flexible product distribution. Zeolite is also used in agriculture, horticulture, as in detergent, pigments, jewelers, etc.^[100] Zeolites are crystalline aluminosilicates, which are built up from primary building units such as SiO_4^- and AlO_4^- -tetrahedra (Figure 1-14).^[101]



Figure 1-14. SiO_4^- and AlO_4^- -tetrahedra in the zeolite.

The tetrahedra are linked at their corners via a common oxygen atom, which results in a distinct three-dimensional framework (Figure 1-15 and Figure 1-16).^[101] The negative charge of the AlO_4^- -tetrahedra in a zeolite framework is compensated by cations like Na^+ , K^+ , H^+ , etc. (Figure 1-15).

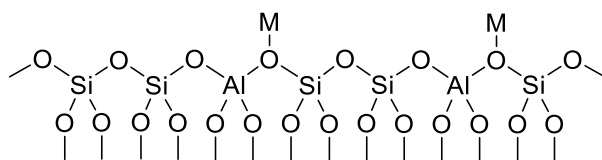


Figure 1-15. Example of $\text{SiO}_4^-/\text{AlO}_4^-$ -cluster in a zeolite.

The combination of primary building units can result in different secondary building units as sodalite unit, pentasil unit, etc. There are currently 229 different known zeolite structures.^[102]

^{103]} The framework of a zeolite includes channels, channel intersections and cages with strictly uniform pore diameters (Figure 1-16).^[82, 104]

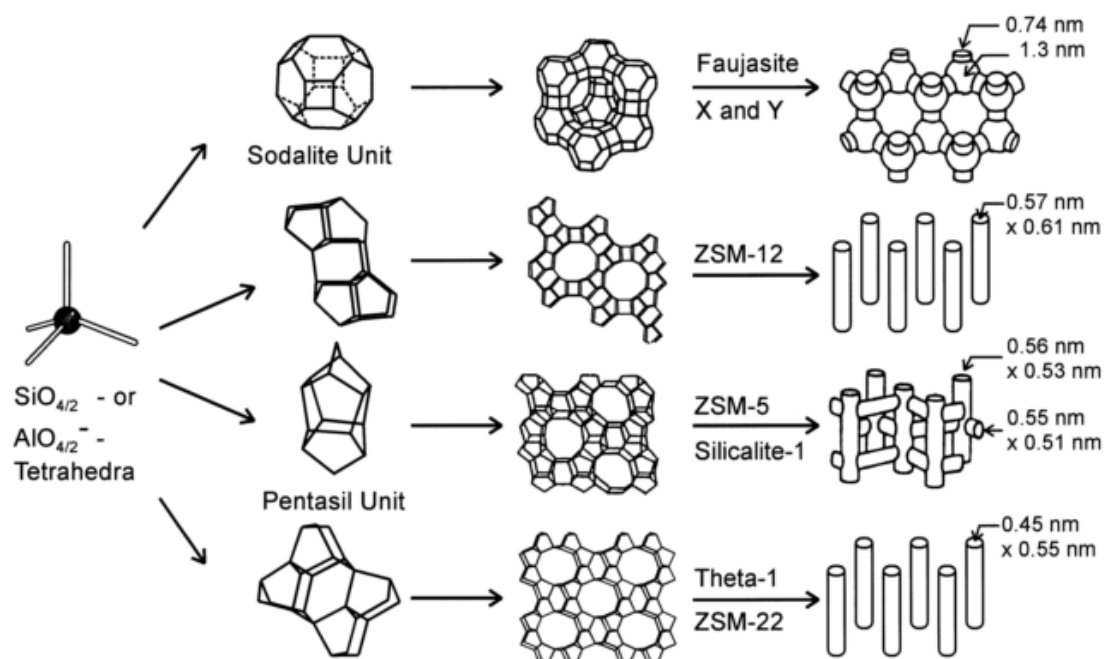


Figure 1-16. Structure and microporous system of Zeolite X, Zeolite Y, ZSM-12, ZSM-5 and ZSM-22.^[104]

Zeolites possess a high thermal and hydrothermal stability. Low-silica containing zeolites display decomposition temperatures up to 700 °C, whereas high-silica containing zeolites are stable up to 1300 °C.^[105] The resistance against acids increases with increasing silicon content.^[105] The nature of an acid site in a zeolite can be distinguished in Brønsted and Lewis acid sites. Acidity in zeolites is generated by substituting a SiO₄-tetrahedra by a AlO₄-tetrahedra. The negative charge in the framework has to be counter-balanced by a metal cation or a hydroxyl proton forming a weak Lewis acid site or strong Brønsted acid site.^[104]

The hydroxyl protons, which act as proton donors are located on oxygen bridges connecting SiO₄⁻ and AlO₄⁻-tetrahedra (Figure 1-17(i)). These hydroxyl groups are structural or bridging hydroxyl groups.^[106] External surface or framework defects are crowded by terminal silanol groups (Figure 1-17(iii)). Framework defects may occur by aluminium removal e.g. via calcination or hydrothermal treatment.

Lewis acidity in a zeolite results from framework defects or extraframework aluminium, which is not tetrahedrally bound in the framework (Figure 1-17(iv)).^[107] Extraframework aluminium is often an artefact of the synthesis process whereby excess of aluminium is not incorporated in the framework. It can be also generated by purposely steaming a zeolite.

Depending on dealumination, healing of the framework and defects by silicon migration, formation of hydroxyl groups at extraframework aluminium can occur (Figure 1-17(ii)).^[108]

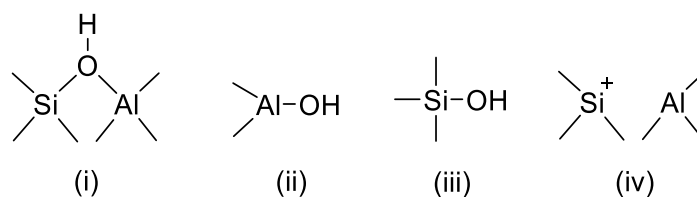


Figure 1-17. Different hydroxyl groups and acid sites, which are present in a zeolite.

Decreasing the Si/Al ratio leads to an increase of the number of acid sites if all the cations are populated by protons.^[104, 105] The strength of acid sites increases with decreasing aluminium content in a zeolite. The gain of acid strength overcompensates the decrease of density/concentration of acid sites.^[104] The acid site strength of zeolites increases up to a Si/Al ratio ~ 10 .^[104]

1.8 Transition Metal Phosphides

Conventional hydrotreating catalysts, namely sulfided NiMo and CoMo, may not be the most appropriate catalysts due to their instability in the absence of sulfur or presence of high concentrations of water. Furthermore, these sulfide catalysts contaminate products through sulfur leaching, and deactivate because of its removal from the surface by a reverse Mars-van Krevelen mechanism.^[109, 110] For the sulfide catalysts, sulfiding agents are added to the feedstock to avoid the catalyst deactivation. This leads to the formation of undesirable S-containing products with increasing investment. Many other materials have been tested ranging from supported metal catalysts, showing very high activity for hydrogenation and hydrogenolysis reactions^[61], to carbides and nitrides. However, metals suffer from deactivation under hydrotreating conditions decomposing sulfur-containing molecules to sulfur atoms, which form a deactivating layer of sulfur on the metal surface^[61]. Therefore, the possibility of blending biomass-derived oil with conventional fossil oil is reduced to supported transition metals. Carbides and nitrides may be more active than conventional sulfide catalysts but are thermodynamically not stable and readily convert to the corresponding sulfides and oxides.^[52, 62, 65-67] An interesting alternative is represented by phosphide of transition metals. Transition metal phosphides are a class of refractory metallic compounds showing simultaneously metallic and acidic properties^[71, 111] formed from the alloying of metals and phosphorus in which P sites have ligand effects on metal sites.^[112]

In general, metal phosphides catalysts can be divided into four groups based on the metal/phosphorous molar ratio as shown in Table 1-6.^[113]

Table 1-6. Classification of metal phosphides.^[113]

Metal phosphide classes	Examples of metal phosphides
Metal-rich phosphides	M_xP_y ($x > y$); Ni_2P , Co_2P , Ni_3P , etc.
Monophosphides	M_xP_y ($x = y$); MoP, WP, CoP, etc.
Phosphorous-rich phosphides	M_xP_y ($x < y$); NiP_2 , FeP_2 , etc.
Ionic phosphides	$M_x^{n+}P_y^{n-}$; Th_3P_4 , etc.

Metal phosphides show high chemical and thermal stability, strong mechanical properties, and good heat and electricity conductivity.^[113, 114] Except for phosphorous-rich metal phosphides the melting points are above 1000 °C.^[113] Especially transition metal phosphides show high inert properties against acids, bases and water, which is a favorable feature for hydroprocessing catalysts.^[113] Metal-rich phosphides show excellent activity for hydrogenation reactions.^[73] The metallic properties of metal phosphides are for each M_xP_y different.^[113] Moreover, phosphides do not form layered structures, and they potentially permit greater access to active corner and edge sites on the crystallite surface.^[114] Metal-rich phosphides combine the properties of metals and ceramics, such as very high thermal/chemical stability, good conduction of heat/electricity and strong mechanical properties (Table 1-7).^[72]

Table 1-7. Physical properties of metal-rich phosphides.^[72]

Ceramic properties		Metallic properties	
Melting point, °C	830-1530	Electrical resistivity, $\mu\Omega\text{cm}$	900-25000
Microhardness, $\text{kg}\cdot\text{mm}^{-2}$	600-1100	Magnetic susceptibility, $10^6 \text{ cm}^3\cdot\text{mol}^{-1}$	110-620
Heat of formation, $\text{kJ}\cdot\text{mol}^{-1}$	30-180	Heat capacity, $\text{J}\cdot(\text{mol}\cdot^\circ\text{C})^{-1}$	20-50

In the last years, metal phosphides have received great attention due to their high activity for hydrodenitrogenation and hydrodesulfurization of petroleum feedstocks.^[115-117] They have been found structurally stable under S- and O-containing conditions^[72-75] and they represent an interesting option as catalyst for hydrodefunctionalization of biomass derived molecules.^[39, 68-71] Among the transition metal phosphides, Ni_2P has been studied in detail and has been reported as the most active phosphide for hydrodesulfurization (HDS).^[68-72] Bulk and supported (usually on SiO_2) metal phosphides (i.e., MoP, WP, Fe_2P , Co_2P , Ni_2P) have been shown active in the HDO of aromatic model compounds representative of lignin pyrolysis oil.^[73-76] Metal phosphides were found to be active and stable when dispersed on SiO_2 in the hydrodeoxygenation of 2-methyltetrahydrofuran, dibenzofuran, methyl laurate, guaiacol and anisole.^[70, 71, 118-122] The acidity and the role of the support has been furthermore investigated studying the effect of Al_2O_3 , Al-SBA-15, SBA-15, MCM-41, activated carbon and zirconia in the hydrodeoxygenation of phenol, guaiacol, methyl oleate, methyl laurate and bio-oils.^{[68, 123-}

^{127]} Noble metal phosphides were also tested in the hydrodeoxygenation of furan, where their activity was found to be higher compared to the corresponding metal.^[128]

1.8.1 Structure of Ni₂P, MoP and WP

In this thesis three phosphides of common base metals, i.e., Ni₂P, MoP and WP, were synthesized and tested for the hydroconversion of triglycerides to fuel. Ni₂P, MoP and WP are metal rich phosphides with covalent bonding and metal-like properties, which make these catalysts suitable for hydrogenation and hydrogenolysis. MoP and WP are structurally similar, with hexagonal layers of P atoms (in the center of triangular prisms) with Mo and W in trigonal prismatic positions.^[115] There is only one kind of metal and one kind of P positions. In particular, MoP has a WC hexagonal structure with the nonmetal-containing prisms stacked on top of each other whereas WP adopts a MnP type structure where the P-prisms is displaced laterally one-half lattice spacing.^[115] The structure of Ni₂P is orthorhombic and has two kinds of metal sites, i.e., distorted tetrahedron, and square pyramid sites. P atoms, coordinating four or five Ni atoms, are located in face-capped trigonal prisms.^[115] In general, P atoms influence the distance between the metal atoms (geometrical effect), compared with the parent metals. Moreover, ligand effects induce charge transfer between metal and P.^[75, 112] Thus, although the catalytic behaviors of phosphide surfaces resemble those of the parent metals, those geometrical and ligand effects render lower reactivity but higher stability in phosphides. MoP and WP have a less density of metal d states near the Fermi level than Ni₂P and consequently they show larger positive charge than Ni. However, among the different Ni- based phosphides, Ni₂P is the one showing the highest positive charge.^[121]

1.9 Scope of the Thesis

The scope of this doctoral thesis is to study the hydroconversion of microalgae and fatty acids to green fuel using active and stable transition metal phosphides as an alternative catalytic system to the more expensive and less stable pure metals or sulfide materials. Promising results in the hydrodeoxygenation of fatty acids have been reported in literature on supported transition metal phosphides. However, the intrinsic properties of such phosphides are hardly understood and the possibility to explore the hydrogenation ability of this class of catalysts during the hydrocracking of paraffins is scarcely addressed.

In Chapter 2 the effect of the transition metal phosphides was explored for the hydrodeoxygenation of palmitic acid by comparing the activity of bulk MoP and Ni₂P. The

properties of the latter were improved with a modified synthesis procedure. Furthermore, the two metal phosphides were compared supported on γ -Al₂O₃ in order to determine the impact of the support on the physicochemical and kinetic properties of the phosphides. Finally, a study focused on Ni₂P-based materials was performed by comparing Ni₂P/Al₂O₃ samples prepared by two synthesis routes which led to different features of the supported phase. An exploratory study of amorphous AlPO₄ applied as a support for Ni₂P and an optimization study for the synthesis of MoP/Al₂O₃ were also shown in this Chapter. However, the support might mask the intrinsic activity on phosphides by mediating some steps of the reaction network towards deoxygenated products or by accumulating P, which renders uncertainty to the identification of supported phases. Therefore, in Chapter 3 three unsupported phosphides of common base metals, i.e., WP, MoP, and Ni₂P were compared for the hydrodeoxygenation of palmitic acid, the corresponding reaction products and a triglyceride mixture. The synthesis was achieved in the presence of citric acid as chelating agent in order to prevent sintering during synthesis and to counteract the low dispersion associated to the lack of a support. In Chapter 3 the results allowed to describe changes in the trends of intrinsic activities with temperature and to correlate the catalytic properties of the materials with measurements of metal surface and concentration of acid sites.

Having shown the stability of the transition metal phosphides during the hydrodeoxygenation of fatty acids and their strong hydrogenation function, in Chapter 4 supported metal phosphides were tested in the hydrocracking of paraffins, in order to evaluate the possibility to use this class of material to perform the hydroconversion of triglycerides to green fuel. *n*-Hexadecane was selected as ideal model compound to represent the alkanes obtained from the deoxygenation of fatty acids derived from biomass. Ni- and W-based phosphides were studied supported on SiO₂ and on zeolite H-USY in order to investigate the hydrogenolysis selectivity of the materials and the effect of the acid support on the product distribution. The zeolite H-USY was selected in order to obtain Brønsted acid sites minimizing diffusion limitation in its relatively large pores. Mechanical mixtures of SiO₂-supported metal phosphides with zeolites were also studied in order to evaluate the effect of the metal loading in the hydrocracking performance avoiding possible effects of the phosphorous precursor on the zeolite.

In Chapter 5, Ni₂P-based catalysts supported on H-USY were compared with Ni-based materials for the hydrocracking of *n*-hexadecane. In particular, the effect of the metal loading and of the metal-acid balance on the stability and selectivity of the catalysts was investigated.

In the case of the Ni₂P-based materials, the effect of the metal/phosphorous molar ratio during the preparation of the catalysts was also addressed.

1.10 References

- [1] International Agency Society, *Key world energy statistics*, **2016**.
- [2] World Energy Resources 2013 Survey, *World energy council*, **2013**.
- [3] P. E. Hodgson, *Nuclear Power and Energy Crisis*, **2008**, 50, 238-246.
- [4] International Energy Agency, *World Energy Outlook 2011*, **2011**.
- [5] J. Van Gerpen, *Fuel Process. Technol.*, **2005**, 86, 1097-1107.
- [6] <https://www.co2.earth/global-co2-emissions>.
- [7] Renewable Energy Policy Network for the 21st Century, *Renewables 2016 Global Status Report*, **2016**.
- [8] <http://www1.eere.energy.gov/biomass/publications.html>.
- [9] J. Zakzeski, P. C. A. Bruijninx, A. L. Jongerius, B. M. Weckhuysen, *Chem. Rev.*, **2010**, 110, 3552-3599.
- [10] European Parliament and the Council, *Directive 2009/28/EC*, **2009**.
- [11] J. Ancheyta, M. S. Rana, *Future Technology in Heavy Oil Processing*, **2004**.
<http://www.eolss.net/sample-chapters/c08/e6-185-22.pdf>
- [12] J. H. Gary, G. E. Handwerk, *Petroleum Refining Technology and Economics (2nd ed.)*, Marcel Dekker, Inc. ISBN 978-0-8247-7150-8, **1984**.
- [13] D. S. J. Jones, P. R. Pujadó, *Handbook of Petroleum Processing*, Springer Verlag: Dordrecht, The Netherlands, **2008**.
- [14] J. Ancheyta, J. G. Speight, *Hydroprocessing of Heavy Oils and Residua*, Taylor & Francis Group, **2007**.
- [15] K. Owen, T. Coley, *Automotive Fuels Reference Book*, Society of Automotive Engineers, Inc., 2nd edition, **1995**.
- [16] Washington, D.C.: Energy Information Administration, *Annual Energy Outlook 2006 with Projections to 2030*, **2006**, DOE/EIA-0383(2006), 52-54.
- [17] http://www.gasification-syngas.org/Docs/Workshops/2007/Indianapolis/06Cicero%20GTC_June2007.pdf.
- [18] M. E. Dry, *J. Chem. Technol. Biotechnol.*, **2002**, 77, 43-50.
- [19] J. G. Speight, *Synthetic Fuels Handbook: Properties, Process, and Performance*. McGraw-Hill Professional, ISBN 978-0-07-149023-8, **2008**, 9-10.

- [20] ENI spa, *World Oil and Gas Review 2012*, Rome, **2012**.
- [21] Exxon Mobil, *Methanol to Gasoline Technology An Alternative for Liquid Fuel Production*, Norris conference center Texas, **2014**.
- [22] P. K. Swain, L. M. Das, S. N. Naik, *Renewable and Sustainable Energy Reviews*, **2011**, *15*, 4917-4933
- [23] European Commission, *Renewable energy statistics*, **2012**.
- [24] S. N. Naik, V. V. Goud, P. K. Rout, A. K. Dalai, *Renewable and Sustainable Energy Reviews*, **2010**, *14*, 578-597.
- [25] G. W. Huber, J. A. Dumesic, *Catal. Today*, **2006**, *111*, 119-132.
- [26] J. Lu, C. Sheahan, P. Fu, *Energy & Environmental Science*, **2011**, *4*, 2451-2466.
- [27] R. E. H. Sims, W. Mabeeb, J. N. Saddlerc, M. Taylord, *Bioresource Technology*, **2010**, *101*, 1570-1580.
- [28] S. Zinoviev, F. Müller-Langer, P. Das, N. Bertero, P. Fornasiero, M. Kaltschmitt, G. Centi, S. Miertus, *ChemSusChem*, **2010**, *3*, 1106-1133.
- [29] A. Ragauskas, C. K. Williams, B. H. Davison, G. Britovsek, J. Cairney, C. A. Eckert, W. J. Frederick, J. P. Hallett, D. J. Leak, C. L. Liotta, J. R. Mielenz, R. Murphy, R. Templer, T. Tschaplinski, *Science*, **2006**, *311*, 484-489.
- [30] Y. Pu, D. Zhang, P. M. Singh, A. J. Ragauskas, *Biofuels, bioproducts and biorefining*, **2008**, *2*, 58-73.
- [31] S. Lestari, P. Mäki-Arvela, J. Beltramini, G. Q. Max Lu, D. Yu. Murzin, *ChemSusChem*, **2009**, *2*, 1109-1119.
- [32] R. Sotelo-Boyás, F. Trejo-Zárraga, F. de Jesús Hernández-Loyo, *InTech*, **2010**, *8*, 187-216.
- [33] L. Brennan, P. Owende, *Renewable and Sustainable Energy Reviews*, **2010**, *14*, 557-577.
- [34] Y. Chisti, *Biofuels*, **2010**, *1*, 233-235.
- [35] P. M. Schenk, S. R. Thomas-Hall, E. Stephens, U. C. Marx, J. H. Mussnug, C. Posten, O. Kruse, B. Hankamer, *Bioenerg. Res.*, **2008**, *1*, 20-43.
- [36] T. M. Mata, A. A. Martins, N. S. Caetano, *Renewable Sustainable Energy Rev.*, **2010**, *14*, 217-232.
- [37] G. W. Huber, S. Iborra, A. Corma, *Chem. Rev.*, **2006**, *106*, 4044-4098.
- [38] Y. Chisti, *Biotechnol. Adv.*, **2007**, *25*, 294-3065.
- [39] E. Furimsky, *Appl. Catal. A*, **2000**, *199*, 147-190.
- [40] K. Sipilä, E. Kuoppala, L. Fagernäs, A. Oasmaa, *Biomass Bioenergy*, **1998**, *14*, 103-113.
- [41] M. Garcia-Perez, A. Chaala, H. Pakdel, D. Kretschmer, C. Roy, *Biomass Bioenergy*, **2007**, *31*, 222-242.

- [42] J. Kent, *Handbook of Industrial Chemistry and Biotechnology*, New York, USA: Springer-Verlag, **2007**.
- [43] F. Ma, M. A. Hanna, *Bioresour. Technol.*, **1999**, *70*, 1-15.
- [44] H. Fukuda, A. Kondo, H. Noda, J. Biosci, *Bioeng.*, **2001**, *92*, 405-416.
- [45] L. C. Meher, D. Vidya Sagar, S. N. Naik, *Renew. Sustain. Energy. Rev.*, **2006**, *10*, 248-268.
- [46] R. Sharma, Y. Chisti, U. C. Banerjee, *Biotechnol. Adv.*, **2001**, *19*, 627-662.
- [47] J. V. Gerpen, G. Knothe, *The biodiesel handbook*, AOCS Press: Champaign, IL, **2005**.
- [48] J. A. Melero, J. Iglesias, G. Morales, *Green Chem.*, **2009**, *11*, 1285-1308.
- [49] B. X. Peng, Q. Shu, J. F. Wang, G. R. Wang, D. Z. Wang, M. H. Han, *Process. Saf. Environ. Prot.*, **2008**, *86*, 441-447.
- [50] M. W. Balakos, E. E. Hernandez, *Catalysis Today*, **1997**, *35*, 415-425.
- [51] J. Ancheyta, F. Trejo, M. S. Rana, *Asphaltenes: Chemical Transformation during Hydroprocessing of Heavy Oils*, New York: CRC Press, **2009**.
- [52] R. Sotelo-Boyás, Y. Liu, T. Minowa, *Ind. Eng. Chem. Res.*, **2011**, *50*, 2791-2799.
- [53] P. Šimáček, D. Kubicka, G. Šebor, M. Pospíšil, *Fuel*, **2009**, *88*, 456-460.
- [54] G. W. Huber, P. O'Connor, A. Corma, *Appl. Catal. A*, **2007**, *329*, 120-129.
- [55] E. G. Baker, D. C. Elliot, *Method for Upgrading Oils Containing Hydrocarbon Compounds to Highly Aromatic Gasoline*. US Patent 5, 180, 868, **1993**.
- [56] M. F. Ali, B. M. El Ali, J. G. Speight, *Handbook of Industrial Chemistry*, McGraw-Hill, **2005**.
- [57] M. Nasikin, B. H. Susanto, A. Hirsaman, A. Wijanarko, *World Appl. Sci. J.*, **2009**, *5*, 74-79.
- [58] S. Mikkonen, *Hydrocarbon Processing*, **2008**, *87*, 63-66.
- [59] B. Peng, Y. Yao, C. Zhao, *Angew. Chem. Int. Ed.*, **2012**, *124*, 2114-2117.
- [60] M. Snåre, I. Kubičková, P. Mäki-Arvela, K. Eränen, D. Y. Murzin, *Ind. Eng. Chem. Res.*, **2006**, *45*, 5708-5715.
- [61] B. Diaz, S. J. Sawhill, D. H. Bale, R. Main, D. C. Phillips, S. Korlann, R. Self, M. E. Bussell, *Catal. Today*, **2003**, *86*, 191-209.
- [62] I. V. Deliy, E. N. Vlasova, A. L. Nuzhdin, *RSC Advances*, **2013**, *5*, 2242-2250.
- [63] O. I. Senol, T. R. Viljava, A. O. I. Krause, *Catalysis Today*, **2005**, *100*, 331-335.
- [64] E. Furimsky, F. E. Massoth, *Catalysis Today*, **1999**, *52*, 381-495.
- [65] S.T. Oyama, *Catal. Today*, **1992**, *15*, 179-200.

- [66] Y. Liu, R. Sotelo-Boyás, K. Murata, T. Minowa, K. Sakanishi, *Energy Fuels*, **2011**, *25*, 4675–4685.
- [67] K. Murata, Y. Liu, M. Inaba, I. Takahara, *Energy Fuels*, **2010**, *24*, 2404–2409.
- [68] Y. Yang, C. Ochoa-Hernández, V. A. De la Peña O’ Shea, J. M. Coronado, D. P. Serrano, *ACS Catal.*, **2012**, *2*, 592-598.
- [69] V. M. L. Whiffen, K. J. Smith, *Energy Fuels*, **2010**, *24*, 4728-4737.
- [70] H. Y. Zhao, D. Li, P. Bui, S.T. Oyama, *Appl. Catal. A*, **2011**, *391*, 305-310.
- [71] K. L. Li, R. J. Wang, J. X. Chen, *Energy Fuels*, **2011**, *25*, 854-863.
- [72] S.T. Oyama, T. Gott, H. Zhao, Y.-K. Lee, *Catal. Today*, **2009**, *143*, 94-107.
- [73] R. Prins, M. E. Bussell, *Catal. Lett.*, **2012**, *142*, 1413-1436.
- [74] A. Rodriguez, J. Kim, J. C. Hanson, S. J. Sawhill, M. E. Bussell, *J. Phys. Chem. B.*, **2003**, *107*, 6276-6285.
- [75] S. Sawhill, K. Layman, D. Vanwyk, M. Engelhard, C. Wang, M. Bussell, *J. Catal.*, **2005**, *231*, 300-313.
- [76] A. Primo, H. Garcia, *Chemical Society Reviews*, **2014**, *43*, 7548-7561.
- [77] J. Weitkamp, *ChemCatChem*, **2012**, *4*, 292-306.
- [78] R. F. Sullivan, J. W. Scott, *Heterogeneous Catalysis*, American Chemical Society, Washington, DC, **1983**, 222, 293-313.
- [79] J. Scherzer, A. J. Gruia, *Hydrocracking science and technology*, Marcel Dekker, Inc., **1996**.
- [80] K. Owen, T. Coley, *Automotive fuels reference book*, Society of Automotive Engineers, **1995**.
- [81] A. de Klerk, *Energy and Environmental Science*, **2011**, *4*, 1177-1205.
- [82] C. Bouchy, G. Hastoy, E. Guillon, J.A. Martens, *Oil & Gas Science and Technology - Rev. IFP*, **2009**, *64*, 91-112.
- [83] V. Calemma, C. Gambaro, W.O. Parker Jr, R. Carbone, R. Giardino, P. Scorletti, *Catal. Today*, **2010**, *149*, 40-46.
- [84] J. Spivey, Y. F. Han, K. M. Dooley, R. Jin, F. Meunier, W. L. Dai, Z. R. Tshentu, D. Murzin, M. O. Coppens, A. Efstathiou, *Catalysis: Volume 28*, Royal Society of Chemistry, **2016**.
- [85] I. E. Maxwell, J. K. Minderhoud, W. H. J. Stork, J. A. R. van Veen, *Handbook of Heterogeneous Catalysis*, VCH, Weinheim, **1997**, 2017-2038.
- [86] P. R. Robinson, G. E. Dolbear, *Practical Advances in Petroleum Processing*, Springer, New York, **2006**, 177-218.
- [87] S. Zhang, D. Liu, W. Deng, G. Que, *Energy & Fuels*, **2007**, *21*, 3057-3062.

- [88] H. L. Coonradt, W. E. Garwood, *Ind. Eng. Chem. Proc. Des. Dev.*, **1964**, *3*, 38-45.
- [89] P. B. Weisz, *Adv. Catal.*, **1962**, *13*, 137-190.
- [90] J. H. Sinfelt, *Adv. Catal.*, **1973**, *23*, 91-119.
- [91] J. Weitkamp, P. A. Jacobs, J. A. Martens, *Appl. Catal.*, **1983**, *8*, 123-141.
- [92] K. Hedden, J. Weitkamp, *Chem. Eng. Technol.*, **1975**, *47*, 505-513.
- [93] Y. Rezgui, M. Guemini, *Applied Catalysis A: General*, **2005**, *282*, 45-53.
- [94] R. Anderson, N. R. Avery, *Journal of Catalysis*, **1967**, *8*, 48-63.
- [95] H. F. Wallace, K. E. Hayes, *Journal of Catalysis*, **1973**, *29*, 83-91.
- [96] W. J. J. Welters, O. H. van der Waerden, H. W. Zandbergen, V. H. J. de Beer, R. A. van Santen, *Industrial & Engineering Chemistry Research*, **1995**, *34*, 1156-1165.
- [97] I. E. Maxwell, *Catalysis Today*, **1987**, *1*, 385-413.
- [98] D. L. Trimm, S. Akashah, A. Bishara, M. Absi-Halabi, *Catalysts in Petroleum Refining 1989*, Elsevier Science, **1990**.
- [99] L. Kubelková, B. Wichterlová, P. A. Jacobs, N. I. Jaeger, *Zeolite Chemistry and Catalysis*, Elsevier Science, **1991**.
- [100] J. Čejka, *Introduction to Zeolite Science and Practice*, Elsevier Science & Technology Books, **2007**.
- [101] M. Bertau, A. Müller, P. Fröhlich, M. Katzberg, *Industrielle Anorganische Chemie*, Wiley-VCH, **2013**.
- [102] <http://webmineral.com/dana/class.shtml#77.1> 09.0082016.
- [103] <http://www.iza-structure.org/databases/>.
- [104] J. Weitkamp, *Solid State Ionics*, **2000**, *131*, 175-188.
- [105] S. M. Auerbach, K. A. Carrado, P. K. Dutta, *Handbook of Zeolite Science and Technology*, Taylor & Francis, **2003**.
- [106] S. Kulprathipanja, *Zeolites in Industrial Separation and Catalysis*, Wiley, **2010**.
- [107] J. Shi, Y. Wang, W. Yang, Y. Tang, Z. Xie, *Chemical Society Reviews*, **2015**, *44*, 8877-8903.
- [108] M. Elanany, M. Koyama, M. Kubo, E. Broclawik, A. Miyamoto, *Applied Surface Science*, **2005**, *246*, 96-101.
- [109] E. Laurent, B. Delmon, *J. Catal.*, **1994**, *146*, 281-291.
- [110] T. R. Viljava, R. S. Komulanien, A. O. I. Krause, *Catal. Today*, **2000**, *60*, 83-92.
- [111] Y. K. Lee, S. T. Oyama, *J. Catal.*, **2006**, *239*, 376-389.
- [112] P. Liu, J. A. Rodriguez, T. Asakura, J. Gomes, K. Nakamura, *J. Phys. Chem.*, **2005**, *109*, 4575-4583.

- [113] D. E. C. Corbridge, *Phosphorus: an outline of its chemistry, biochemistry and technology*, Elsevier Scientific Publishing Company, **1978**.
- [114] Q. Guan, W. Li, M. Zhang, K. Tao, *Journal of Catalysis*, **2009**, 263, 1-3.
- [115] S. T. Oyama, *J. Catal.*, **2003**, 216, 343-352.
- [116] A. Infantes-Molina, C. Moreno-León, B. Pawelec, J. L.G. Fierro, E. Rodríguez-Castellón, A. Jiménez-López, *Appl. Catal. B.*, **2012**, 113–114, 87-99.
- [117] J. A. Cecilia, A. Infantes-Molina, E. Rodríguez-Castellón, A. Jiménez-López, *Appl. Catal. B.*, **2009**, 92, 100-113.
- [118] P. Bui, J. A. Cecilia, S. T. Oyama, A. Takagaki, A. Infantes-Molina, H. Zhao, D. Li, E. Rodríguez-Castellón, A. J. López, *Journal of Catalysis*, **2012**, 294, 184-198.
- [119] N. Koike, S. Hosokai, A. Takagaki, S. Nishimura, R. Kikuchi, K. Ebitani, Y. Suzuki, S. T. Oyama, *Journal of Catalysis*, **2016**, 333, 115-126.
- [120] J. A. Cecilia, A. Infantes-Molina, E. Rodríguez-Castellón, A. Jiménez-López, S.T. Oyama, *Applied Catalysis B: Environmental*, **2013**, 136, 140-149.
- [121] J. Chen, H. Shi, L. Li, K. Li, *Applied Catalysis B: Environmental*, **2014**, 144, 870-884.
- [122] M. B. Griffin, F. G. Baddour, S. E. Habas, D. A. Ruddy, J. A. Schaidle, *Top Catal.*, **2016**, 59, 124-137.
- [123] A. Berenguer, T. M. Sankaranarayanan, G. Gómez, I. Moreno, J. M. Coronado, P. Pizarro, D. P. Serrano, *Green Chem.*, **2016**, 18, 1938-1951.
- [124] Y. Yang, J. Chen, H. Shi, *Energy Fuels*, **2013**, 27, 3400-3409.
- [125] Q. Guan, F. Wan, F. Han, Z. Liu, W. Li, *Catalysis Today*, **2016**, 259, 467-473.
- [126] C. Guo, K. T. V. Rao, E. Reyhanitash, Z. Yuan, S. Rohani, C. Xu, *AIChE Journal*, **2016**, 62, 3664-3672.
- [127] S. K. Wu, P. C. Lai, Y. C. Lin, H. P. Wan, H. T. Lee, Y. H. Chang, *ACS Sustainable Chem. Eng.*, **2013**, 1, 349-358.
- [128] R. H. Bowker, M. C. Smith, M. L. Pease, K. M. Slenkamp, L. Kovarik, M. E. Bussell, *ACS Catal.*, **2011**, 1, 917-922.

Chapter 2

Bulk and γ - Al_2O_3 -supported Ni_2P and MoP for hydrodeoxygenation of palmitic acid

The use of a series of bulk and supported Ni_2P and MoP materials in the hydrodeoxygenation of palmitic acid, shows that their catalytic performance can be tuned by the presence of Al_2O_3 as a support. Al_2O_3 promotes acid-catalyzed pathways, and influences the phosphide functionality. A series of strategies can be followed to successfully decrease the phosphide particle size, i.e., the use of citric acid (applied to bulk Ni_2P), and the use of low reduction temperatures (applied to $\text{Ni}_2\text{P}/\text{Al}_2\text{O}_3$) during the preparation steps. The effects of synthesis parameters and the support on the properties of the phosphides were determined by, e.g., X-ray diffraction, transmission electron microscopy, BET analysis, CO adsorption and NH_3 -TPD. Small particle size of phosphides does not necessarily lead to a large exposed surface of metal phosphide due to residual carbon or to agglomeration of phosphide particles. The specific activities (per gram of material) follow the trend $\text{MoP}/\text{Al}_2\text{O}_3$ -TPR (high temperature synthesis) < Ni_2P -CA (citric acid in the synthesis) < $\text{Ni}_2\text{P}/\text{Al}_2\text{O}_3$ -LT (low temperature synthesis) < $\text{Ni}_2\text{P}/\text{Al}_2\text{O}_3$ -TPR < MoP, whereas the rates normalized per metal site (TOF) followed the trend: $\text{MoP}/\text{Al}_2\text{O}_3$ -TPR < MoP < Ni_2P -CA < $\text{Ni}_2\text{P}/\text{Al}_2\text{O}_3$ -TPR < $\text{Ni}_2\text{P}/\text{Al}_2\text{O}_3$ -LT. Thus, the Ni_2P phase is intrinsically more active than MoP, although the overall activity is determined by the interplay between intrinsic activity and exposed active surface. The conversion of palmitic acid was achieved in a trickle bed flow reactor at varying temperature and residence times. The model reaction follows three different pathway: hydrodeoxygenation (HDO): $\text{C}_{15}\text{H}_{31}\text{COOH} \rightarrow \text{C}_{15}\text{H}_{31}\text{CHO} \rightarrow \text{C}_{16}\text{H}_{33}\text{OH} \rightarrow \text{C}_{16}\text{H}_{34}$; decarboxylation/decarbonylation (DCO): $\text{C}_{15}\text{H}_{31}\text{COOH} \rightarrow [\text{C}_{15}\text{H}_{31}\text{CHO}] \rightarrow \text{C}_{15}\text{H}_{32}$; and esterification: $\text{C}_{15}\text{H}_{31}\text{COOH} + \text{C}_{16}\text{H}_{33}\text{OH} \rightarrow \text{C}_{15}\text{H}_{31}\text{COOC}_{16}\text{H}_{33}$. The presence of Al_2O_3 increases the esterification rates due to relative high acidity, and makes the supported Ni_2P phase more selective towards C-C bond cleavage than bulk Ni_2P or $\text{MoP}/\text{Al}_2\text{O}_3$ -TPR.

This chapter is based on:

M. Peroni, G. Mancino, E. Baráth, O. Y. Gutiérrez, J. A. Lercher, Applied Catalysis B: Environmental, 2016, 180, 301-311. Reprinted with permission from Elsevier, 2016

2.1 Introduction

Due to environmental concerns, legislations have driven increasing contribution of biomass derived oil to fuel production. Therefore, refineries have to treat feedstocks with increasing concentrations of oxygen, which has to be removed in order to meet fuel requirements *via* hydrodeoxygenation (HDO).^[1] In this scenario, typical Co-Mo or Ni-Mo sulfide materials may not be the most appropriate catalysts due to their instability in the absence of sulfur or presence of high concentrations of water. In response to this challenge, many other materials have been tested ranging from supported metal catalysts to carbides and nitrides.^[2–6] However, the application of transition metals reduces the possibility of blending biomass-derived oil with conventional fossil oil, because the high concentrations of sulfur and nitrogen in the latter could adversely impact on the performance of metal catalysts. Carbides and nitrides may be more active than conventional sulfide catalysts but are thermodynamically not stable and readily convert to the corresponding sulfides and oxides.

An interesting alternative to the materials mentioned before are phosphide of transition metals. These materials have been proven very active for hydrodesulfurization and, more importantly, have been found structurally stable under S- and O-containing conditions (although they may undergo surface modifications).^[7–10] Ni₂P (usually supported on SiO₂) has been studied in detail and has been reported as the most active phosphide for hydrodesulfurization (HDS).^[7–11] Fewer studies focused on HDO applications of phosphide materials are found in literature. Namely, bulk and SiO₂-supported phosphides of base metals (i.e., MoP, WP, Fe₂P, Co₂P, Ni₂P) have been shown to be active in the HDO of aromatic model compounds representative of lignin-based pyrolysis oil.^[12–15]

In this work, we have prepared bulk and alumina supported Ni₂P and MoP to explore their catalytic activity in the hydrodeoxygenation pathways of palmitic acid, which has been selected as an ideal model compound for bio-oil derived from, e.g., algae (third generation biofuel).^[16,17] The phosphides of Ni and Mo have been selected because these elements are two of the most common base metals in hydrotreating catalysts. Additionally, we have tested a few preparation methods in order to investigate the intrinsic properties of the phosphide phases and those of the carrier, as well as the possible synergy between them.

The effect of the transition metal was explored by comparing the activity of bulk MoP and Ni₂P. The latter was prepared with a modified synthesis procedure in order to obtain reasonable surface area. Furthermore, these two phosphides were also prepared on Al₂O₃ in order to determine the impact of the support on the physicochemical and kinetic properties of the

phosphides. Finally, a study focused on Ni_2P -based materials was performed by comparing $\text{Ni}_2\text{P}/\text{Al}_2\text{O}_3$ samples prepared by two synthesis routes which lead to different features of the supported phase. An exploratory study of amorphous AlPO_4 applied as a support for Ni_2P and an optimization study for the synthesis of $\text{MoP}/\text{Al}_2\text{O}_3$ are presented in the Appendix.

2.2 Experimental

2.2.1 Synthesis of the catalysts: Temperature programmed reduction method (TPR)

Supported and unsupported nickel phosphide (Ni_2P) and molybdenum phosphide (MoP) were prepared by a temperature programmed reduction method^[4] starting from the correspondent metal salt ($\text{Ni}(\text{NO}_3)_2 \cdot 6\text{H}_2\text{O}$ from Alfa Aesar or $(\text{NH}_4)_6\text{Mo}_7\text{O}_{24} \cdot 4\text{H}_2\text{O}$ from Sigma Aldrich) and $(\text{NH}_4)_2\text{HPO}_4$ (Sigma Aldrich) dissolved in water. The solutions were prepared with a Ni/P molar ratio of 0.5 and a Mo/P molar ratio of 1. For unsupported catalysts, the solution was dried overnight at 383 K. The solid recovered was thermally treated in air at 773 K for 5 hours ($5 \text{ K} \cdot \text{min}^{-1}$) and afterwards in H_2 for 2 hours at 923 K (heated at $5 \text{ K} \cdot \text{min}^{-1}$ from room temperature to 573 K and at $2 \text{ K} \cdot \text{min}^{-1}$ from 573 K to 923 K).

Ni_2P and MoP supported on Al_2O_3 (SCFa140 Sasol, porosity of $0.8 \text{ ml} \cdot \text{g}^{-1}$), were prepared through incipient wetness impregnation of the support with solutions of the metal salt ($\text{Ni}(\text{NO}_3)_2 \cdot 6\text{H}_2\text{O}$ or $(\text{NH}_4)_6\text{Mo}_7\text{O}_{24} \cdot 4\text{H}_2\text{O}$) and $(\text{NH}_4)_2\text{HPO}_4$. The metal/P molar ratio was 0.5 whereas the content of metal was 10 wt. % in the initial solution. After drying at 383 K, the impregnated samples were then treated in air at 773 K for 5 hours ($5 \text{ K} \cdot \text{min}^{-1}$) and reduced in H_2 (up to 923 K for Ni_2P and 1073 K for MoP).

2.2.2 Synthesis of the catalysts: Low temperature method (LT)

Ni_2P supported on Al_2O_3 , was synthesized with a method based on a low temperature treatment in flowing N_2 .^[30] The sample was prepared by impregnating a certain amount of commercial Al_2O_3 (SCFa140 Sasol, porosity of $0.8 \text{ ml} \cdot \text{g}^{-1}$) with an aqueous solution of sodium hypophosphite ($\text{NaH}_2\text{PO}_2 \cdot \text{H}_2\text{O}$, Sigma Aldrich) and nickel chloride ($\text{NiCl}_2 \cdot 6\text{H}_2\text{O}$, Sigma Aldrich). The Ni/P molar ratio was 0.5 and the metal content in the initial solution was 10 wt. %. After drying, the impregnated solid was heated in a fixed-bed reactor to 573 K and kept for 1 h in flowing N_2 ($30 \text{ ml} \cdot \text{min}^{-1}$). The material was cooled to room temperature under N_2 and was washed several times with deionized water to remove ionic impurities.

2.2.3 Synthesis of the catalysts: Citric acid method (CA)

A bulk Ni₂P sample was prepared following the TPR procedure but adding citric acid to the aqueous solution during the initial precipitation of the precursor salts.^[18,19] Citric acid (CA) was added to the salt solution to give a 2:1 CA:metal molar ratio. The solution was kept in an oil bath at 363 K for 3 days. The obtained gel was dried at 393 K for two days. Prior to calcination at 773 K, a thermal treatment step at 513 K for 1 h in air was required because of the high exothermicity of the decomposition of citric acid. During this step, the concentration of O₂ in N₂ was increased slowly from 1 vol. % to 20 vol. %. Further reduction in H₂ was performed for 2 hours at 923 K. All the catalysts were passivated in a flow of 1 vol. % O₂ in N₂ (20 ml·min⁻¹) to stabilize the catalysts for handling after reduction or inert treatment.

2.2.4 Characterization of the catalysts

N₂-physisorption isotherms were measured at liquid nitrogen temperature using a PMI automated sorptometer (Sorptomatic 1960). The samples were outgassed at 520 K for 2 h prior to N₂ adsorption. The data were employed to determine the texture of the oxide precursors, that is, surface area (BET analysis), pore volume, and pore size distribution (BJH method). X-ray powder diffraction (XRD) was performed with a Phillips/PANalytical's X'Pert PRO system (Cu K α radiation, 0.154056 nm) operating at 45 kV and 40 mA. The XRD patterns were recorded using a scan speed of 1.08 °·min⁻¹. TEM images were recorded on a JEM-2010 JEOL transmission microscope operated at 120 kV. Samples were prepared by depositing drops of suspensions of the materials in ethanol on Cu grids with supporting carbon films. The statistical analysis of particle size was performed by measuring at least 300 particles per sample distributed in micrographs taken from different regions of the sample. The elemental contents of Mo, Ni and P in the materials were measured with a photometer Shimadzu UV-160. Carbon was quantified with an EURO EA (HEKA tech) instrument. CO chemisorption was applied to probe the metal sites by passing CO pulses (0.33 vol. % CO in He) through samples of the materials at 298 K. The CO uptake was monitored by a Balzers mass spectrometer (m/z=28). Prior to the CO pulses, the passivated materials were activated in H₂ at 723 K for 2 h (Ni₂P/Al₂O₃ LT was reactivated at 573 K). The acidity was determined by temperature programmed desorption of NH₃ in a homemade vacuum-TPD set-up. After thermal treatment of the materials in hydrogen at 723 K, 1 mbar ammonia was adsorbed at 373 K for 1 h. The TPD was carried out up to 1043 K after outgassing physisorbed NH₃ for 4 h. The evolution of ammonia was monitored using a mass spectrometer (m/z=16, Pfeiffer QMS 200).

2.2.5 Catalytic test

The HDO of palmitic acid was performed in a trickle fixed-bed reactor equipped with high pressure mass flow meters and a HPLC pump. A stainless steel, glass-coated tubular reactor was loaded with 0.04 g of catalyst (160-280 μm), diluted in 0.88 g of SiC. The entire reactor volume was packed with SiC (60-90 μm), which was held by quartz wool. Prior to activity tests, the phosphide catalysts were activated in a flow of 20 $\text{ml}\cdot\text{min}^{-1}$ of H₂ for 2 h at 723 K to remove the passivated layer. Ni₂P/Al₂O₃ LT was activated for 2 h in H₂ at 573 K. The catalytic tests were performed at 4 MPa, contact times were between 0.3 and 2 h and temperature between 453 and 573 K. The contact time is defined as the inverse of the weight hour space velocity (WHSV), which is calculated as the mass flow of palmitic acid divided by the mass of catalyst. The reactant mixture consisted of palmitic acid (1.2 wt. %) in dodecane and H₂ fed in downward and concurrent modes, keeping the molar ratio of H₂ to palmitic acid of 1000. Aliquots of 1 ml were periodically taken and analyzed by gas chromatography using a Shimadzu 2010 instrument with a HP-5 capillary column (30 m \times 250 μm) and flame ionization detector. All samples used for the analysis were taken after 16 h on stream. Conversions and yields were calculated following classical definitions as shown in Equations (2.1)-(2.3), where C_{a_0} , and C_{a_f} are the concentrations of the reactant in the feed and in the effluent, and C_i is the concentration of the product I in the effluent. The concentrations of all products were determined by applying the corresponding response factors obtained from calibrations with pure compounds.

$$\text{Conversion } [\%] = \frac{C_{a_0} - C_{a_f}}{C_{a_0}} \cdot 100 \quad (2.1)$$

$$\text{Selectivity}_i [\%] = \frac{C_i}{C_{a_0} - C_{a_f}} \cdot 100 \quad (2.2)$$

$$\text{Yield}_i [\%] = \frac{\text{Conversion} \cdot \text{Selectivity}_i}{100} \quad (2.3)$$

2.3 Results and discussion

2.3.1 Exploratory studies

SiO₂ is usually preferred as a support for phosphides, because it does not interact strongly with phosphorous as Al₂O₃ does.^[20] However, the carrier may play a catalytic role beyond only dispersing the phase with metal functionality and silica is largely inert. Thus, in this work we have taken alumina as a support. In order to reduce the migration of phosphorous towards alumina, we have attempted to support Ni₂P on amorphous aluminophosphate (AlPO), with the hypothesis that the P-saturated carrier would benefit the synthesis of the phosphide. We have succeeded in preparing Ni₂P/AlPO, as reported in the Appendix. However, the activity of the material is very low due to a large collapse of the support during synthesis of the phosphide. Details of synthesis and results are presented in the Appendix.

We followed reports in literature in order to prepare supported Ni₂P, which was successful. However, the synthesis of supported MoP was much more challenging as many attempts led to metallic Mo. Thus, an optimization study had to be done in order to prepare the desired MoP phase. Aiming to contribute to the knowledge of material preparation, we reported the optimization study in the Appendix.

2.3.2 Physicochemical properties

An overview of the materials that were prepared in this study, the corresponding precursors and thermal treatments, are presented in Table 2-1. Note that the metal to P ratio used in the solutions impregnated on Al₂O₃ were 0.5. That is, phosphorous was present in excess in order to compensate for the losses due to the thermal treatment. All materials discussed below contained the Ni₂P or MoP phases as confirmed by XRD (vide infra). The metal to phosphorous molar ratios derived from the elemental analysis of the unsupported phosphides (Ni₂P, Ni₂P-CA, and MoP) (Table 2-2) were in perfect agreement with the expected stoichiometry of the phosphides. In contrast, the metal to phosphorous molar ratios of the supported phosphides, were all about 0.5, that is much lower than the stoichiometry of the phosphides (2 and 1 for Ni₂P and MoP, respectively). This was attributed to the well know migration of phosphorous into the Al₂O₃ support, leading to excess of phosphorous in the bulk of the material.^[20]

Table 2-1. List of catalysts used in this work, corresponding precursors, proportions used in the initial solutions and thermal treatments.

Catalyst	Metal/P molar ratio	Metal precursor	Phosphorus precursor	Reduction
Ni ₂ P	1/2	Ni(NO ₃) ₂ ·6H ₂ O	(NH ₄) ₂ HPO ₄	2 h 923 K H ₂
Ni ₂ P-CA	1/2	Ni(NO ₃) ₂ ·6H ₂ O	(NH ₄) ₂ HPO ₄	2 h 923 K H ₂
MoP	1	(NH ₄) ₆ Mo ₇ O ₂₄ ·4H ₂ O	(NH ₄) ₂ HPO ₄	2 h 923 K H ₂
Ni ₂ P/Al ₂ O ₃ -LT	1/2	NiCl ₂ ·6H ₂ O	NaH ₂ PO ₂ ·H ₂ O	1 h 573 K N ₂
Ni ₂ P/Al ₂ O ₃ -TPR	1/2	Ni(NO ₃) ₂ ·6H ₂ O	(NH ₄) ₂ HPO ₄	2 h 923 K H ₂
MoP/Al ₂ O ₃ -TPR	1/2	(NH ₄) ₆ Mo ₇ O ₂₄ ·4H ₂ O	(NH ₄) ₂ HPO ₄	2 h 1073 K H ₂

Figure 2-1 shows the N₂ physisorption isotherms of the phosphide catalysts. The N₂-isotherm of the parent Al₂O₃ support and the pore size distributions are presented in the Appendix. The wide hysteresis loop observed in the N₂-physisorption isotherm of Ni₂P-CA suggests a porous solid with a broad distribution of pore sizes due to the presence of relatively large cavities connected with narrower pores. Furthermore, a large contribution of micropores to the pore volume of the material is indicated by the large volume adsorbed at low relative pressures and confirmed by the high contribution of pores smaller than 5 nm to the porosity (Figure 2A-5 of the Appendix). The supported catalysts (Ni₂P/Al₂O₃-LT, Ni₂P/Al₂O₃-TPR, and MoP/Al₂O₃) exhibit isotherms that correspond to the mesoporous structures of the bare Al₂O₃ support (type IV isotherms). The hysteresis loops of the phosphide catalysts broaden and shift to higher relative pressures with respect to pure alumina (presented in Figure 2A-4). These two effects reflect changes in the porous structure of the support during thermal treatment as observed in the pore size distributions of the Al₂O₃-containing materials (Appendix). That is, compared to pure Al₂O₃ (with a pore size distribution centered at ~10 nm), the pore distributions of the supported catalysts broaden and are centered at smaller pore sizes. The isotherm of bulk MoP (Figure 2-1B) indicates that the material has only macroporosity derived from the agglomeration of solid particles.

The surface area and pore volume of all materials are presented in Table 2-2. Compared to the bare Al₂O₃, the decrease in surface area of Ni₂P/Al₂O₃-TPR and MoP/Al₂O₃-TPR is larger than expected from the density increase after the deposition of the supported phase (from 144 m²·g⁻¹ in Al₂O₃ to 84 m²·g⁻¹ and 88 m²·g⁻¹ in Ni₂P/Al₂O₃-TPR and MoP/Al₂O₃-TPR, respectively). The pore volume also decreases dramatically (from 0.52 cm³·g⁻¹ in Al₂O₃ to 0.265 cm³·g⁻¹ and 0.225 cm³·g⁻¹ in Ni₂P/Al₂O₃-TPR, and MoP/Al₂O₃-TPR, respectively). This confirms that the pore structure of alumina changes during the thermal treatments as discussed above. In contrast, the decrease of surface area in Ni₂P/Al₂O₃-LT (130 m²·g⁻¹, compared to 144 m²·g⁻¹ of pure alumina) corresponds to what is expected from an ideal phosphide deposition. Thus, a more homogeneous distribution of the supported phase inside the pores of the carrier is

obtained in Ni₂P/Al₂O₃-LT (which would, in turn, decrease the pore volume from 0.52 cm³·g⁻¹ in Al₂O₃ to 0.295 cm³·g⁻¹). This is well in line with the minor shift of the hysteresis loop accompanied by a small broadening in the N₂-isotherm of Ni₂P/Al₂O₃-LT discussed above.

Bulk MoP exhibits very low surface area (6 m²·g⁻¹) as expected from the lack of microporosity and mesoporosity. In stark contrast, Ni₂P-CA had an outstanding surface area (230 m²·g⁻¹) and porosity (0.197 cm³·g⁻¹) which has been related to the high carbon content of the material. This carbon, residue from the synthesis, seems to host the high microporosity observed in the pore distribution in addition to mesoporosity (*vide supra*).

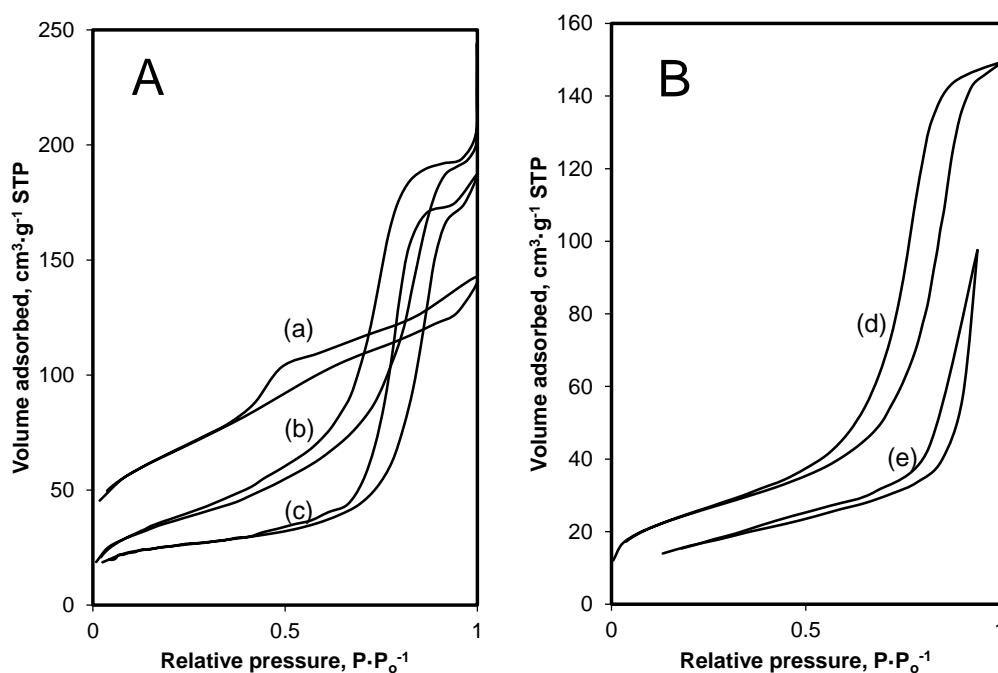


Figure 2-1. N₂ physisorption isotherms of (A) Ni-based and (B) Mo-based phosphide catalysts: Ni₂P-CA (a); Ni₂P/Al₂O₃-LT (b); Ni₂P/Al₂O₃-TPR (c); MoP/Al₂O₃-TPR (d); MoP (e).

The X-ray diffractograms of all materials are presented in Figure 2-2 (Ni₂P-containing catalysts) and Figure 2-3 (MoP-containing catalysts). Only the phases Ni₂P (ICOD: 01-074-1385) and MoP (ICOD: 00-024-0771) were identified in the materials. As expected, the crystallinity depended on the presence of support and the synthesis temperature. The bulk materials exhibited sharp and intense reflections, whereas the supported phosphides exhibited small reflections, especially MoP/Al₂O₃ and Ni₂P/Al₂O₃-LT where the small reflections of the phosphide phases strongly overlap with those of alumina. However, direct comparison of the diffractogram of the catalysts with that of pure alumina (Figure 2-3) indicates that the expected phosphide phases are present in the Appendix. The material Ni₂P/Al₂O₃-LT was treated at high temperature in order to corroborate the formation of the phosphide phase. The X-ray diffractogram of this sample is shown in the Appendix.

Table 2-2. Physicochemical properties of Al₂O₃ and phosphide catalysts.

Catalyst	Elemental analysis			Texture		Phosphide properties
	Metal, wt. %	P, wt. %	Metal/P, Molar ratio	BET Surface area, m ² ·g ⁻¹	Pore volume, cm ³ ·g ⁻¹	Particle size, nm
Al ₂ O ₃	-	-	-	144	0.520	-
Ni ₂ P/Al ₂ O ₃ -TPR	6.5	7.8	0.44	84	0.265	24.3 ^b
Ni ₂ P/Al ₂ O ₃ -LT	6.2	6.3	0.52	130	0.295	14 ^c
Ni ₂ P	61.4	22.4	1.45	< 5	n.d ^d	132.4 ^b
Ni ₂ P-CA ^a	50.2	12.5	2.10	230	0.197	49.0 ^b
MoP/Al ₂ O ₃ -TPR	7.4	5.0	0.48	89	0.225	12 ^c
MoP	65.9	21.0	1.01	6	n.d ^d	29.2 ^b

^a The content of C in Ni₂P-CA is 25.6 wt. %.

^b Obtained from XRD analysis using the Scherrer equation.

^c Obtained from TEM analysis.

^d n.d. not determined.

The crystal sizes derived from the X-ray diffractograms are reported in Table 2-2, whereas particle sizes of MoP/Al₂O₃ and Ni₂P/Al₂O₃-LT, were calculated from a statistical analysis of TEM micrographs (Figure 2-4). The average size determined from the analysis of TEM images is larger than expected from the tiny reflections of the XRD diffractograms. This disagreement is likely due to overestimation of the size from TEM images, where small phosphide particles would escape from detection. MoP forms smaller particles than Ni₂P, i.e., 29 nm for MoP and 132 nm for Ni₂P. On alumina (MoP/Al₂O₃-TPR and Ni₂P/Al₂O₃-TPR) MoP, and Ni₂P particles are 13 nm and 24 nm, respectively. The low temperature method leads to smaller Ni₂P particles than the typical TPR approach. That is, 13.5 nm in Ni₂P/Al₂O₃-LT, and 24 nm in Ni₂P/Al₂O₃-TPR.

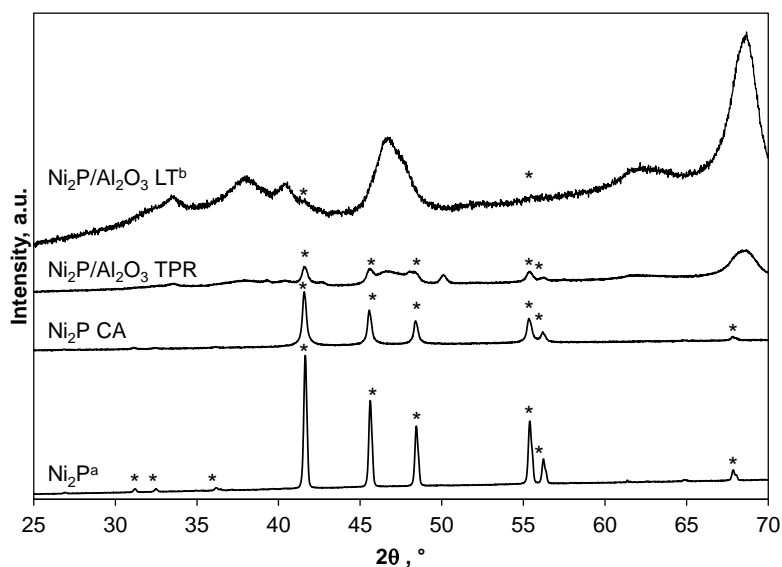


Figure 2-2. X-ray diffractograms of Ni₂P-based catalysts. (*) Ni₂P; the diffractions not labeled correspond to Al₂O₃. ^a Multiplied by a factor of 0.3. ^b Multiplied by a factor of 5.

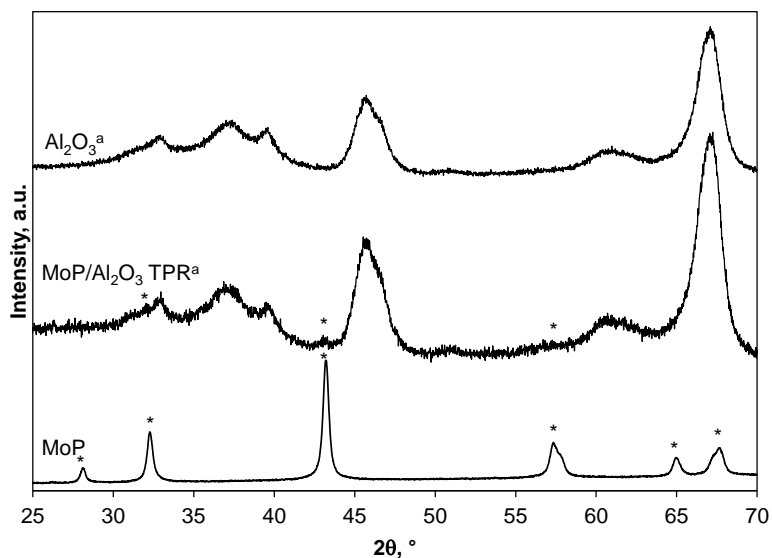


Figure 2-3. X-ray diffractograms of MoP-based catalysts and Al_2O_3 . (*) MoP; the diffractions not labeled correspond to Al_2O_3 . ^a Multiplied by a factor of 10.

The use of citric acid during the synthesis reduces the crystal size (as derived from XRD) of Ni_2P from 132 nm (Ni_2P) to 49 nm (Ni_2P -CA). This is in excellent agreement with several studies, where the addition of citric acid allows obtaining active phases with high dispersion and activity. This is due to the chelating properties of citric acid, which forms complexes with the catalyst precursors slowing the sintering of active phases.^[21–23]

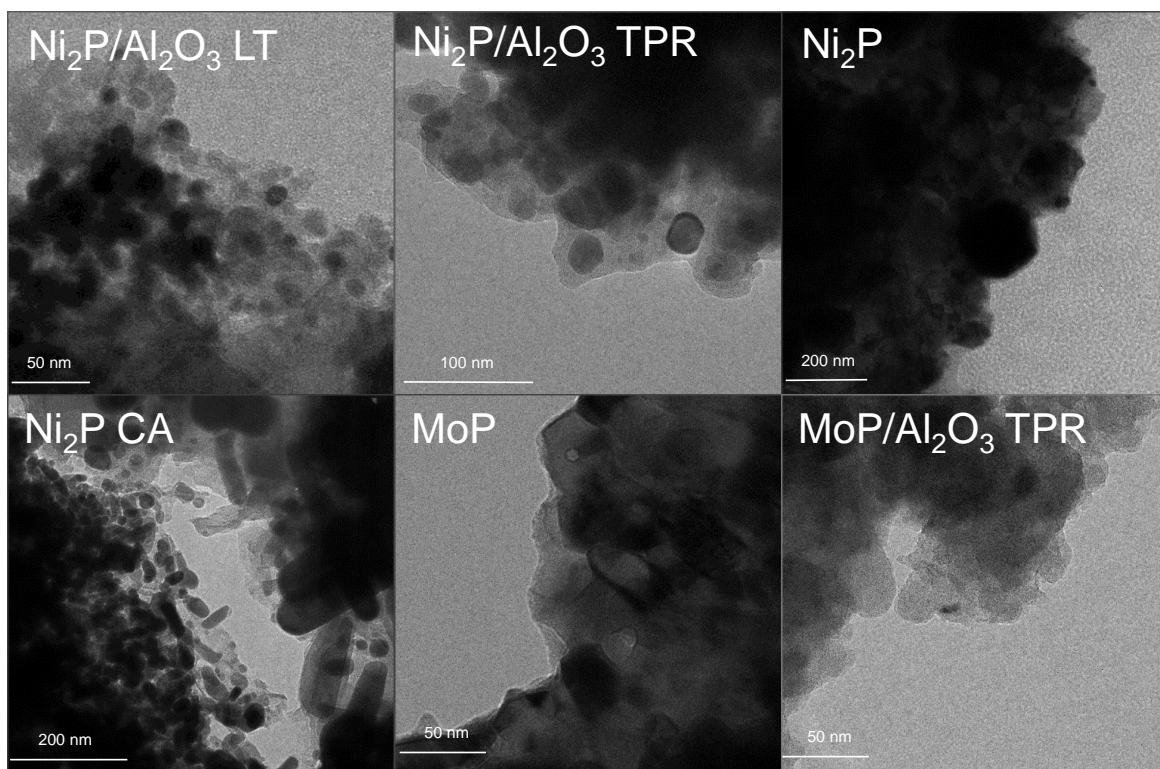


Figure 2-4. Representative TEM micrographs of the phosphide catalysts.

Figure 2-4 shows selected TEM micrographs of the phosphide particles in the materials. The images confirm that the typical TPR method leads to larger Ni₂P particles than the low temperature approach. Interestingly, the Ni₂P particles in Ni₂P/Al₂O₃-LT are smaller than on Ni₂P/Al₂O₃-TPR, however, they form large assemblies as presented in Figure 2-4. This has important implication for catalytic activity (vide infra). The micrographs of Ni₂P-CA demonstrate that the phosphide crystals are embedded in a carbonaceous structure, which increases the porosity of the catalysts and the dispersion of the Ni₂P particles. Figures 2-2 (XRD) and 2-4 (TEM), show that the particle size in the Ni₂P-CA is much smaller than on Ni₂P. Thus, the role of citric acid is twofold, it prevents the Ni₂P particles from sintering and the residual carbon supports these particles. The drawback of this C-Ni₂P system is that the phosphide surface is covered by carbon (vide infra) to extents that must depend on the synthesis conditions. The TEM images also confirm smaller particle size for MoP than Ni₂P in bulk and supported materials.

A complete discussion of the properties of the phosphides studied in this work requires the determination of metal and acid site concentrations. These properties are assessed by adsorption of CO and TPD of NH₃. The concentration of both probe compounds adsorbed by the materials is presented in Table 2-3.

Table 2-3. Concentration of CO or NH₃ adsorbed on the phosphide catalysts as determined by pulse and TPD experiments, respectively.

Catalyst	CO, $\mu\text{mol}\cdot\text{g}^{-1}$	NH ₃ , $\text{mmol}\cdot\text{g}^{-1}$
Ni ₂ P-CA	0.23	0.077
MoP	10.1	0.040
Ni ₂ P/Al ₂ O ₃ -LT	0.29	0.244
Ni ₂ P/Al ₂ O ₃ -TPR	0.61	0.190
MoP/Al ₂ O ₃ -TPR	6.40	0.191
Ni ₂ P	-	0.019

Among unsupported materials, the concentration of adsorbed CO is much higher in MoP (10 $\mu\text{mol}\cdot\text{g}^{-1}$) than in Ni₂P-CA (0.23 $\mu\text{mol}\cdot\text{g}^{-1}$), in contrast to the surface area trend determined by N₂ physisorption. This is a confirmation of the strong effect of residual carbon, which covers a large proportion of metal surface on the latter. Among supported catalysts, which exhibit higher CO uptake than Ni₂P-CA but lower than MoP, the concentration of adsorbed CO increases as follows: Ni₂P/Al₂O₃-LT (0.29 $\mu\text{mol}\cdot\text{g}^{-1}$) < Ni₂P/Al₂O₃-TPR (0.61 $\mu\text{mol}\cdot\text{g}^{-1}$) < MoP/Al₂O₃-TPR (6.4 $\text{mmol}\cdot\text{g}^{-1}$). The total acidity of the bulk materials is one order of magnitude lower than that of the supported catalysts. The materials obtained by TPR have the same acid site concentration of 0.19 $\text{mmol}\cdot\text{g}^{-1}$, whereas Ni₂P/Al₂O₃-LT has an acid site

concentration of 0.244 mmol·g⁻¹. The parent alumina has an acid site concentration of 0.1 mmol·g⁻¹. That is, lower than that of the supported phosphide catalysts. This is attributed to the formation of aluminum phosphate due to the migration of phosphorous towards the support. As reference, the AlPO₄ material synthesized in exploratory experiments exhibits an acidity of 0.292 mmol·g⁻¹ (see the Appendix).

2.3.3 Catalytic tests at constant temperature and reaction network

The catalytic activity of bulk and supported phosphides is investigated in the conversion of palmitic acid under hydrodeoxygenation (HDO) conditions at constant temperature or constant residence time. Figure 2-5 shows the conversion of palmitic acid at 573 K, 4 MPa, and varying residence time. Table 2-4 reports rate constants (k) at 573 K assuming first order kinetics. The bare Al₂O₃ support and the bulk Ni₂P sample exhibit conversions of palmitic acid below 10 % with k values of 0.05 h⁻¹ and 0.04 h⁻¹, respectively, at 573 K. The activity of the other catalysts increases following the trend: MoP/Al₂O₃ ($k=0.57$ h⁻¹) < Ni₂P-CA ($k=0.66$ h⁻¹) < Ni₂P/Al₂O₃-LT ($k=1.92$ h⁻¹) < Ni₂P/Al₂O₃-TPR ($k=2.86$ h⁻¹) < MoP ($k=5.64$ h⁻¹). The products of the reaction are hexadecanal (in trace concentrations), hexadecanol, palmityl palmitate, hexadecane, and pentadecane. The yields of these products, along with residence time on Ni₂P- and MoP-containing catalysts, are presented in Figures 2-6 and 2-7, respectively (yield versus conversion plots are presented in the Appendix).

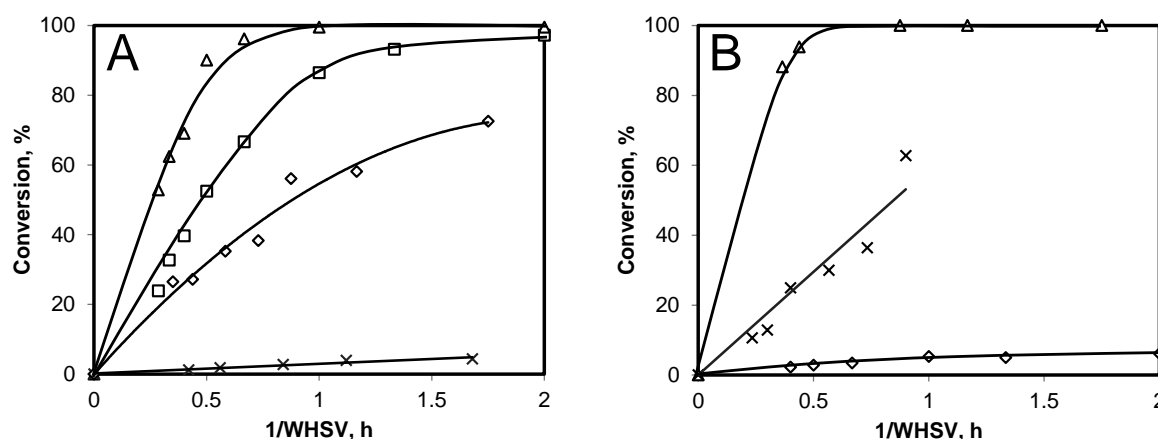


Figure 2-5. Effect of residence time on the conversion of palmitic acid at varying residence time at 573 K, and 4 MPa H₂. (A) Ni-based phosphides: Ni₂P (x), Ni₂P-CA (◇), Ni₂P/Al₂O₃-LT (□), and Ni₂P/Al₂O₃-TPR (Δ); (B) Mo-based catalysts and alumina: MoP (Δ), MoP/Al₂O₃-TPR (x), Al₂O₃ (◇).

The product distributions on the most active catalysts (on, i.e., Ni₂P/Al₂O₃-TPR, and MoP) show that the alkanes are final products of the reaction at the experimental conditions (steady yields at full conversion of palmitic acid), as intuitively expected. On the other hand, the yields on materials with low activity (Al₂O₃, Ni₂P) allow concluding that hexadecane is also a secondary product as its concentration increases exponentially with increasing residence time. Pentadecane behaves as a primary product as its concentration increases linearly at short residence times. Hexadecanol, palmityl palmitate, and hexadecanal are products of the reaction. If present in quantitative amounts, hexadecanal behaves as a primary product. Hexadecanol and palmityl palmitate behave as primary products on most catalysts. However, their secondary nature is revealed on phosphides with very low activity.

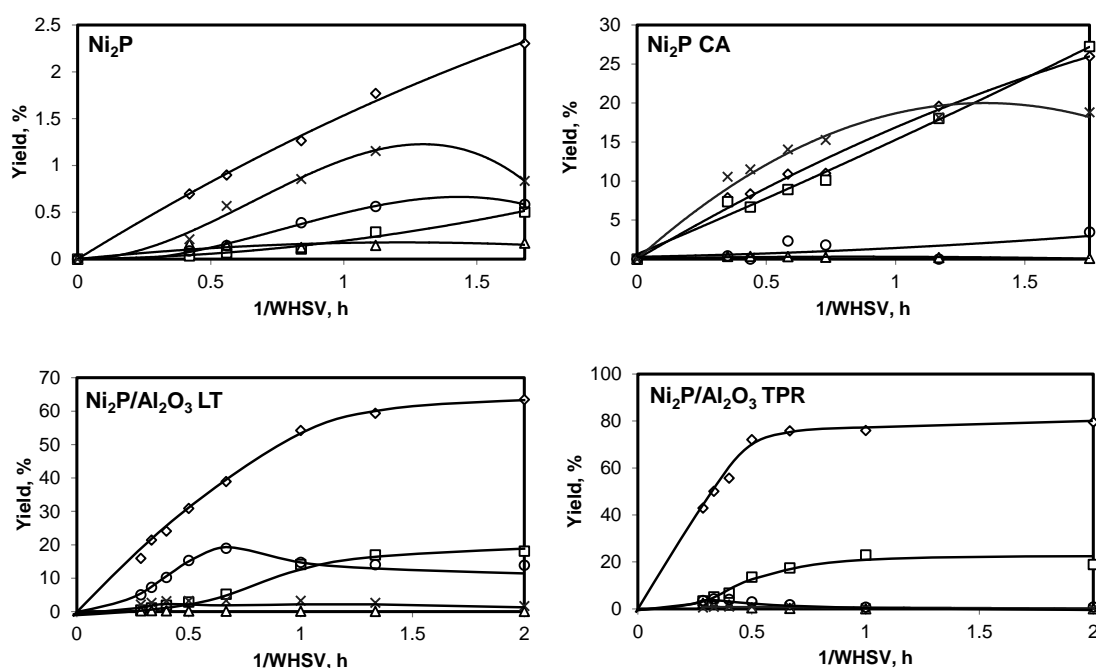


Figure 2-6. Effect of residence time on the yields of pentadecane (◇), hexadecane (□), hexadecanal (Δ), hexadecanol (x) and palmityl palmitate (○) at different residence times on Ni₂P-based catalysts.

The analysis of the product distribution in dependence of residence time, and conversion of palmitic acid, allows adapting the reaction networks proposed for the HDO of microalgae oil on Ni-based catalysts and methyl laurate on phosphides supported on silica to the HDO of palmitic acid on phosphides.^[16,17] The resulting network is shown in Figure 2-8. The first step of a route without carbon losses is the hydrogenolysis of the carboxylic group in palmitic acid to hexadecanal. This intermediate rapidly converts *via* hydrogenation to hexadecanol, which yields hexadecane *via* consecutive dehydration to a terminal alkene, and hydrogenation to hexadecane. The alkene is not observed in this study (likely due to fast hydrogenation under

high hydrogen partial pressure); hence, it is not included in the reaction network of Figure 2-8. Pentadecane is produced either by decarbonylation of hexadecanal or by direct decarboxylation of palmitic acid. Another parallel reaction is the rapid esterification reaction between hexadecanol and palmitic acid to palmityl palmitate.

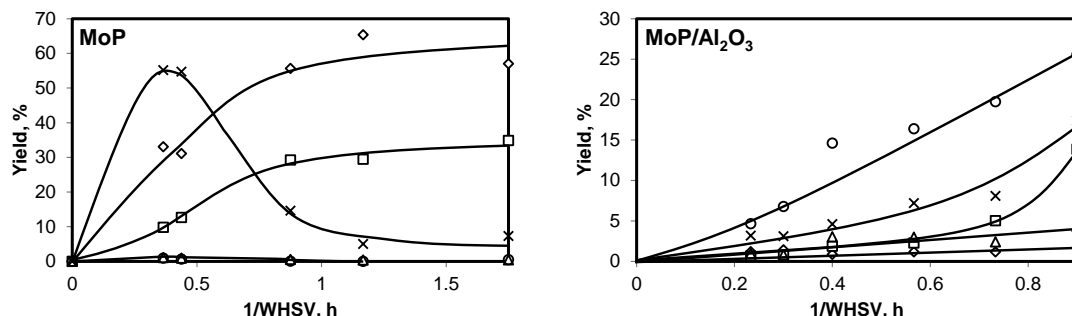


Figure 2-7. Effect of residence time on the yields of pentadecane (\diamond), hexadecane (\square), hexadecanal (Δ), hexadecanol (\times) and palmityl palmitate (\circ) at different space times on MoP-based catalysts.

On bulk Ni_2P -CA and MoP, hexadecanal and palmityl palmitate are produced only in trace concentrations. Hexadecanol is the main product at short residence times whereas alkanes dominate at long residence times. Ni_2P -CA produces hexadecane and pentadecane in similar concentrations, whereas MoP favors the formation of pentadecane over hexadecane. The supported catalysts lead to increased yields of palmityl palmitate and low concentrations of hexadecanal. These observations imply that hydrogenolysis of palmitic acid to hexadecanal is slow and further conversion of the latter is fast. In turn, hydrogenation of hexadecanal to hexadecanol is faster than decarboxylation and decarbonylation (the sum of hexadecanol and hexadecane yields is larger than the pentadecane yield). Further transformation of the alcohol to hexadecane is relatively slow.

On the supported catalysts, the yields of hexadecanal are also very low, which confirms the slow hydrogenolysis of palmitic acid towards hexadecanal compared to further reaction steps. In the presence of Al_2O_3 , the yields of hexadecanol are drastically reduced compared to bulk phosphides. Conversely, the yields of palmityl palmitate significantly increase. This is a consequence of the esterification of hexadecanol and palmitic acid, which is catalyzed by Al_2O_3 (bare Al_2O_3 produced mainly palmityl palmitate as shown in the Appendix). On supported Ni_2P ($\text{Ni}_2\text{P}/\text{Al}_2\text{O}_3$ -LT, $\text{Ni}_2\text{P}/\text{Al}_2\text{O}_3$ -TPR), the high pentadecane yields indicated that decarbonylation/decarboxylation is preferred over hydrogenation. This is attributed to an effect of supporting the phosphide phase, because pure Al_2O_3 did not lead to important pentadecane production. Furthermore, esterification is concluded to be faster than the hydrogenation steps

leading to hexadecane as its yield increases only when the concentrations of palmitic acid are very low, and therefore fast decomposition of palmityl palmitate is allowed. MoP/Al₂O₃ leads to low pentadecane yield, which indicates low decarboxylation/decarbonylation selectivity. Furthermore, substantial concentrations of hexadecanol and palmityl palmitate (found as the main products in the whole conversion range) suggest that on this catalyst, dehydration and hydrogenation of the alcohol is much slower than esterification.

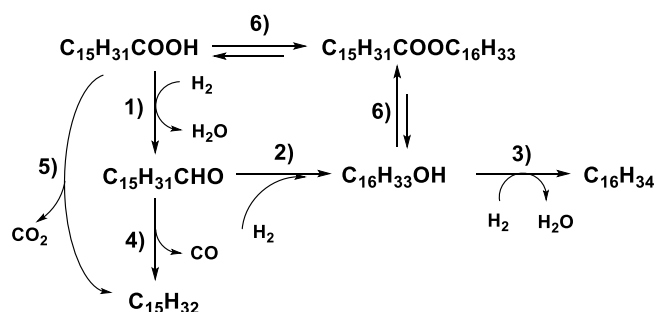


Figure 2-8. Proposed reaction network; the reaction steps are hydrogenolysis (1), hydrogenation (2), dehydration-hydrogenation (3), decarbonylation (4), decarboxylation (5), and esterification (6).

In order to illustrate the differences among Ni₂P-containing materials (discussed below), Figure 2-9 shows a direct comparison of the product distribution at similar conversions, constant temperature and residence time (553 K, 1 h). On the supported phosphides, large concentrations of palmityl palmitate are obtained (more on Ni₂P/Al₂O₃-LT than on Ni₂P/Al₂O₃-TPR), whereas very little of this ester is formed on Ni₂P-CA. In contrast, this bulk material yields hexadecanol as the main product (at around 50 % conversion of palmitic acid), whereas the Al₂O₃-supported phosphides yield only minor concentrations of this alcohol. Another significant difference is that the supported materials produce low concentrations of hexadecane but very high concentrations of pentadecane while the unsupported Ni₂P-CA leads to higher hexadecane selectivity compared to pentadecane. The hexadecanal yields were very low on all materials.

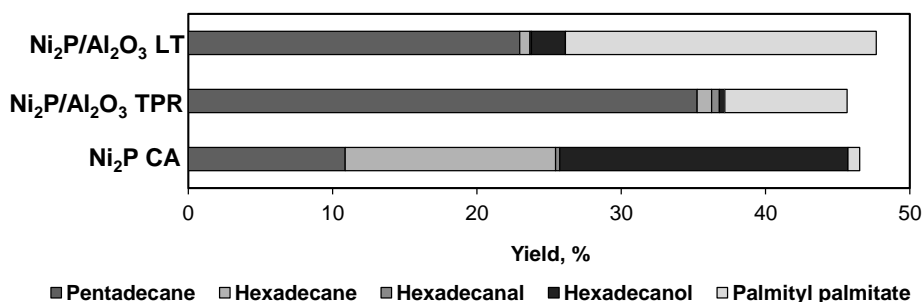


Figure 2-9. Comparison of the product yields of Ni₂P-based catalysts at similar conversions, 553 K, 40 MPa, and 1 h.

2.3.4 Catalytic tests at varying temperatures and kinetic parameters

The HDO activity of the phosphide catalysts is also explored at varying temperatures (Figure 2-10).

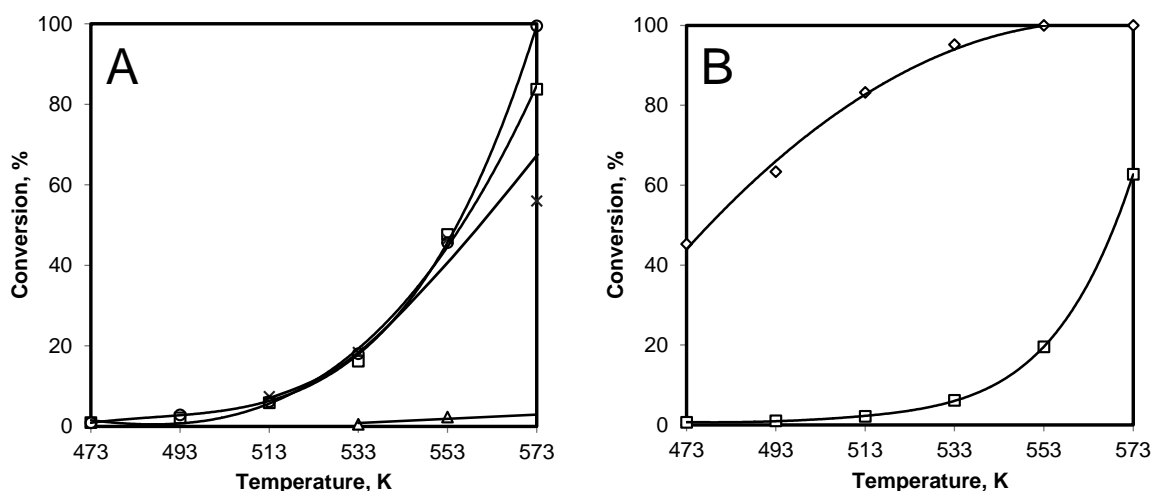


Figure 2-10. Effect of temperature on the conversion of palmitic acid at varying temperatures at WHSV 1 h^{-1} , and 4 MPa H_2 . (A) Ni-based phosphides: Ni_2P (Δ), $\text{Ni}_2\text{P CA}$ (x), $\text{Ni}_2\text{P}/\text{Al}_2\text{O}_3$ LT (\square), $\text{Ni}_2\text{P}/\text{Al}_2\text{O}_3$ TPR (\circ): (B) Mo-based catalysts. MoP (\diamond), $\text{MoP}/\text{Al}_2\text{O}_3$ TPR (\square).

On all Ni_2P catalysts ($\text{Ni}_2\text{P-CA}$, $\text{Ni}_2\text{P}/\text{Al}_2\text{O}_3\text{-TPR}$, and $\text{Ni}_2\text{P}/\text{Al}_2\text{O}_3\text{-LT}$), surprisingly, almost the same conversions of palmitic acid was observed in the range of 473–573 K. Therefore, the observations done at 573 K and varying residence time hold true for the whole temperature range. That is, bulk $\text{Ni}_2\text{P-CA}$ produces small concentrations of palmityl palmitate and hexadecanal, considerable concentrations of hexadecanol (main product below 573 K), and similar concentrations of hexadecane and pentadecane. This implies that on $\text{Ni}_2\text{P-CA}$, the rate of hydrogenolysis of the acid is much faster than esterification, whereas the decarboxylation of the acid (or decarbonylation of the aldehyde) and hydrogenation of the intermediate aldehyde have similar rates. In contrast, supporting the Ni_2P phase on Al_2O_3 , considerably decreases the selectivity to hexadecanol, hexadecanal, and hexadecane yielding pentadecane and palmityl palmitate as main products. On $\text{Ni}_2\text{P}/\text{Al}_2\text{O}_3\text{-TPR}$, pentadecane is the most abundant product (i.e., decarbonylation/decarboxylation is the fastest pathway), whereas on $\text{Ni}_2\text{P}/\text{Al}_2\text{O}_3\text{-LT}$, the yield of palmityl palmitate equals that of pentadecane below 553 K (decarbonylation/decarboxylation, and esterification have very similar rates).

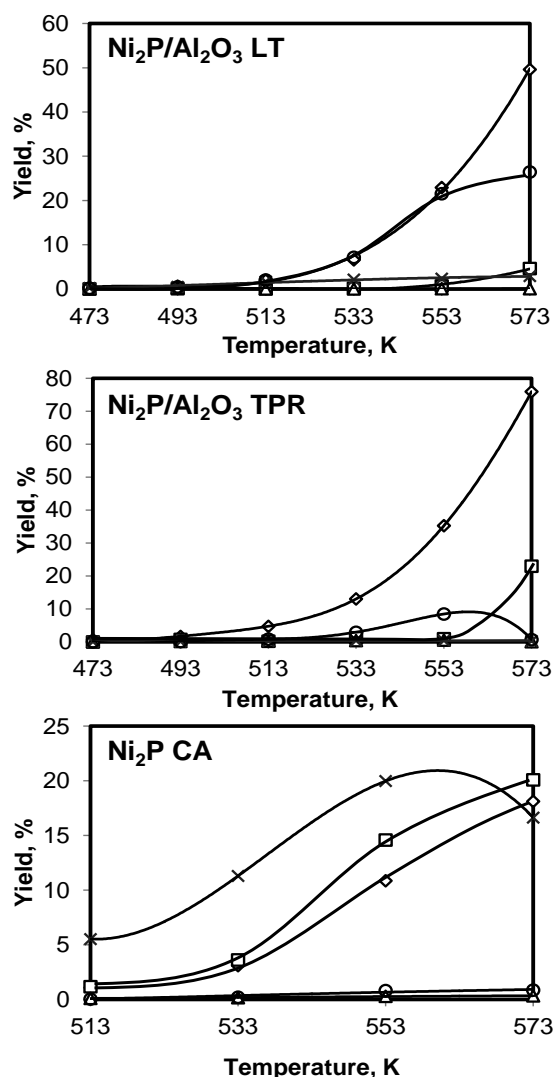


Figure 2-11. Effect of temperature on the yields of pentadecane (◇), hexadecane (□), hexadecanal (Δ), hexadecanol (x) and palmityl palmitate (○) on Ni_2P -based catalysts at varying temperature, WHSV 1 h^{-1} , and 4 MPa H_2 .

The HDO activity of bulk MoP is much higher than that of $\text{MoP}/\text{Al}_2\text{O}_3$ in the whole temperature range. In turn, the former is more active and the latter less active than all Ni_2P catalysts. MoP yields large concentrations of hexadecanol, which is the major product in most of the tested temperature range. The offset for hexadecane and pentadecane production is 533 K , both alkanes being produced at similar rates. On $\text{MoP}/\text{Al}_2\text{O}_3$ -TPR, palmityl palmitate is the predominant product followed by hexadecanol. The offset for the production of the alkanes was 553 K . These observations indicate that decarbonylation of hexadecanal and dehydration-hydrogenation of hexadecanol, are much slower than hydrogenolysis of palmitic acid (and slower than esterification on $\text{MoP}/\text{Al}_2\text{O}_3$ -TPR).

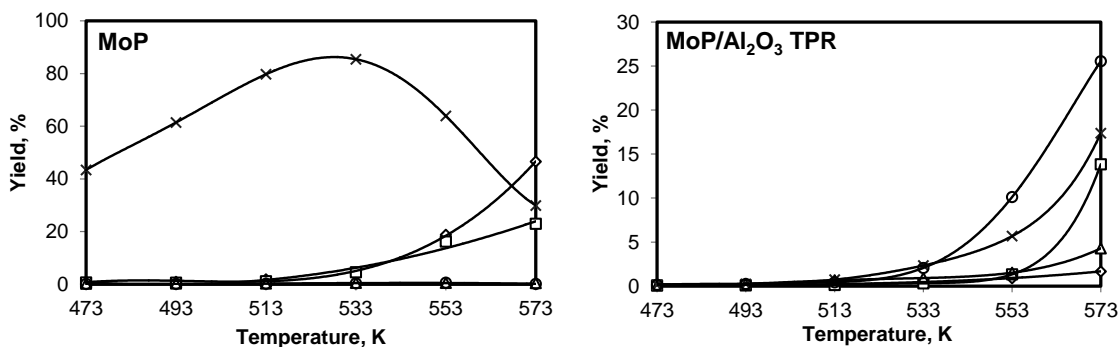


Figure 2-12. Effect of temperature on the yields of pentadecane (◇), hexadecane (□), hexadecanal (Δ), hexadecanol (x) and palmityl palmitate (○) on MoP-based catalysts at varying temperature, WHSV 1 h^{-1} , and 4 MPa H_2 .

Results of the experiments at varying temperatures allow determining the apparent activation energies (E_a) shown in Table 2-4. As expected from the comparable conversions on the studied temperature range, very similar E_a values were found on all Ni_2P catalysts, i.e., 112 – $120 \text{ kJ}\cdot\text{mol}^{-1}$. The E_a of MoP and MoP/ Al_2O_3 -TPR was $56 \text{ kJ}\cdot\text{mol}^{-1}$ and $84 \text{ kJ}\cdot\text{mol}^{-1}$, respectively. Table 2-4 also presents the initial rates at 573 K per gram of material in the catalysts. The initial rates follow the same trends as the conversion and k values, i.e., MoP/ Al_2O_3 -TPR < Ni_2P -CA < $\text{Ni}_2\text{P}/\text{Al}_2\text{O}_3$ -LT < $\text{Ni}_2\text{P}/\text{Al}_2\text{O}_3$ -TPR < MoP. In turn, these trends correspond to the concentration of metal sites probed by CO adsorption within each phosphide series, i.e., MoP/ Al_2O_3 -TPR < MoP, and Ni_2P < Ni_2P -CA < $\text{Ni}_2\text{P}/\text{Al}_2\text{O}_3$ -LT < $\text{Ni}_2\text{P}/\text{Al}_2\text{O}_3$ -TPR (Table 2-3). This confirms, as expected, that the first, and rate limiting step of the reaction, occurs on the surface of either MoP or Ni_2P (regardless of the involvement of active sites on Al_2O_3). The activity of $\text{Ni}_2\text{P}/\text{Al}_2\text{O}_3$ -LT is lower than expected from the small particle size of the supported phosphide likely due to the agglomeration of the Ni_2P particles (detected by TEM), which reduces the proportion of exposed metal area as shown by the trend of CO uptake.

The rates normalized per active site as determined by CO adsorption (Turnover frequencies, TOF) follow the trend: MoP/ Al_2O_3 -TPR < MoP < Ni_2P -CA < $\text{Ni}_2\text{P}/\text{Al}_2\text{O}_3$ -TPR < $\text{Ni}_2\text{P}/\text{Al}_2\text{O}_3$ -LT. These values show that Ni_2P is intrinsically more active than MoP. Furthermore, the TOF values on Ni_2P catalysts increase with decreasing particle size. Bulk MoP is an outstanding material because it exhibits higher CO chemisorption and TOF than the supported counterpart (in contrast to the Ni_2P series). At present we speculate that this difference is related to the absence of any carrier (Al_2O_3 in the case of the supported catalysts or the carbon structure for Ni_2P -CA), i.e., support-active phase interphase. This could minimize the differences between the geometric surface (what correspond to the crystal size) and the exposed surface (effectively available for adsorption).

Table 2-4. Kinetic parameters for the conversion of palmitic acid on selected materials.

Catalyst	k ^a , h ⁻¹	E _a , KJ·mol ⁻¹	Initial rate ^b , mmol·(g _{cat} ·h) ⁻¹	TOF ^c , h ⁻¹ × 10 ⁻³
Al ₂ O ₃	0.05	n.d. ^d	0.20	n.d. ^d
Ni ₂ P/Al ₂ O ₃ -TPR	2.86	117	7.23	11.8
Ni ₂ P/Al ₂ O ₃ -LT	1.92	112	4.89	16.8
Ni ₂ P	0.04	n.d. ^d	0.09	n.d. ^d
Ni ₂ P-CA	0.66	120	2.44	10.5
MoP/Al ₂ O ₃ -TPR	0.57	84	1.25	0.2
MoP	5.64	56	14.28	1.4

^a Calculated at 573 K assuming a first order reaction.

^b Calculated at 573 K at conversion below 20 %.

^c Calculated at 573 K as the initial molar conversion rate per mol of metal phosphide in the catalyst.

^d n.d. not determined.

^e Calculated at 573 K, dividing the initial rate by the concentration of adsorbed CO reported in Table 2-3.

2.3.5 On the role of support and phosphide phase in the hydrodeoxygenation of palmitic acid

Ni₂P and MoP are metal rich phosphides. MoP consists of hexagonal layers of P with Mo in the trigonal prismatic positions. All Mo atoms are equivalent as well as all P atoms.^[7,8] Ni₂P has two kinds of metal sites, distorted tetrahedron (four coordinate), and square pyramid (five coordinate). All P atoms are located in face-capped trigonal prisms, but there are also two kinds of P sites depending on their coordination with 4- and 5-coordinate Ni atoms.^[7,8] The net charges of metal and phosphorous atoms depend on their position within the phosphide structure. In MoP the charges of Mo and P are just slightly positive and negative, respectively, whereas in Ni₂P Ni is slightly positive or negative and P slightly positive^[9] Hence these phosphides have covalent bonding and metal-like character.

Phosphorous exerts electronic effects on the metal atoms, which have been evoked as ligand effects (Ni→P charge transfer).^[24,25] Moreover, structural effects of P on the metals result from increasing the distances between the metal sites, compared to the pure metal structure.^[24, 26] These effects result in lower reactivity than the corresponding pure transition metals, and improved stability towards phase transitions (e.g., towards sulfides in S-containing environments). In turn, P atoms may hold and provide H atoms for hydrogenation and hydrogenolysis of reactants adsorbed at the metal atoms.

Apart from the metal sites (metal atoms or metal-P ensembles), OH groups have been identified at the surface of phosphides as a result of strong P-O bonds.^[27,28] These OH groups have been attributed with acidic properties giving bifunctional character to phosphide catalysts. On the other hand, hydrogenolysis and hydrogenation selectivities have been associated to varying concentration of OH groups.^[29]

The differences in activity between Ni_2P and MoP arise from different intrinsic rates of the rate determining steps for the hydrogenolysis of the adsorbed intermediates. According to the TOF values observed in this work, Ni_2P is intrinsically more active than MoP . This is the same case for the parent pure transition metals, i.e., Ni is a better hydrogenolysis catalyst than Mo. Following this analogy, the adsorption of the carboxyl group on the metal surface may occur on heterolytic or homolytic dissociation of the OH group deriving a bidentate structure via the carboxylate oxygen atoms (carboxylate intermediate).^[30, 31] Subsequent hydrogen additions would lead to the hydrogenolysis of one C-O bond towards a $\eta_1(\text{C})$ -acyl intermediate and then an adsorbed aldehyde.^[32]

The aldehyde (hexadecanal), produced from the hydrogenolysis of the acid (palmitic acid), adsorbs again on the phosphide, metal-like, phase yielding aldehyde or acyl intermediates. Those intermediates may lead to hydrogenation (hexadecanol) or decarbonylation (pentadecane).^[33, 34] The preference for one pathway or another also depends on the intrinsic properties of the phosphide. A simple analogy with the pure transition metals would indicate that Ni_2P is more active for decarbonylation than MoP as Ni has a much higher activity than Mo for C-C bond cleavage.^[35] Although this analogy is questionable because the electronic properties of MoP differ substantially from those of Mo (as in the case of Mo carbide and nitride^[36]), lower decarbonylation has indeed been observed on MoP , compared to Ni_2P .^[17] In line with this, the yields of pentadecane on Ni_2P series are higher, as a function of temperature and contact time, than on the MoP catalysts.

Hexadecanol reacted with palmitic acid to palmityl palmitate *via* esterification. This reaction occurred on the acid sites of Al_2O_3 as indicated by the facts that palmityl palmitate is the main product on alumina, and that it is formed with large yields on the alumina-supported phosphides. Accordingly, the concentration of acid sites is much larger on the catalysts with Al_2O_3 . In contrast, unsupported phosphides exhibit a much lower acidity, which leads to very low esterification rates. Thus, in the absence of Al_2O_3 , palmitic acid is unable to react with hexadecanol, which is the main C16 product with the bulk phosphides within large ranges of palmitic acid conversion. The mechanism of esterification is the same with heterogeneous and homogenous catalysts.^[37] That is, the interaction of the carbonyl group in the acid (palmitic acid) activates the carbon in the carbonyl as an electrophile, which interacts with the hydroxyl group in an alcohol (hexadecanol). As a result of rearrangement, a hydroxyl group of the adsorbed complex converts into water, which is a good leaving group. In the final step, the ester (palmityl palmitate) desorbs regenerating the acid site. $\text{Ni}_2\text{P}/\text{Al}_2\text{O}_3$ -LT produces more ester than $\text{Ni}_2\text{P}/\text{Al}_2\text{O}_3$ -TPR, likely due to the higher concentration of acid sites of the former as determined

from NH₃ TPD. In turn, the higher acid site concentration might be due to lower dehydration of the alumina at the relatively mild conditions of the low temperature approach. At high temperatures used for Ni₂P/Al₂O₃-TPR, fewer acidic sites are expectable.

The acidity of alumina also plays an important role in the transformation of hexadecanol to hexadecane as concluded by the accumulation of the alcohol (without ester formation) on bulk phosphides. However, it is not a single site in alumina, which catalyzed this step (pure alumina produced only trace amounts of hexadecanol and hexadecane). Thus, a synergy has to exist between the acid sites of the Al₂O₃ support and the metal sites on the supported phosphide phases as concluded for the Ni catalysts supported on metal oxides or zeolites.^[38, 39] This synergy consists of consecutive alcohol dehydration on alumina (a well-studied reaction^[40]) and hydrogenation of the resulting alkene on the phosphide phase. Moreover, the hydrogenation on the phosphide phase is much faster than dehydration as hexadecene was not detected.

The yield of hexadecane on supported phosphides increases with high conversions of palmitic acid at high residence times or at high temperatures. This is attributed to the decrease of the surface coverage of palmitic acid, which increases the possibility that hexadecanol reacts with the acid sites on alumina yielding the intermediate hexadecene. Note however, that the phosphide phase is not at all unreactive towards the production of hexadecane (consecutive dehydration and hydrogenation). Ni₂P-CA produces similar concentrations of pentadecane and hexadecane, whereas on MoP and Ni₂P, the yield of hexadecane remains low but increases rapidly with increasing residence time and temperature. This feature has to be highlighted as it contrasts the observations done for HDO of fatty acids on Ni supported on not-acidic materials, where alcohol hydrogenation does not occur.^[39] In turn, the implication of this pathway (hexadecanol to hexadecane) on phosphides is that the low acidity detected by NH₃-TPD indeed catalyzes some steps of the reaction network to some extent. Remarkably, these acid sites of bulk phosphides are able to dehydrate hexadecanol but are less active for esterification. Another consequence of fast dehydration rates of the alcohol on the bulk phosphides is the high yield of hexadecane observed on Ni₂P-CA, compared to Al₂O₃-supported Ni₂P. At present, we speculate that the reason of these differences is due to the fact that esterification is strongly dependent on steric hindrance, because the two bulky molecules, hexadecanol and palmitic acid, have to coincide on at least one acid site. Dehydration, in contrast, is a monomolecular reaction. Similar conclusions have been reached for transesterification and ether production.^[41, 42] Alumina would offer sites that both, hexadecanol and palmitic acid can access simultaneously, whereas the sites on bulk phosphides may favor monomolecular reactions. Alternatively, the type of acidity may lead to the observed differences, alumina is typically a material with high Lewis

acidity, whereas the acid sites in the phosphide phase might originate from residual OH (Brønsted acid sites) groups. The details of this are currently under investigation.

2.4 Conclusions

The hydrodeoxygenation (HDO) performance of Ni₂P and MoP materials was explored (using palmitic acid as a model compound for bio-mass derived oils) in function of the identity of the transition metal, the presence of Al₂O₃ as a support and the synthesis procedure. For the synthesis of highly active bulk Ni₂P, citric acid was added during the synthesis, which led to a material with small crystal size, high specific surface, and a carbon structure acting as support for the phosphide phase. The concentration of metal sites, as determined by CO adsorption increased as follows Ni₂P-CA (0.23 $\mu\text{mol}\cdot\text{g}^{-1}$) < Ni₂P/Al₂O₃-LT (0.29 $\mu\text{mol}\cdot\text{g}^{-1}$) < Ni₂P/Al₂O₃-TPR (0.61 $\mu\text{mol}\cdot\text{g}^{-1}$) < MoP/Al₂O₃-TPR (6.4 $\mu\text{mol}\cdot\text{g}^{-1}$) < MoP (10 $\mu\text{mol}\cdot\text{g}^{-1}$). The TOFs of the HDO of palmitic acid increased in the order: MoP/Al₂O₃-TPR < MoP < Ni₂P-CA < Ni₂P/Al₂O₃-TPR < Ni₂P/Al₂O₃-LT (the TOFs of the Ni₂P catalysts were very similar). Hence, Ni₂P is intrinsically more active than MoP. The activity per gram of catalysts is determined by the interplay between this intrinsic activity and the concentration of metal sites accessible to the reactant giving the specific activity trend: MoP/Al₂O₃-TPR (high temperature synthesis) < Ni₂P-CA (citric acid in the synthesis) < Ni₂P/Al₂O₃-LT (low temperature synthesis) < Ni₂P/Al₂O₃-TPR < MoP.

Unsupported Ni₂P and MoP favored hydrodeoxygenation ($\text{C}_{15}\text{H}_{31}\text{COOH} \rightarrow \text{C}_{15}\text{H}_{31}\text{CHO} \rightarrow \text{C}_{16}\text{H}_{33}\text{OH} \rightarrow \text{C}_{16}\text{H}_{34}$) over decarbonylation ($\text{C}_{15}\text{H}_{31}\text{COOH} \rightarrow \text{C}_{15}\text{H}_{31}\text{CHO} \rightarrow \text{C}_{15}\text{H}_{32}$), and decarboxylation ($\text{C}_{15}\text{H}_{31}\text{COOH} \rightarrow \text{C}_{15}\text{H}_{32}$). Esterification ($\text{C}_{15}\text{H}_{31}\text{COOH} + \text{C}_{16}\text{H}_{33}\text{OH} \rightarrow \text{C}_{15}\text{H}_{31}\text{COOC}_{16}\text{H}_{33}$) does not significantly occur on unsupported phosphides. The presence of Al₂O₃ as a support significantly increased the rates of esterification due to its high concentration of acid sites. Interestingly, supporting Ni₂P on Al₂O₃ increased its selectivity towards decarbonylation and decarboxylation. As a result pentadecane was the favored product on Ni₂P/Al₂O₃, whereas C16 products dominate on MoP/Al₂O₃. For Ni₂P/Al₂O₃, a relative low-temperature method led to smaller phosphide particle size than more typical methods at high temperature. However, the catalyst with larger particle sizes was more active than the one with smaller particle size due to agglomeration of phosphide particles in the latter, which decreased its effective active surface. The activation energy for HDO is higher on Ni₂P than on MoP (112-120 $\text{kJ}\cdot\text{mol}^{-1}$, and 56-84 $\text{kJ}\cdot\text{mol}^{-1}$, respectively). This work demonstrates that MoP- and Ni₂P-

based catalysts are active and stable in HDO applications. Further, the performance of the catalysts can be selectively tuned by varying the transition metal and adding a support.

2.5 Acknowledgements

The authors would like to thank Prof. Roel Prins for the critical discussion of the results. We also thank Dr. Stefano Cimino and Dr. Luciana Lisi for the scientific support. We are also grateful to Dr. Marianne Hanzlik for TEM measurements, to Dipl.-Ing. Xaver Hecht for technical support and to Insu Lee for the contribution given during his Bachelor Thesis. Funding by the German Federal Ministry of Food and Agriculture in the framework of the Advanced Biomass Value project (03SF0446A) is gratefully acknowledged.

2.6 References

- [1] E. Furimsky, *Appl. Catal. A Gen.*, **2000**, *199*, 147-190.
- [2] S. T. Oyama, *Catal. Today.*, **1992**, *15*, 179-200.
- [3] B. Diaz, S. J. Sawhill, D. H. Bale, R. Main, D. C. Phillips, S. Korlann, R. Self, M. E. Bussell, *Catal. Today.*, **2003**, *86*, 191-209.
- [4] Y. Liu, R. Sotelo-Boyás, K. Murata, T. Minowa, K. Sakanishi, *Energy and Fuels*, **2011**, *25*, 4675-4685.
- [5] K. Murata, Y. Liu, M. Inaba, I. Takahara, *Energy and Fuels*, **2010**, *24*, 2404-2409.
- [6] R. Sotelo-boy, Y. Liu, T. Minowa, *Ind. Eng. Chem. Res.*, **2011**, *50*, 2791-2799.
- [7] S. T. Oyama, T. Gott, H. Zhao, Y. K. Lee, *Catal. Today.*, **2009**, *143*, 94-107.
- [8] R. Prins, M. E. Bussell, *Catal. Letters.*, **2012**, *142*, 1413-1436.
- [9] A. Rodriguez, J. Kim, J. C. Hanson, S. J. Sawhill, M. E. Bussell, *J. Phys. Chem. B.*, **2003**, *107*, 6276-6285.
- [10] S. Sawhill, K. Layman, D. Vanwyk, M. Engelhard, C. Wang, M. Bussell, *J. Catal.*, **2005**, *231*, 300-313.
- [11] P. Liu, A. Rodriguez, *J. Am. Chem. Soc.*, **2005**, *127*, 14871-14878.
- [12] V. M. L. Whiffen, K. J. Smith, S. K. Straus, *Appl. Catal. A Gen.*, **2012**, *419-420*, 111-125.
- [13] V. M. L. Whiffen, K. J. Smith, *Energy and Fuels*, **2010**, *24*, 4728-4737.
- [14] H. Y. Zhao, D. Li, P. Bui, S. T. Oyama, *Appl. Catal. A Gen.*, **2011**, *391*, 305-310.
- [15] K. Li, R. Wang, J. Chen, *Energy and Fuels*, **2011**, *25*, 854-863.

- [16] B. Peng, Y. Yao, C. Zhao, J. A. Lercher, *Angew. Chem. Int. Ed. Engl.*, **2012**, *51*, 2072-2075.
- [17] J. Chen, H. Shi, L. Li, K. Li, *Appl. Catal. B Environ.*, **2014**, *144*, 870-884.
- [18] R. Wang, K. J. Smith, *Appl. Catal. A Gen.*, **2010**, *380*, 149-164.
- [19] V. M. L. Whiffen, K. J. Smith, *Top. Catal.*, **2012**, *55*, 981-990.
- [20] A. Montesinos-Castellanos, T. A. Zepeda, B. Pawelec, J. L. G. Fierro, J. A. de los Reyes, *Chem. Mater.*, **2007**, *19*, 5627-5636.
- [21] N. Rinaldi, Usman, K. Al-Dalama, T. Kubota, Y. Okamoto, *Appl. Catal. A Gen.*, **2009**, *360*, 130-136.
- [22] C. Yu, J. Hu, W. Zhou, Q. Fan, *J. Energy Chem.*, **2014**, *23*, 235-243.
- [23] R. Cheng, Y. Shu, L. Li, J. Sun, X. Wang, T. Zhang, *Thermochim. Acta.*, **2006**, *450*, 42-46.
- [24] P. Liu, A. Rodriguez, T. Asakura, J. Gómez, K. Nakamura, *J. Phys. Chem. B*, **2005**, *109*, 4575-4583.
- [25] P. Liu, J. A. Rodriguez, Y. Takahashi, K. Nakamura, *J. Catal.*, **2009**, *262*, 294-303.
- [26] P. Liu, A. Rodriguez, *J. Am. Chem. Soc.*, **2005**, *127*, 14871-14878.
- [27] S. T. Oyama, Y. Lee, *J. Phys. Chem. B*, **2005**, *109*, 2109-2119.
- [28] Y. Lee, S. Oyama, *J. Catal.*, **2006**, *239*, 376-389.
- [29] J. S. Moon, E. G. Kim, Y. K. Lee, *J. Catal.*, **2014**, *311*, 144-152.
- [30] X. Yang, Z. H. He, X. J. Zhou, S. H. Xu, K. T. Leung, *Appl. Surf. Sci.*, **2006**, *252*, 3647-3657.
- [31] S. Yanagisawa, T. Tsuneda, K. Hirao, Y. Matsuzaki, *J. Mol. Struct. THEOCHEM.*, **2005**, *716*, 45-60.
- [32] J. Lu, S. Behtash, A. Heyden, *J. Phys. Chem. C.*, **2012**, *116*, 14328-14341.
- [33] D. Mei, A. M. Karim, Y. Wang, *ACS Catal.*, **2012**, *2*, 468-478.
- [34] F. Delbecq, F. Vigné, *J. Phys. Chem. B*, **2005**, *109*, 10797-10806.
- [35] J. H. Sinfelt, *Ad. Catal.*, **1973**, *23*, 91-119.
- [36] A. F. Guillermet, M. Korling, *Phys. Rev.*, **1993**, *48*, 11685-11691.
- [37] Y. Liu, E. Lotero, J. Goodwinjr, *J. Catal.*, **2006**, *242*, 278-286.
- [38] B. Peng, C. Zhao, S. Kasakov, S. Foraita, J. A. Lercher, *Chem. Eur. J.*, **2013**, *19*, 4732-4741.
- [39] B. Peng, X. Yuan, C. Zhao, J.A. Lercher, *J. Am. Chem. Soc.*, **2012**, *134*, 9400-9405.
- [40] H. Knözinger, *Angew. Chem. Int. Ed.*, **1968**, *7*, 791-805.
- [41] S. Yan, S. O. Salley, K. Y. Simon Ng, *Appl. Catal. A Gen.*, **2009**, *353*, 203-212.

[42] W. Turek, J. Haber, A. Krowiak, *Appl. Surf. Sci.*, **2005**, 252, 823-827.

2.7 Appendix

2.7.1 Ni_2P supported on AlPO_4

AlPO_4 was synthesized with a P/Al molar ratio of 1 and using citric acid in order to increase the surface area of the final material. A solution of $\text{Al}(\text{NO}_3)_3 \cdot 9\text{H}_2\text{O}$ and citric acid (Sigma Aldrich) was initially prepared. After aging at room temperature for 30 minutes, H_3PO_4 (85 % Sigma Aldrich) was added to the solution drop wise. NH_4OH (25 wt. % Sigma Aldrich) was added in order to set the pH of the solution at 5. An additional aging at pH 5 without stirring the solution at room temperature for 5 h was completed before the evaporation step. The evaporation of the solution was performed in a rotavapor, stepwise to avoid changes in the pH of the solution, until obtaining a white gel at 368 K and 50 mbar. The gel was dried overnight at 363 K. The solid recovered was thermally treated in air at 1073 K for 3 hours (heated at $0.5 \text{ K} \cdot \text{min}^{-1}$ from room temperature to 573 K and at $5 \text{ K} \cdot \text{min}^{-1}$ from 573 K to 1073 K).

Ni_2P supported on AlPO_4 , was synthesized with a method based on a low temperature treatment in flowing N_2 . The supported phosphide was prepared by impregnating a certain amount of AlPO_4 with aqueous solutions of nickel chloride ($\text{NiCl}_2 \cdot 6\text{H}_2\text{O}$, Sigma Aldrich) and sodium hypophosphite ($\text{NaH}_2\text{PO}_2 \cdot \text{H}_2\text{O}$, Sigma Aldrich), keeping the Ni/P molar ratio of 0.5. The content of metal in the impregnating solution was 10 wt. %. After drying, the impregnated solid was heated in a fixed-bed reactor to 573 K and kept for 1 h in a flowing N_2 ($30 \text{ ml} \cdot \text{min}^{-1}$). The material was cooled to room temperature under N_2 and was washed several times with deionized water to remove ionic impurities.

Table 2A-1 shows the physicochemical properties of the initial AlPO_4 and the AlPO_4 -supported phosphide. AlPO_4 showed a surface area of $211 \text{ m}^2 \cdot \text{g}^{-1}$ and an amorphous structure as seen in the corresponding XRD pattern (Figure 2A-1). The acidity of this material, as determined from NH_3 -TPD was $0.292 \text{ mmol} \cdot \text{g}^{-1}$. A representative TEM micrograph of AlPO_4 is shown in Figure 2A-2. The structure of the AlPO_4 collapsed after the deposition of the phosphide phase as seen from the dramatic decrease of surface area to $60 \text{ m}^2 \cdot \text{g}^{-1}$ after impregnation and below $5 \text{ m}^2 \cdot \text{g}^{-1}$ after treatment at 573 K.

Table 2A-1. Physicochemical properties of AlPO_4 -containing materials.

Catalyst	Elemental analysis			Texture		Phosphide properties
	Metal, wt. %	P, wt. %	Metal/P, Molar ratio	BET Surface area, $\text{m}^2\cdot\text{g}^{-1}$	Pore volume, $\text{cm}^3\cdot\text{g}^{-1}$	Particle size ^a , nm
AlPO_4	-	25.4	-	211	0.1398	-
$\text{Ni}_2\text{P}/\text{AlPO}_4\text{-LT}$	7.2	20.3	0.19	< 5	n.d. ^b	19.5

^a Obtained from XRD analysis using Scherrer equation.

^b n.d. not determined.

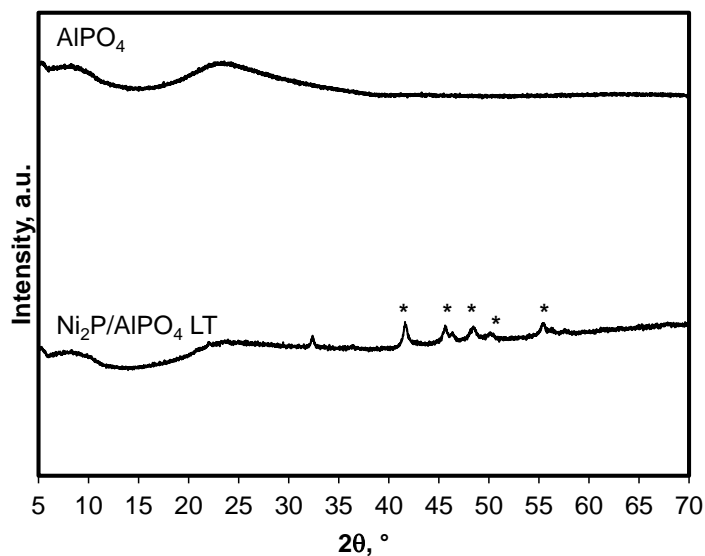


Figure 2A-1. X-ray diffractograms of AlPO_4 and $\text{Ni}_2\text{P}/\text{AlPO}_4\text{-LT}$. Ni_2P (*), the reflections not labeled correspond to the amorphous aluminophosphate.

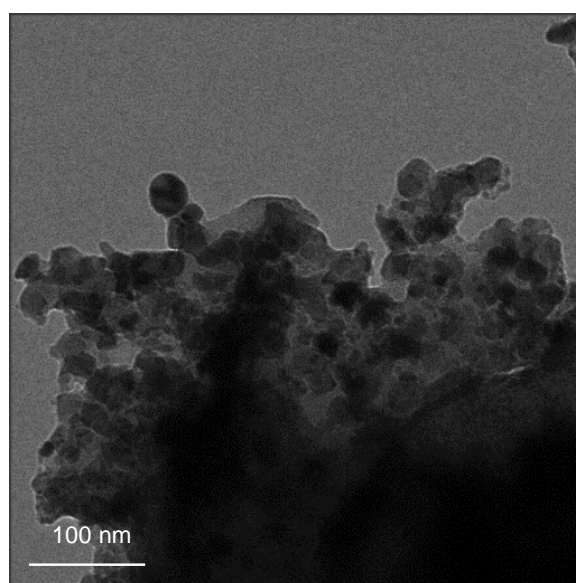


Figure 2A-2. Selected TEM micrograph $\text{Ni}_2\text{P}/\text{AlPO}_4$.

2.7.2 Preparation of MoP supported on Al_2O_3

2.7.2.1 Temperature programmed reduction method (TPR)

The preparation of MoP supported on Al_2O_3 (SCFa140 Sasol, porosity of $0.8 \text{ ml}\cdot\text{g}^{-1}$), was attempted through incipient wetness impregnation of the support with solutions of $(\text{NH}_4)_6\text{Mo}_7\text{O}_{24}\cdot 4\text{H}_2\text{O}$ and $(\text{NH}_4)_2\text{HPO}_4$. The Mo/P molar ratio was 0.5 or 1, whereas the content of metal was 10 wt. % in the initial solution. After drying at 383 K, these two samples were then treated in air at 773 K for 5 hours ($5 \text{ K}\cdot\text{min}^{-1}$) and reduced in H_2 at 1073 K.

2.7.2.2 Low temperature method (LT)

The sample was prepared by impregnating a certain amount of commercial Al_2O_3 (SCFa140 Sasol, porosity of $0.8 \text{ ml}\cdot\text{g}^{-1}$) with an aqueous solution of sodium hypophosphite ($\text{NaH}_2\text{PO}_2\cdot\text{H}_2\text{O}$, Sigma Aldrich) and molybdenum chloride (MoCl_2 , Sigma Aldrich). The Mo/P molar ratio was 1 and the metal content in the initial solution was 10 wt. %. After drying, the impregnated solid was heated in a fixed-bed reactor to 923, 723 and 573 K, and kept for 1 h in a flowing N_2 ($30 \text{ ml}\cdot\text{min}^{-1}$). The material was cooled to room temperature under N_2 and was washed several times with deionized water to remove ionic impurities.

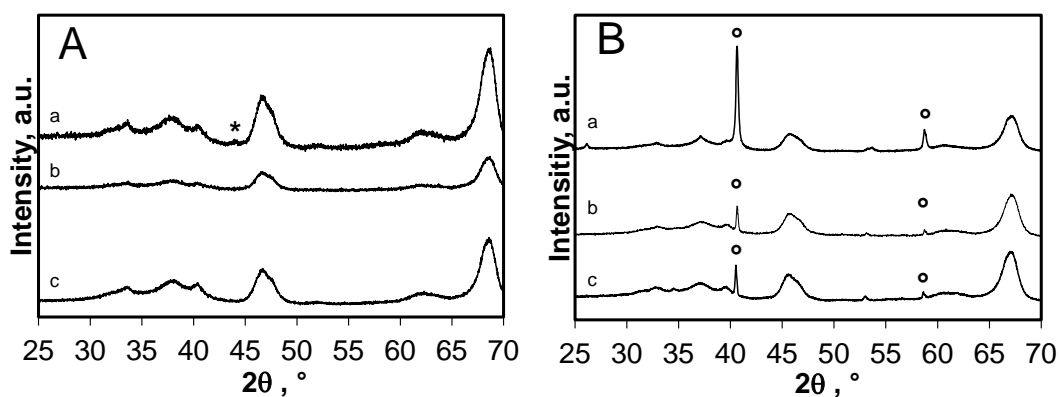


Figure 2A-3. X-ray diffractograms of MoP-based catalysts and alumina. (A) MoP/ Al_2O_3 -TPR synthesized using Mo/P molar ratio of 0.5 (a); MoP/ Al_2O_3 TPR synthesized using a molar ratio Mo/P of 1 (b); Al_2O_3 (c). The peak labeled with “*” corresponds to MoP. (B) MoP/ Al_2O_3 -LT reduced at 923 K in N_2 with a Mo/P molar ratio of 1 (a); MoP/ Al_2O_3 -LT reduced at 723 K in N_2 with a Mo/P molar ratio of 1 (b); MoP/ Al_2O_3 -LT reduced at 573 K in N_2 with a Mo/P molar ratio of 1 (c). The reflections marked with “o” correspond to metallic Mo, the not labeled signals correspond to the alumina support.

The synthesis of bulk MoP by the temperature programmed method described in the main text (923 K) is straightforward. The achievement of the MoP phase on alumina, in contrast, is very difficult because phosphorous tends to migrate inside alumina. This phenomenon is enhanced on the catalysts prepared by the low temperature method as shown in Figure 2A-3. In a series of materials prepared with the low temperature method, the only Mo-containing phase in the catalysts was metallic Mo, whose crystallinity increases with the temperature of the synthesis. Elemental analysis showed that the initial amount of phosphorous was in the catalysts but not forming phosphide phases. On the supported catalysts prepared by TPR, the MoP phase was obtained increasing the reduction temperature from 923 K to 1073 K and increasing the content of initial phosphorous in the catalysts as shown in Figure 2A-3A.^[S1]

2.7.3 N_2 physisorption isotherms and pore size distributions

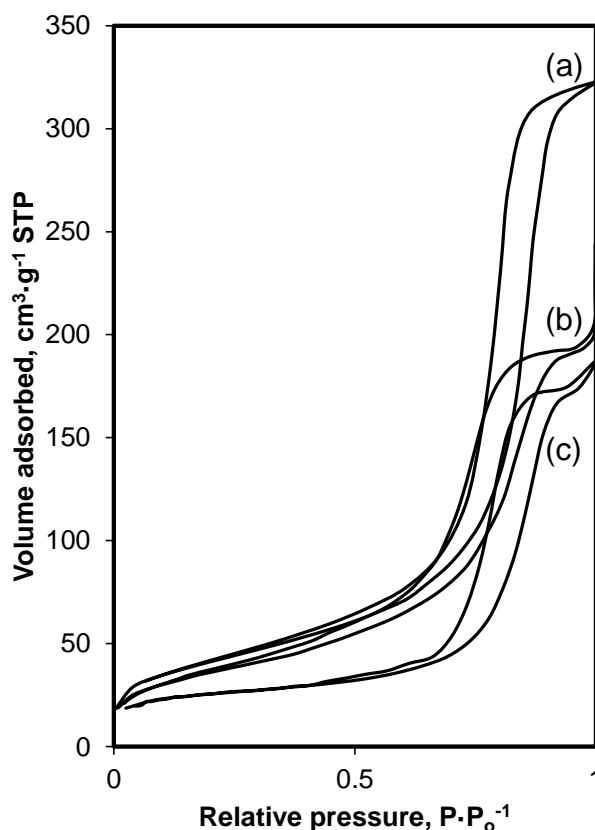


Figure 2A-4: N_2 physisorption isotherms of Al_2O_3 (a), $\text{Ni}_2\text{P}/\text{Al}_2\text{O}_3$ -LT (b), and $\text{Ni}_2\text{P}/\text{Al}_2\text{O}_3$ -TPR (c).

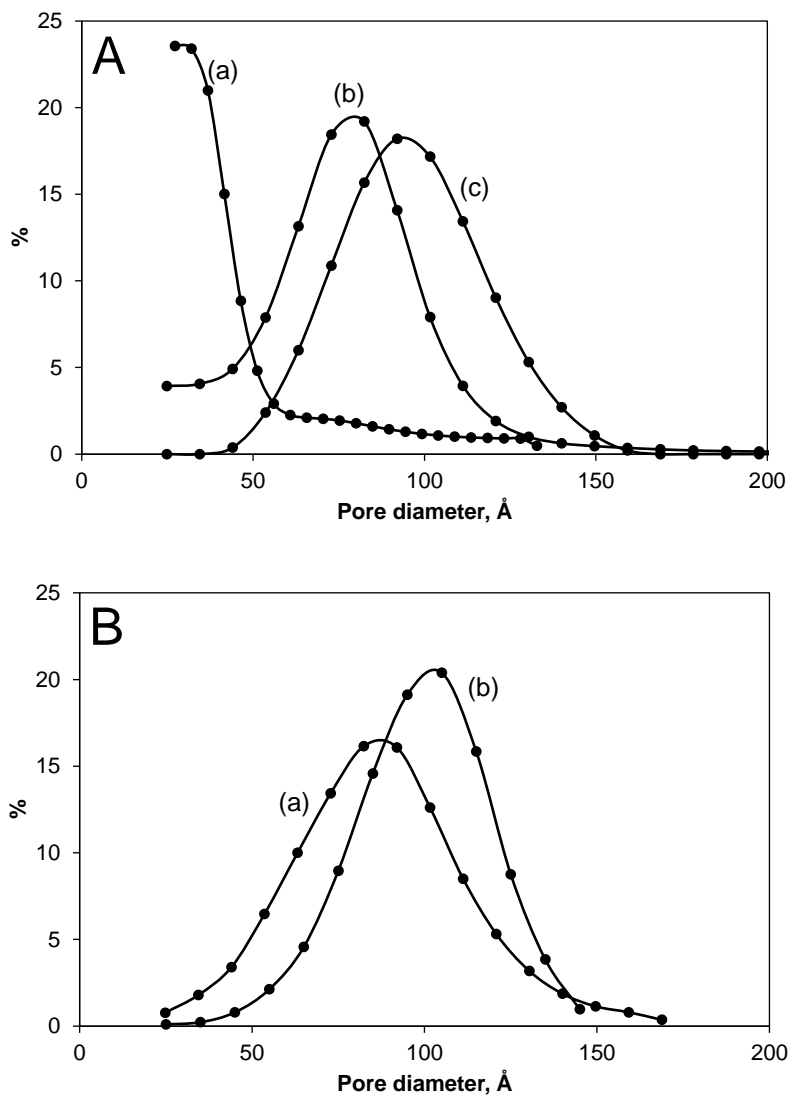


Figure 2A-5. Pore size distributions of (A) Ni-based phosphides (Ni_2P CA (a); $\text{Ni}_2\text{P}/\text{Al}_2\text{O}_3$ LT (b); $\text{Ni}_2\text{P}/\text{Al}_2\text{O}_3$ TPR(c)), and (B) $\text{MoP}/\text{Al}_2\text{O}_3$ TPR (a), and Al_2O_3 (b).

2.7.4 X-ray diffractograms of selected Ni_2P catalysts

Direct comparison of the diffractogram of $\text{Ni}_2\text{P}/\text{Al}_2\text{O}_3$ -LT with that of Ni_2P shows that Ni_2P effectively forms on the supported catalyst. A sample of $\text{Ni}_2\text{P}/\text{Al}_2\text{O}_3$ -LT was treated in H_2 at 723 K. The reflections of the Ni_2P phase are better defined than in the as-prepared catalyst. However, a reflection assigned to Ni_{11}P_5 evolves indicating reduction of the sample.

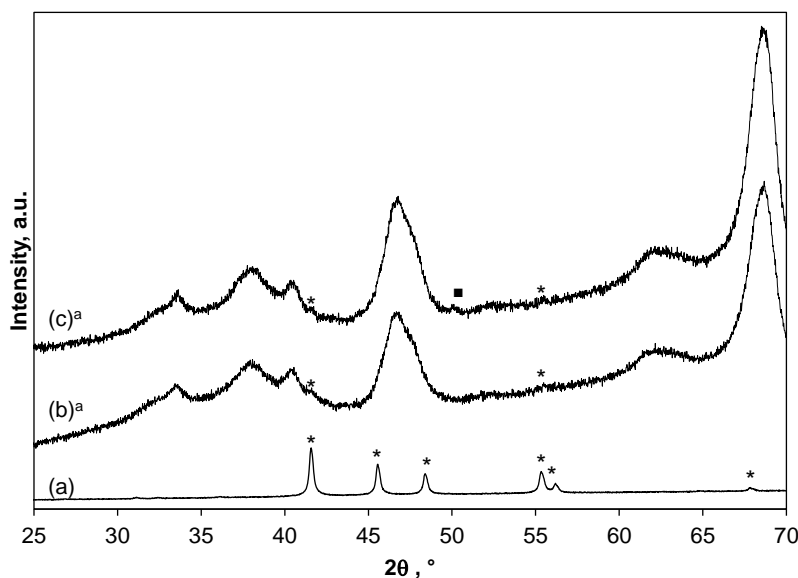


Figure 2A-6. X-ray diffractograms of selected Ni₂P-based catalysts: Ni₂P CA (a), Ni₂P/Al₂O₃-LT (b), and Ni₂P/Al₂O₃-LT after treatment in H₂ at 723 K for 2 h (c). The labeled signals are Ni₂P (*), and Ni₁₂P₅ (■). ^a multiplied by a factor of 7. The not labeled signals correspond to the alumina support.

2.7.5 Catalytic HDO of palmitic acid at 573 K and WHSV 1 h⁻¹

Table 2A-2. Hydrodeoxygenation of palmitic acid on different metal phosphide catalysts.

Catalyst	Conversion, %	HDO Yield ^b , %	Selectivity, %					HDO/DCO ^d (mol/mol)
			C15 ^c	C16 ^c	Aldehyde	Alcohol	Ester	
Al ₂ O ₃	5.3	0.6	11.3	1.1	6.3	0	81.3	0.1
Ni ₂ P/AlPO ₄ -LT	8.7	4.5	15.4	36.3	2.0	6.7	39.5	2.4
Ni ₂ P/Al ₂ O ₃ -TPR	99.9	98.8	75.9	22.9	0.1	0.3	0.7	0.3
Ni ₂ P/Al ₂ O ₃ -LT	86.5	68.3	62.7	16.3	0.1	3.8	17.1	0.3
Ni ₂ P	2.7	1.4	46.3	3.9	4.5	31.1	14.1	0.1
Ni ₂ P-CA	56.1	38.2	32.3	35.8	0.6	29.7	1.5	1.1
MoP/Al ₂ O ₃ -TPR	62.8	15.5	2.7	22.1	6.8	27.7	40.7	8.2
MoP	100.0	84.9	55.6	29.2	0.5	14.6	0.0	0.5

^a Reaction conditions: Flow reactor, palmitic acid 0.037 M in dodecane, 40 mg catalyst, WHSV 1 h⁻¹, 573 K, 4 MPa H₂, particle size of catalyst: 160 μm-280 μm, particle size SiC 60 μm-90 μm, H₂/palmitic acid molar ratio: 1000, activation: 2 h at 723 K in a flow of 20 ml·min⁻¹ of H₂, stabilization: 16h TOS.

^b Yield of deoxygenation (C15 + C16).

^c C15 and C16 are pentadecane and hexadecane.

^d Calculated as C16/C15.

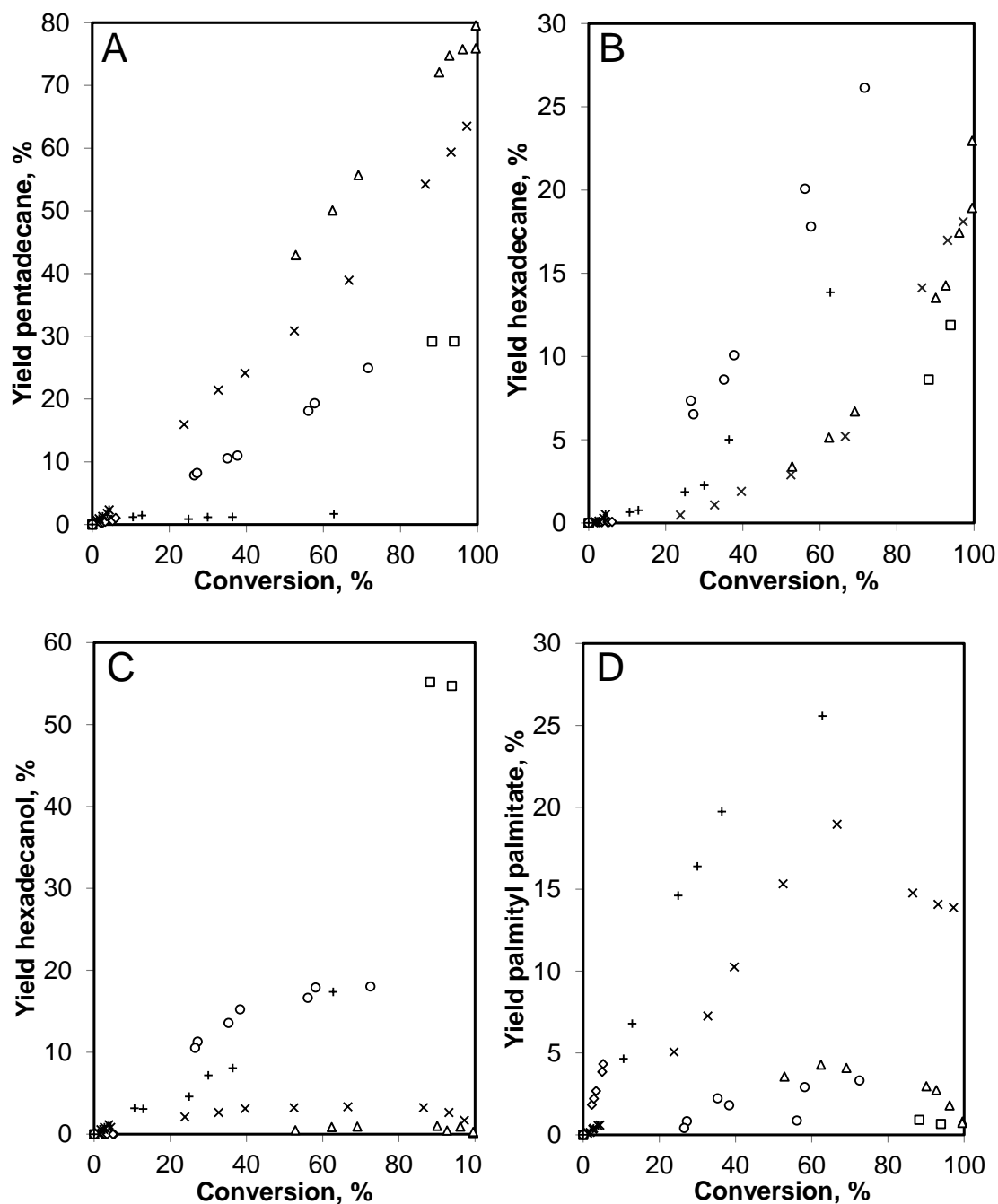


Figure 2A-7. (A) Yield of pentadecane, (B) hexadecane, (C) hexadecanol, and (D) palmityl palmitate as a function of the conversion at 573 K on Ni₂P (*), Ni₂P CA (○), Ni₂P/Al₂O₃ LT (x), Ni₂P/Al₂O₃ TPR (Δ), MoP (□), MoP/Al₂O₃ TPR (+), and Al₂O₃ (◇).

2.7.6 References

[S1] P. A. Clark, T. Oyama, *J. Catal.*, **2003**, 218, 78-87.

Chapter 3

Deoxygenation of palmitic acid on unsupported WP, MoP, and Ni₂P

Transition metal phosphides (WP, MoP, or Ni₂P) with high activity were synthesized and used for the catalytic hydrodeoxygenation of palmitic acid, hexadecanol, hexadecanal, and microalgae oil. The specific activities in the deoxygenation of palmitic acid correlated in general with the concentration of exposed metal cation sites, although the relative rates changed with temperature due to activation energies varying from 57 kJ·mol⁻¹ for MoP to 142 kJ·mol⁻¹ for WP. On WP, the conversion of palmitic acid proceeds via R-CH₂COOH → R-CH₂CHO → R-CH₂CH₂OH → R-CH₂CH₂ → R-CH₂CH₃ (hydrodeoxygenation, HDO). Decarbonylation of the intermittently formed aldehyde (R-CH₂COOH → R-CH₂CHO → R-CH₃) was an additional important pathway on MoP and Ni₂P. Conversion via dehydration to a ketene, followed by its decarbonylation occurred only on Ni₂P. The rates of alcohol dehydration (R-CH₂CH₂OH → R-CH₂CH₂) correlate with the Lewis acidity of the phosphides. The reduction of the fatty acid to the aldehyde occurs through a Langmuir-Hinshelwood mechanism, where the rate-determining step is the addition of the second H to the hydrocarbon.

This chapter is based on:

M. Peroni, X. Huang, I. Lee, E. Baráth, O. Y. Gutiérrez, J. A. Lercher, “Deoxygenation of palmitic acid on unsupported WP, MoP, and Ni₂P”. *Paper ready for submission.*

3.1 Introduction

Hydrodeoxygenation of oxygenates is the key to the conversion of biogenic feedstocks into hydrocarbons.^[1, 2] Elimination of heteroatoms by hydrotreating on sulfides is the most straightforward approach, because of a wide variety of industrial processes relying on sulfide catalysts.^[3-8] In the quest to find catalysts with higher hydrogenation activity, both noble and base metals have been explored.^[9-21] Promising results with transition metal phosphides (TMP) have also been reported.^[22-24] TMP would be an economically feasible alternative to sulfides, as many are more poison tolerant than base and noble metals and are intrinsically more active for hydrogenation than sulphides.^[25-30] Reports have shown that phosphides are active and stable under hydrotreating conditions in the presence of oxygenated hydrocarbons.^[31-34] Thus, TMP have been widely tested for hydrotreating applications including hydrodeoxygenation (HDO) of bio-oil surrogates.^[35-44] Indeed, supported TMP have been shown to be active in HDO of aromatic hydrocarbons, typically for pyrolysis oil.^[27, 29, 35-38] Much less is known, however, about the catalytic properties of TMP for the HDO of triglycerides and products of their transformation, which are primary constituents of bio-oils derived from, e.g., seeds and algae.^[2]

The intrinsic activities of different TMPs vary remarkably, with Ni₂P having the highest intrinsic activities.^[27-28] The metal character of TMP has allowed to conclude that the reactions at the surface resemble those expected on metal catalysts, whereas surface OH groups have been hypothesized to stabilize the activated H.^[26, 28] The elementary steps of the reductive oxygen elimination and the effect of the nature of TMP on such steps have, however, been hardly addressed.^[2] TMP are mostly prepared on supports in order to increase its dispersion. Yet, the support might mask the intrinsic activity on phosphides by mediating some steps of the reaction network towards deoxygenated products or by accumulating phosphorus, which renders uncertainty to the identification of supported phases.^[34]

Thus, in this work we have prepared three unsupported phosphides of common base metals, i.e., WP, MoP, and Ni₂P. The synthesis was achieved in the presence of citric acid as chelating agent in order to prevent sintering during synthesis and to counteract the low dispersion associated to the lack of a support. We have investigated their catalytic performance for the hydrodeoxygenation of palmitic acid, the corresponding reaction products and a triglyceride mixture. The results allowed to describe changes in the trends of intrinsic activities with temperature and to correlate the catalytic properties of the materials with measurements of metal surface and concentration of acid sites.

3.2 Experimental

3.2.1 Synthesis of the catalysts: Temperature programmed reduction of precursors synthesized in the absence of citric acid (TPR-phosphides)

The synthesis of the phosphides comprised two experimental steps: (i) preparation of the precursors and (ii) temperature programmed reduction of the precursors.^[16] The first step in the preparation of the TPR-series consisted of dissolving the precursor salts Ni(NO₃)₂·6H₂O (99.99 %, Alfa Aesar), (NH₄)₆Mo₇O₂₄·4H₂O (≥ 99.0 %, Sigma Aldrich), (NH₄)₆W₁₂O₃₉·xH₂O (≥ 99.0 %, Sigma Aldrich), and (NH₄)₂HPO₄ (≥ 99.0 %, Sigma Aldrich) in water. The solutions were prepared with a Ni:P molar ratio of 0.5, and Mo:P and W:P molar ratios of 1. The solutions were dried overnight at 110 °C and the recovered solids were thermally treated in air at 500 °C for 5 hours (5 °C·min⁻¹). In the second step of the preparation the precursors were treated in H₂ for 2 hours at 650 °C (5 °C·min⁻¹ from room temperature to 300 °C, and 2 °C·min⁻¹ from 300 °C to 650 °C). Subsequently, the materials were exposed to mixtures of O₂ in N₂ with increasing O₂ concentrations (from 1 vol. % to 20 vol. %) in order to passivate the materials and allow their handling.

3.2.2 Synthesis of the catalysts: Temperature programmed reduction of precursors synthesized in the presence of citric acid (CA-phosphides)

Organic chelating agents are structural promoters for the preparation of unsupported metal phosphides avoiding sintering during the reduction.^[45-47] The first step in the preparation of the CA-series consisted of dissolving the precursor salts in water.^[46, 47] The solutions were prepared with a Ni:P molar ratio of 0.5, Mo:P and W:P molar ratios of 1, and citric acid (CA, ≥ 99.5%, Sigma Aldrich) with a 2:1 CA:metal molar ratio. An additional Ni₂P material was prepared using Ni(OCOCH₃)₂·4H₂O (≥ 99.0 %, Sigma Aldrich). The solvent was vaporized at 90 °C and the resulting gel was dried at 120 °C to obtain a brown foam-like solid. This solid was thermally treated at 240 °C for 1 h in O₂/N₂ mixtures with increasing O₂ concentration from 1 vol. % to 20 vol. %. The final thermal treatment was performed at 500 °C for 5 hours (5 °C·min⁻¹) in synthetic air to obtain the catalyst precursor. The final treatments in H₂ and diluted O₂ to obtain passivated phosphides were applied as described for the TPR-phosphides series.

3.2.3 Characterization of the catalysts

N₂-physisorption isotherms were measured at liquid nitrogen temperature using a PMI automated sorptometer (Sorptomatic 1960). The samples were outgassed at 300 °C for 2 h prior to N₂ adsorption. Surface areas and pore size distributions were obtained by BET and BJH analysis, respectively. X-ray powder diffraction (XRD) was performed with a Phillips/PANalytical's X'Pert PRO system (Cu K α radiation, 0.154056 nm) operating at 45 kV and 40 mA. The XRD patterns were recorded using a scan speed of 1.08 °·min⁻¹. TEM images were recorded on a JEM-2010 JEOL transmission microscope operated at 120 kV. Samples were prepared by depositing drops of suspensions of the materials in ethanol on Cu grids with supporting carbon films. The statistical analysis of particle sizes was performed by measuring at least 300 particles per sample distributed in micrographs taken from different regions of the sample. The elemental contents of Ni, Mo, W and P in the materials were measured with a photometer Shimadzu UV-160. Carbon was quantified with a EURO EA (HEKA tech) instrument. CO chemisorption was applied by passing CO pulses (0.33 vol. % CO in He) through samples of the materials at 25 °C. The CO uptake was monitored by a Balzers mass spectrometer ($m/z = 28$). Prior to the CO pulses, the passivated catalysts were activated in H₂ at 450 °C for 2 h. The acidity was determined by temperature programmed desorption (TPD) of NH₃ and *n*-propylamine in a homemade vacuum-TPD set-up. After thermal treatment of the materials in hydrogen at 450 °C, 1 mbar NH₃ or *n*-propylamine was adsorbed at 100 °C for 1 h. The TPD was performed from room temperature to 770 °C (5 °C·min⁻¹) after outgassing the sample for 4 h. The evolution of ammonia, propene, and *n*-propylamine was monitored using a mass spectrometer Pfeiffer QMS 200 ($m/z = 16, 41, \text{ and } 30$, respectively).

3.2.4 Catalytic tests

Catalytic tests were performed in a trickle fixed-bed reactor equipped with high-pressure mass flow meters and a HPLC pump. A stainless steel, glass-coated tubular reactor was loaded with 0.04 g of passivated catalyst (160-280 μm), diluted in 0.88 g of SiC. The entire reactor volume was packed with SiC (60-90 μm), which was held by quartz wool. Prior to activity tests, the phosphide catalysts were activated in a flow of 20 ml·min⁻¹ of H₂ for 2 h at 450 °C. The catalytic tests were performed at 4 MPa, contact times between 0.33 and 2 h, and temperatures between 180 °C and 300 °C. The contact time was expressed as the mass of catalyst divided by the mass flow of palmitic acid. The reactant mixture consisted of palmitic acid, hexadecanol, hexadecanal, or microalgae oil (1.2 wt. %) in dodecane and H₂ fed in downward and concurrent

modes. The fatty acid composition in the triglyceride mixture of microalgae oil is presented in Table 3A-1. Aliquots of 1 ml were periodically taken and analyzed by gas chromatography using a Shimadzu 2010 instrument with a HP-5 capillary column (30 m × 250 μm) and flame ionization detector. All samples used for the analysis were taken after 16 h time on stream after reaching steady state. In selected experiments, the gas phase was monitored using an on-line gas chromatograph (Agilent 7890B) with DB-1, HayeSepQ and Molecular Sieve 13X columns separating the product stream. The GC was equipped with FID and TCD detectors.

Reaction orders in H₂ were determined at 40 bar by varying its partial pressure from 20 bar to 36 bar at a constant partial pressure of palmitic acid of 35 mbar (N₂ was used as diluting gas). The reaction orders in palmitic acid were determined varying its partial pressure from 17 to 35 mbar at 40 bar keeping the H₂ partial pressure at 36 bar. The reaction temperature was 240 °C during these experiments. In order to minimize the effect of secondary reactions, the reaction orders for the conversion of palmitic acid were measured at conversions below 5 %.

H₂-D₂ scrambling experiments were performed at atmospheric pressure in a quartz reactor inside a ceramic oven. 0.1 g of passivated catalyst (160-280 μm) were placed in the reactor and activated at 450 °C in H₂ for 2 h. The H₂-D₂ scrambling was performed as space time (defined as the mass of the catalyst divided by the molar flow of H₂ and D₂) dependent experiments at 80 °C, keeping equimolar concentrations of H₂ and D₂. The effluent of the reactor was analyzed on-line with a mass spectrometer (Pfeiffer Vacuum QME 200) recording the signals of the masses (m/z) 2 (H₂), 3 (HD), and 4 (D₂).

3.3 Results and discussion

3.3.1 Physicochemical properties

Two groups of catalysts were studied in the present contribution, one based on highly crystalline, large crystal phosphides (TPD series), and the other based on materials with much smaller crystal size (CA series). A list of the catalysts studied in this work, the corresponding precursor salts, and proportions used during the synthesis, is presented in Table 3-1. A brief characterization of the oxide catalyst precursors is described in the Appendix. The Ni₂P material obtained in the absence of citric acid exhibited very low surface area, large crystal size, and concomitant low catalytic activity.^[34] Therefore, in the following we compare two Ni₂P materials obtained using two different precursors in the presence of citric acid. Ni₂P-CA1 was

synthesized using Ni(NO₃)₂·6H₂O as metal salt, whereas Ni₂P-CA2 was obtained using Ni(OCOCH₃)₂·4H₂O.

Table 3-1. Catalysts used in this work, corresponding precursors and proportions used in the synthesis of the precursors.

Catalyst	Synthesis method	Precursor salts	Phosphorous precursors	Metal/P molar ratio
Ni ₂ P-CA1	TPR-CA ^b	Ni(NO ₃) ₂ ·6H ₂ O	(NH ₄) ₂ HPO ₄	1/2
Ni ₂ P-CA2	TPR-CA ^b	Ni(OCOCH ₃) ₂ ·4H ₂ O	(NH ₄) ₂ HPO ₄	1/2
MoP	TPR ^a	(NH ₄) ₆ Mo ₇ O ₂₄ ·4H ₂ O	(NH ₄) ₂ HPO ₄	1
MoP-CA	TPR-CA ^b	(NH ₄) ₆ Mo ₇ O ₂₄ ·4H ₂ O	(NH ₄) ₂ HPO ₄	1
WP	TPR ^a	(NH ₄) ₆ W ₁₂ O ₃₉ ·xH ₂ O	(NH ₄) ₂ HPO ₄	1
WP-CA	TPR-CA ^b	(NH ₄) ₆ W ₁₂ O ₃₉ ·xH ₂ O	(NH ₄) ₂ HPO ₄	1

^a Solutions of the metal precursors were dried. The resulting solids were exposed to synthetic air at 500 °C and subsequently to H₂ at 650 °C.

^b Solutions of the metal precursors were mixed with citric acid and dried. The resulting foam-like materials were subsequently exposed to 1% O₂ at 240 °C, to synthetic air at 500 °C, and to H₂ at 650 °C.

Only the phases Ni₂P (ICOD: 01-074-1385), MoP (ICOD: 00-024-0771), and WP (ICOD: 96-900-8944) were present in the reduced materials (Figure 3-1), in agreement with the metal to phosphorous stoichiometry reflected in elemental analyses (Table 3-2). The crystal sizes (reported in Table 3-2) derived from the X-ray diffractograms indicate that the use of citric acid during the synthesis reduced the crystal sizes from 29 nm to 22 nm for MoP, from 32 nm to 20 nm for WP, whereas varying the metal precursor decreased the crystal size from 49 nm to 34 nm for Ni₂P.

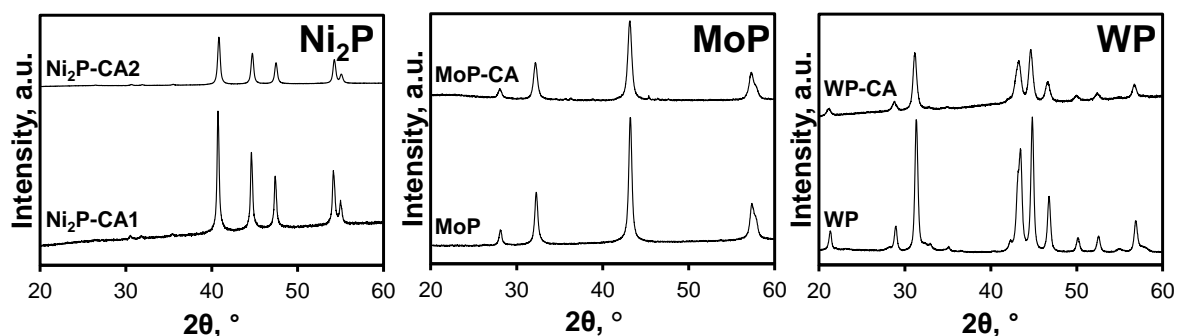


Figure 3-1. X-ray diffractograms of the phosphide catalysts. All reflections are assigned to Ni₂P, MoP, or WP.

TEM allowed visualization of the agglomerates of large crystals of the TPR-series (Figure 3-2). In comparison, smaller crystal sizes were observed for the CA-series, whereby the differences in average crystal sizes between the samples Ni₂P-CA1 and Ni₂P-CA2 were verified. The average crystal sizes of all samples were in line with the sizes calculated from XRD analysis (summarized in Table 3-2). The translucent material surrounding the phosphide particles of the CA-series is speculated to be the residual carbon detected by elemental analysis, which varies within a large range. WP-CA had only 0.1 wt. % C while MoP-CA, and Ni₂P-

CA2 had 6 wt. % and 3.4 wt. %, respectively. In contrast, Ni₂P-CA1 had 26 wt. % C (Table 3-2). The materials of the TPR-series exhibited very low surface area ($6 \text{ m}^2 \cdot \text{g}^{-1}$ or less), whereas the use of citric acid during the synthesis led to higher specific surface areas (Table 3-2). Accordingly, the pore volume of the TPR-series was too low to be measured, whereas the pore volume of the CA-series ranged from $0.04 \text{ cm}^3 \cdot \text{g}^{-1}$ to $0.19 \text{ cm}^3 \cdot \text{g}^{-1}$. The N₂ adsorption isotherm of Ni₂P-CA2 and MoP-CA was type II (IUPAC) pointing to non-porous material (Figure 3A-2). The hysteresis loops at high relative pressures indicated macroporosity derived from the agglomeration of solid particles. In contrast, the hysteresis shape in the isotherm of Ni₂P-CA1 suggested relatively large cavities connected with narrower pores. Furthermore, the large volume adsorbed at low relative pressures indicates a large contribution of micropores to the pore volume of the material. This outstanding porosity is attributed to the residual carbon.

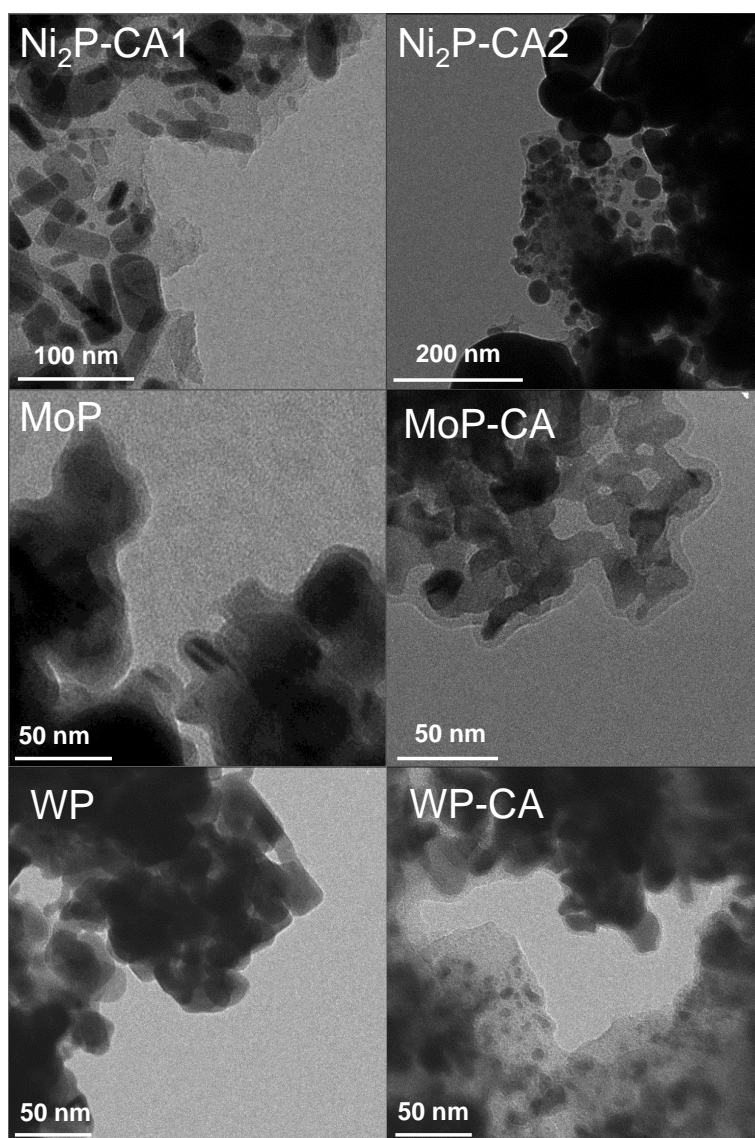


Figure 3-2. Selected TEM micrographs of Ni₂P-, MoP-, and WP-based catalysts.

The NH₃ desorption profiles of the phosphides showed the main desorption peaks between 150 and 300 °C and a broad component with low intensity between 300 and 400 °C (Figure 3A-3 in the Appendix). Thus, most of the adsorption sites of the phosphides are weakly acidic compared with the reference H-MFI-90 zeolite (SiO₂/Al₂O₃ molar ratio of 90), which exhibited one intense desorption signal between 250 °C and 400 °C.

The TPD of *n*-propylamine showed desorption of NH₃, propene, and unreacted *n*-propylamine (Figure 3A-4). NH₃ and propene are products of the decomposition of propyl ammonium ions formed upon the adsorption of *n*-propylamine on Brønsted acid sites.^[48, 49] In contrast, *n*-propylamine adsorbs and desorbs molecularly on Lewis sites. Thus, quantification of Brønsted and Lewis acid sites was performed by quantifying the amounts of NH₃ and *n*-propylamine desorbed during the TPD experiments as shown in Table 3-3. The concentration of Brønsted sites was about one order of magnitude higher than the concentration of Lewis sites for all tested materials. The sum of the concentrations of desorbed *n*-propylamine and NH₃ (equimolar to the concentrations of propene) during the TPD of *n*-propylamine (Table 3-3) satisfactorily equaled the concentrations of NH₃ desorbed during ammonia TPD (Table 3-2). Thus, we conclude that NH₃ and *n*-propylamine adsorb on the same sites in the phosphides, having most of them Brønsted nature when interacting with amines.

Table 3-2. Physicochemical properties of phosphides.

Catalyst	Elemental analysis		Texture		Phosphide properties		
	Metal/P, molar ratio	C, wt. %	Surface area, m ² ·g ⁻¹	Pore volume, cm ³ ·g ⁻¹	Particle size ^a , nm	CO chemisorbed, μmol·g ⁻¹	Desorbed NH ₃ , μmol _{NH₃} ·g _{cat} ⁻¹
Ni ₂ P-CA1	2.10	25.6	230	0.197	49	0.2	77
Ni ₂ P-CA2	1.92	3.4	10	0.042	34	0.5	35
MoP	1.01	-	9	n.d. ^b	26	6.8	78
MoP-CA	0.97	6.0	17	0.040	22	9.0	99
WP	1.10	-	< 5	n.d. ^b	32	2.4	38
WP-CA	1.01	0.1	11	0.041	20	4.5	71

^a Obtained from XRD analysis applying the Scherrer equation on the reflections (111) for Ni₂P, (101) for MoP, and (011) for WP (located at 40.8, 43.2 and 31.1 °2θ respectively).

^b Not determined.

Table 3-3. Lewis and Brønsted acidity derived from TPD of *n*-propylamine.

Catalyst	Lewis Sites ^a , μmol·g _{cat} ⁻¹	Brønsted Sites ^b , μmol·g _{cat} ⁻¹	Total Sites ^c , μmol·g _{cat} ⁻¹
Ni ₂ P-CA2	5	38	43
MoP-CA	2	99	101
WP-CA	9	62	71

^a Determined as the concentration of desorbed *n*-propylamine.

^b Determined as the concentration of desorbed NH₃.

^c Determined as the sum of concentration of desorbed *n*-propylamine and NH₃.

The concentrations of chemisorbed CO were higher for the phosphides of the CA series than for the TPR series (Table 3-2). Interestingly, the concentrations of CO chemisorbed on the phosphides correlated linearly with the concentrations of NH₃ evolved during ammonia TPD and with the concentrations of adsorbed *n*-propylamine (desorbed as NH₃ and propene) as shown in Figure 3-3. As CO adsorbs on metal sites at room temperature, we conclude that this correlation indicates that the concentrations of sites for adsorption of the base depends on the exposed active surface instead of intrinsic changes in the coordinatively unsaturated sites of the materials. On the other, the discrepancy between the rankings of active surface and surface area (or average crystal size) is attributed to the residual carbon in the CA-series, which covered the active surface to varying extents.

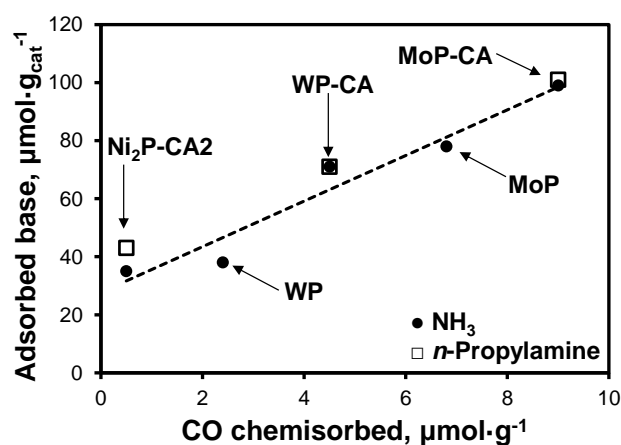


Figure 3-3. Correlation between concentration of chemisorbed CO and concentration of adsorbed bases (NH₃ and *n*-propylamine) on selected phosphides.

3.3.2 Catalytic tests at varying temperatures and kinetic parameters

The dependence of the reaction rate constants for the conversion of palmitic acid on temperature is shown in Figure 3-4A. The corresponding apparent activation energies (E_a) are listed in Table 3-4. MoP exhibited the lowest E_a (57 and 72 kJ·mol⁻¹ for MoP, and MoP-CA, respectively), followed by Ni₂P (123 and 128 kJ·mol⁻¹ for Ni₂P-CA1 and Ni₂P-CA2, respectively), and WP (129 and 142 kJ·mol⁻¹ for WP, and WP-CA, respectively). The activity (per gram of catalyst) ranking below 260 °C (full conversion was reached on most of the catalysts above 260 °C) was as follows: Ni₂P-CA1 < Ni₂P-CA2 < WP < WP-CA < MoP < MoP-CA. As an example of this trend, the initial conversion rates at 240 °C are presented in Table 3-4. The conversion rates increased with the concentration of exposed active surface as determined by CO, NH₃, and *n*-propylamine chemisorption.

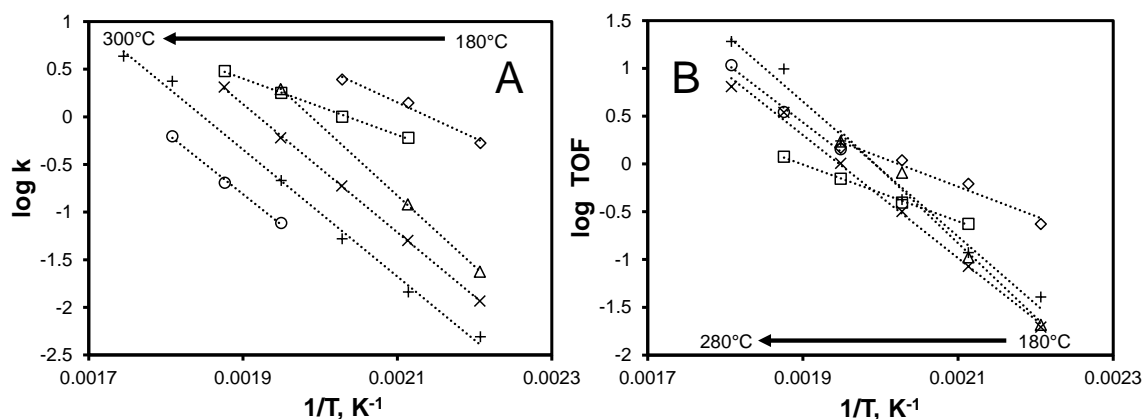


Figure 3-4. Variation of the first order rate constants (A) and of the TOF (B) for the conversion of palmitic acid at varying temperature on Ni₂P-CA1 (○), Ni₂P-CA2 (+), WP (x), WP-CA (Δ), MoP (□) and MoP-CA (◇). Palmitic acid (0.037 M) in dodecane, WHSV 1 h⁻¹, 40 bar H₂. *k* has a unit of mg_{pa}·(mg_{cat}·h)⁻¹ whereas TOF is defined as mmol_{pa}·(h·mmol_{CO})⁻¹.

Figure 3-4B shows the variation of the intrinsic activities (turnover frequency, TOF), determined from the initial reaction rates and the concentrations of adsorbed CO, with temperature. The different activation energies led to changing intrinsic activity trends along the studied temperature range. Above 240 °C, Ni₂P is intrinsically more active than the other phosphides, whereas below 240 °C, MoP is the most active material. In order to illustrate the TOF of the reaction, the values determined at 240 °C (a transition temperature for the trends of intrinsic activities) are shown in Table 3-4. At this temperature, the differences in intrinsic activity among all phosphides are minor. In general, MoP-CA and WP-CA showed higher TOF than the TPR counterparts while TOF on Ni₂P-CA2 was higher than on Ni₂P-CA1, i.e., intrinsic activities are higher on particles with smaller crystal size. This has been attributed to the most active planes being preferentially exposed with decreasing crystal sizes, e.g., the Ni (001) face exposing Ni sites surrounded by five P atoms, and the (001) plane on MoP.^[50, 51]

Table 3-4. Exemplary initial rates and TOFs for the conversion of palmitic acid measured at 240 °C, activation energies determined in the range of 200-260 °C, and TOF for H₂-D₂ scrambling at 80 °C.

Catalyst	Rate, mmol _{pa} ·(g _{cat} ·h) ⁻¹	TOF, x10 ⁻³ h ⁻¹	Ea, kJ·mol ⁻¹	TOF(H ₂ -D ₂), x10 ⁻³ h ⁻¹
Ni ₂ P-CA1	0.3	1.4	123	n.d. ^a
Ni ₂ P-CA2	0.9	1.7	128	32
MoP	7.1	1.0	57	n.d. ^a
MoP-CA	13.1	1.5	72	Eq. ^b
WP	2.4	1.0	129	n.d. ^a
WP-CA	7.8	1.7	142	9

^a Not determined.

^b H₂-D₂ scrambling was equilibrated hindering determination of reaction rates.

Hexadecanol, hexadecane, and pentadecane were observed as main products, whereas hexadecanal, and palmityl palmitate were present only in minor concentrations. Hexadecene (not observed on MoP-based materials) was present as traces on WP- and Ni₂P-based catalysts. The yield of hexadecanol (the most abundant product on all phosphides below 280 °C) increased with increasing temperature passing through a maximum between 240 °C and 280 °C (Figure 3-5). In contrast, the yields of pentadecane and hexadecane increased steadily with temperature (Figure 3-5). On Ni₂P catalysts, the yields of the main products were similar below 280 °C, whereas on MoP and WP hexadecanol dominated the product distribution and the yields of alkanes reached a similar value only at 300 °C. These observations indicate that the rate of hexadecanol production was faster than its conversion below 280 °C. Palmityl palmitate, hexadecanal, and hexadecene are intermediate products, which readily react further at all temperatures.

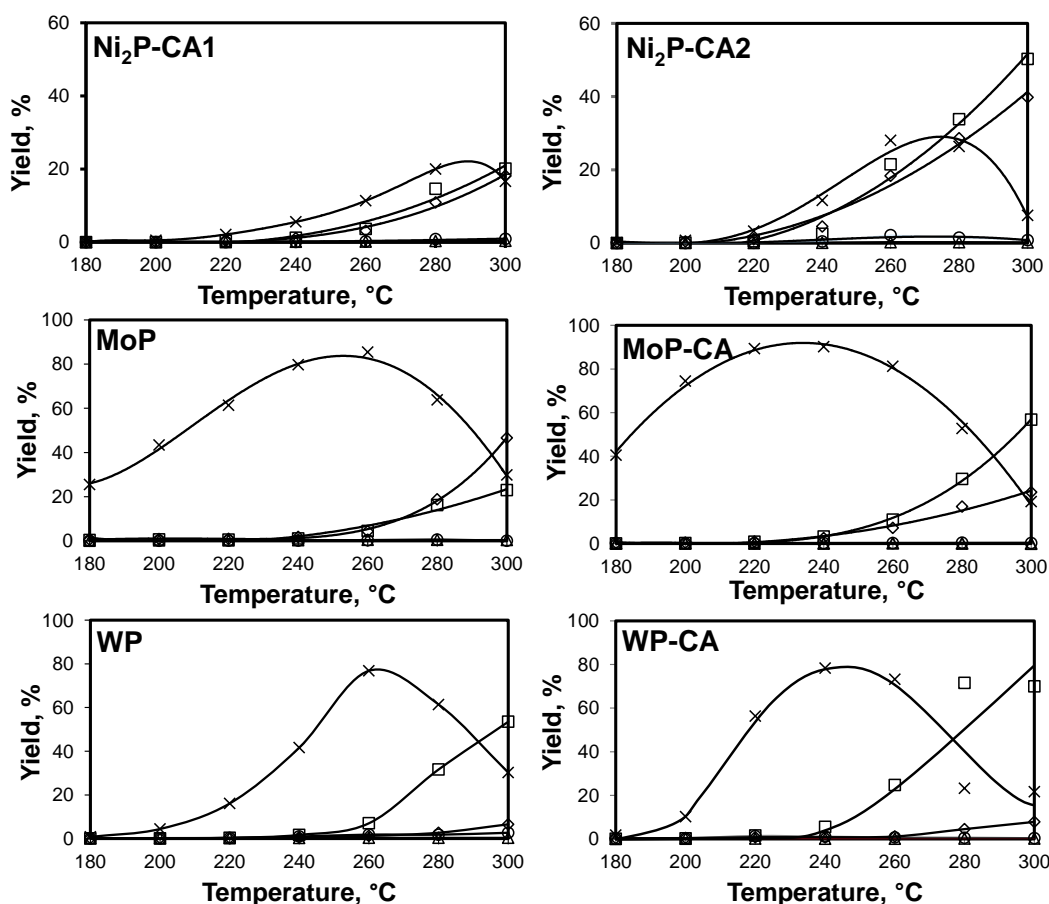


Figure 3-5. Yields of pentadecane (◇), hexadecane and hexadecene (□), hexadecanal (Δ), hexadecanol (x) and palmityl palmitate (○) at different temperatures. Palmitic acid (0.037 M) in dodecane, WHSV 1 h⁻¹, 40 bar H₂.

3.3.3 Reaction network

Figure 3A-5 (Appendix) shows the conversion of palmitic acid on Ni₂P-CA2, WP-CA and MoP-CA at varying contact time and 240 °C. The activities increased in the sequence Ni₂P-CA2 < WP-CA < MoP-CA. Hexadecanol was the most abundant primary product on MoP-CA and WP-CA (Figure 3-6 and Figure 3A-6 in the Appendix). Hexadecane and pentadecane were secondary products on MoP-CA, while only hexadecane and hexadecene were formed on WP-CA as secondary products. On MoP-CA and WP-CA, the alkanes did not form in considerable concentrations below 90 % conversion. In contrast, Ni₂P-CA2 led to comparable yields of alkanes (with hexadecane being more abundant than pentadecane) and hexadecanol already at low conversions.

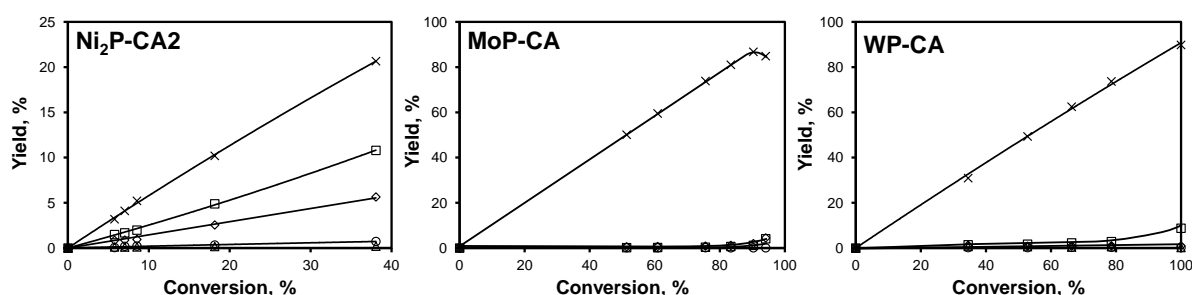


Figure 3-6. Yields of pentadecane (◇), hexadecane and hexadecene (□), hexadecanol (Δ), hexadecanol (x) and palmityl palmitate (○) at different conversions on CA-phosphides. Palmitic acid (0.037 M) in dodecane, 240 °C, 40 bar H₂.

The product profiles are in line with the reaction network in Figure 3-7, which is further validated by the experiments using hexadecanal and hexadecanol as starting reactants. Palmitic acid can be directly converted into pentadecene via dehydration to the ketene followed by its decarbonylation (on Ni₂P) as well as into hexadecanal formed by acid reduction. Pentadecene is rapidly hydrogenated to pentadecane, while hexadecanal is readily converted to pentadecane (decarbonylation) or hexadecanol (hydrogenation). The latter step may be in equilibrium depending on the rate of the subsequent dehydration of the alcohol to hexadecene. In turn, hexadecene (observed only in small amounts) readily hydrogenates to hexadecane. We have omitted the possible esterification between hexadecanol and palmitic acid in Figure 3-7, because palmityl palmitate did not form in significant amounts and does not participate in a pathway towards a deoxygenated product.

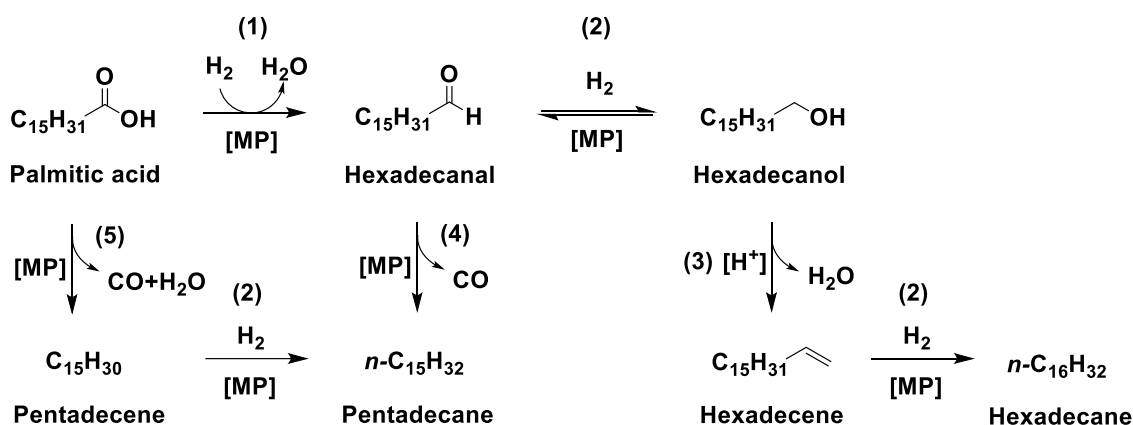


Figure 3-7. Proposed reaction network for the conversion of palmitic acid on WP, MoP, or Ni₂P. The reaction steps are acid reduction to the aldehyde (1), hydrogenation (2), dehydration (3), decarbonylation (4), and dehydration/decarbonylation (5). [MP] and [H⁺] denote sites with metal (metal phosphide) or acid functionality, respectively.

Figure 3-8 illustrates the differences among the catalysts at 240 °C and conversions between 38 % and 53 %. MoP-CA and WP-CA yielded hexadecanol as the dominant product. WP-CA produced higher concentration of hexadecanal and alkanes than MoP-CA (which yields selectively hexadecanol). In contrast, Ni₂P-CA2 yielded hexadecanol and alkanes in comparable concentrations. Hence, the reaction mainly follows the hydrodeoxygenation “HDO” pathway on WP and MoP, i.e., palmitic acid → hexadecanal → hexadecanol → hexadecene → hexadecane. In contrast, there is an important contribution of “carbon loss” pathways on Ni₂P, i.e., palmitic acid → pentadecene → pentadecane (dehydration to the ketene followed by decarbonylation), or palmitic acid → hexadecanal → pentadecane. Thus, the course of the reaction is strongly influenced by the intrinsic functionalities of the catalysts.

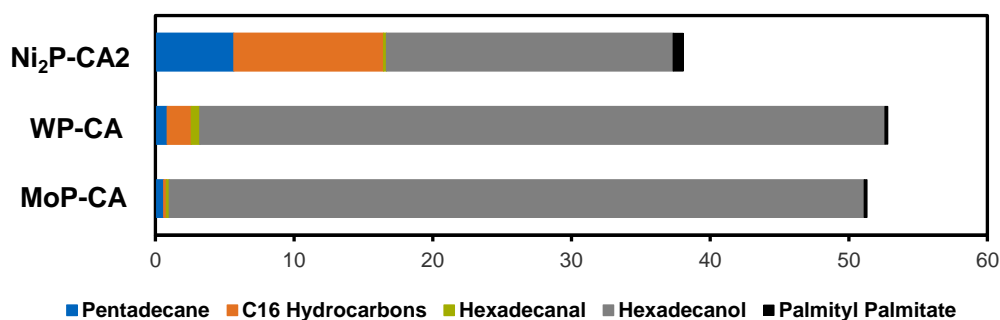


Figure 3-8. Comparison of the product yields on CA-phosphides at similar conversions (x axis) at 240 °C.

The activity of the phosphides for the conversion of hexadecanol increased in the sequence Ni₂P-CA2 < MoP-CA < WP-CA (Figure 3-9 and Figure 3A-7). The E_a were ~125 kJ·mol⁻¹ (Figure 3A-8) on all phosphides, which suggests that the sites catalyzing this step have similar nature in all phosphides. On WP-CA, the conversion of hexadecanol led only to hexadecane and hexadecene (Figure 3-9) confirming that the HDO route (water elimination and subsequent hydrogenation) dominates on this material. In contrast, MoP-CA led to similar formation rates of pentadecane and hexadecane (Figure 3-9). Thus, hexadecanol dehydrogenates to hexadecanal (detected in minor amounts), which undergoes decarbonylation to pentadecane (DCO), in parallel to HDO. Ni₂P-CA2 yielded hexadecane as main product although appreciable amounts of pentadecane indicated that the sequence dehydrogenation-DCO (hexadecanol → hexadecanal → pentadecane) also occurs on this material (Figure 3-9). The initial rates of alcohol dehydration to the corresponding mixture of alkene and alkane at 260 °C were 0.18 mmol·(g_{cat}·h)⁻¹ on MoP-CA, 0.21 mmol·(g_{cat}·h)⁻¹ on Ni₂P-CA, and 2 mmol·(g_{cat}·h)⁻¹ on WP.

Hexadecanal was readily converted to hexadecanol even at 200 °C (Figure 3A-9). Hexadecanol was the only main product, while hexadecane and pentadecane are present in small concentrations below 240 °C. The decrease of the hexadecanol yield mirrored the increase in the yield of hexadecane, which confirms the dehydration-hydrogenation of the former. Decarbonylation of hexadecanal to pentadecane occurs to a lower extent, and requires higher temperatures than its hydrogenation to hexadecanol and the production of hexadecane. The rates of pentadecane production from hexadecanal were higher on MoP-CA than on Ni₂P-CA in line with the observations from the conversion of hexadecanol. Thus, the pentadecane formed on MoP during the reaction of palmitic acid is produced from decarbonylation of hexadecanal. In contrast, the low formation rates of pentadecane (compared to hexadecane) observed during the reactions of hexadecanal and hexadecanol on Ni₂P-CA2 indicate that the high pentadecane formation rates during the conversion of palmitic acid are produced by direct carbon loss. In order to interrogate the nature of the carbon loss step from the fatty acid on Ni₂P-CA2, transient experiments were performed, where the flow of H₂ was switched to N₂. Figure 3A-10 shows that under H₂, the C16 products of the HDO route (hexadecanal, hexadecanol, hexadecane, and hexadecene) were formed with higher yields than pentadecane, whereas pentadecene was present in trace amounts. When the gas flow switched to N₂, the yield of C16 products and pentadecane dropped, while the concentration of pentadecenes steeply increased. In parallel, the gas phase contained CO in much larger concentrations than CO₂. Under H₂ and N₂ the concentration of CO in the gas phase was one order of magnitude higher than CO₂. The

simultaneous formation of pentadecane/CO or pentadecene/CO (under H₂ and N₂, respectively) shows that the main route for C-C bond cleavage from palmitic acid is decarbonylation as on Ni-promoted MoS₂ sulfides, in contrast to carbon loss on Ni, which proceeds via decarboxylation.^[52, 53]

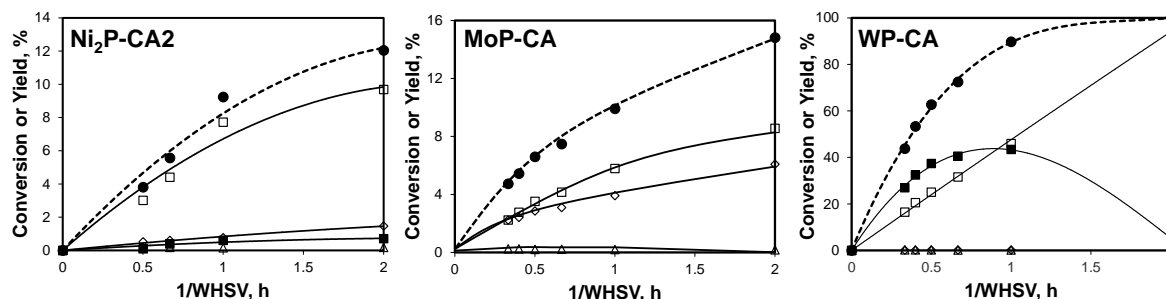


Figure 3-9. Conversion of hexadecanol on Ni₂P-CA₂, MoP-CA, and WP-CA at varying residence time. Conversion (●), pentadecane (◇), hexadecane (□), hexadecene (■), hexadecanal (Δ). Hexadecanol (0.037 M) in dodecane, 260 °C, 40 bar H₂.

MoP was the most active catalyst per gram of material in the overall conversion of palmitic acid due to its large active surface. Thus, MoP was selected to perform the conversion of microalgae oil. Figure 3A-11 shows its conversion and the product distribution at increasing temperature and at 260 °C at varying residence times. The exponential increase of conversion with temperature (up to 73 % at 300 °C) corresponds to the apparent activation energy of 79 kJ·mol⁻¹, which is similar to that observed for the conversion of palmitic acid on the same material. Below 260 °C, the hydrogenation of the microalgae oil only yielded fatty acids with stearic acid being the most abundant one (due to the high concentration of C18 unsaturated fatty acids in the oil). Above 260 °C the yields of alkanes increased being heptadecane and octadecane the most abundant as they are produced by decarbonylation and hydrogenation, respectively, of stearic acid. Likewise, pentadecane and hexadecane were produced from palmitic acid. The decarbonylation products (heptadecane and pentadecane) were more abundant than the HDO products (octadecane and heptadecane) similarly to palmitic acid conversion on the same material.

The profiles of all products at 260 °C and varying residence times (Figure 3A-11) point to hydrogenation of the unsaturated fatty acids and the hydrogenolysis of tryglicerides to fatty acids as primary steps followed by decarbonylation or hydrogenation to alkanes. As the profiles of the alkanes point to the reaction network deduced from the model compounds, the observations made by studying the conversion of the model compound can be generalized to predict the behavior of the materials when converting real microalgae oil.

3.3.4 Mechanism and active sites

The rates of H₂-D₂ scrambling at 80 °C are at least one order of magnitude faster than the rates of palmitic acid conversion at 240 °C (Table 3-4) on all phosphides. Thus, dissociative H₂ activation was concluded not to be the rate-determining step. The reaction orders in H₂ of ~1 for the HDO of palmitic acid on all phosphides (Table 3-5) indicate that, assuming a Langmuir-Hinshelwood mechanism, the rate determining step is concluded to be the addition of a second H to the adsorbed hydrocarbon. In contrast, the reaction order in H₂ for DCO (observed only on Ni₂P) was zero in agreement with the stoichiometry of the reaction, which does not require H.

The reaction orders of palmitic acid for the HDO route were close to zero on Ni₂P-CA2 and WP-CA, and negative (-0.8) on MoP-CA. For DCO on Ni₂P-CA2, the reaction order in palmitic acid was also negative (-0.3). These observations indicate that the phosphides adsorb palmitic acid very strongly, which leads to surfaces with very high hydrocarbon coverages or, in case of HDO on MoP or DCO on Ni₂P, inhibition of the reaction by the substrate.

MoP, and WP are metal rich phosphides with covalent bonding and metal-like properties. Accordingly, the net charges of metal and P atoms are slightly positive (0.09 e) and negative (-0.09 e), respectively, in MoP.^[32] In Ni₂P, metal charges are slightly negative or positive (-0.08 e to 0.06 e), whereas P is slightly positive in average (0.02 e).^[32] Thus, reaction mechanisms for the transformations of fatty acids on phosphides have to comprise elementary steps expected for organic molecules adsorbed on metal surfaces, i.e., hydrogen (radical) addition and reductive elimination.

Table 3-5. Reaction orders in palmitic acid and H₂ for hydrodeoxygenation (HDO) and direct decarbonylation (DCO) routes on selected phosphides at 240 °C and 40 MPa, contact time 0.8 h on Ni₂P-CA2 and 0.167 h on WP and MoP.

Catalyst	Palmitic acid		H ₂	
	HDO ^a	DCO ^b	HDO ^a	DCO ^b
Ni ₂ P-CA2	0.3	-0.3	0.9	0
MoP-CA	-0.8	n.f. ^c	1.2	n.f. ^c
WP-CA	0.2	n.f. ^c	1.1	n.f. ^c

^a Hydrodeoxygenation, calculated from the formation rate of hexadecanal and hexadecanol.

^b Decarbonylation, calculated from the formation rate of pentadecane.

^c Not formed at the conditions used to determine the reaction orders.

The question arises as to the nature of the active sites for the HDO and DCO of fatty acids. Ni₂P has an orthorhombic structure, where Ni is located in two different geometries, i.e., distorted tetrahedron and square pyramid. In the former position, Ni is surrounded by four P atoms and eight more distant Ni neighbors. In the square pyramid geometry, Ni has five P atoms

as nearest neighbors and six Ni next nearest neighbors.^[22, 24] DFT calculations indicate that the most stable surface is terminated by a Ni₃P₂ layer.^[54] In such a surface, upon dissociatively H₂ adsorption and in the presence of other adsorbates, H atoms migrates to P (or a bridging P-Ni) sites, whereas the second adsorbate locates on threefold hollow Ni sites.^[54, 55, 56]

MoP has a hexagonal structure with Mo in the trigonal prismatic positions, whereas P is contained in the prisms.^[31] The structure of WP also contains hexagonal prisms but the P atoms form P-P chains.^[57] In MoP and WP there is only one kind of metal or P position. Thus, the surfaces of MoP and WP can be terminated by metal only or by alternating metal and P atoms. The metal surfaces of these phosphides, similarly to the parent Mo and W metals, adsorb H too strongly to be active in reactions involving hydrogen.^[51, 58] Thus, the alternating metal-P surface is likely the active plane for hydrogenation, whereby P sites would act as “H-delivery” sites.^[51]

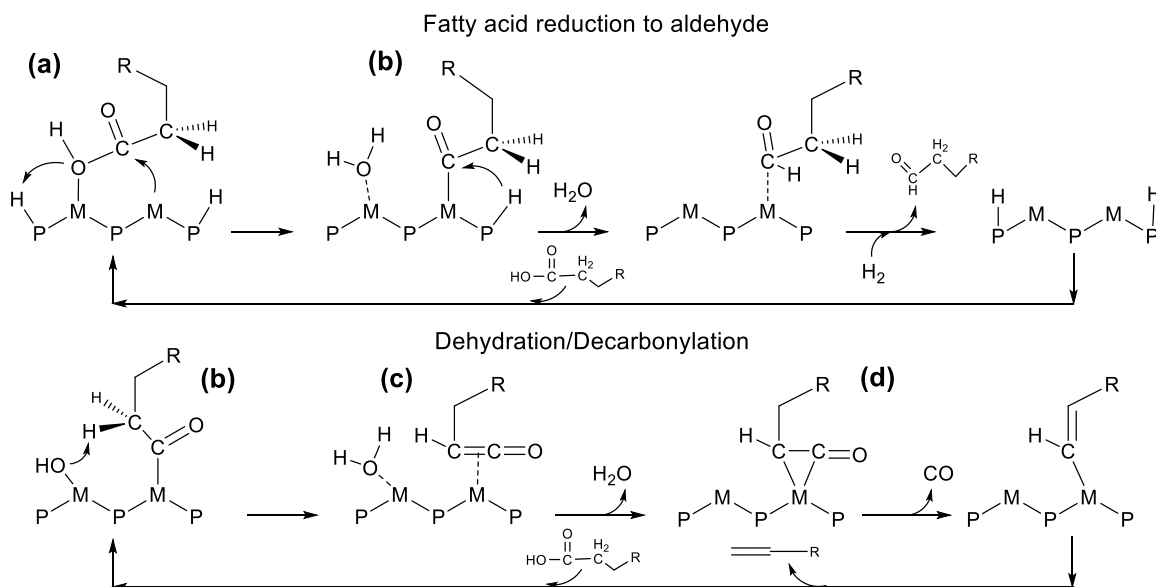


Figure 3-10. Proposed mechanisms for acid reduction to aldehyde and dehydration/decarbonylation of fatty acids on metal phosphide surfaces. Note that as a generalization, the position of P and metal atoms do not correspond to the real location on the phosphide surface. The labels in the structures are discussed in the text.

Hence, we propose that the fatty acid reduction to aldehyde on MoP, WP, and Ni₂P follows the mechanism shown in Figure 3-10, whereby H is provided by P sites and the hydrocarbon undergoing conversion adsorbs on metal atoms. The reaction order in H₂ of 1 implies a sequential reaction with two H, thus, the C-O cleavage is likely initiated by a H attacking a surface carboxylate species “a” yielding a $\eta^1(\text{C})$ -acyl species “b”.^[59, 60] Species “a” is presented in Figure 3-10 as a monodentate species although both oxygens may bind the surface (with only one C-O bond cleaved in the route towards the product).^[61-65] The second hydrogen addition

and reductive elimination would produce an aldehyde, whereas water is produced by recombination of OH groups and H.

In the decarbonylation route on Ni₂P, the acyl species “b” loses a H leading to a ketene intermediate “c”, which has been related to carbon loss during deoxygenation of fatty acids on Ni, Pd, and Ni-MoS₂.^[21, 52, 66] An intermediate state, prior to C-C bond scission, might be the $\eta^2(\text{C-C})$ complex “d”.^[67, 68] The products of this process, which does not require H, are CO, H₂O, and a C_{n-1} alkene. In line with this proposal, C-C bond activation on Ni₂P has been related with the 4-fold coordinated Ni sites, which can accommodate the $\eta^2(\text{C-C})$ complex, in contrast to the 5-fold coordination sites that have been related to hydrogenation.^[25] On the other hand, DFT calculations indicate that Ni₂P has higher density of metal d states near the Fermi level than MoP and WP, which aids C-C bond cleavage.^[32]

3.3.5 Role of acid sites

The phosphides explored in this work exhibited varying concentrations of relatively weak acid sites with a dominant Brønsted nature (Table 3-3). We attribute this acidity to P-OH groups, which have been identified at phosphide surfaces as a result of strong P-O bonds that persist from synthesis and passivation to activation and reaction.^[2, 22, 69] The concentration of these sites correlated linearly with the fraction of exposed metal (Figure 3-3). However, the correlation does not cross the origin, which suggests that the Brønsted acid sites (as titrated with amines) is not necessarily bound to the metallic function of the phosphides although their concentration increased as the metal surface increases. This hypothesis is in agreement with DFT calculations showing that metal sites activate H₂ without requiring O-metal pairs^[54, 55], in contrast to the role of S-metal pairs in sulfide catalysts.^[70] However, we cannot discard P-OH groups as sites for storing H active for hydrogenation and H₂-D₂ scrambling.

The rates of alcohol dehydration towards a mixture of C16 alkanes and alkenes (MoP-CA < Ni₂P-CA2 << WP-CA), an acid-catalyzed reaction, do not correlate with the concentration of Brønsted acid sites (or the concentration of metal sites). Thus, the P-OH groups do not catalyze the dehydration step of the alcohol. The P-OH groups catalyze the decomposition of *n*-propylamine as shown in the probing experiments, but not the dehydration of hexadecanol during reaction likely due to the stronger basic character of the amine (pK_a=10.7 and pK_a= -2.4 for the conjugate protonated acid of *n*-propylamine and hexadecanol, respectively) and the weaker N-C bond strength (358 kJ·mol⁻¹ in *n*-propylamine, compared to the C-O bond strength of the alcohol (390 kJ·mol⁻¹)). Instead, the rates of alcohol dehydration correlated the concentrations of Lewis acid sites (Table 3-2). This correlation is unexpected as Brønsted acid

sites are regarded as more active than Lewis sites for dehydration. However, mechanistic proposals exist, where Lewis acid sites are needed to chemisorb the alcohol prior to protonation by Brønsted sites.^[71] We identify the Lewis acid sites as polarizable sites at the surface of the catalyst. We speculate that the polarization of the surface results from the presence of phosphate species, which might be indirectly related to the formation of the P-OH groups (P is more oxophilic than the metals) with the identity of the cation being less important as the activation energy for the alcohol conversion was similar ($\sim 125 \text{ kJ}\cdot\text{mol}^{-1}$) on all phosphides.^[28]

The alkenes produced by dehydration are hydrogenated on sites with metal function. Thus, the proportion of alkenes and alkanes is controlled by the relative concentrations of acid and metal site. Accordingly, the proportion of alkenes in the product mixture was the highest on WP-CA, which had the highest concentration of Lewis acid sites, but comparatively low concentration of metal sites. In contrast, hexadecene was not observed on MoP-CA due to its low concentration of Lewis sites compared to the large concentration of metal sites available to hydrogenate the alkene. Low concentration of Lewis sites in MoP-CA indirectly favored the selectivity to pentadecane because hexadecanol dehydrogenates to the aldehyde if the dehydration pathway is comparatively slow.^[21] In turn, hexadecanal undergoes decarbonylation to pentadecane.

The rates of hexadecanol dehydration increased appreciable with temperature only above 250 °C, likely because the acid sites on the phosphides are relatively weak and scarce. However, this feature of unsupported phosphides has to be highlighted as it differs from the HDO of fatty acids on metals, where alcohol hydrogenation does not occur without the presence of an acidic material as support.^[21] On the other side, the phosphides do not lead to esterification between the acid and the alcohol, a step that easily occurs on catalysts comprising strongly acidic materials.

3.4 Conclusions

The intrinsic activities of stable Ni₂P, MoP, and WP in the deoxygenation of fatty do not differ significantly in the temperature range explored in this study (200-260 °C). Thus, the activity per gram of material depends on the proportion of exposed active surface (titrated by CO adsorption). The addition of citric acid during the synthesis of oxide precursors limits the growing of precursor and phosphide crystals during thermal treatment increasing the activity of the catalysts. However, residual C may cover metal surface. Because of this compromise, MoP (with the highest fraction of exposed metal sites) was the most active phosphide per gram of

material. Conversion of microalgae oil on MoP showed that the observations made with model compounds represent well the performances with real feeds.

The dominant route for the conversion of the fatty acid on WP and MoP is hydrodeoxygenation (HDO), i.e., the reduction of the acid to aldehyde followed by hydrogenation to alcohol and final conversion to the alkane via consecutive dehydration and hydrogenation ($R-CH_2COOH \rightarrow R-CH_2CHO \rightarrow R-CH_2CH_2OH \rightarrow R-CH_2CH_2 \rightarrow R-CH_2CH_3$). Dehydration is the only step catalyzed by acid sites, which were assessed by TPD of NH₃ and *n*-propylamine. Alcohol dehydration is much faster on WP than on MoP due to the higher concentration of acid sites of the former. The low Lewis acidity of MoP indirectly increases the selectivity of the decarbonylation route ($R-CH_2COOH \rightarrow R-CH_2CHO \rightarrow R-CH_3$) by hindering alcohol dehydration ($R-CH_2CH_2OH \rightarrow R-CH_2CH_2$) and allowing for the dehydrogenation of the alcohol ($R-CH_2CH_2OH \rightarrow R-CH_2CHO$). Ni₂P catalyzes HDO, the decarbonylation route via the aldehyde, and the direct C-C bond cleavage in the acid via decarbonylation ($R-CH_2-CH_2COOH \rightarrow R-CH_2=CH_2$). Thus, high surface WP seems the best option for conversion of fatty acids without carbon losses although MoP and Ni₂P are intrinsically more active.

The reduction of the fatty acid to aldehyde on all phosphides proceeds via a Langmuir-Hinshelwood mechanism, where H₂ adsorb dissociatively and the fatty acid adsorbs without C-O bond cleavage. The product is formed with consecutive addition of adsorbed hydrogen with the second addition being the rate-determining step. Decarbonylation on Ni₂P, as expected from the stoichiometry of the reaction, does not depend on the coverage of adsorbed H.

3.5 Acknowledgements

The author would like to thank Roel Prins for the critical discussion of the results. The author is also grateful to Xaver Hecht for technical support. Funding by the German Federal Ministry of Food and Agriculture in the framework of the Advanced Biomass Value project (03SF0446A) is gratefully acknowledged.

3.6 References

- [1] E. Furimsky, *Appl. Catal. A Gen.*, **2000**, *199*, 147-190.
- [2] J. Chen, H. Shi, L. Li, K. Li, *Appl. Catal. B Environ.*, **2014**, *144*, 870-884.
- [3] W. Li, F. Y. Ma, F. Su, L. Ma, S. Q. Zhang, Y. H. Guo, *ChemSusChem*, **2011**, *4*, 744-756.

- [4] T. V. Choudhary, C. B. Phillips, *Appl. Catal. A Gen.*, **2011**, 397, 1-12.
- [5] B. Donnis, R. G. Egeberg, P. Blom, K. G. Knudsen, *Top. Catal.*, **2009**, 52, 229-240.
- [6] S. Bezergianni, A. Dimitriadis, *Fuel*, **2013**, 103, 579-584.
- [7] D. Kubička, L. Kaluža, *Appl. Catal. A Gen.*, **2010**, 372, 199-208.
- [8] G. W. Huber, P. O'Connor, A. Corma, *Appl. Catal. A Gen.*, **2007**, 329, 120-129.
- [9] J. G. Immer, M. J. Kelly, H. H. Lamb, *Appl. Catal. A Gen.*, **2010**, 375, 134-139.
- [10] M. Snåre, I. Kubičková, K. Eränen, P. Mäki-Arvela, D. Yu. Murzin, *Ind. Eng. Chem. Res.*, **2006**, 45, 5708-5715.
- [11] E. W. Ping, R. Wallace, J. Pierson, T. F. Fuller, C. W. Jones, *Microporous Mesoporous Mater.*, **2010**, 132, 174-180.
- [12] G. Onyestyák, S. Harnos, Á. Szegedi, D. Kalló, *Fuel*, **2012**, 102, 282-288.
- [13] K. Murata, Y. Liu, M. Inaba, I. Takahara, *Energy and Fuels*, **2010**, 24, 2404-2409.
- [14] R. Sotelo-Boyas, Y. Liu, T. Minowa, *Ind. Eng. Chem. Res.*, **2011**, 50, 2791-2799.
- [15] L. Zhou, A. Lawal, *Catal. Sci. Technol.*, **2016**, 6, 1442-1454.
- [16] Y. Liu, R. Sotelo-Boyas, K. Murata, T. Minowa, K. Sakanishi, *Energy and Fuels*, **2011**, 25, 4675-4685.
- [17] B. Veriansyah, J. Y. Han, S. K. Kim, S. A. Hong, Y. J. Kim, J. S. Lim, Y. W. Shu, S. G. Oh, J. Kim, *Fuel*, **2011**, 94, 578-585.
- [18] V. O. Dundich, S. A. Khromova, D. Y. Ermakov, M. Y. Lebedev, V. M. Novopashina, V. G. Sister, A. I. Yakimchuk, V. A. Yakovlev, *Kinet. Catal.*, **2010**, 51, 704-709.
- [19] B. Peng, X. Yuan, C. Zhao, J. A. Lercher, *J. Am. Chem. Soc.*, **2012**, 134, 9400-9405.
- [20] B. Peng, Y. Yao, C. Zhao, J. A. Lercher, *Angew. Chem. Int. Ed. Engl.*, **2012**, 51, 2072-2075.
- [21] B. Peng, C. Zhao, S. Kasakov, S. Foraita, J. A. Lercher, *Chem. Eur. J.*, **2013**, 19, 4732-4741.
- [22] S. T. Oyama, Y. Lee, *J. Phys. Chem. B*, **2005**, 109, 2109-2119.
- [23] R. Prins, M. E. Bussell, *Catal. Letters.*, **2012**, 142, 1413-1436.
- [24] S. T. Oyama, *J. Catal.*, **2003**, 216, 343-352.
- [25] Y. Yang, C. Ochoa-Hernández, V. A. de la Peña O'Shea, J. M. Coronado, D. P. Serrano, *ACS Catal.*, **2012**, 2, 592-598.
- [26] V. M. L. Whiffen, K. J. Smith, *Energy and Fuels*, **2010**, 24, 4728-4737.
- [27] H. Y. Zhao, D. Li, P. Bui, S.T. Oyama, *Appl. Catal. A Gen.*, **2011**, 391, 305-310.
- [28] K. L. Li, R. J. Wang, J. X. Chen, *Energy and Fuels*, **2011**, 25, 854-863.

- [29] A. Infantes-Molina, C. Moreno-León, B. Pawelec, J. L. G. Fierro, E. Rodríguez-Castellón, A. Jiménez-López, *Appl. Catal. B Environ.*, **2012**, *87*, 113-114.
- [30] J. A. Cecilia, A. Infantes-Molina, E. Rodríguez-Castellón, A. Jiménez-López., *Appl. Catal. B Environ.*, **2009**, *92*, 100-113.
- [31] S.T. Oyama, T. Gott, H. Zhao, Y. K. Lee, *Catal. Today*, **2009**, *143*, 94-107.
- [32] A. Rodriguez, J. Kim, J. C. Hanson, S. J. Sawhill, M. E. Bussell, *J. Phys. Chem. B.*, **2003**, *107*, 6276-6285.
- [33] S. Sawhill, K. Layman, D. Vanwyk, M. Engelhard, C. Wang, M. Bussell, *J. Catal.*, **2005**, *231*, 300-313.
- [34] M. Peroni, G. Mancino, E. Baráth, O. Y. Gutiérrez, J. A. Lercher, *Appl. Catal. B Environ.*, **2016**, *180*, 301-311.
- [35] P. Bui, J. A. Cecilia, S. T. Oyama, A. Takagaki, A. Infantes-Molina, H. Zhao, D. Li, E. Rodríguez-Castellón, A. J. López, *J. Catal.*, **2012**, *294*, 184-198.
- [36] N. Koike, S. Hosokai, A. Takagaki, S. Nishimura, R. Kikuchi, K. Ebitani, Y. Suzuki, S. T. Oyama, *J. Catal.*, **2016**, *333*, 115-126.
- [37] J. A. Cecilia, A. Infantes-Molina, E. Rodríguez-Castellón, A. Jiménez-López, S.T. Oyama, *Appl. Catal. B Environ.*, **2013**, *136*, 140-149.
- [38] M. B. Griffin, F. G. Baddour, S. E. Habas, D. A. Ruddy, J. A. Schaidle, *Top Catal.*, **2016**, *59*, 124-137.
- [39] A. Berenguer, T. M. Sankaranarayanan, G. Gómez, I. Moreno, J. M. Coronado, P. Pizarro, D. P. Serrano, *Green Chem.*, **2016**, *18*, 1938-1951.
- [40] Y. Yang, J. Chen, H. Shi, *Energy and Fuels*, **2013**, *27*, 3400-3409.
- [41] Q. Guan, F. Wan, F. Han, Z. Liu, W. Li, *Catal. Today*, **2016**, *259*, 467-473.
- [42] C. Guo, K. T. V. Rao, E. Reyhanitash, Z. Yuan, S. Rohani, C. Xu, *AIChE Journal*, **2016**, *62*, 3664-3672.
- [43] S. K. Wu, P. C. Lai, Y. C. Lin, H. P. Wan, H. T. Lee, Y. H. Chang, *ACS Sustainable Chem. Eng.*, **2013**, *1*, 349-358.
- [44] R. H. Bowker, M. C. Smith, M. L. Pease, K. M. Slenkamp, L. Kovarik, M. E. Bussell, *ACS Catal.*, **2011**, *1*, 917-922.
- [45] V. M. L. Whiffen, K. J. Smith, S. K. Straus, *Appl. Catal. A Gen.*, **2012**, *419-420*, 111-125.
- [46] R. Wang, K. J. Smith, *Appl. Catal. A Gen.*, **2010**, *380*, 149-164.
- [47] V. M. L. Whiffen, K. J. Smith, *Top. Catal.*, **2012**, *55*, 981-990.
- [48] J. G. Tittensor, R. J. Gorte, D. M. Chapman, *J. Catal.*, 1992, *138*, 714-720.

- [49] R. Ramos Pinto, P. Borges, M.A.N.D.A. Lemos, F. Lemos, J.C. Vedrine, E.G. Derouane, F. Ramoa Ribeiro, *Appl. Catal. A Gen.*, **2005**, *284*, 39-46.
- [50] S. T. Oyama, Y. K. Lee, *J. Catal.*, **2008**, *258*, 393-400.
- [51] P. Xiao, M. A. Sk, L. Thia, X. Ge, R. J. Lim, J. Y. Wang, K. H. Lim, X. Wang, *Energy Environ. Sci.*, **2014**, *7*, 2624-2629.
- [52] M. F. Wagenhofer, E. Baráth, O. Y. Gutiérrez, J. A. Lercher, Submitted to *ACS Catal.*, **2016**.
- [53] M. W. Schreiber, D. Rodriguez-Niño, O. Y. Gutiérrez, J. A. Lercher, *Catal. Sci. Technol.*, **2016**, *6*, 7976-7984.
- [54] A. E. Nelson, M. Sun, A. S. M. Junaid, *J. Catal.*, **2006**, *241*, 180-188.
- [55] J. S. Moon, E. G. Kim, Y. K. Lee, *J. Catal.*, **2014**, *311*, 144-152.
- [56] X. Liu, J. Chen, J. Zhang, *Ind. Eng. Chem. Res.*, **2008**, *47*, 5362-5368.
- [57] S. T. Oyama, P. Clark, X. Wang, T. Shido, Y. Iwasawa, S. Hayashi, J. M. Ramallo-López, F. G. Requejo, *J. Phys. Chem. B*, **2002**, *106*, 1913-1920.
- [58] J. K. Nørskov, T. Bligaard, A. Logadottir, J. R. Kitchin, J. G. Chen, S. Pandelov, U. Stimming, *J. Electrochem. Soc.*, **2005**, *152*, J23-J26.
- [59] J. L. Davis, M. A. Barteau, *Surface Science*, **1990**, *235*, 235-248.
- [60] J. Lu, S. Behtash, A. Heyden, *J. Phys. Chem. C.*, **2012**, *116*, 14328-14341.
- [61] M. Mavrikakis, M. A. Barteau, *J. Mol. Catal. A Chem.*, **1998**, *131*, 135-147.
- [62] J. L. Davis, M. A. Barteau, *Surface Science*, **1991**, *256*, 50-66.
- [63] J. L. Davis, M. A. Barteau, *Langmuir*, **1989**, *5*, 1299-1309.
- [64] X. Yang, Z. H. He, X. J. Zhou, S. H. Xu, K. T. Leung, *Appl. Surf. Sci.*, **2006**, *252*, 3647-3657.
- [65] S. Yanagisawa, T. Tsuneda, K. Hirao, Y. Matsuzaki, *J. Mol. Struct. THEOCHEM.*, **2005**, *716*, 45-60.
- [66] S. A. W. Hollak, J. H. Bitter, J. v. Haveren, K. P. d. Jong, D. S. v. Es, *RSC Advances*, **2012**, *2*, 9387-9391.
- [67] G. L. Geoffroy, S. L. Bassner, In *Adv. Organomet. Chem.*; Stone, F. G. A., Robert, W., Eds.; Academic Press: **1988**; Vol. 28, p 1.
- [68] A. Miyashita, R. H. Grubbs, *Tetrahedron Lett.*, **1981**, *22*, 1255-1256.
- [69] Y. Lee, S. T. Oyama, *J. Catal.*, **2006**, *239*, 376-389.
- [70] E. Schachtl, E. Kondratieva, O. Y. Gutiérrez, J. A. Lercher, *J. Phys. Chem.*, **2015**, *6*, 2929-2932.
- [71] G. S. Foo, D. Wei, D. S. Sholl, C. Sievers, *ACS Catal.*, **2014**, *4*, 3180-3192.

3.7 Appendix

3.7.1 Fatty acid composition in triglyceride mixture of microalgae oil

The crude microalgae oil was obtained by Verfahrenstechnik Schwedt GmbH.^[S1]

Table 3A-1. Fatty acid composition in triglyceride mixture of microalgae oil, wt. %.

C _{14:0}	0.04
C _{16:0}	4.41
C _{18:2}	56.20
C _{18:1}	32.20
C _{18:0}	4.41
C _{20:4}	0.07
C _{20:0}	0.43
C _{22:6}	0.13
C _{22:4}	0.19
C _{22:1}	0.97
C _{22:0}	0.44
C _{24:0}	0.36
Sterol	0.12

Nomenclature in lipid numbers:
C_{x:y}: x number of carbon atoms in fatty acid chain; y number of double bonds in fatty acid chain.

3.7.2 Characterization of oxide precursors

The oxide catalyst precursors (prior to temperature programmed reduction) were characterized only by XRD (Figure 3A-1). MoO₃ (ICOD: 00-001-0706), and Ni₂P₄O₁₂ (ICOD: 01-086-2160) were the only crystalline species identified in the oxide precursors of MoP and Ni₂P, respectively. With the presence of citric acid during the synthesis, the intensity of the XRD reflections decreased pointing to smaller crystalline domains. The precursors of WP only exhibited signals of amorphous phases. Their intensity, however, also decreased with the use of citric acid. The same trend, i.e., reduced crystal sizes by using citric acid was observed for the phosphide materials as described in the main text.

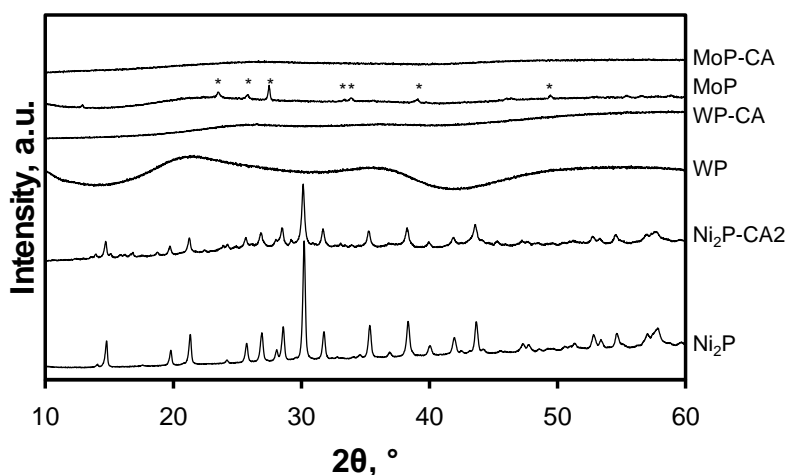


Figure 3A-1. X-ray diffractograms of the oxide precursors (materials before temperature programmed reduction) of the phosphides. The labels show to the names of the corresponding phosphides. The reflections in the patterns of Ni₂P and Ni₂P-CA2 are assigned to Ni₂P₄O₁₂. The reflections of MoP labeled with (*) are assigned to MoO₃.

3.7.3 Characterization of CA-phosphide materials

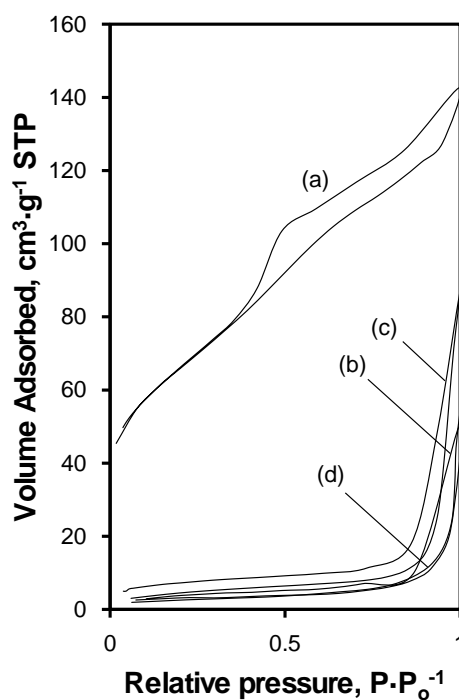


Figure 3A-2. N₂ physisorption isotherms of Ni₂P-CA1 (a), Ni₂P-CA2 (b), MoP-CA (c), and WP-CA (d).

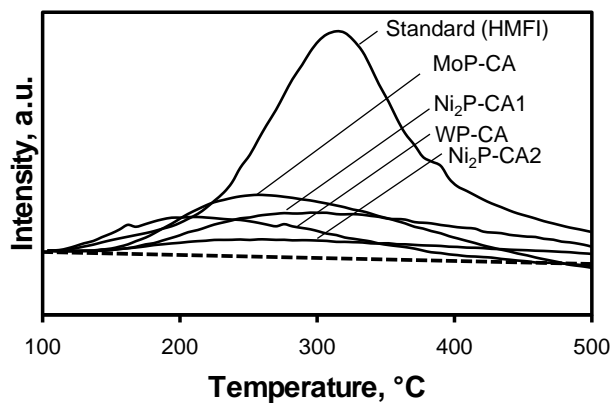


Figure 3A-3. NH₃ desorption profiles from CA-phosphide materials and from the reference HMFI (SiO₂/Al₂O₃ molar ratio of 90).

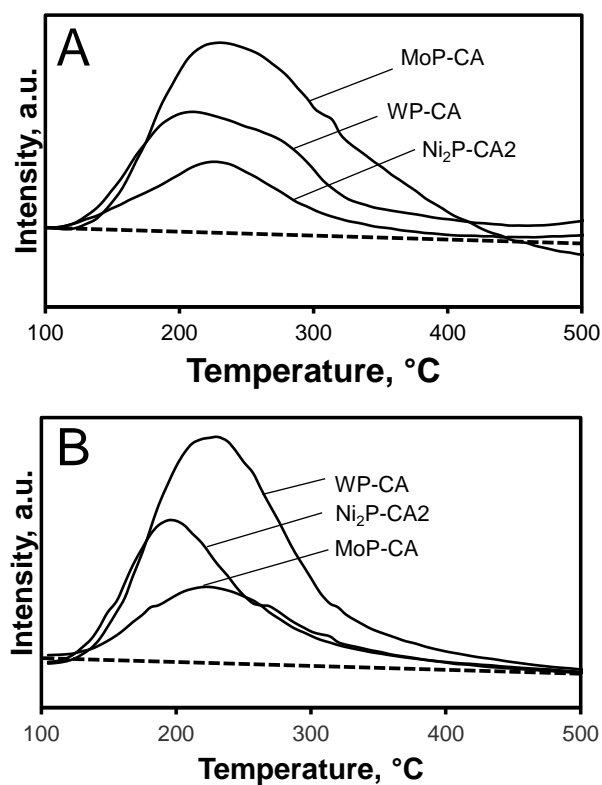


Figure 3A-4. TPD of *n*-propylamine: (A) NH₃ desorption profiles; (B) unreacted *n*-propylamine desorption profiles.

3.7.4 Catalytic tests at constant temperature

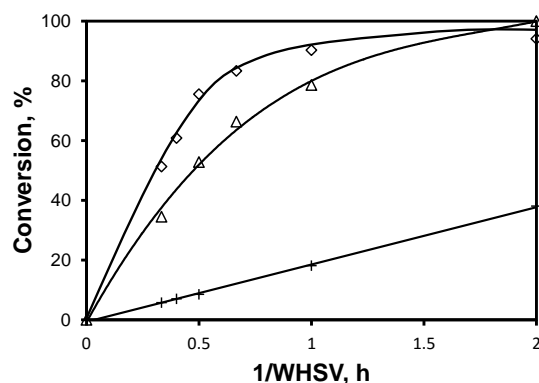


Figure 3A-5. Conversion of palmitic acid at varying residence time on Ni₂P-CA₂ (+), WP-CA (Δ), and MoP-CA (◇). Palmitic acid (0.037 M) in dodecane, 240 °C, 40 bar H₂, H₂/palmitic acid molar ratio = 1000.

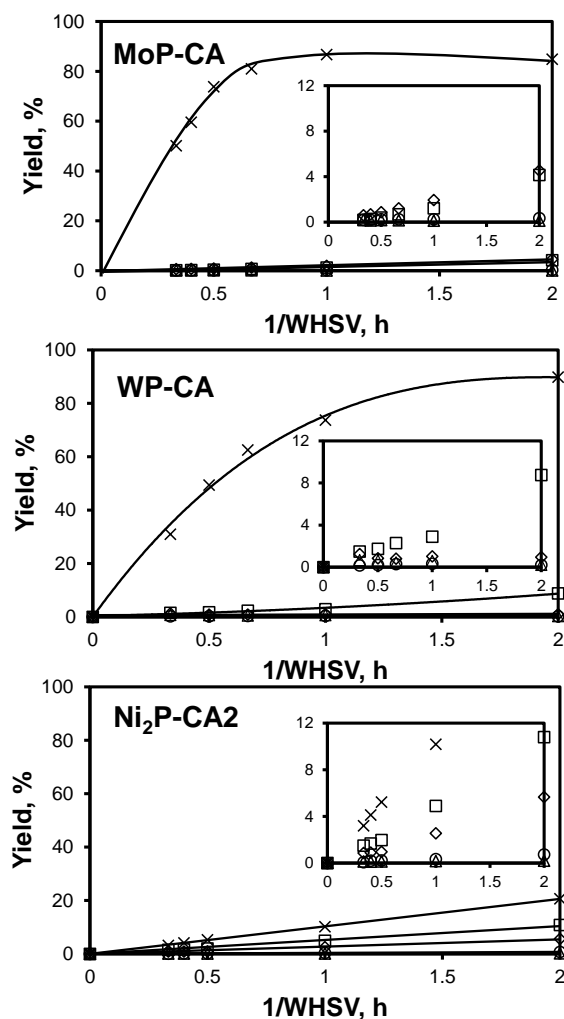


Figure 3A-6. Yields of pentadecane (◇), hexadecane (□), hexadecanal (Δ), hexadecanol (x) and palmityl palmitate (○) at different contact times on CA-phosphides. Palmitic acid (0.037 M) in dodecane, 240 °C, 40 bar H₂.

3.7.5 Conversion of hexadecanol at varying temperatures

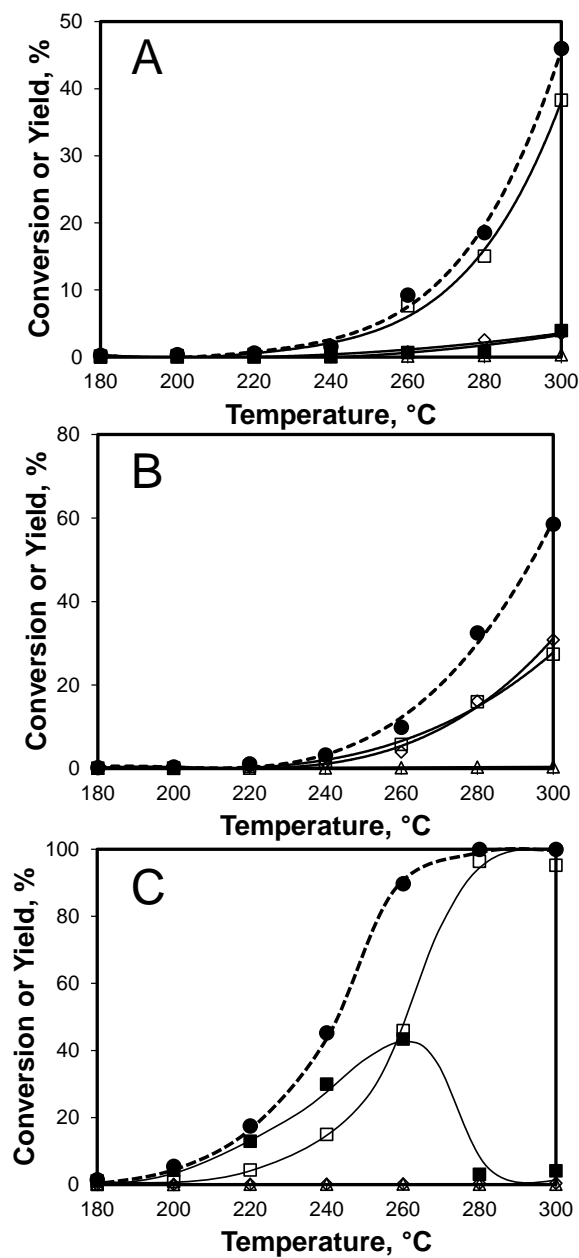


Figure 3A-7. Conversion of hexadecanol on Ni₂P-CA₂ (A), MoP-CA (B) and WP-CA (C) at varying temperatures. Conversion (●), pentadecane (◇), hexadecane (□), hexadecene (■), hexadecanal (Δ). Hexadecanol (0.037 M) in dodecane, WHSV = 1 h⁻¹, 40 bar H₂.

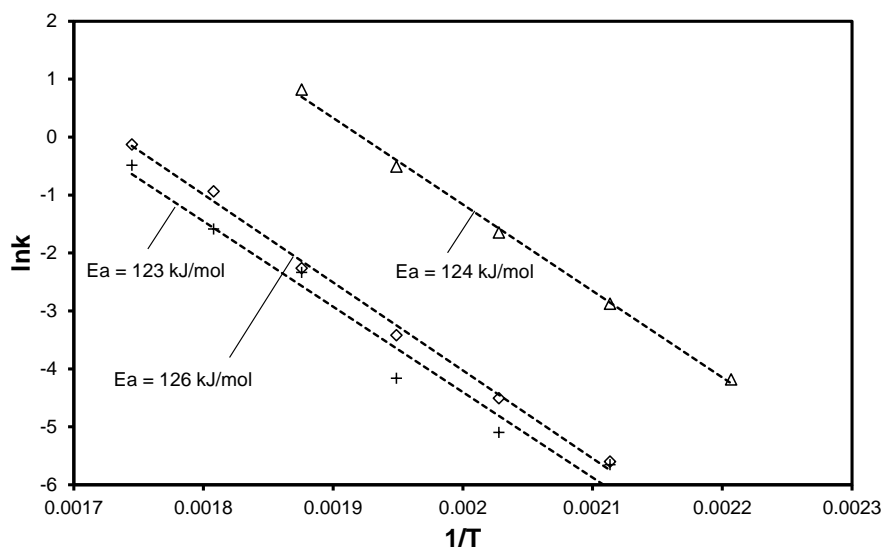


Figure 3A-8. Conversion of hexadecanol at different temperature. Ni₂P-CA2 (+), WP CA (Δ), MoP CA (◇). Hexadecanol (0.037 M) in dodecane, WHSV 1 h⁻¹, 40 bar H₂, H₂/hexadecanol molar ratio = 1000.

3.7.6 Conversion of hexadecanal at varying temperatures

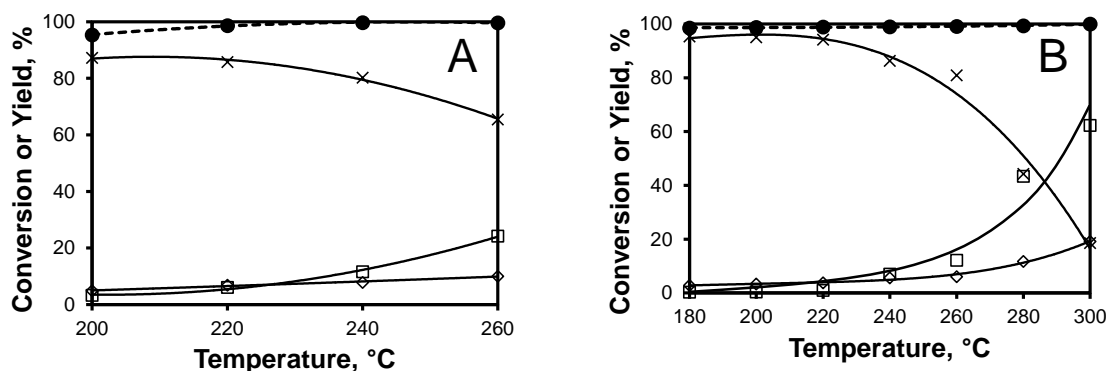


Figure 3A-9. Conversion of hexadecanal on (A) Ni₂P-CA2 and (B) MoP-CA at different temperatures. Conversion (●), pentadecane (◇), hexadecane (□), hexadecanal (x). Hexadecanal (0.037 M) in dodecane, WHSV = 1 h⁻¹, 40 bar H₂.

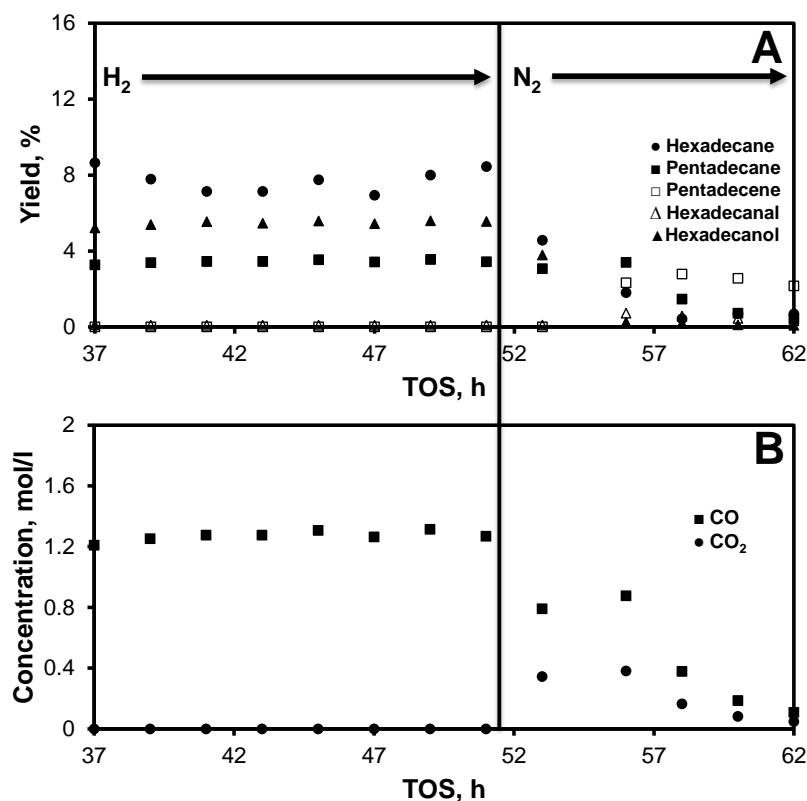
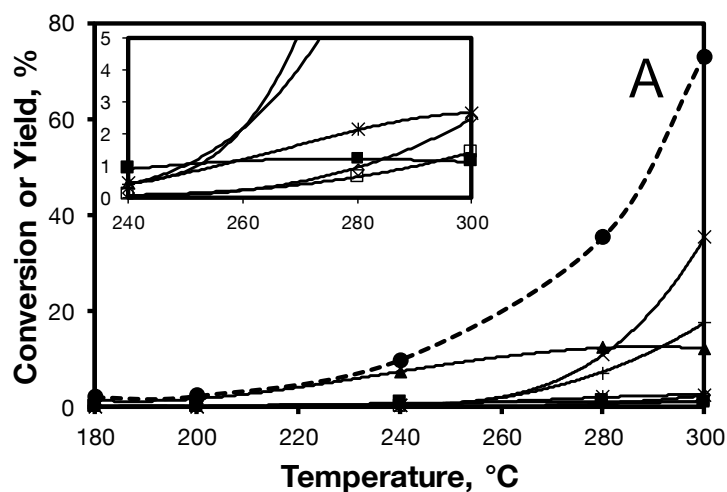
3.7.7 Study of the carbon loss mechanism on Ni₂P-CA

Figure 3A-10. Transient experiments on Ni₂P in order to study the carbon loss mechanism switching from H₂ to N₂ at 40 bar and contact time of 2.5 h. Stabilization: 16 h at 240 °C in H₂ and contact time 0.8 h. (A) Yield % distribution. (B) Concentration in mol/l of CO and CO₂.

3.7.8 Conversion of microalgae oil on MoP



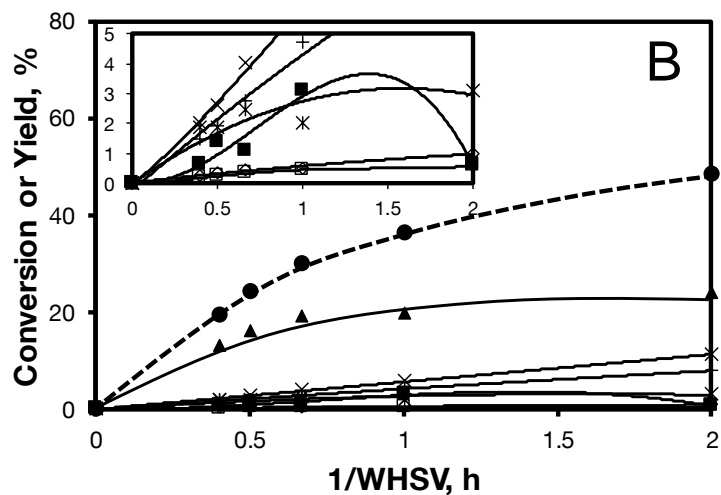


Figure 3A-11. Conversion of microalgae oil on MoP at (A) different temperatures (WHSV = 1 h⁻¹) and at (B) different WHSV (260 °C). Microalgae oil (0.012 M) in dodecane, 40 bar H₂. Conversion (●), pentadecane (◇), hexadecane (□), heptadecane (x), octadecane (+), stearic acid (▲), palmitic acid (■), other alkanes (*).

3.7.9 References

[S1] B. Peng, X. Yuan, C. Zhao, J. A. Lercher, *J. Am. Chem. Soc.*, **2012**, *134*, 9400-9405.

Chapter 4

Hydrocracking of paraffins on Ni- and W-based phosphide catalysts

The present work highlights the possibility to use metal phosphides to provide the (de)hydrogenation function during the hydrocracking of paraffins. WP and Ni₂P were tested in combination with zeolite H-USY for the hydrocracking of n-hexadecane. The phosphide-zeolite composites were prepared by mechanically mixing the zeolite with phosphides supported on SiO₂ or by supporting the phosphides on the zeolite directly.

n-Hexadecane conversion was not observed on phosphides supported on SiO₂, whereas the use of H-USY leads to low conversion and high selectivity to secondary cracking. Mechanically mixing the zeolite with the SiO₂-supported phosphides increased the conversion and the selectivity to primary cracking. In turn, the performance of the catalysts depended on the amount of phosphide, which provided the metal function. The activity of mechanical mixtures of WP/SiO₂ or Ni₂P/SiO₂ with H-USY peaked at the phosphide/H-USY weight ratio of 0.33 with increasing phosphide content. Increasing the amount of metal phosphide, without modification in the acid properties of the zeolite, is the key parameter for reaching ideal hydrocracking. Indeed, the selectivity to primary cracking products increased with the metal/acid sites atomic ratio of the materials, whereas at temperature higher than 350 °C the selectivity to products of secondary cracking was highly increased. At the same phosphide/H-USY weight ratio, Ni₂P-based mixtures exhibited higher concentration of metal sites and lower acidity than WP-based mixtures. Thus, the performance on Ni₂P-based catalysts resembles ideal hydrocracking better than WP-based catalysts. Supporting the phosphides on H-USY doubled the active phosphide surface per gram of catalyst. Therefore, the n-hexadecane conversion rates were higher and the product distribution resembles ideal hydrocracking better over H-USY-supported phosphides than over mechanical mixtures. WP supported on H-USY showed lower activity and higher formation of light alkanes than the Ni₂P counterpart due to higher acidity and lower metal site concentration.

This chapter is based on:

M. Peroni, I. Lee, O. Y. Gutiérrez, J. A. Lercher, DGMK-Tagungsbericht 2016-3, ISBN 978-3-941721-66-1, 183-190. Reprinted with permission from DGMK Deutsche Wissenschaftliche Gesellschaft für Erdöl, Erdgas und Kohle, 2016

4.1 Introduction

Transition metal phosphides (TMP) are refractory compounds with metallic and acidic properties with increasing applications in catalysis.^[1-4] In the last years, metal phosphides have received great attention due to their high activity for hydrodenitrogenation and hydrodesulfurization of petroleum feedstocks.^[1-8] TMP are stable under S- and O-containing conditions, intrinsically more active than sulfides, and more poison tolerant than most base and noble metals.^[2, 4] Recent reports have shown that phosphides are also active and stable for deoxygenation applications.^[9-13] Their bifunctionality and hydrogenation function could make TMP suitable for the conversion of biomass to green fuel. However, the performance of TMP in hydrocracking, in combination with strongly acid materials, has been scarcely explored. Ideal hydrocracking, in which an *n*-alkane (C_n) is converted to a skeletal isomer (*iso*- C_n) at low conversion or to a mixture of shorter hydrocarbons with symmetric distribution of carbon numbers at high conversion, requires a strong hydrogenation/dehydrogenation function in proximity to the Brønsted acid sites.^[14] On the metal sites, the reactant is dehydrogenated to an *n*-alkene, which diffuses to a Brønsted acid site, where it is protonated to a secondary alkylcarbenium ion, which undergoes skeletal rearrangements and carbon-carbon bond scissions. The hydrogenation function has to be strong enough to hydrogenate olefinic intermediates desorbed from the acid sites avoiding secondary cracking.

In this work, supported metal phosphides were tested in the hydrocracking of paraffins in combination with H-USY. *n*-Hexadecane was selected as ideal model compound to represent the alkanes obtained from the deoxygenation of fatty acid derived from biomass. Ni- and W-based phosphides were studied supported on SiO₂ and on zeolite H-USY, the latter was selected in order to obtain Brønsted acid sites minimizing diffusion limitation in its relatively large pores. Mechanical mixtures of SiO₂-supported metal phosphides with zeolites were also studied in order to investigate the effect of the metal loading in the hydrocracking performance avoiding possible effects of the phosphorous precursor on the zeolite.

4.2 Experimental

4.2.1 Synthesis of the catalysts

The materials prepared in this study are listed in Table 4-1. Ni₂P and WP supported on SiO₂

were synthesized by incipient wetness impregnation with solutions containing $\text{Ni}(\text{NO}_3)_2 \cdot 6\text{H}_2\text{O}$ (99.99 %, Alfa Aesar) or $(\text{NH}_4)_6\text{W}_{12}\text{O}_{39} \cdot \text{H}_2\text{O}$ (≥ 99.0 %, Sigma Aldrich) and $(\text{NH}_4)_2\text{HPO}_4$ (≥ 99.0 %, Sigma Aldrich). The solutions were prepared with a Ni/P molar ratio of 0.5 and a W/P molar ratio of 1. The impregnated materials were dried overnight at 120 °C and treated in air at 500 °C for 5 h ($5 \text{ }^\circ\text{C} \cdot \text{min}^{-1}$). The final phosphides were obtained after reduction in H_2 for 2 h at 650 °C ($5 \text{ }^\circ\text{C} \cdot \text{min}^{-1}$ from room temperature to 300 °C and $2 \text{ }^\circ\text{C} \cdot \text{min}^{-1}$ from 300 °C to 650 °C). The final concentration of metal phosphide on SiO_2 was 25 wt. %. The supported phosphides, denoted as $\text{Ni}_2\text{P}(25)/\text{SiO}_2$ and $\text{WP}(25)/\text{SiO}_2$, were mechanically mixed with the H-USY zeolite (Zeolyst CBV720, Si/Al molar ratio of 15). In order to perform the mixtures, denoted as MIX series, the phosphides supported on SiO_2 were mixed with the zeolite in *n*-pentane. After aging for one hour under stirring at room temperature, the suspensions were dried overnight at room temperature. Phosphides supported on the zeolite, denoted as $\text{Ni}_2\text{P}(25)/\text{H-USY}$ and $\text{WP}(25)/\text{H-USY}$, were also synthesized by incipient wetness impregnation with 25 wt. % of phosphide loading. All materials were passivated after synthesis (1 vol. % O_2/N_2) and activated *in-situ* with H_2 prior to physicochemical and kinetic characterization.

Table 4-1. List of catalysts used in this work (TMP stands for Ni_2P or WP) and contents of the components.

Catalyst	TMP/(TMP + H-USY), weight ratio %	TMP/H-USY, weight ratio	TMP, wt. %	SiO_2 , wt. %	H-USY, wt. %
$\text{Ni}_2\text{P}(25)/\text{SiO}_2^{\text{a}}$	-	-	25	75	0
$\text{Ni}_2\text{P}(25)/\text{SiO}_2 + \text{H-USY MIX10}^{\text{b}}$	10	0.11	7.7	23.1	69.2
$\text{Ni}_2\text{P}(25)/\text{SiO}_2 + \text{H-USY MIX25}^{\text{b}}$	25	0.33	14.2	42.9	42.9
$\text{Ni}_2\text{P}(25)/\text{H-USY}^{\text{a}}$	25	0.33	25	0	75
$\text{WP}(25)/\text{SiO}_2^{\text{a}}$	-	-	25	75	0
$\text{WP}(25)/\text{SiO}_2 + \text{H-USY MIX10}^{\text{b}}$	10	0.11	7.7	23.1	69.2
$\text{WP}(25)/\text{SiO}_2 + \text{H-USY MIX25}^{\text{b}}$	25	0.33	14.2	42.9	42.9
$\text{WP}(25)/\text{H-USY}^{\text{a}}$	25	0.33	25	0	75

^a Supported phosphide.

^b Supported phosphide mechanically mixed with zeolite H-USY.

4.2.2 Characterization of the catalysts

All catalysts were characterized by X-ray diffraction (XRD), nitrogen adsorption, transmission electron microscopy (TEM), elemental analysis, CO chemisorption and temperature programmed desorption (TPD) of NH_3 as described in 3.2.3. Indeed, X-ray powder diffraction (XRD) was performed with a Phillips/PANalytical's X'Pert PRO system (Cu $K\alpha$ radiation, 0.154056 nm) operating at 45 kV and 40 mA. Surface areas and pore size distributions were obtained by BET and BJH analysis measuring N_2 -physisorption isotherms at liquid nitrogen temperature using a PMI automated sorptometer (Sorptomatic 1960). TEM

images were recorded on a JEM-2010 JEOL transmission microscope operated at 120 kV. The elemental contents of Ni, W and P in the materials were measured with a photometer Shimadzu UV-160. CO chemisorption was measured by passing CO pulses (0.17 vol. % CO in He) through samples of the materials at 25 °C. The acidity was determined by temperature programmed desorption (TPD) of NH₃.

4.2.3 Catalytic tests

Catalytic tests were performed in the same trickle fixed-bed reactor used for the hydrodeoxygenation of fatty acids in Chapter 2 and Chapter 3. A stainless steel, glass-coated tubular reactor was loaded with the passivated catalyst (160-280 μm, 34-79 mg), diluted in 0.88 g of SiC (60-90 μm). The amount of catalyst introduced in the reactor for each reaction was calculated in order to keep 34 mg of zeolite in the catalytic bed. The entire reactor volume was packed with SiC, which was held by quartz wool. Prior to activity tests, the catalysts were activated in a flow of 20 ml·min⁻¹ of H₂ for 2 h at 450 °C. The catalytic tests were performed at 4 MPa, contact times with zeolite between 0.38 and 1.51 min, and temperatures between 280 °C and 400 °C. Pure *n*-hexadecane and H₂ were fed in downward and concurrent modes keeping the molar ratio of H₂ to *n*-hexadecane of 9.

4.3 Results and discussion

4.3.1 Physicochemical properties

All materials contained the Ni₂P (ICOD: 01-074-1385) or WP (ICOD: 96-900-8944) phase as reported in Figure 4-1. Ni-based phosphides were synthesized with excess of P. However, the metal to phosphorous molar ratios of supported Ni₂P were lower than the stoichiometric value of 2 (Table 4-2). This is attributed to the migration of phosphorous into the support leading to excess of phosphorous in the bulk of the material.^[15] In contrast, supported WP, synthesized with the stoichiometric molar ratio of 1, did not exhibit any excess of P attributable to accumulation into the support.

The impregnated Ni₂P-based materials show lower surface area than the corresponding WP-based catalysts. This is attributed to the excess of phosphorous used during the synthesis of Ni₂P-based materials, which reduces the porosity as indicated, for instance, by the lower intensity of the H-USY reflections for Ni₂P- than for WP-carrying H-USY (Figures 4-1A and

4-1B). Therefore, for Ni-based catalysts the MIX series show higher surface area and porosity compared to the corresponding impregnated materials, being the crystallinity of the H-USY not compromised by the phosphorous precursor.

Table 4-2. Physicochemical properties of phosphides, SiO₂ and H-USY.

	Metal/P, molar ratio	Surface area, m ² ·g ⁻¹	Pore volume, cm ³ ·g ⁻¹	Particle size ^a , nm	CO chemisorbed, μmol·g ⁻¹	Acidity, mmol _{NH₃} ·g _{cat} ⁻¹
SiO ₂	-	191	0.34	-	-	0
H-USY	-	732	0.50	-	-	0.52
Ni ₂ P(25)/SiO ₂	1.4	52	0.18	13	8.5	0.14
Ni ₂ P(25)/SiO ₂ + H-USY MIX10	1.4	460 (523) ^b	0.35 (0.40) ^b	14	3.0 (2.6) ^b	0.31 (0.40) ^b
Ni ₂ P(25)/SiO ₂ + H-USY MIX25	1.4	211 (344) ^b	0.28 (0.32) ^b	14	7.8 (4.9) ^b	0.21 (0.30) ^b
Ni ₂ P(25)/H-USY	1.3	267	0.24	10	15.3	0.36
WP(25)/SiO ₂	1.0	117	0.37	16	6.0	0.18
WP(25)/SiO ₂ + H-USY MIX10	1.0	419 (543) ^b	0.31 (0.46) ^b	13	2.1 (1.8) ^b	0.27 (0.41) ^b
WP(25)/SiO ₂ + H-USY MIX25	0.9	328 (381) ^b	0.27 (0.43) ^b	15	3.1 (3.4) ^b	0.24 (0.33) ^b
WP(25)/H-USY	0.7	458	0.33	6	4.6	0.42

^a Obtained from TEM images.

^b In parentheses the calculated theoretical value considering separately the properties of supported TMP on SiO₂ and H-USY and the relative amount of the two parts in the final mechanical mixture.

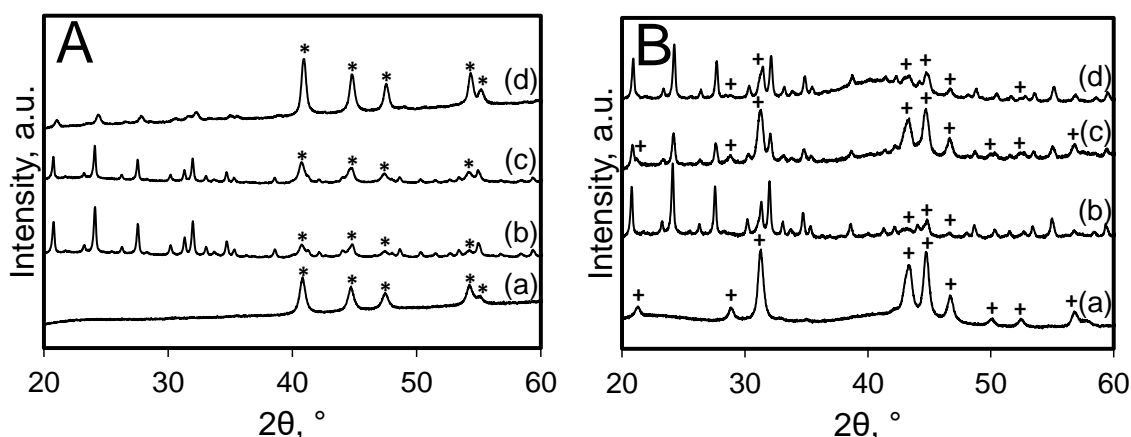


Figure 4-1. X-ray diffractograms of the studied Ni-based phosphides (A): Ni₂P(25)/SiO₂ (a), Ni₂P(25)/SiO₂ + H-USY MIX10 (b), Ni₂P(25)/SiO₂ + H-USY MIX25 (c), Ni₂P(25)/H-USY (d); and W-based phosphides (B): WP(25)/SiO₂ (a), WP(25)/SiO₂ + H-USY MIX10 (b), WP(25)/SiO₂ + H-USY MIX25 (c), WP(25)/H-USY (d). The labeled reflections correspond to Ni₂P (*) or WP (+). The unlabeled reflections correspond to USY.

However, the surface area and pore volume of the MIX series are lower than the calculated theoretical ones (Table 4-2). We speculate that during the physical mixture of TMP/SiO₂ with the zeolite part of the surface of H-USY is blocked as suggested by the closeness of TMP/SiO₂ to the H-USY surface observed in the TEM pictures of Figure 4-2. The catalysts prepared by direct impregnation of the H-USY show smaller TMP crystal size compared to the

corresponding MIX catalysts (Table 4-2). The concentration of surface metal sites and acidity, measured by CO chemisorption and NH₃ TPD, respectively, is much higher for TMP/H-USY than for the corresponding MIX materials. In general, Ni₂P-based catalysts have more metal sites than the corresponding WP-based ones, whereas the latter show higher acidity. For the MIX series, the measured concentrations of chemisorbed CO increase with the metal loading compared to the theoretical ones.

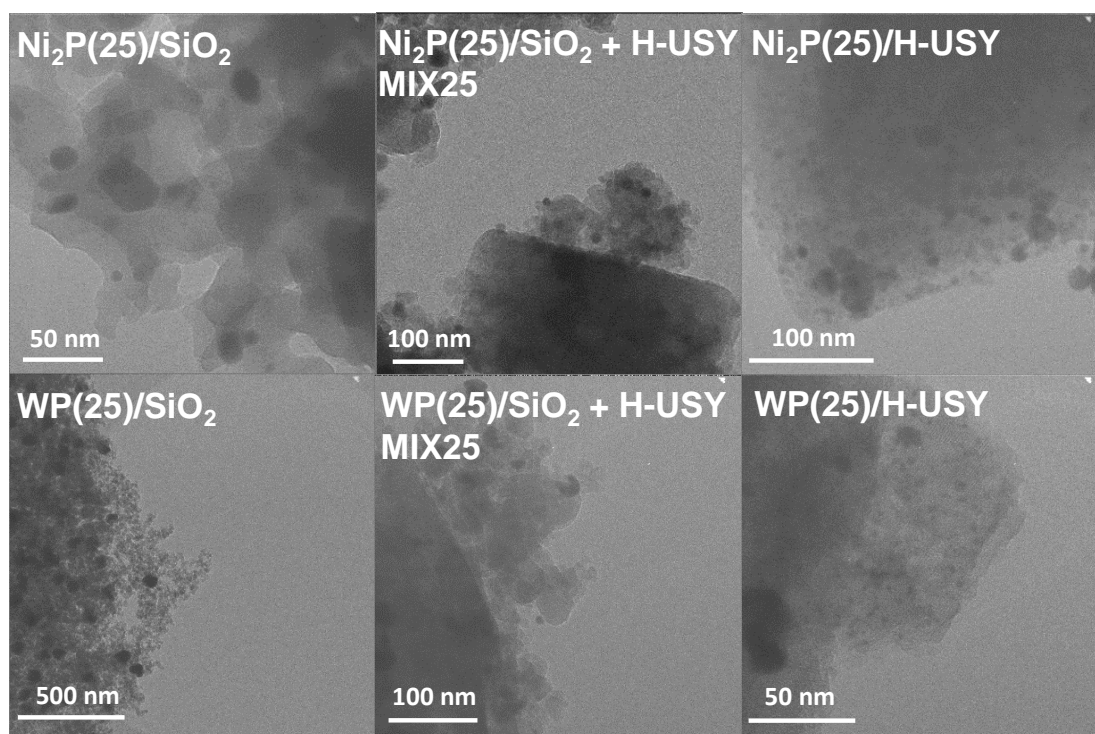


Figure 4-2. Selected TEM micrographs of the supported Ni-based and W-based phosphides.

4.3.2 Catalytic tests at varying temperatures

The conversions of *n*-hexadecane are presented in Figure 4-3, while Table 4-3 reports the total amount of catalyst, of metal sites, and of acid sites applied in each catalytic test. Acid sites are required to obtain high activity in alkane hydrocracking as demonstrated from the very low conversion on Ni₂P(25)/SiO₂ and WP(25)/SiO₂. This indicates the absence of hydrogenolysis activity of Ni₂P and WP under the investigated conditions. H-USY showed higher activity than the SiO₂-supported TMPs but the mechanical mixtures, taking advantage of the synergy between metal sites of TMP/SiO₂ and the acid sites of the zeolite, were much more active than the zeolite alone. Increasing the TMP/SiO₂ content in the MIX-series enhanced the performance of the catalysts due to the higher number of metal sites. However, Ni₂P(25)/H-USY, being the catalyst with the highest metal/acid sites atomic ratio (Table 4-3), showed the highest activity

among the tested catalysts. The activation energies increased with increasing concentration of metal sites relative to that of acid sites (Table 4-3), which points to a gradual shift of the rate determining step from a metal catalyzed step to an acid catalyzed one.

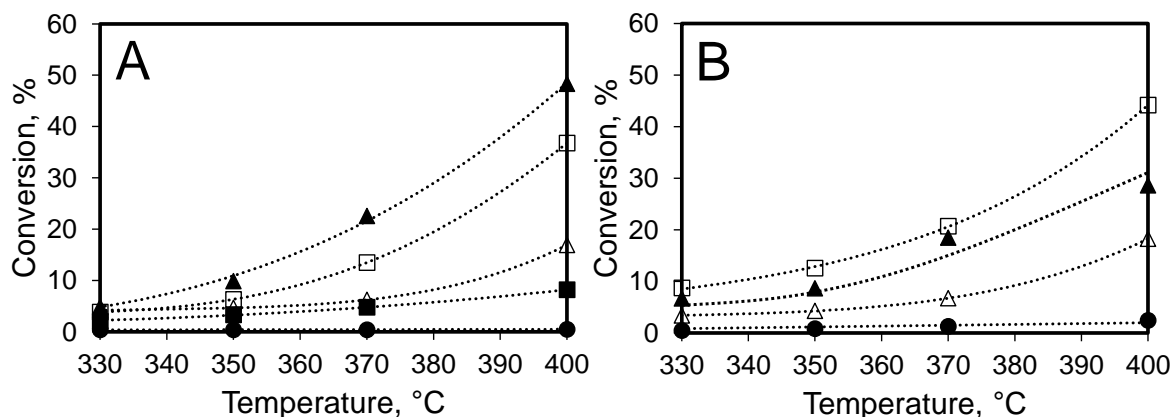


Figure 4-3. Hydrocracking of *n*-hexadecane at varying temperatures at contact time with zeolite of 0.76 min, and 4 MPa H₂. Ni-based phosphides and H-USY (A): Ni₂P(25)/SiO₂ (●), H-USY (■), Ni₂P(25)/SiO₂ + H-USY MIX10 (Δ), Ni₂P(25)/SiO₂ + H-USY MIX25 (□), Ni₂P(25)/H-USY (▲). W-based phosphides (B): WP(25)/SiO₂ (●), WP(25)/SiO₂ + H-USY MIX10 (Δ), WP(25)/SiO₂ + H-USY MIX25 (□), WP(25)/H-USY (▲).

Table 4-3. Mass of catalyst introduced in the reactor, effective concentration of metal and acid sites per reaction and activation energies.

Catalyst	Catalyst, mg	Metal sites per reaction ^a , μmol	Total acidity per reaction ^b , μmol _{NH₃}	Metal/Acid sites atomic ratio, x 10 ²	E _a , KJ·mol ⁻¹
H-USY	34	-	17.8	0	75
Ni ₂ P(25)/SiO ₂ + H-USY MIX10	49.1	0.15	15.3	1.0	71
Ni ₂ P(25)/SiO ₂ + H-USY MIX25	79.1	0.62	16.6	3.7	129
Ni ₂ P(25)/H-USY	45	0.69	16.1	4.3	127
WP(25)/SiO ₂ + H-USY MIX10	49.1	0.10	13.3	0.8	73
WP(25)/SiO ₂ + H-USY MIX25	79.1	0.24	18.9	1.3	90
WP(25)/H-USY	45	0.21	18.8	1.1	81

^a Calculated from the amount of CO chemisorbed, considering the mg of catalyst introduced in the reactor.

^b Calculated from the total acidity, considering the mg of catalyst introduced in the reactor.

Product distributions on Ni₂P-, WP-based catalysts, and H-USY at 370 °C are shown in Figure 4-4. At higher temperatures, secondary catalytic cracking was largely favoured on all materials increasing the selectivity to light alkanes. H-USY showed high selectivity to secondary cracking (small hydrocarbons) without formation of *iso*-C16. That is, the zeolite without metal functions (monofunctional acidic catalyst) readily catalyzes cracking of the primary products.^[14] Upon adding the metal function, the selectivity to high alkanes and *iso*-C16 drastically increased. In the case of Ni₂P(25)/H-USY, with the highest concentration of metal sites, a symmetric product distribution curve with high selectivity to *iso*-C16 was

observed. This product distribution is typical for bifunctional catalysts, where only skeletal isomerization and pure primary cracking takes place.

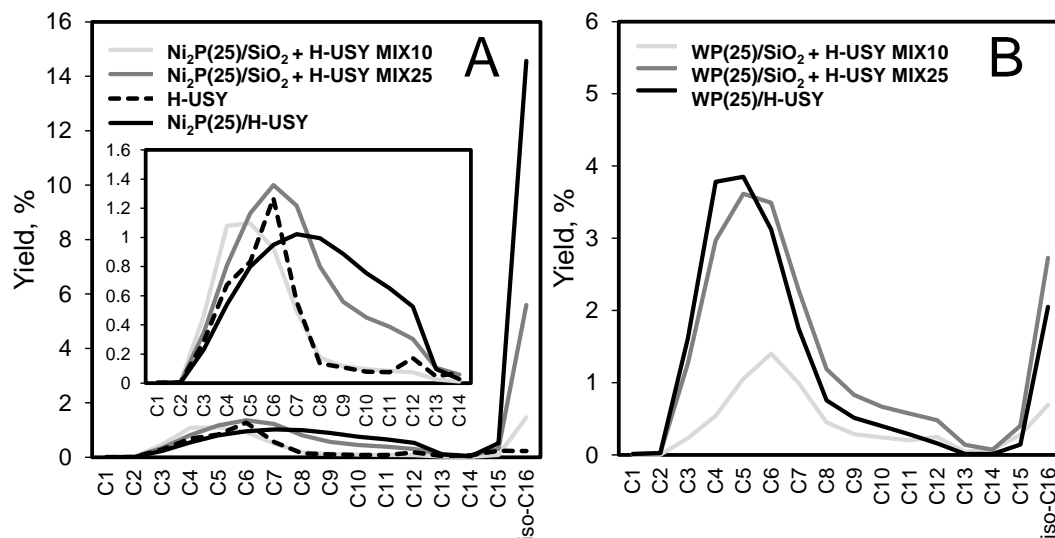


Figure 4-4. Distribution of products at 370 °C, contact time with zeolite 0.76 min, 4 MPa H₂, H₂/hexadecane molar ratio: 9. Ni-based phosphides and H-USY (A). W-based phosphides (B).

4.3.3 Catalytic tests at constant temperature

The catalytic activity of the WP- and Ni₂P-based materials in the conversion of *n*-hexadecane was also explored varying the residence time at 400 °C (Figure 4-5). The activity of all catalysts follows the order: Ni₂P(25)/SiO₂ < WP(25)/SiO₂ < H-USY < WP(25)/SiO₂ + H-USY MIX10 < Ni₂P(25)/SiO₂ + H-USY MIX10 ≤ WP(25)/H-USY < WP(25)/SiO₂ + H-USY MIX 25 ≤ Ni₂P(25) + H-USY MIX 25 < Ni₂P(25)/H-USY. That is, Ni₂P-based catalysts showed higher activity than the WP-based catalysts due to stronger dehydrogenation/hydrogenation function.

Figure 4-6 shows a direct comparison of the product distribution at 400 °C and at similar *n*-hexadecane conversions. At this temperature, the yield of secondary cracking is very high. Ni₂P(25)/H-USY exhibited higher production of primary cracking products and *iso*-C16 than Ni₂P(25)/SiO₂ + H-USY MIX25 (Figure 4-6A). This is ascribed to the higher atomic ratio of metal sites to acid sites of the impregnated catalyst (Table 4-3). The effect of the relative amount of metal sites per number of acid sites is also observed in Figure 4-6B, which shows that WP(25)/SiO₂ + H-USY MIX25 exhibits the highest selectivity to primary cracking and *iso*-C16 among WP materials. H-USY does not produce *iso*-C16 due to the absence of metal sites.

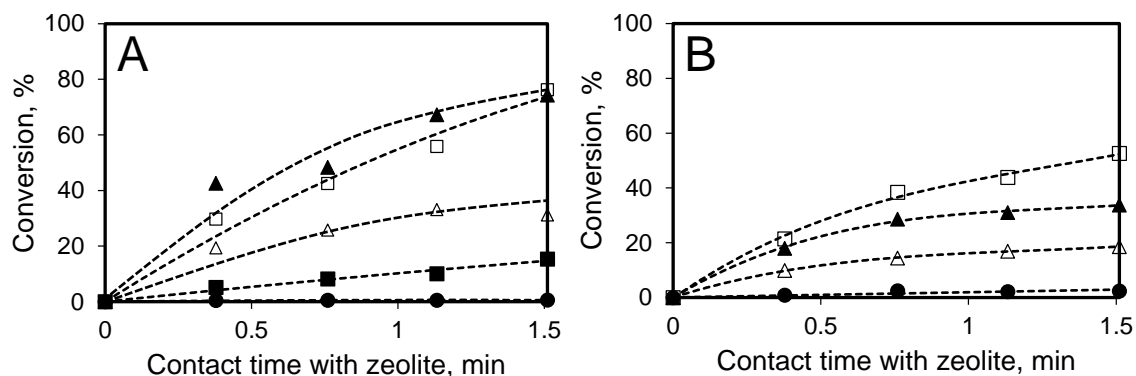


Figure 4-5. Effect of the contact time with zeolite on the hydrocracking of *n*-hexadecane at 400 °C and 4 MPa H₂. Ni-based phosphides and H-USY (A): Ni₂P(25)/SiO₂ (●), H-USY (■), Ni₂P(25)/SiO₂ + H-USY MIX10 (Δ), Ni₂P(25)/SiO₂ + H-USY MIX25 (□), Ni₂P(25)/H-USY (▲). W-based phosphides (B): WP(25)/SiO₂ (●), WP(25)/SiO₂ + H-USY MIX10 (Δ), WP(25)/SiO₂ + H-USY MIX25 (□), WP(25)/H-USY (▲).

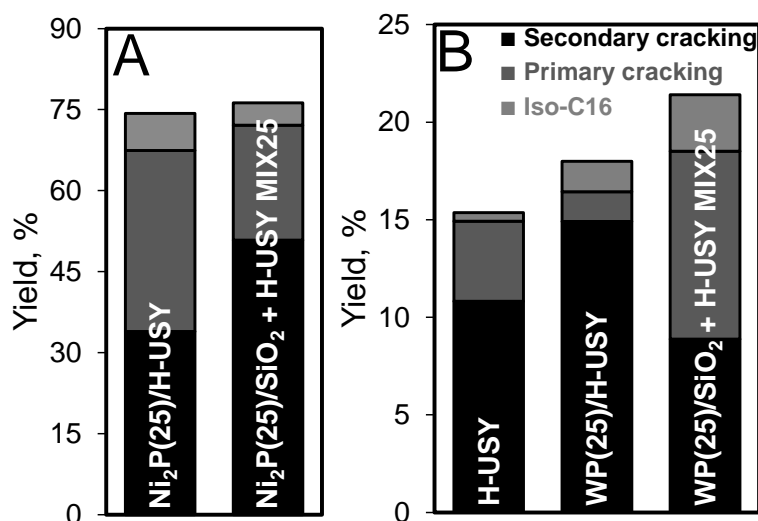


Figure 4-6. Comparison of the product yields at 400 °C, at similar conversions. (A) Ni-based phosphides (Ni₂P/H-USY, weight ratio 0.33). (B) H-USY and W-based phosphide (WP/H-USY, weight ratio 0.33).

The discussion of our results indicates that the metal/acid sites ratio is a key parameter to tune the hydrocracking performance of supported metal phosphides. Accordingly, Figure 4-7 shows the correlation between the rate of hydrocracking of *n*-hexadecane and the metal/acid sites ratio at different temperatures. The effect of the relative amount of metal sites is stronger at higher temperatures.

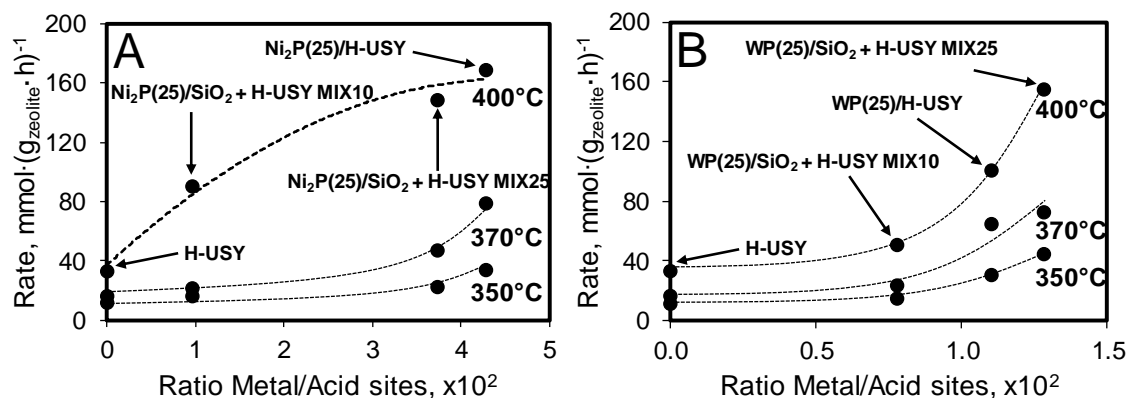


Figure 4-7. Correlation between the rate of hydrocracking of *n*-hexadecane and the metal/acid sites ratio at 350 °C, 370 °C, and 400 °C, contact time with zeolite 0.76 min and 4 MPa H₂. Ni-based phosphides (A) and W-based phosphides (B).

4.4 Conclusions

Metal phosphides can provide the hydrogenation/dehydrogenation function during hydrocracking. Ideal hydrocracking, which yields skeletal isomers of the initial alkane and symmetric distribution of shorter alkanes, is reached with increasing metal/acid sites ratios below 370 °C. Ni₂P(25)/SiO₂ and WP(25)/SiO₂ are not active alone due to lack of hydrogenolysis functionality and the low amount of Brønsted acid sites. The activity of the materials follows the order: H-USY < WP(25)/SiO₂ + H-USY MIX10 < Ni₂P(25)/SiO₂ + H-USY MIX10 ≤ WP(25)/H-USY < WP(25)/SiO₂ + H-USY MIX 25 ≤ Ni₂P(25) + H-USY MIX 25 < Ni₂P(25)/H-USY. Brønsted acidity is mandatory for the hydrocracking activity. High concentration of metal sites, however, is also necessary to improve the activity and the selectivity to ideal hydrocracking. Ni₂P-based phosphides show higher amount of metal sites compared to W-based catalysts and, therefore, higher selectivity to primary cracking and *iso*-C16. WP-based materials, being more acidic than Ni₂P-catalysts, exhibit high selectivity to secondary cracking. Ni₂P(25)/H-USY, prepared by incipient wetness impregnation of H-USY, is the catalyst with performance close to ideal hydrocracking. For future developments, the metal/acid sites atomic ratio should increase further in order to increase the activity of zeolite-supported phosphides. The lowest boundary in acid site concentration needed for hydrocracking with phosphides remains undefined.

4.5 Acknowledgements

The author would like to thank Paola Alejandra Sáenz Cavazos, Robert Schober and Marc J. Kloberg for their scientific contribution. Funding by the German Federal Ministry of Food and Agriculture in the framework of the Advanced Biomass Value project (03SF0446A) is gratefully acknowledged.

4.6 References

- [1] K. L. Li, R. J. Wang, J. X. Chen, *Energy and Fuels*, **2011**, 25, 854-863.
- [2] Y. K. Lee, S. T. Oyama, *J. Catal.*, **2006**, 239, 376-389.
- [3] S. T. Oyama, *J. Catal.*, **2003**, 216, 343-352.
- [4] R. Prins, M. E. Bussell, *Catal. Lett.*, **2012**, 142, 1413-1436.
- [5] A. Infantes-Molina, C. Moreno-León, B. Pawelec, J. L. G. Fierro, E. Rodríguez-Castellón, A. Jiménez-López, *Appl. Catal. B*, **2012**, 113, 87-99.
- [6] J. A. Cecilia, A. Infantes-Molina, E. Rodríguez-Castellón, A. Jiménez-López., *Appl. Catal. B*, **2009**, 92, 100-113.
- [7] H. Y. Zhao, D. Li, P. Bui, S. T. Oyama, *Appl. Catal. A*, **2011**, 391, 305-310.
- [8] S. Sawhill, K. Layman, D. Vanwyk, M. Engelhard, C. Wang, M. Bussell, *J. Catal.*, **2005**, 231, 300-313.
- [9] V. M. L. Whiffen, K. J. Smith, *Energy and Fuels*, **2010**, 24, 4728-4737.
- [10] S. T. Oyama, T. Gott, H. Zhao, Y. K. Lee, *Catal. Today*, **2009**, 143, 94-107.
- [11] A. Rodriguez, J. Kim, J. C. Hanson, S. J. Sawhill, M. E. Bussell, *J. Phys. Chem. B*, **2003**, 107, 6276-6285.
- [12] M. Peroni, G. Mancino, E. Baráth, O. Y. Gutiérrez, J. A. Lercher, *Appl. Catal. B Environmental*, **2016**, 180, 301-311.
- [13] J. Chen, H. Shi, L. Li, K. Li, *Appl. Catal. B Environmental*, **2014**, 144, 870-884.
- [14] J. Weitkamp, *ChemCatChem*, **2012**, 4, 292-306.
- [15] A. Montesinos-Castellanos, T. A. Zepeda, B. Pawelec, J. L. G. Fierro, J. A. de losReyes, *Chem. Mater.*, **2007**, 19, 5627-5636.

Chapter 5

Ni₂P/H-USY and Ni/H-USY catalysts for hydrocracking of n-hexadecane

Series of Ni and Ni₂P catalysts supported on a zeolite H-USY were tested in the hydrocracking/hydroisomerization of n-hexadecane. Most of the Ni/H-USY materials tested were not stable under the applied reaction conditions due to accelerated coke deposition and showed high selectivity to light alkanes (C1-C6). At the same metal loadings, Ni₂P/H-USY catalysts provided the metallic function needed for (de)hydrogenation during hydrocracking of hexadecane without marked deactivation. The combination of Ni₂P and H-USY also provided more flexibility than Ni/H-USY in order to tune the final product distribution. Indeed, Ni/H-USY catalysts are highly selective to light alkanes whereas the selectivity of Ni₂P/H-USY can be tuned by the metal/acid sites atomic ratio. Ni₂P/SiO₂ had low activity due to low acidity and weak hydrogenolysis function, whereas H-USY exhibited high selectivity to secondary cracking. In the Ni₂P/H-USY catalysts, increasing the content of Ni₂P shifted the rate determining step from dehydrogenation on metal sites to acid-catalyzed C-C bond cleavage on the zeolite. Hence, the ratio of the concentration of metal and acid sites (as determined by CO chemisorptions and NH₃-TPD, respectively) allows predicting the selectivity of Ni₂P/H-USY catalysts in the hydrocracking of paraffins. The total conversion rates depended linearly on the concentration of Brønsted acid sites (determined by TPD of NH₃ and n-propylamine) on the material showing enough metal sites to ensure quasi-equilibrium in the (de)hydrogenation function, whereas the rate of hydroisomerization depended linearly on the concentration of metal sites. Product distributions corresponding to ideal hydrocracking (quasi-equilibrated hydrogenation/dehydrogenation on metal sites) were reached with 15 wt. % Ni₂P on H-USY, which corresponded to an atomic ratio of metal/acid sites of 0.25, at temperatures ≤ 370 °C.

This chapter is based on:

M. Peroni, I. Lee, O. Y. Gutiérrez, J. A. Lercher, “Ni₂P/H-USY catalysts for hydrocracking of n-hexadecane”. *Paper in preparation.*

5.1 Introduction

Hydrocracking is one of the most important processes in petroleum refining as it allows converting heavy gasoil, vacuum gasoil, and gasoil from coke into lighter and more valuable fractions as diesel, jet fuel and gasoline by simultaneous C-C bond cleavage and hydrogenation.^[1-4] In hydrocracking of alkanes the hydrocarbon is first dehydrogenated on a metal site to a corresponding alkene, which diffuses to a Brønsted acid site. There, the alkene is protonated to a carbenium ion, which undergoes skeletal rearrangements and C-C bond scissions.^[4-7] The resulting smaller alkenes are finally hydrogenated to alkanes on the metal sites. The hydrogenation function has to be strong enough to saturate olefinic intermediates desorbed from the acid sites avoiding secondary cracking.^[4]

Under optimum conditions (ideal hydrocracking), the dehydrogenation and hydrogenation reactions on the metal sites are equilibrated and there is an efficient transport of the primary products from the acid sites to the metal sites.^[6] The rate determining steps are the acid-catalyzed cracking reactions.^[4, 7-11] Under ideal hydrocracking, an *n*-alkane (C_n) is converted to a skeletal isomer (*iso*-C_n) at low conversion or to a mixture of shorter hydrocarbons with a symmetric distribution of carbon numbers at high conversion, i.e., selectivity is totally shifted to primary hydrocracking. Ideal hydrocracking, in contrast with fluid catalytic cracking, allows obtaining a wide range of product composition ranging from diesel fuel, over jet fuel to gasoline.^[12]

The parameters that affect the product selectivity are the metal-acid site balance^[13], the intimacy between these, the dehydrogenation/hydrogenation ability and properties of metal sites^[14], the strength, distribution and concentration of acid sites and the pore structure and type of support.^[15-18] Strong acidity promotes the hydrocracking, whereas medium strength acidity is favorable to isomerization.^[19, 20] Based on the composition of the desired product, the acidic support ranges from chlorinated aluminas, zeolites (Y, beta, mordenite, ZSM-5, ZSM-22), amorphous silica-alumina, silicoalumina phosphates (SAPO 11, SAPO 31, SAPO 41) to alumina.^[14, 18, 21-32] The metal component in the bifunctional catalysts might include Pt or Pd, having high hydroisomerization selectivity^[15, 27, 33-39], Ni^[40-42], and Ni(Co)-Mo(W) sulfides^[43] used to increase the selectivity to cracking products.^[44, 45] However, the use of noble metals has been discouraged due to their high cost, whereas an increasing number of studies targets the use of base metals and sulfides. Transition metal sulfides are promising catalysts for hydrodesulfurization^[46-51] but their performance strongly depends on the S content in the feed, i.e., optimum hydrotreating performance of sulfides requires a minimum S chemical

potential.^[52-55] Ni is widely available in industry and has higher catalytic activity than other base metals.^[56, 57] Ni-based catalysts are used, i.e., for hydrogenation of CO into methane.^[58, 59] However, Ni is promptly oxidized and sulfided depending on the environment, which suppresses its hydrogenation activity. Transition metal phosphides (TMP) have recently received great attention due to their stability and high activity for hydrotreating in the presence of heterocompounds.^[60-73] The changes associated with S- and O-containing environments seem to be restricted to the surface while the hydrogenation function remains unaltered.^[66, 68-70] Thus, TMP are more poison tolerant than most base and noble metals^[61, 68] with Ni₂P having the highest intrinsic activities.^[60, 65]

Despite of the potential of Ni and its phosphide counterpart Ni₂P as metal components in bifunctional catalysts, its combination with strongly acidic materials has been explored only in few studies.^[74-77] Thus, in the quest for flexible and active hydrocracking catalysts, we have characterized and tested series of Ni/H-USY and Ni₂P/H-USY materials in the hydrocracking of paraffins. We hypothesized that both phases (Ni and Ni₂P) can provide the metal functionality needed for hydrocracking although much higher loadings than noble metals could be required due to their comparable lower activity. The questioned arose as to what is the impact of the high metal loadings on the acid concentration and strength and how the particular metal-acid balance influence their performance in hydrocracking. *n*-Hexadecane was selected as model compound of paraffins obtained from the deoxygenation of fatty acid or those in hydrocracker feeds.^[71, 73] H-USY, on the other hand, is widely used in the petroleum refining industry, particularly in gas oil cracking^[75], due to its relatively large pores.

5.2 Experimental

5.2.1 Synthesis of the catalysts

The catalysts were prepared by impregnating H-USY (Zeolyst CBV720, Si/Al molar ratio of 15) with aqueous solutions of Ni(NO₃)₂·6H₂O (99.99 %, Alfa Aesar) for Ni-based catalysts and Ni(NO₃)₂·6H₂O and (NH₄)₂HPO₄ (≥ 99.0 %, Sigma Aldrich) for Ni₂P-based catalysts. The nominal metal loadings varied from 5 wt. % to 25 wt. %. The Ni/P molar ratio was 0.5 for Ni₂P-based materials with metal loading ≤ 15 wt. % whereas it was 2/3 at 25 wt. % of metal loading. The effect of the Ni/P molar ratio on Ni₂P-based catalysts at the metal loading of 25 wt. % is reported in the Appendix. Citric acid (≥ 99.5 %, Sigma Aldrich) or concentrated nitric acid (65 %, Sigma Aldrich) were added to the solution containing Ni(NO₃)₂·6H₂O and (NH₄)₂HPO₄ in

order to dissolve the precipitate formed when dissolving both salts. The impregnated materials were dried overnight at 120 °C and treated in air at 500 °C for 5 h (5 °C·min⁻¹). Ni and Ni₂P phases were obtained after reduction of the oxide precursors in H₂ for 2 h at 650 °C (5 °C·min⁻¹ from room temperature to 300 °C and 2 °C·min⁻¹ from 300 °C to 650 °C). After cooling to room temperature, all materials were passivated with a flow of 1 vol. % O₂/N₂. Prior to physicochemical and kinetic characterization, the passivated materials were activated in-situ with H₂ at 450 °C. Table 5-1 lists the materials prepared and studied, which are denoted in the following as Ni(*x*)/H-USY and Ni₂P(*x*)/H-USY (*x* is the metal content in wt. %).

Table 5-1. List of catalysts and amount of precursors used.^a

Catalyst	Metal, wt. %	Ni(NO ₃) ₂ ·6H ₂ O, g ^b	(NH ₄) ₂ HPO ₄ , g ^b	Citric acid, g ^b	Nitric acid, ml ^b	H-USY, g	Metal/P, Molar ratio
Ni(5)/H-USY	5	1.23	-	-	-	4.75	-
Ni(10)/H-USY	10	2.47	-	-	-	4.50	-
Ni(15)/H-USY	15	3.71	-	-	-	4.25	-
Ni(25)/H-USY	25	6.19	-	-	-	3.75	-
Ni ₂ P(5)/H-USY	5	0.98	0.89	0.35	-	4.75	1/2
Ni ₂ P(10)/H-USY	10	1.96	1.78	-	0.7	4.50	1/2
Ni ₂ P(15)/H-USY	15	2.94	2.67	-	2.0	4.25	1/2
Ni ₂ P(25)/H-USY ^c	25	4.90	3.33	1.56	-	3.75	2/3

^a Amounts adjusted to obtain 5 g of catalyst.

^b Amounts dissolved in distilled water.

^c Two impregnation steps were needed. After the first impregnation the material was dried overnight and impregnated again.

5.2.2 Characterization of the catalysts

N₂-physisorption isotherms were measured at liquid nitrogen temperature using a PMI automated sorptometer (Sorptomatic 1960) after outgassing approximately 200 mg of sample at 300 °C for 2 h. The surface areas and the pore size distributions were obtained by BET and BJH analyses. X-ray powder diffraction (XRD) was performed with a Phillips/PANalytical's X'Pert PRO system (Cu K α radiation, 0.154056 nm) operating at 45 kV and 40 mA. The XRD patterns were recorded using a scan speed of 1.08 °·min⁻¹. TEM images were recorded in a JEM-2010 JEOL transmission microscope using a LaB₆-cathode operated at 120 kV. Small amounts of catalyst were suspended in ethanol and treated with an ultrasonic probe with an oscillation amplitude of 20 %. Samples were prepared by depositing drops of the suspensions on Cu grids with supporting carbon films. The statistical analysis of particle sizes was performed by measuring at least 300 particles per sample distributed in micrographs taken from different regions of the sample. The elemental contents of Ni and P in the materials were measured with a photometer Shimadzu UV-160. Carbon and hydrogen were quantified with a

EURO EA (HEKA tech) instrument. The concentration of surface metal atoms was determined by passing CO pulses (0.17 vol. % CO in He) through 100 mg of material at 25 °C in a homemade set-up. The CO uptake was monitored by a Balzers mass spectrometer ($m/z = 28$). Prior to the CO pulses, the passivated catalysts were activated in H₂ at 450 °C for 2 h. The acidity of the materials was determined by temperature programmed desorption (TPD) of NH₃ and *n*-propylamine in a homemade 6-fold parallel reactor vacuum-TPD set-up using an H-MFI-90 zeolite (SiO₂/Al₂O₃ molar ratio of 90) as reference. After thermal treatment of the materials in hydrogen at 450 °C for 2 h (heating rate 10 °C·min⁻¹), 1 mbar of NH₃ or *n*-propylamine was adsorbed at 100 °C for 1 h. The samples were outgassed for 4 h prior TPD experiments performed from room temperature to 770 °C (5 °C·min⁻¹). The evolution of ammonia, propene, and *n*-propylamine was monitored using a mass spectrometer Pfeiffer QMS 200 ($m/z = 16, 41$, and 30, respectively).

5.2.3 Catalytic tests

The catalytic tests were performed in a reactor system equipped with high-pressure mass flow meters (Bronkhorst High-Tech) and a HPLC pump (GILSON). The trickle-bed reactor was a stainless steel, glass-coated tube, with downward liquid and gas flow. For all reactions, the amount of catalyst (160-280 μm) introduced in the reactor was varied in order to keep a constant amount of H-USY (34 mg). The concentrations of metal and acid sites (calculated based on site titrations with CO and *n*-propylamine) in each reaction are compiled in Table 5A-1 of the Appendix. Each catalyst sample was mixed with 0.88 mg of silicon carbide (63-90 μm) in order to keep a constant catalyst bed volume within the isothermal region of the reactor. The entire reactor volume was packed with SiC, which was held by quartz wool, in order to obtain good mixing. Prior to activity tests, the passivated catalysts were activated in a flow of 20 ml·min⁻¹ of H₂ for 2 h at 450 °C. The catalytic tests were performed at 4 MPa with contact times between 0 and 2.06 min, and temperatures between 300 °C and 400 °C, after a stabilization period of 12 h time on stream at 400 °C, 4 MPa and 1.13 min contact time. The contact time was defined as the mass of H-USY in the reactor divided by the mass flow of the liquid reactant that consisted of pure *n*-hexadecane (≥ 99.0 %, Sigma Aldrich). *n*-Hexadecane and H₂ were fed in downward and concurrent modes keeping the molar ratio of H₂ to *n*-hexadecane of 9. Aliquots of 1 ml were periodically taken and analyzed by gas chromatography using a Shimadzu 2010 (GCMS-QP2010S) instrument with a HP-5 capillary column (30 m × 250 μm) and flame ionization detector. The gas phase was monitored using an on-line gas chromatograph (Agilent 7890B) with DB-1, HayeSepQ and Molecular Sieve 13X columns. This GC was

equipped with FID and TCD detectors. Control experiments with varying particle size of the catalyst pellets (from 63-90 μm to 160-280 μm) or varying the catalyst loading and flow rate keeping the residence time constant yielded identical catalytic performance. Thus, transport artifacts were discarded.

5.3 Results and discussion

5.3.1 Physicochemical properties

Ni(*x*)/H-USY and Ni₂P(*x*)/H-USY materials with varying metal contents (*x* varying from 5 wt. % to 25 wt. %) were investigated in this work (Table 5-1). The XRD characterization of the corresponding oxide precursors (prior to temperature programmed reduction) is reported in the Appendix. An exploratory study of the effect of the metal/P molar ratio of impregnated solutions on the properties of Ni₂P(25)/H-USY is also reported in the Appendix.

On the reduced catalysts, only the phases Ni (ICOD: 00-004-0850) and Ni₂P (ICOD: 01-074-1385) were identified by XRD as shown in Figure 5-1 and Figure 5-2 (apart from the signals of the zeolite). The intensity of the corresponding reflections increased with increasing metal loading indicating decreasing dispersion of the supported phases. The deposition of Ni did not influence the crystallinity of the H-USY. In contrast, for Ni₂P-catalysts the intensities of the reflections of H-USY decreased with the metal loading. An exploratory study on the stability of H-USY during the preparation of the catalysts (described in the Appendix) showed that the structure of the zeolite is strongly affected by the solution containing (NH₄)₂HPO₄.

On Ni₂P-based catalysts, the metal to phosphorous molar ratios, derived from the elemental analysis, were lower than the stoichiometric ones (2 for Ni₂P). This is attributed to the migration of phosphorous into the support during the reduction of the material, leading to excess of phosphorous in the bulk.^[78, 79] The surface area and the pore volume of all materials decreased with the metal loading as expected from the particles deposited on the surface of the zeolite covering its pores (TEM, see below). On Ni-based materials the surface areas varied from 700 $\text{m}^2\cdot\text{g}^{-1}$ for Ni(5)/H-USY to 527 $\text{m}^2\cdot\text{g}^{-1}$ for Ni(25)/H-USY. On Ni₂P-based materials the decrease in surface area was more pronounced ranging from 550 $\text{m}^2\cdot\text{g}^{-1}$ for Ni₂P(5)/H-USY to 204 $\text{m}^2\cdot\text{g}^{-1}$ for Ni₂P(25)/H-USY, which reflects the deterioration of the H-USY framework.

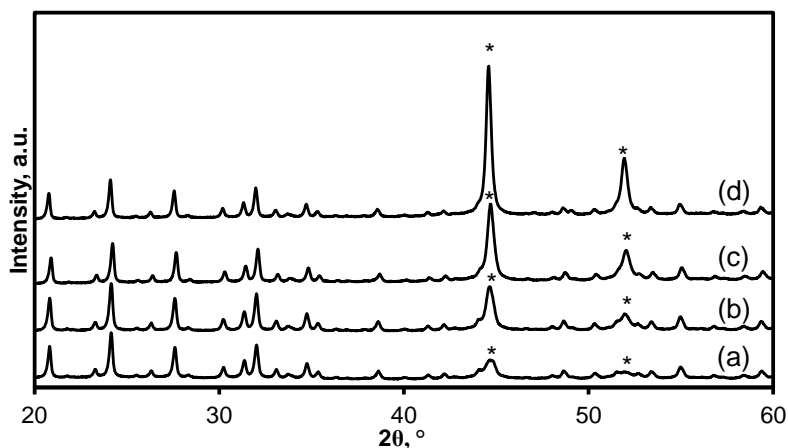


Figure 5-1. X-ray diffractograms of the Ni-based catalysts: (a) Ni(5)/H-USY, (b) Ni(10)/H-USY, (c) Ni(15)/H-USY, (d) Ni(25)/H-USY. The reflections labeled with (*) are assigned to Ni. The reflections not labeled are assigned to H-USY.^[74]

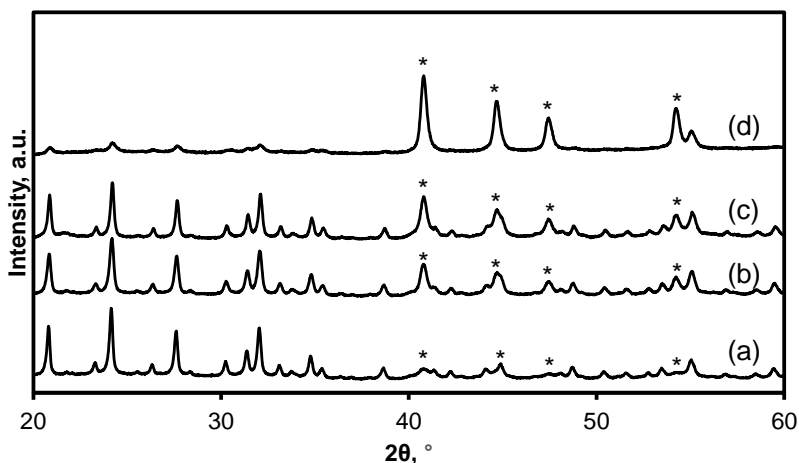


Figure 5-2. X-ray diffractograms of Ni₂P-based catalysts: (a) Ni₂P(5)/H-USY, (b) Ni₂P(10)/H-USY, (c) Ni₂P(15)/H-USY, (d) Ni₂P(25)/H-USY. The reflections labeled with (*) are assigned to Ni₂P. The reflections not labeled are assigned to H-USY.^[74]

The N₂ physisorption of the bare zeolite (Figure 5-3A) showed a large contribution of micropores to the pore volume, as indicated by the large volume adsorbed at low relative pressures. The wide hysteresis loop observed at higher relative pressure indicates a porous solid with a broad distribution of pore sizes due to the presence of relatively large cavities connected by narrower pores. The hysteresis loop is flat below the relative pressure of 0.8, which suggests ink-bottle type mesopores. The deposition of Ni onto the zeolite decreased the surface area and pore volume of the materials (Table 5-2) although keeping unchanged the hysteresis loop. At the same metal loading Ni₂P-based catalysts showed lower porosity compared to the corresponding Ni-based materials (Figure 5-3B and Table 5-2). In addition to the decrease in porosity with increasing metal loading, the isotherms of the Ni₂P-based catalysts exhibited a

more pronounced upward bending at high relative pressures than the Ni-based counterparts, which is attributed to increasing contribution of macroporosity derived from the partial loss of the pore system of the zeolite.

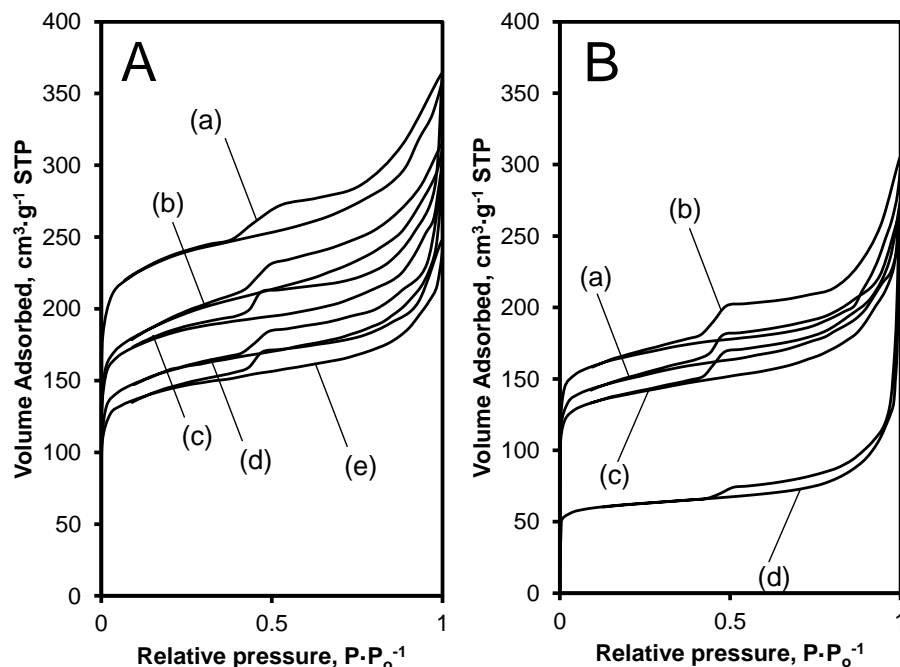


Figure 5-3. N₂ physisorption isotherms of the Ni-based catalysts (A): H-USY (a), Ni(5)/H-USY (b), Ni(10)/H-USY (c), Ni(15)/H-USY (d), and Ni(25)/H-USY (e). N₂ physisorption isotherms of the Ni₂P-based catalysts (B): Ni₂P(5)/H-USY (a), Ni₂P(10)/H-USY (b), Ni₂P(15)/H-USY (c), and Ni₂P(25)/H-USY (d).

TEM micrographs of the Ni-based catalysts (see Figure 5-4 for representative pictures) showed metal particles with wide distributions of particle sizes. The average particle size of the metal remained constant (14-15 nm) up to 10 wt. % Ni but increased up to 42 nm at 25 wt. % Ni (Table 5-2). In good agreement with XRD and N₂ physisorption, the structure of the zeolite did not seem affected by the presence of Ni particles even at the highest metal loading.

In Ni₂P-based catalysts, the average crystal sizes were smaller and the size distributions were more homogenous than for the Ni-counterparts at the same metal loading (representative TEM micrographs are shown in Figure 5-5) as reported in Appendix (Figure 5A-5). The average size of the Ni₂P particles ranged from 9 nm to 12 nm within the 5 wt. % - 25 wt. % range (Table 5-2). The TEM characterization also showed the deterioration of the H-USY structure as observed for Ni₂P(25)/H-USY, when increasing the phosphorous precursor (Appendix).

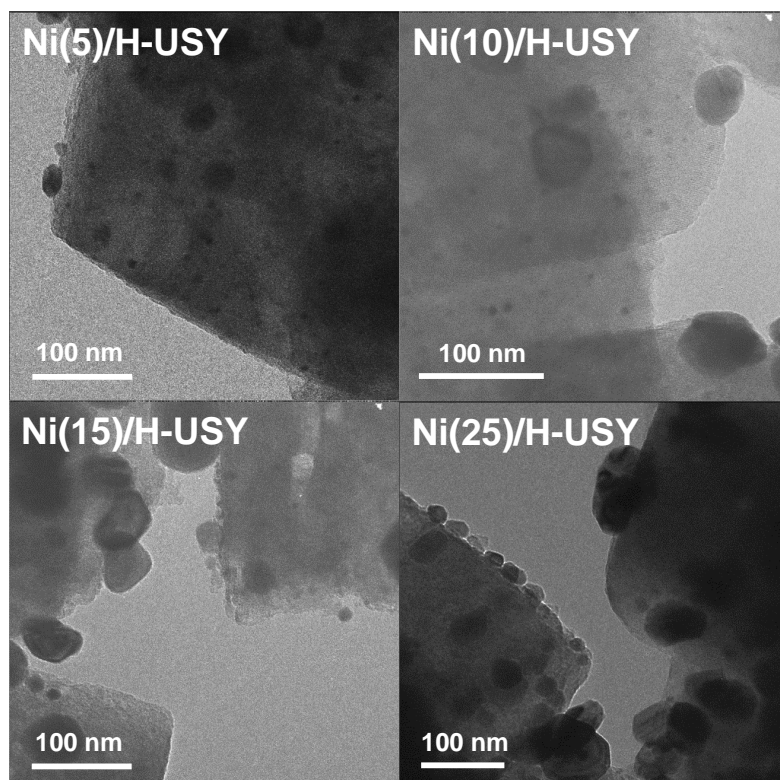


Figure 5-4. Selected TEM micrographs of the Ni-based catalysts.

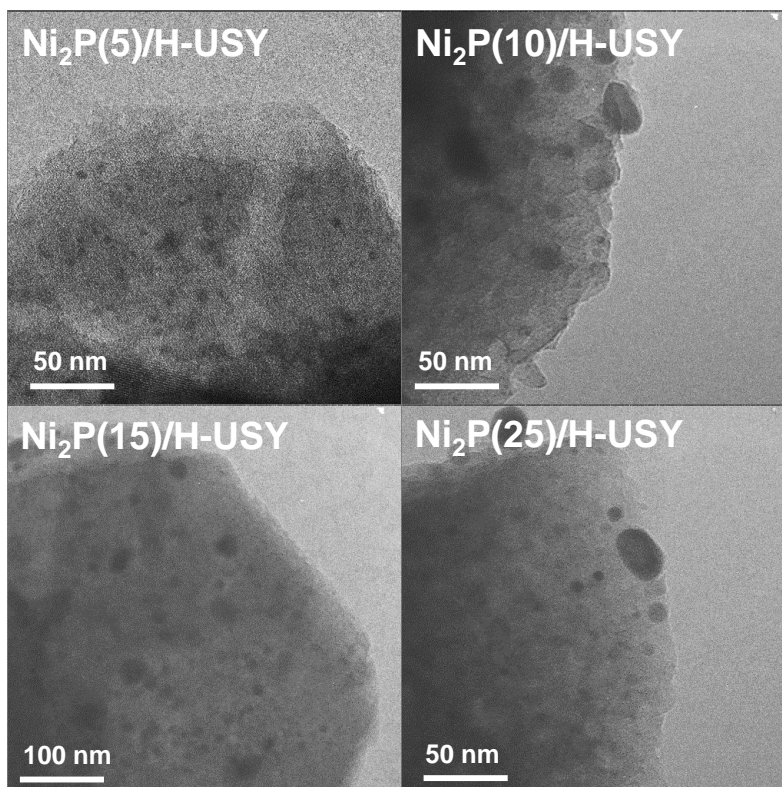


Figure 5-5. Selected TEM micrographs of the Ni_2P -based catalysts.

Table 5-2. Physicochemical properties of the studied materials.

Catalyst	Metal/P, molar ratio	BET Surface area, m ² ·g ⁻¹	Mesopores surface area, m ² ·g ⁻¹	Pore volume, cm ³ ·g ⁻¹	Particle size ^b , nm	CO uptake, μmol·g ⁻¹	Acidity, mmol _{NH₃} ·g ⁻¹
H-USY ^a	-	732	100	0.50	-	0	0.52
Ni(5)/H-USY	-	700	129	0.43	15	6.0	0.37
Ni(10)/H-USY	-	664	67	0.39	14	12.7	0.41
Ni(15)/H-USY	-	578	82	0.34	28	24.1	0.32
Ni(25)/H-USY	-	527	82	0.31	42	21.1	0.28
Ni ₂ P(5)/H-USY	0.69	550	77	0.34	9	5.7	0.38
Ni ₂ P(10)/H-USY	0.83	604	123	0.38	12	9.6	0.29
Ni ₂ P(15)/H-USY	1.41	510	70	0.32	8	29.9	0.18
Ni ₂ P(25)/H-USY	1.01	230	37	0.17	12	12.8	0.19

^a Calcined at 500 °C.^b Obtained from TEM images.

The concentration of chemisorbed CO increased with increasing metal loading up to 15 wt. %, i.e., from 6 μmol·g⁻¹ to 24.1 μmol·g⁻¹ for Ni(*x*)/H-USY and from 5.7 μmol·g⁻¹ to 29.9 μmol·g⁻¹ for Ni₂P(*x*)/H-USY. The materials with 25 wt. % metal exhibited decreasing metal site concentrations (21.1 μmol·g⁻¹ for Ni(25)/H-USY and 12.8 for Ni₂P(25)/H-USY) likely due to the agglomeration of the metal phases.

The acidity of the materials was assessed with TPD of NH₃ and *n*-propylamine. The reference materials Ni(25)/SiO₂ and Ni₂P(25)/SiO₂ showed concentrations of adsorbed NH₃ of 6 μmol·g⁻¹ and 140 μmol·g⁻¹, respectively (Table 5A-2). This indicates that the Ni₂P phase has adsorption sites for NH₃. Most of these sites are Brønsted sites as identified by TPD of *n*-propylamine (see below). This concentration of acid sites, however, is smaller than that exhibited by, e.g., H-USY (520 μmol·g⁻¹) and the sites are also weaker as the desorption temperature was lower for Ni₂P(25)/SiO₂ than for H-USY (Figure 5A-6). On Ni-based catalysts, the increase of the metal loading led to decreasing concentrations of acid sites, i.e., from 370 μmol·g⁻¹ in Ni(5)/H-USY to 280 μmol·g⁻¹ in Ni(25)/H-USY (Table 5-2). The decrease of acidity with metal loading was more pronounced on Ni₂P-based materials, i.e., from 378 μmol·g⁻¹ on Ni₂P(5)/H-USY to 185 μmol·g⁻¹ on Ni₂P(25)/H-USY (Table 5-2). Comparison of the NH₃-TPD profiles of the parent H-USY and the Ni₂P(*x*)/H-USY catalysts indicates that the decrease of the acidity is due to the suppression of the strongest acid sites in the zeolite (Figure 5A-6).

The differentiation between Brønsted and Lewis acidity was achieved by the TPD of *n*-propylamine (Figure 5A-7 and 5A-8) as it decomposes to NH₃ and propene when desorbed from Brønsted acid sites, whereas it does not react on Lewis acid sites.^[80, 81] The sum of the concentrations of Brønsted and Lewis acid sites were similar to the concentrations of NH₃ desorbed during NH₃-TPD (Table 5-2 and Table 5-3). The concentrations of Brønsted and

Lewis acid sites decreased with the metal loading for both Ni- and Ni₂P-based catalysts. Interestingly, the deposition of Ni decreases the concentration of Lewis acid sites stronger than the concentration Brønsted acid sites, whereas Ni₂P affects more the Brønsted acid sites (the Brønsted/Lewis acid site ratio of the bare H-USY increases and decreases with Ni and Ni₂P incorporation, respectively).

Table 5-3. Lewis and Brønsted acidity.

Catalyst	Brønsted Acidity, $\mu\text{mol}\cdot\text{g}_{\text{cat}}^{-1}$	Lewis Acidity, $\mu\text{mol}\cdot\text{g}_{\text{cat}}^{-1}$	Total Acidity, $\mu\text{mol}\cdot\text{g}_{\text{cat}}^{-1}$	Brønsted/Lewis acidity, molar ratio
H-USY	338	170	508	2.0
Ni(5)/H-USY	269	92	361	2.9
Ni(10)/H-USY	293	109	402	2.7
Ni(15)/H-USY	189	76	265	2.5
Ni(25)/H-USY	200	83	284	2.4
Ni ₂ P(5)/H-USY	278	157	435	1.8
Ni ₂ P(10)/H-USY	163	112	275	1.5
Ni ₂ P(15)/H-USY	122	97	218	1.3
Ni ₂ P(25)/H-USY	106	117	223	0.9

5.3.2 On the stability of Ni/H-USY and Ni₂P/H-USY

The conversion of *n*-hexadecane was monitored during the stabilization time of twelve hours. The steady state was reached on all catalysts after that period. The bare H-USY exhibited low activity and deactivated quickly in the first eight reaction hours. Strong deactivation was observed for most of the Ni-based materials (Figure 5-6A). For instance, the *n*-hexadecane conversion on Ni(5)/H-USY and Ni(15)/H-USY dropped from ~50 % to 8 % within 10 h. On Ni(25)/H-USY, the conversion was already low after 2 h of reaction. Ni(10)/H-USY, in contrast, is a remarkable catalyst as it remained stable (at 72 % *n*-hexadecane conversion) after a slight deactivation during the first 4 h of reaction. This observation is in agreement with a previous study, where the optimum Ni loading for hydrocracking catalysts in terms of activity was 8 wt. %.^[82] The Ni₂P-based catalysts were stable as they deactivated only slightly within the first four hours of reaction (Figure 5-6B).

After the reaction, the spent catalysts contained high carbon concentrations (Table 5A-3). The spent H-USY contained 31 wt. % C, whereas the Ni-based catalysts contained at least 50 % more carbon than the Ni₂P-based catalysts at the same metal loading. Furthermore, the C contents were proportional to their deactivation with time on stream. For instance, Ni(15)/H-USY, which showed the highest deactivation rate had the highest C content after the reaction (28.9 wt. %), whereas Ni(10)/H-USY (the most stable Ni catalyst) showed the lowest carbon content (16.9 wt. %) among the Ni-based materials. In contrast, all Ni₂P/H-USY spent catalysts

exhibited C contents in the range of 2-12.5 wt. % and the specific values also resembled the observed deactivation trend. Thus, we conclude that the main cause of deactivation on all catalysts was coke deposition, which is further supported by the C/H molar ratios below 1 of the spent catalysts and direct observations of carbon deposits on the zeolite and on the metal surface performed by TEM (Table 5A-3 and Figure 5A-10).

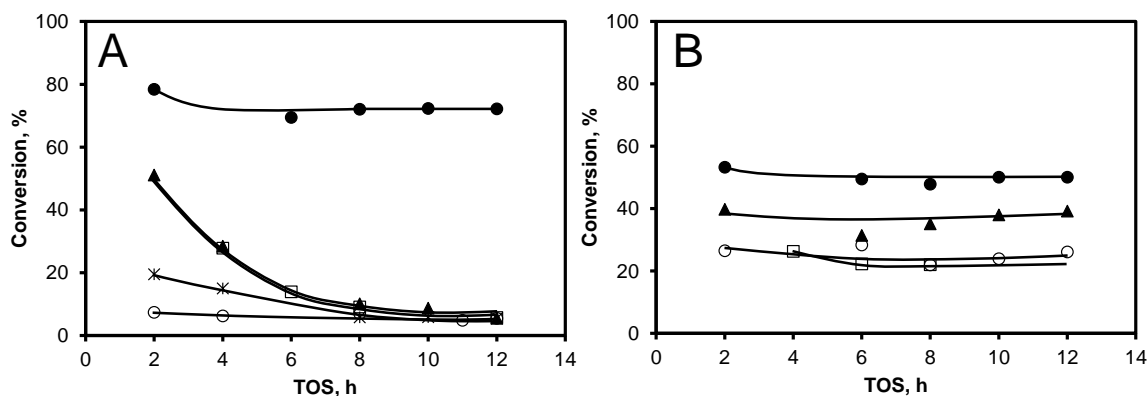


Figure 5-6. *n*-Hexadecane conversion as a function of time on stream on H-USY and Ni/H-USY catalysts (A): Ni(5)/H-USY (□), Ni(10)/H-USY(●), Ni(15)/H-USY(▲), Ni(25)/H-USY(○), and bare H-USY (*). *n*-Hexadecane conversion as a function of time on stream on Ni₂P/H-USY catalysts (B): Ni₂P(5)/H-USY (□), Ni₂P(10)/H-USY (●), Ni₂P(15)/H-USY(▲), Ni₂P(25)/H-USY(○). Reaction conditions: 400 °C, 1.13 min of contact time with the H-USY, 4 MPa H₂, H₂/hexadecane molar ratio of 9. The activation of the passivated catalysts was performed at 450 °C 2 h in H₂.

The strong acid sites of the zeolite are known to catalyze the formation of coke precursors, which subsequently undergo condensation reactions to form large polynuclear aromatic molecules that can physically coat catalytic surfaces, block catalyst pores or rapid poison the acid sites.^[83] Thus, we conclude that the low formation of coke in Ni₂P/H-USY and its concomitant stability during hydrocracking are due to their low concentration of acid sites, which are also milder compared to the acid sites present in Ni/H-USY catalysts.

In addition, coke precursors may be formed on the metal via hydrogenolysis and migrate to the support and undergo polymerization and cyclization reactions.^[84] Ni-based catalysts, unlike the Ni₂P-based catalysts, showed the formation of methane during the conversion of *n*-hexadecane (see below). On the Ni(25)/SiO₂, in particular, only hydrogenolysis was observed and the activity of the catalyst dropped rapidly from 25 % to 2 % in 10 h (Figure 5A-11). Hydrogenolysis is a coke-sensitive reaction, where unreactive coke is deposited on active sites leading to strong deactivation.^[84] On Ni(25)/SiO₂ the content of carbon after the reaction was 22 wt. % and the C/H molar ratio was 0.7, which characterizes hard coke.^[85] On Ni₂P-based

catalysts, the C/H molar ratio was low compared to the corresponding Ni-based counterparts and the small deposits identify soft coke. No coke deposition was observed on the metal surface of the Ni₂P-based catalysts.

Among Ni-based materials, Ni(10)/H-USY was the optimum catalyst, exhibiting remarkable stability due to the high dispersion of metal particles and an optimum metal/acid site ratio. On Ni-based catalysts at metal loading higher than 10 wt. % the particles were big and agglomerated. In this case, the path of diffusion of olefinic intermediates might be too large. The olefinic intermediates have high probability to be further transformed on the acid sites before encounter a metal site to be hydrogenated. Therefore, condensation reactions can occur with coke formation that can block the high microporosity of the Ni-based materials or even cover the metal sites.^[86] In the case of Ni(5)/H-USY, the metal particles are small and well dispersed but not enough to fast hydrogenate the olefinic intermediates. In addition, the acidity of Ni(5)/H-USY is the highest among the Ni-based with the consequence of a very low metal/acid sites ratio.

The smaller particles, the better distribution of particles on the support and the mild acidity and microporosity of the Ni₂P-based catalysts are key factors to avoid the coke formation keeping the catalyst stable and pushing the rate determining step on the acid sites.^[34]

5.3.3 Effect of the metal phosphide loading on the hydrocracking of *n*-hexadecane

The previous study of Ni/H-USY and Ni₂P/H-USY hydrocracking catalysts showed that the latter system is stable allowing high activities within a wide range of ratios of acid sites and metal sites concentration. Thus, in the following we focus on analyzing the effect of varying the Ni₂P loading on the properties of the catalysts and the consequences for their performance.

The activity of the catalysts for the conversion of *n*-hexadecane followed the trend: Ni₂P(5)/H-USY < Ni₂P(25)/H-USY < Ni₂P(15)/H-USY < Ni₂P(10)/H-USY (Figure 5-7A). The corresponding activation energies increased from 88 kJ·mol⁻¹ to 119 kJ·mol⁻¹ with increasing metal/acid site ratio present during the experiment (Table 5-4 and Figure 5-7B). We interpret this as a shift in the rate-determining step from (de)hydrogenation on the phosphide to the acid-catalyzed C-C cleavage.

Indeed, the TOF related to the Brønsted acid sites is comparable on Ni₂P(10)/H-USY, Ni₂P(15)/H-USY and Ni₂P(25)/H-USY (Figure 5-7C) pointing to the fact that the dehydrogenation/hydrogenation step approaches the quasi-equilibrium increasing the metal/acid site ratio. In contrast, on Ni₂P(5)/H-USY the TOF is much lower compared to the

other Ni₂P-based materials, and the low amount of metal sites on this material shift the rate determining step on the dehydrogenation/hydrogenation function. As an example of this trend, the initial conversion rates and the TOFs at 370 °C are presented in Table 5-4.

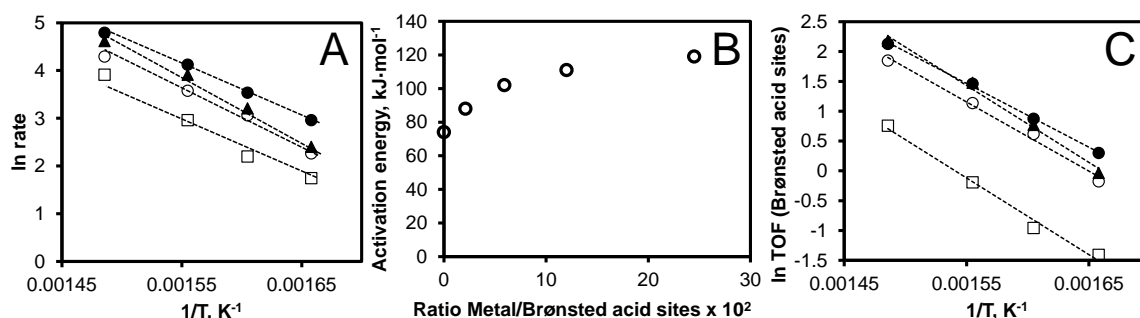


Figure 5-7. Variation of the reaction rate (A), variation of the activation energy as a function of the metal/acid sites atomic ratio (B) and variation of TOF related to the acid sites (C) for the conversion of *n*-hexadecane at varying temperature on Ni₂P-based phosphide catalysts ((□) Ni₂P(5)/H-USY; (●) Ni₂P(10)/H-USY; (▲) Ni₂P(15)/H-USY; (○) Ni₂P(25)/H-USY) at 1.13 min of contact time with the H-USY and 4 MPa H₂ in a flow reactor. H₂/hexadecane molar ratio: 9, activation: 2 h at 450 °C in H₂, stabilization: 16 h. The rate is calculated based on the grams of H-USY introduced in the reactor.

Table 5-4. Kinetic parameters for the conversion of *n*-hexadecane on Ni₂P-based catalysts.

Catalyst	Metal/Brønsted Acid sites molar ratio, x 10 ²	Rate ^a , mmol·(g _{H-USY} ·h) ⁻¹	TOF (Brønsted acid sites) ^a , min ⁻¹	E _a , kJ·mol ⁻¹
Ni ₂ P(5)/H-USY	2.1	19.3	1.1	88
Ni ₂ P(10)/H-USY	5.9	61.7	5.6	102
Ni ₂ P(15)/H-USY	24.5	50.0	5.8	119
Ni ₂ P(25)/H-USY	12.0	35.8	4.2	111

^a Calculated at 370 °C.

The conversion of *n*-hexadecane was studied also at 370 °C and different residence times as shown in Figure 5-8. The activity of the Ni₂P-based catalysts between 0 and 2.06 min of contact time with the H-USY followed the trend: Ni₂P(5)/H-USY < Ni₂P(25)/H-USY < Ni₂P(15)/H-USY < Ni₂P(10)/H-USY.

This experiment allows comparing the selectivity of the catalysts at the same conversion at a temperature, where the activity of the materials is high but the rate of overcracking does not dominate (Figure 5-9). The reaction followed the ideal hydrocracking mechanism on Ni₂P(15)/H-USY due to its high metal/acid sites ratio (0.25). At low conversion, only mono-branched *iso*-hexadecane was formed, whereas with increasing conversion, the mono-branched/multi-branched product molar ratio decreased and the formation of cracking products increased. In the case of Ni₂P(25)/H-USY, the relatively low metal/acid molar ratio (0.12) resulted in decreasing mono-branched/multi-branched product molar ratio at low conversion

and in increased selectivity to cracking products. Decreasing further the metal/acid sites ratio to 0.06 and 0.02 on Ni₂P(10)/H-USY and Ni₂P(5)/H-USY respectively, led to very high selectivity to cracking products and very low amounts of mono-branched and multi-branched *iso*-hexadecanes.

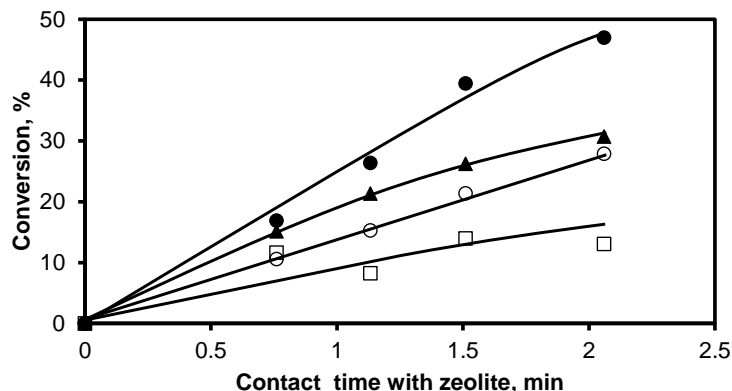


Figure 5-8. *n*-Hexadecane conversion at varying contact times with zeolite on Ni₂P-based phosphide catalysts ((□) Ni₂P(5)/H-USY; (●) Ni₂P(10)/H-USY; (▲) Ni₂P(15)/H-USY; (○) Ni₂P(25)/H-USY) at 370 °C and 4 MPa H₂ in a flow reactor. H₂/hexadecane molar ratio: 9, activation: 2 h at 450 °C in H₂, stabilization: 16 h.

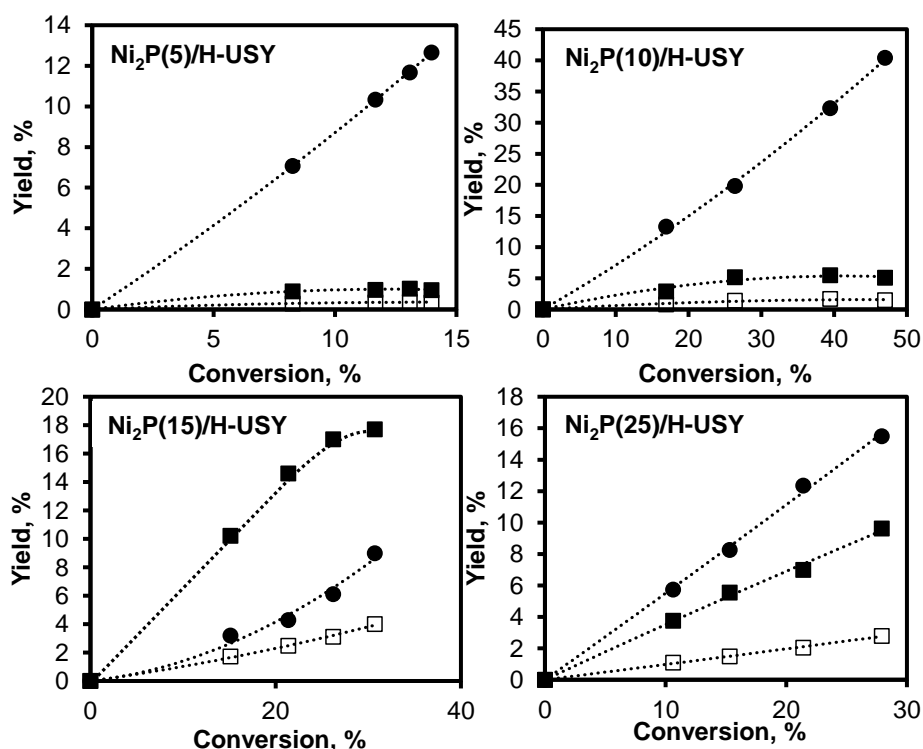


Figure 5-9. Yield-conversion plots for the Ni₂P-based catalysts: mono-branched hexadecanes (■); multi-branched hexadecanes (□); cracking products (●). 370 °C and 4 MPa H₂ in a flow reactor. H₂/hexadecane molar ratio: 9. Activation: 2 h at 450 °C in H₂. Stabilization: 16 h.

Figure 5-10 shows the reaction network of the hydrocracking of *n*-hexadecane and the dependence from the metal/acid site ratio.

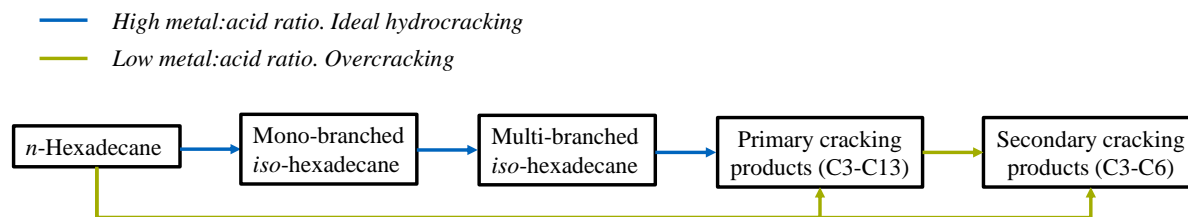


Figure 5-10. Reaction network of the hydrocracking of *n*-hexadecane as a function of the metal/acid sites ratio.

During ideal hydrocracking, enabled by high metal/acid site ratios, the olefins formed upon skeletal rearrangements are fast hydrogenated to *iso*-hexadecane without further secondary β -scission. However, with increasing conversions, consecutive reactions occur at the acid sites. Secondary branching rearrangement leads to dibranched *iso*-alkenes that, upon hydrogenation at the metal sites, convert to dibranched *iso*-hexadecane. Upon increasing the conversion further, tribranched alkylcarbenium ions form upon tertiary rearrangement at the acid site undergoing β -scission into alkylcarbenium ($C_jH_{2j+1}^+$) ions and alkenes ($C_{(16-j)}H_{2(16-j)}$) as shown in Figure 5-11.^[4] On a catalyst with high acidity but low metal/acid site ratio the formation of light alkanes is a primary step and the selectivity to hydroisomerization is limited.

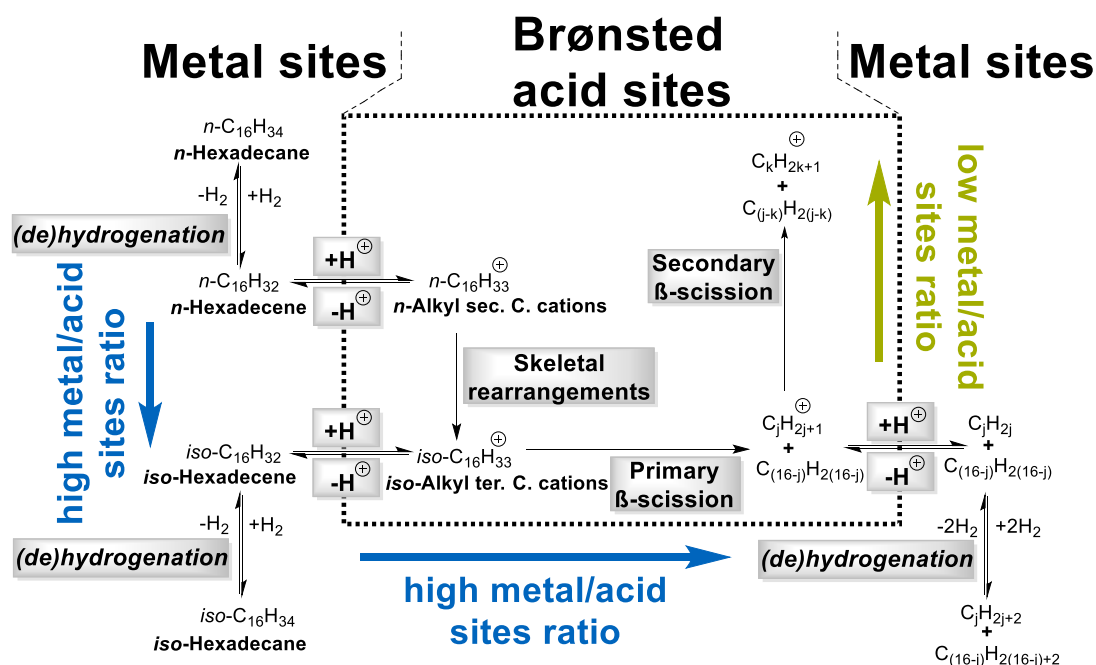


Figure 5-11. Proposed *n*-hexadecane hydroisomerization and hydrocracking mechanism on Ni₂P-based catalysts.^[4]

These results are in agreement with studies conducted on Pt/H-USY catalysts on hydroisomerization and hydrocracking of pure *n*-alkanes^[34], that show that activity, selectivity

and stability are function of the ratio between the concentration of accessible Pt and acid sites (C_{Pt}/C_A). Based on the C_{Pt}/C_A ratio, three regimes were distinguished. At C_{Pt}/C_A lower than 0.03 secondary cracking and condensation reactions (coke formation) were highly favored and the limiting step was the diffusion of the alkene. At $0.03 \leq C_{Pt}/C_A \leq 0.17$ the acid catalyzed step limited the process and dibranched isomers appeared as primary products. Deactivation could still be observed. At $C_{Pt}/C_A \geq 0.17$, no deactivation and no secondary β -scission were observed.

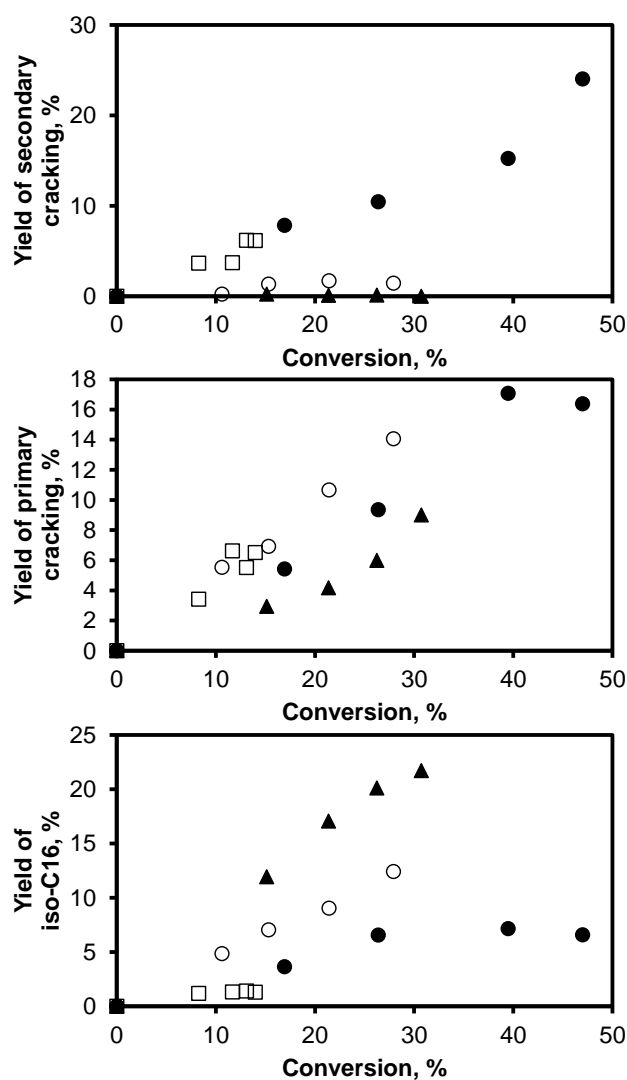


Figure 5-12. Yields of secondary cracking, primary cracking and *iso*-hexadecane formation at varying conversions on Ni₂P-based phosphide catalysts ((□) Ni₂P(5)/H-USY; (●) Ni₂P(10)/H-USY; (▲) Ni₂P(15)/H-USY; (○) Ni₂P(25)/H-USY) at 370 °C and 4 MPa H₂ in a flow reactor. H₂/hexadecane molar ratio: 9, activation: 2 h at 450 °C in H₂, stabilization: 16 h.

Figure 5-12 shows the yields of secondary cracking, primary cracking and *iso*-hexadecane formation at varying conversions. Primary cracking takes place when one carbon-carbon bond in the reactant is cleaved and the hydrocracked product desorbs before a second carbon-carbon bond scission.^[4] This is the case on Ni₂P(15)/H-USY and Ni₂P(25)/H-USY, where the acidity

is not excessively high and the large relative number of metal sites guarantees an efficient primary β -scission to alkenes, which upon hydrogenation on the metal sites appear in the product as alkanes with a bell-shaped molar carbon number distribution. On Ni₂P(25)/H-USY and Ni₂P(15)/H-USY the formation of secondary cracking products is extremely limited and at low conversion the material shows high selectivity to hydroisomerization.

If the hydrogenation/dehydrogenation sites are not enough compared to the active acid sites, the primary cracked products undergo a secondary β -scission and light alkanes form as in the case of Ni₂P(5)/H-USY and Ni₂P(10)/H-USY. In this case, the rate determining step is the diffusion of the alkenes and the hydrogenation/dehydrogenation step not at quasi-equilibrium.

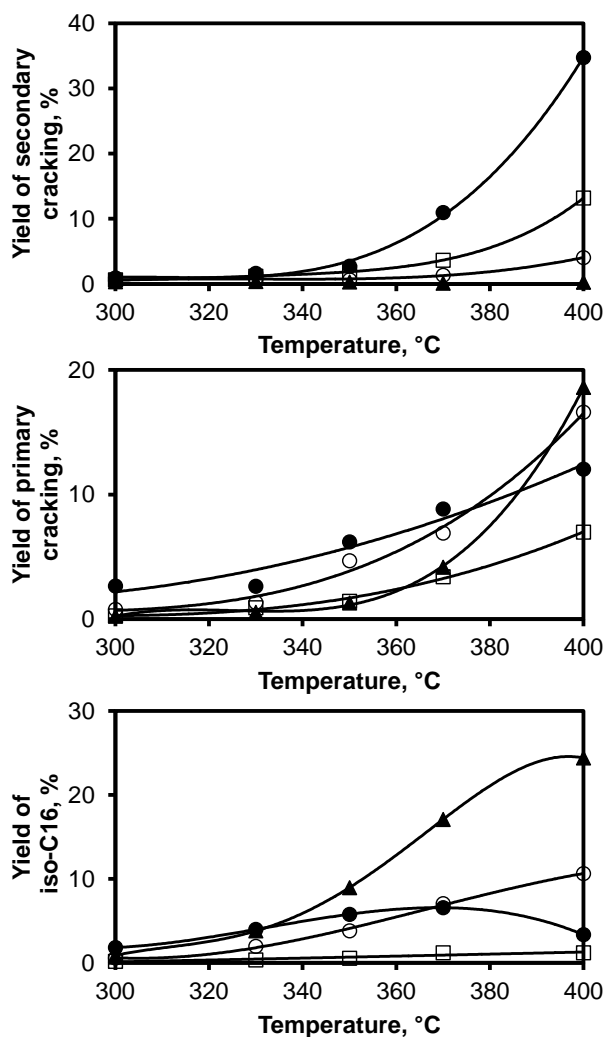


Figure 5-13. Yields of secondary cracking, primary cracking and *iso*-hexadecane formation at varying temperatures on Ni₂P-based phosphide catalysts ((□) Ni₂P(5)/H-USY; (●) Ni₂P(10)/H-USY; (▲) Ni₂P(15)/H-USY; (○) Ni₂P(25)/H-USY) at 1.13 min of contact time with the H-USY and 4 MPa H₂ in a flow reactor. H₂/hexadecane molar ratio: 9, activation: 2 h at 450 °C in H₂, stabilization: 16 h.

On Figure 5-13 the yields of isomerization and cracking at different temperatures are reported. Ni₂P(15)/H-USY having the highest metal/acid site ratio, showed no selectivity to secondary cracking in the studied temperature range. In general, increasing the hydrogenation/dehydrogenation function, the catalyst showed higher selectivity to hydroisomerization at low temperatures. Increasing the reaction temperature, the hydrocracking was strongly favored and the selectivity to *iso*-hexadecane rapidly decreased. However, on the most acidic materials the rate of secondary cracking dominated on the rate of primary cracking at increasing temperatures.

As a summary of the differences between the synthesized Ni₂P-based materials, Figure 5-14 shows a direct comparison at similar conversion (14-17 %) of the yield % of secondary cracking, primary cracking and isomerization, whereas Figure 5-15 compares the product distribution at 370 °C and at a contact time of 1.13 min. In Figure 5-14 it can be observed that no secondary cracking products were formed at low conversion on Ni₂P(15)/H-USY, whereas the catalyst showed high selectivity to hydroisomerization. The product distribution on this material showed the typical bell-shaped curves (Figure 5-15). The hydroisomerization selectivity decreased on Ni₂P(25)/H-USY, whereas Ni₂P(5)/H-USY and Ni₂P(10)/H-USY showed very low amounts of *iso*-hexadecane and very high selectivity to secondary cracking. Therefore, the product distribution on Ni₂P(5)/H-USY and Ni₂P(10)/H-USY was strongly shifted to light alkanes (Figure 5-15).

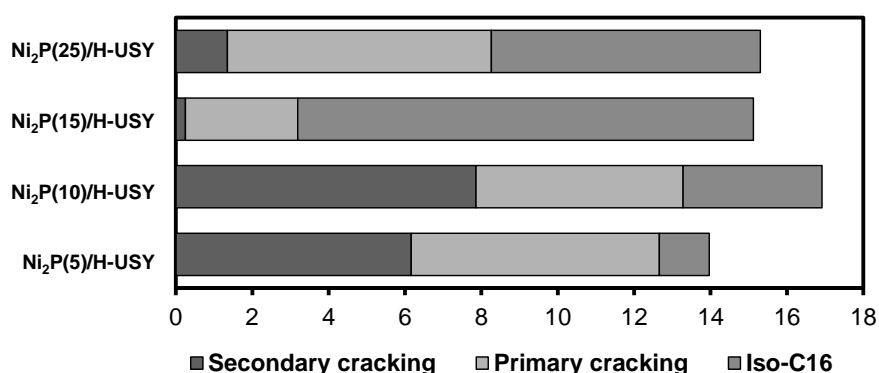


Figure 5-14. Comparison of product yields (%) at similar conversion (14-17 %). Reaction conditions: 370 °C and 4 MPa.

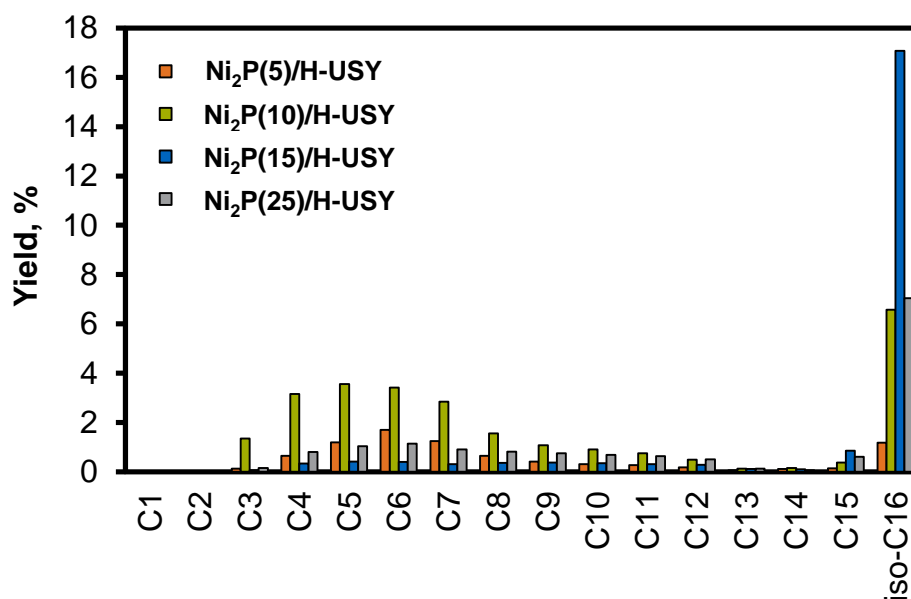


Figure 5-15. Distribution of products at 370 °C, contact time with zeolite 1.13 min, 4 MPa H₂, H₂/hexadecane molar ratio: 9.

Figure 5-16A shows the correlation between the Brønsted acidity and the overall reaction rate. For catalysts having a sufficient number of metal sites, the rate of *n*-hexadecane conversion increases linearly with the acidity of the material. On Ni₂P(5)/H-USY and on the bare H-USY, the rate is very low due to the low amount of metal sites that causes strong deactivation or diffusion limitation. On Figure 5-16B the correlation between the metal sites and the rate is reported. Increasing the amount on metal sites the rate increases until a maximum where the dehydrogenation/hydrogenation is at quasi-equilibrium.

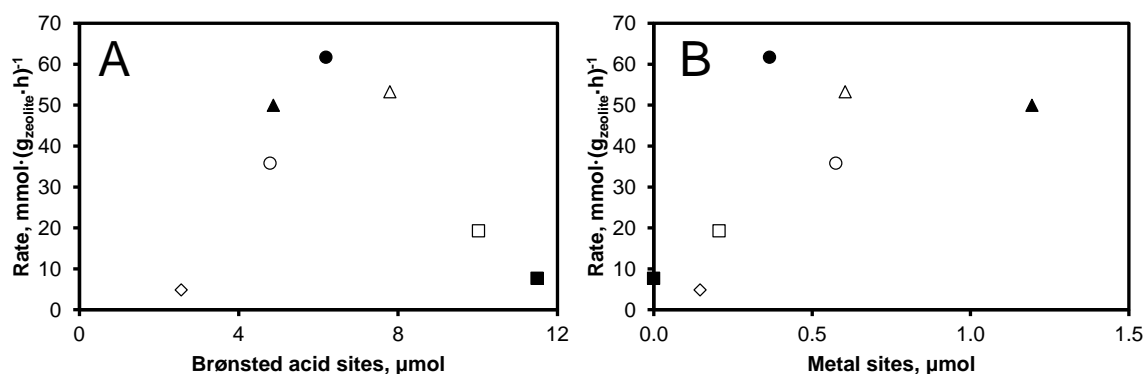


Figure 5-16. (A) Correlation between the Brønsted acid sites and the rate of conversion of *n*-hexadecane. (B) Correlation between the metal sites and the rate of conversion of *n*-hexadecane. (□) Ni₂P(5)/H-USY; (●) Ni₂P(10)/H-USY; (▲) Ni₂P(15)/H-USY; (○) Ni₂P(25)/H-USY; (◇) Ni₂P(25)/H-USY/(1:2) (Appendix); (Δ) Ni₂P(25)/H-USY/(1:1) (Appendix); (■) H-USY. 370 °C and 4 MPa H₂ in a flow reactor. H₂/hexadecane molar ratio: 9, activation: 2 h at 450 °C in H₂, stabilization: 16 h.

The rate of primary cracking also depends on the Brønsted acid sites, whereas secondary cracking tends to increase with the acidity of the material but it is correlated with the rate of accessible metal/acid sites (Figure 5-17A and Figure 5-18).

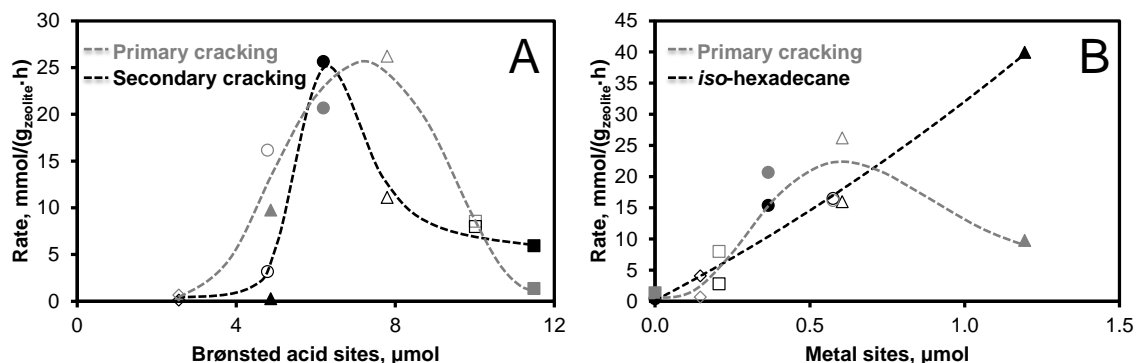


Figure 5-17. (A) Correlation between the Brønsted acid sites and the rate of primary and secondary cracking during the conversion of *n*-hexadecane. (B) Correlation between the metal sites and the rate of primary cracking and *iso*-hexadecane formation during the conversion of *n*-hexadecane. (□) Ni₂P(5)/H-USY; (●) Ni₂P(10)/H-USY; (▲) Ni₂P(15)/H-USY; (○) Ni₂P(25)/H-USY; (◇) Ni₂P(25)/H-USY/(1:2) (Appendix); (Δ) Ni₂P(25)/H-USY/(1:1) (Appendix); (■) H-USY. 370 °C and 4 MPa H₂ in a flow reactor. H₂/hexadecane molar ratio: 9, activation: 2 h at 450 °C in H₂, stabilization: 16 h.

On Ni₂P-based catalysts, at 370 °C, the rate of primary cracking reaches a maximum at a metal/acid sites ratio of 0.08 (Figure 5-18), whereas the rate of hydroisomerization depends linearly on the amount of metal sites (Figure 5-17B) and it strongly increases with the metal/acid sites ratio (Figure 5-18). At value of metal/acid sites ratio higher than 0.15 the secondary cracking selectivity goes to zero (Figure 5-18).

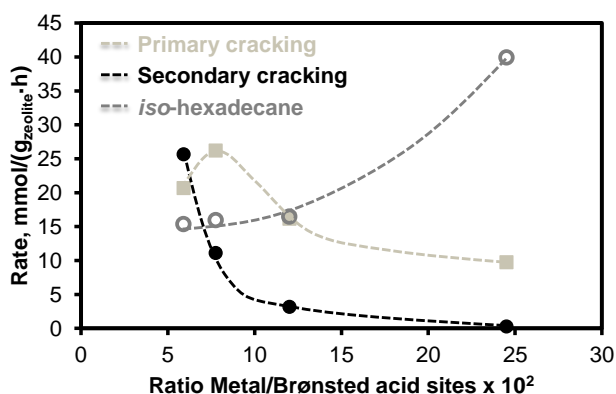


Figure 5-18. Correlation between the Metal/Brønsted Acid sites ratio and the rate of primary and secondary cracking and *iso*-hexadecane formation on Ni₂P-based catalysts supported on H-USY. 370 °C and 4 MPa H₂ in a flow reactor. H₂/hexadecane molar ratio: 9, activation: 2 h at 450 °C in H₂, stabilization: 16 h.

5.3.4 Comparative study of the hydrocracking of *n*-hexadecane on Ni and Ni₂P-based phosphides

Among the Ni-based catalysts tested in this contribution Ni(10)/H-USY was the only one that did not deactivate during the first hours of reaction at 400 °C. For this reason in this chapter Ni(10)/H-USY was compared with Ni₂P(10)/H-USY having the same metal loading and comparable amount of metal sites (Table 5-5). However, the acidity of the two materials was different being the Ni(10)/H-USY more acidic than the corresponding phosphide counterpart. Therefore the metal/acid sites ratio of Ni₂P(10)/H-USY (0.06) was significantly higher than the one on Ni(10)/H-USY (0.04). The high acidity of the latter made this catalyst more active. However, all the activation energies (overall rate and TOF per acid site) were strongly higher on the phosphide (Figure 5-19). Exemplary data of the initial conversion rates and the TOFs at 370 °C are presented in Table 5-5.

Table 5-5. Kinetic parameters for the conversion of *n*-hexadecane on Ni(10)/H-USY and Ni₂P(10)/H-USY.

Catalyst	Metal/Brønsted Acid sites atomic ratio, x 10 ²	Rate ^a , mmol·(g _{H-USY} ·h) ⁻¹	TOF (Brønsted acid sites) ^a , min ⁻¹	E _a , kJ·mol ⁻¹
Ni(10)/H-USY	4.3	98.2	3.9	84
Ni ₂ P(10)/H-USY	5.9	61.7	4.3	102

^a Calculated at 370 °C.

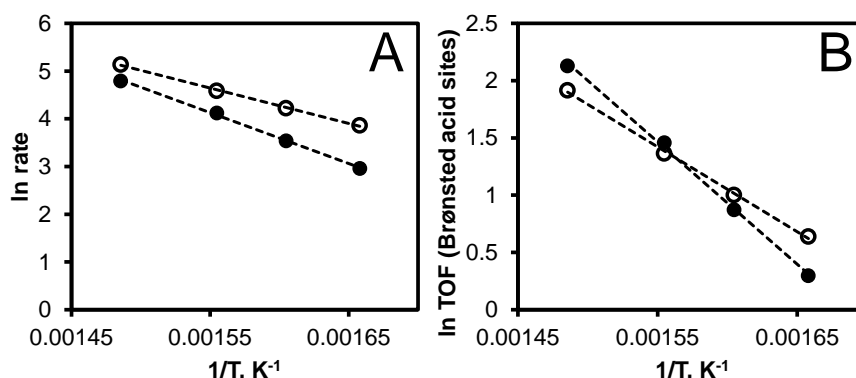


Figure 5-19. Variation of the reaction rate (A) and the TOF related to the acid sites (B) for the conversion of *n*-hexadecane at varying temperature on (○) Ni(10)/H-USY and (●) Ni₂P(10)/H-USY at 1.13 min of contact time with the H-USY and 4 MPa H₂ in a flow reactor. H₂/hexadecane molar ratio: 9, activation: 2 h at 450 °C in H₂, stabilization: 16 h.

Figure 5-20 shows the activity of the two catalysts at 370 °C and different contact times. This experiment gives the possibility to compare the selectivity of the two materials as a function of the conversion as shown in Figure 5-21 and Figure 5-22.

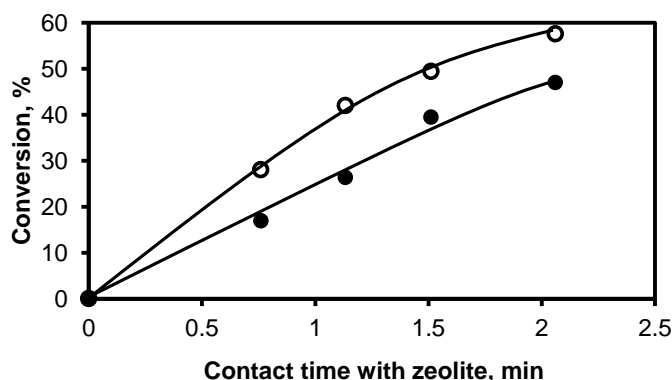


Figure 5-20. *n*-Hexadecane conversion at varying contact times with zeolite on (○) Ni(10)/H-USY and (●) Ni₂P(10)/H-USY at 370 °C and 4 MPa H₂ in a flow reactor. H₂/hexadecane molar ratio: 9, activation: 2 h at 450 °C in H₂, stabilization: 16 h.

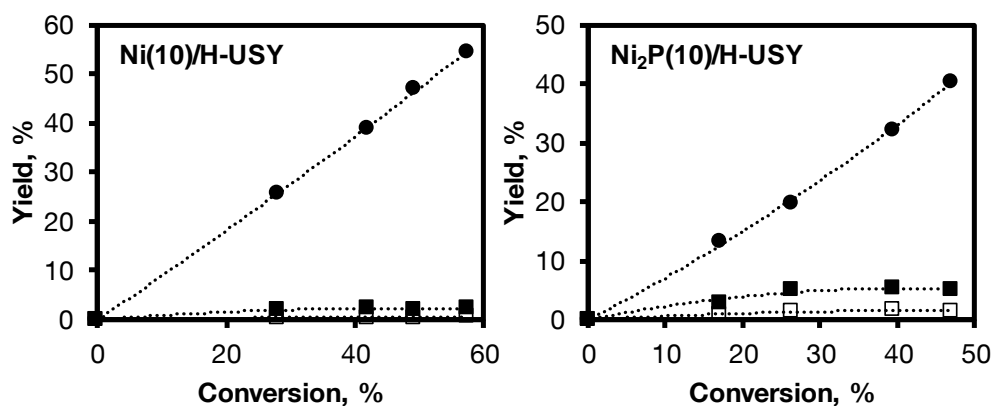


Figure 5-21. Yield/conversion plots on Ni(10)/H-USY and Ni₂P(10)/H-USY: mono-branched hexadecanes (■); multi-branched hexadecanes (□); cracking products (●). 370 °C and 4 MPa H₂ in a flow reactor. H₂/hexadecane molar ratio: 9, activation: 2 h at 450 °C in H₂, stabilization: 16 h.

Ni₂P(10)/H-USY was more selective to hydroisomerization products than the Ni-based counterpart due to the higher metal/acid sites ratio (0.06) of the former compared to Ni(10)/H-USY (0.04). The formation of *iso*-hexadecane on Ni(10)/H-USY was negligible, whereas on Ni₂P(10)/H-USY at low conversion the *iso*-hexadecane formation represented the 25 % of the total products. However, due to the high acidity of the material, at increasing conversions the formation of *iso*-hexadecane reached a maximum, whereas the formation of cracking products increased exponentially. Indeed, on Ni₂P(10)/H-USY at 370 °C the selectivity to secondary cracking increased exponentially with the conversion, whereas at around 40 % conversion the catalyst showed a maximum in selectivity to primary cracking products (Figure 5-22). In conclusion, Ni(10)/H-USY showed higher selectivity to secondary cracking and lower selectivity to primary cracking and *iso*-hexadecane than Ni₂P(10)/H-USY at the same conversion as clearly shown in Figure 5-23 at a conversion between 26.5 % and 28 %.

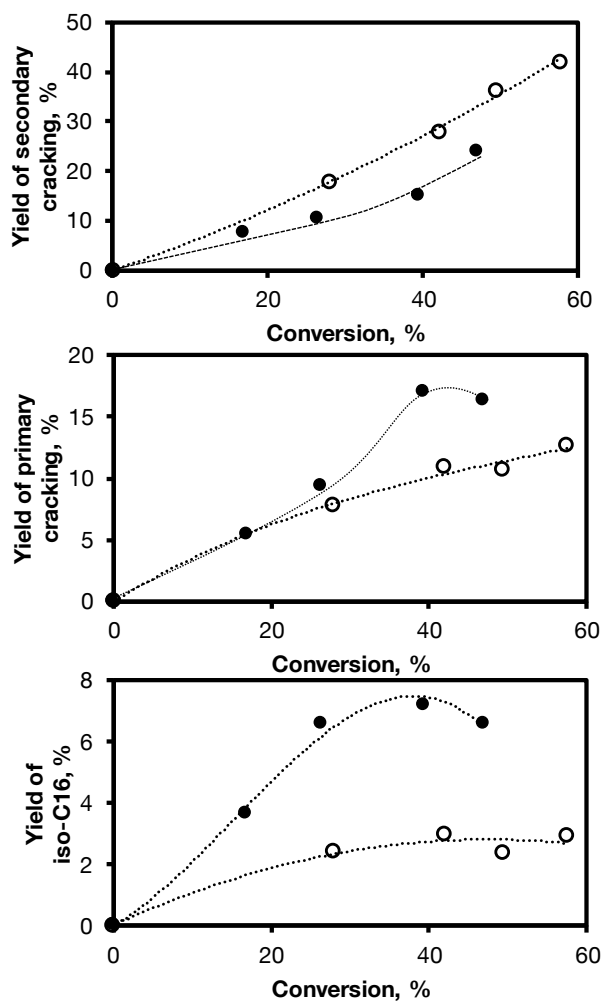


Figure 5-22. Yields of secondary cracking, primary cracking and *iso*-hexadecane at varying conversions on (○) Ni(10)/H-USY and (●) Ni₂P(10)/H-USY at 370 °C and 4 MPa H₂ in a flow reactor. H₂/hexadecane molar ratio: 9, activation: 2 h at 450 °C in H₂, stabilization: 16 h.

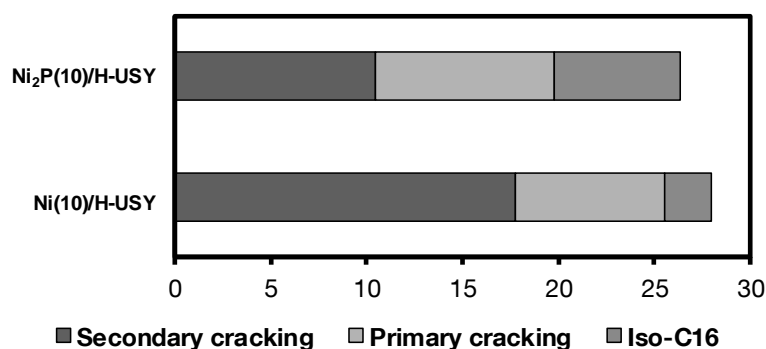


Figure 5-23. Comparison of the yield % at similar conversion (26.5-28 %) at 370 °C and 4 MPa on Ni(10)/H-USY and Ni₂P(10)/H-USY.

The same trend was found studying the product distribution at different temperatures. Ni(10)/H-USY showed high selectivity to secondary cracking within the tested reaction

temperatures (Figure 5-24). In contrast, at low temperatures Ni₂P(10)/H-USY showed high selectivity to hydroisomerization. At temperatures higher than 370 °C the selectivity to hydroisomerization started to decrease and the secondary cracking was highly favored on both the materials being stronger on Ni(10)/H-USY. Figure 5-25 shows the direct comparison of the product distribution on the two materials at 370 °C and 1.13 min of contact time with the zeolite. In both cases the distribution is non-symmetrical, i.e., metal/acid sites ratio is not high enough to avoid the diffusion of the alkenes being the limiting step, causing an increase of secondary β -scission and therefore an increase of light alkanes. However, Ni₂P(10)/H-USY having higher metal/acid molar ratio showed higher selectivity to hydroisomerization and less asymmetry in the product distribution compared to the Ni-based counterpart.

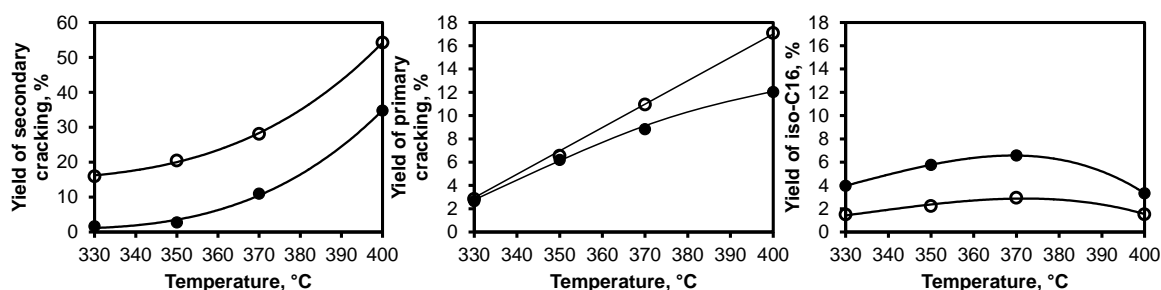


Figure 5-24. Yields of secondary cracking, primary cracking and *iso*-hexadecane at varying temperatures on (○) Ni(10)/H-USY and (●) Ni₂P(10)/H-USY at 1.13 min of contact time with the H-USY and 4 MPa H₂ in a flow reactor. H₂/hexadecane molar ratio: 9, activation: 2 h at 450 °C in H₂, stabilization: 16 h.

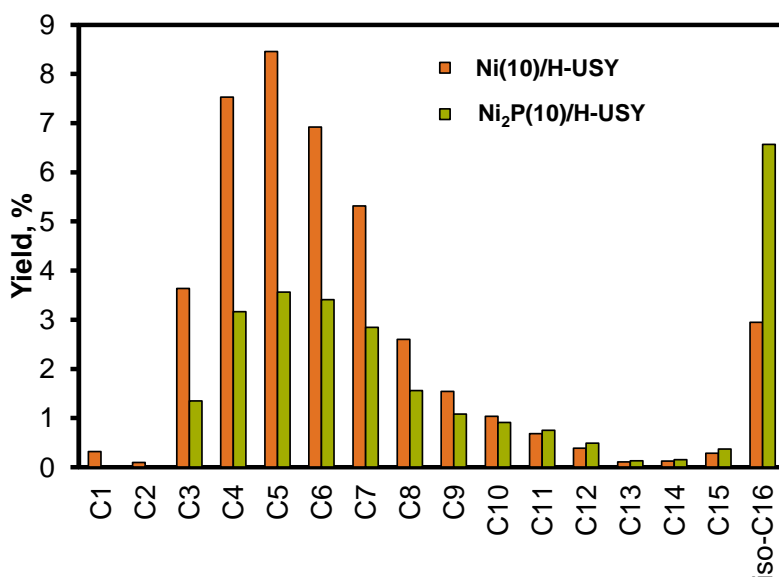


Figure 5-25. Distribution of products at 370 °C, contact time with zeolite 1.13 min, 4 MPa H₂, H₂/hexadecane molar ratio: 9 on Ni(10)/H-USY and Ni₂P(10)/H-USY.

The main difference between nickel phosphides and pure nickel is in the electronic and geometrical properties, which are ascribed to the ligand and ensemble effects of P^[87] that make the Ni₂P-based catalysts more selective to hydroisomerization compared to the Ni-based materials. Ni-based catalysts showed high selectivity to light alkanes having high activity for the C-C bond cleavage. Indeed, Ni-based catalysts were active to hydrogenolysis reactions as demonstrated in addition from the production of methane on this materials (Figure 5-25).

5.4 Conclusions

Ni- and Ni₂P-based catalysts supported on H-USY are active for hydrocracking and might represent an alternative to expansive noble metals. However, Ni-based catalysts exhibit high selectivity to multiple C-C bond cleavage and marked deactivation, which is associated to the difficulty to obtain supported metal particles with high dispersion. Among the Ni-based catalysts tested in this contribution, only Ni(10)H-USY (10 wt.% Ni) was stable after the stabilization period but it was highly selective to light alkanes. In contrast, Ni₂P-based catalysts can provide the hydrogenation/dehydrogenation function during hydrocracking in a wide composition range. Probably due to the ligand properties of phosphorous, Ni₂P particles are better dispersed on the zeolitic support and more stable than Ni catalysts. Ni₂P-based catalysts do not suffer from deactivation and they showed higher metal/acid sites molar ratio compared to the Ni-based counterparts. On Ni₂P/H-USY, the product distribution during hydrocracking of *n*-hexadecane is easily tuned by the metal/acid sites ratio. High selectivity to light alkanes was reached with metal loadings below 10 wt. % Ni₂P, especially at temperatures above 370 °C, whereas high selectivity to hydroisomerization or to primary cracking products was achieved with increasing metal loading. However, due to the interaction between the phosphorous precursor and the H-USY during the synthesis of the catalyst, at 25 wt. % of Ni₂P loading the structure of H-USY is compromised and the catalyst losses activity. In order to avoid the deterioration of the crystallinity of the H-USY and the reduction of the number of accessible acid sites, less phosphorous precursor must be used during the synthesis of the Ni₂P(25)/H-USY. In this way, decreasing the amount of phosphorous results in more active catalysts. However, regardless of the phosphorous amount, at 25 wt. % Ni₂P, the agglomeration of the particles is higher than at lower loadings. Therefore, 15 wt. % of Ni₂P loading is the optimum metal loading for hydrocracking catalysts under the conditions applied in this study. The high metal/acid sites ratio (0.25) in Ni₂P(15)/H-USY allows reaching the ideal hydrocracking mechanism. In general, on the Ni₂P-based catalysts the rate of primary cracking

depends on the Brønsted acid sites, whereas secondary cracking is strongly correlated with the rate of accessible metal/acid sites. At 370 °C and metal/acid sites ratio higher than 0.15, the secondary cracking selectivity went to zero whereas the rate of primary cracking reached a maximum at the metal/acid sites ratio of 0.08. The rate of hydroisomerization depends linearly on the amount of metal sites and strongly increases with the metal/acid sites ratio.

5.5 Acknowledgements

The author would like to thank the German Federal Ministry of Food and Agriculture in the framework of the Advanced Biomass Value project (03SF0446A).

5.6 References

- [1] J. A. R. van Veen, J. K. Minderhoud, L. G. Huve, W. H. J. Stork, *Handbook of Heterogeneous Catalysis*, **2008**, 2, 2778-2808.
- [2] C. Marcilly, *Editions Technip*, **2006**, 2, 666-717.
- [3] A. Primo, H. Garcia, *Chemical Society Reviews*, **2014**, 43, 7548-7561.
- [4] J. Weitkamp, *ChemCatChem*, **2012**, 4, 292-306.
- [5] H. L. Coonradt, W. E. Garwood, *Industrial & Engineering Chemistry Process Design and Development*, **1964**, 3, 38-45.
- [6] P. B. Weisz, *Advances in Catalysis*, **1962**, 13, 137-190.
- [7] J. Weitkamp, *Prepr. Pap. – Am. Chem. Soc., Div. Pet. Chem.*, **1975**, 20, 489-507.
- [8] H. Pichler, H. Schulz, H. O. Reitemeyer, J. Weitkamp, *Erdöl Kohle Erdgas Petrochem.*, **1972**, 25, 494-505.
- [9] J. Weitkamp, *Hydrocracking and Hydrotreating*, **1975**, 20, 1-27.
- [10] J. Weitkamp, *Erdöl Kohle Erdgas Petrochem.*, **1978**, 31, 13-22.
- [11] C. Bouchy, G. Hastoy, E. Guillon, J. A. Martens, *Oil & Gas Science and Technology*, **2009**, 64, 91-112.
- [12] K. Hedden, J. Weitkamp, *Chem. Eng. Technol.*, **1975**, 47, 505-513.
- [13] J. Weitkamp, *Ind. Eng. Chem. Prod. Res. Dev.*, **1982**, 21, 550-558.
- [14] F. Regali, L. F. Liotta, A. M. Venezia, M. Boutonneta, S. Järåsa, *Applied Catalysis A: General*, **2014**, 469, 328-339.
- [15] H. Deldari, *Applied Catalysis A: General*, **2005**, 293, 1-10.

- [16] M. Guisnet, F. Alvarez, G. Giannetto, G. Perot, *Catal. Today*, **1987**, *1*, 415-433.
- [17] J. A. Martens, M. Tielen, P. A. Jacobs, *Studies in Surface Science and Catalysis*, **1989**, *46*, 49.
- [18] R. J. Taylor, R. H. Petty, *Applied Catalysis A: General*, **1994**, *119*, 121-138.
- [19] K. C. Park, S. Ihm, *Applied Catalysis A: General*, **2000**, *203*, 201-209.
- [20] X. Ren, N. Li, J. Cao, Z. Wang, S. Liu, S. Xiang, *Applied Catalysis A: General*, **2006**, *298*, 144-151.
- [21] J. Scherzer, A. J. Gruia, *Hydrocracking Science and Technology*, **1996**, 13-72.
- [22] J. L. Carter, J. A. Cusumano, J. H. Sinfelt, *Journal of Catalysis*, **1971**, *20*, 223-229.
- [23] G. C. Bond, *Platinum Met. Rev.*, **1975**, *19*, 126-134.
- [24] F. Alvarez, F. R. Ribeiro, G. Perot, C. Thomazeau, M. Guisnet, *Journal of Catalysis*, **1996**, *162*, 179-189.
- [25] A. Sequeira, *Lubricant Base Oil and Wax Processing*, **1994**, *6* and *8*, 119-152 and 194-224.
- [26] M. Y. Wen, I. Wender, J. W. Tierney, *Energy and Fuels*, **1990**, *4*, 372-379.
- [27] W. Souverijns, J. A. Martens, G. F. Froment, P. A. Jacobs, *Journal of Catalysis*, **1998**, *174*, 177-184.
- [28] S. J. Miller, *Microporous Materials*, **1994**, *2*, 439-449.
- [29] W. E. Garwood, Q. N. Le, S. S. Wong, *US Pat. 4 975 177*, **1990**, to Mobil Corp.
- [30] I. A. Cody, D. H. Dumfries, A. H. Neal, K. L. Riley, *US Pat. 5 182 248*, **1993**, to Exxon Res. Eng. Comp.
- [31] P. Mériaudeau, V. A. Tuan, V. T. Nghiem, S. Y. Lai, L. N. Hung, C. Naccache, *Journal of Catalysis*, **1997**, *169*, 55-66.
- [32] C. Perego, L. Zanibelli, C. Flego, A. Del Bianco, G. Bellussi, *EP Pat. 582 347*, **1994**, to Eniricerche.
- [33] V. M. Akhmedov, S. H. Al-Khowaiter, *Catalysis Reviews*, **2007**, *49*, 33-139.
- [34] C. Geng, F. Zhang, *Catalysis Today*, **2004**, *93*, 485-491.
- [35] Y. Liu, C. Liu, C. Liu, Z. Tian, L. Lin, *Energy & Fuels*, **2004**, *18*, 1266-1271.
- [36] B. Parlitz, E. Schreier, H. L. Zubowa, R. Eckelt, E. Lieske, G. Lischke, R. Fricke, *Journal of Catalysis*, **1995**, *155*, 1-11.
- [37] J. M. Campelo, F. Lafont, J. M. Marinas, *Applied Catalysis A: General*, **1998**, *170*, 139-144.
- [38] D. Karthikeyan, N. Lingappan, B. Sivasankar, N. J. Jabarathinam, *Industrial and Engineering Chemistry Research*, **2008**, *47*, 6538-6546.

- [39] A. K. Sinha, S. Sivasanker, P. Ratnasamy, *Industrial and Engineering Chemistry Research*, **1998**, *37*, 2208-2214.
- [40] K. Fang, W. Wei, J. Ren, Y. Sun, *Catalysis Letters*, **2004**, *93*, 235-242.
- [41] M. D. Romero, J. A. Calles, A. Rodríguez, J. C. Cabanelas, *Industrial and Engineering Chemistry Research*, **1998**, *37*, 3846-3852.
- [42] P. A. M. Garrido, M. J. B. Souza, A. O. S. Silva, D. M. A. Melo, A. S. Araujo, *Catalysis Communications*, **2006**, *7*, 791-796.
- [43] G. Shi, D. Fang, J. Shen, *Microporous and Mesoporous Materials*, **2009**, *120*, 339-345.
- [44] R. C. Archibald, B. S. Greensfelder, G. Holzman, D. H. Rowe, *Industrial & Engineering Chemistry*, **1960**, *52*, 745-750.
- [45] J. W. Gibson, G. M. Good, G. Holzman, *Industrial & Engineering Chemistry*, **1960**, *52*, 113-116.
- [46] W. Li, F. Y. Ma, F. Su, L. Ma, S. Q. Zhang, Y. H. Guo, *ChemSusChem*, **2011**, *4*, 744-756.
- [47] T. V. Choudhary, C. B. Phillips, *Applied Catalysis A: General*, **2011**, *397*, 1-12.
- [48] B. Donnis, R. G. Egeberg, P. Blom, K. G. Knudsen, *Topics in Catalysis*, **2009**, *52*, 229-240.
- [49] S. Bezergianni, A. Dimitriadis, *Fuel*, **2013**, *103*, 579-584.
- [50] D. Kubička, L. Kaluža, *Applied Catalysis A: General*, **2010**, *372*, 199-208.
- [51] G. W. Huber, P. O'Connor, A. Corma, *Applied Catalysis A: General*, **2007**, *329*, 120-129.
- [52] P. Dufresne, A. Quesada, S. Mignard, *Studies in Surface Science and Catalysis*, **1990**, *53*, 301-315.
- [53] J. Leglise, J. M. Manoli, C. Potvin, G. Djega-Mariadassou, D. Cornet, *Journal of Catalysis*, **1995**, *152*, 275-290.
- [54] R. Cid, J. Neira, J. Godoy, J.M. Palacios, A. Lopez Agudo, *Applied Catalysis A: General*, **1995**, *125*, 169-183.
- [55] W. J. J. Welters, G. Vorbeck, H. W. Zandbergen, J. W. de Haan, V. H. J. de Beer, R. A. van Santen, *Journal of Catalysis*, **1994**, *150*, 155-169.
- [56] W. Keim, *Angewandte Chemie International Edition*, **1990**, *29*, 235-244.
- [57] M. Snåre, I. Kubičková, P. Mäki-Arvela, K. Eränen, D. Y. Murzin, *Industrial & Engineering Chemistry Research*, **2006**, *45*, 5708-5715.
- [58] M. Agnelli, H. M. Swaan, C. Marquez-Alvarez, G.A. Martin, C. Mirodatos, *Journal of Catalysis*, **1998**, *175*, 117-128.
- [59] D. W. Goodman, R. D. Kelley, T. E. Madey, J. T. Yates Jr., *Journal of Catalysis*, **1980**, *63*, 226-234.

- [60] K. L. Li, R. J. Wang, J. X. Chen, *Energy and Fuels*, **2011**, 25, 854-863.
- [61] Y. K. Lee, S. T. Oyama, *Journal of Catalysis*, **2006**, 239, 376-389.
- [62] S. T. Oyama, *Journal of Catalysis*, **2003**, 216, 343-352.
- [63] A. Infantes-Molina, C. Moreno-León, B. Pawelec, J. L. G. Fierro, E. Rodríguez-Castellón, A. Jiménez-López, *Applied Catalysis B: Environmental*, **2012**, 113, 87-99.
- [64] J. A. Cecilia, A. Infantes-Molina, E. Rodríguez-Castellón, A. Jiménez-López., *Applied Catalysis B: Environmental*, **2009**, 92, 100-113.
- [65] H. Y. Zhao, D. Li, P. Bui, S. T. Oyama, *Applied Catalysis A: General*, **2011**, 391, 305-310.
- [66] S. Sawhill, K. Layman, D. Vanwyk, M. Engelhard, C. Wang, M. Bussell, *Journal of Catalysis*, **2005**, 231, 300-313.
- [67] V. M. L. Whiffen, K. J. Smith, *Energy and Fuels*, **2010**, 24, 4728-4737.
- [68] R. Prins, M. E. Bussell, *Catalysis letters*, **2012**, 142, 1413-1436.
- [69] S.T. Oyama, T. Gott, H. Zhao, Y. K. Lee, *Catal. Today*, **2009**, 143, 94-107.
- [70] A. Rodriguez, J. Kim, J. C. Hanson, S. J. Sawhill, M. E. Bussell, *The Journal of Physical Chemistry. B*, **2003**, 107, 6276-6285.
- [71] M. Peroni, G. Mancino, E. Baráth, O. Y. Gutiérrez, J. A. Lercher, *Applied Catalysis B: Environmental*, **2016**, 180, 301-311.
- [72] J. Chen, H. Shi, L. Li, K. Li, *Applied Catalysis B: Environmental*, **2014**, 144, 870-884.
- [73] M. Peroni, X. Huang, I. Lee, E. Baráth, O. Y. Gutiérrez, J. A. Lercher, Deoxygenation of palmitic acid on unsupported WP, MoP, and Ni₂P, *ready for submission*.
- [74] R. Zarchin, M. Rabaev, R. Vidruk-Nehemya, M. V. Landau, M. Herskowitz, *Fuel*, **2015**, 139, 684-691.
- [75] Y. Lee, Y. Shu, S. T. Oyama, *Applied Catalysis A: General*, **2007**, 322, 191-204.
- [76] Y. Kim, G. Yun, Y. Lee, *Catalysis Communications*, **2014**, 45, 133-138.
- [77] S. Tian, J. Chen, *Fuel Processing Technology*, **2014**, 122, 120-128.
- [78] A. Montesinos-Castellanos, T. A. Zepeda, B. Pawelec, J. L. G. Fierro, J. A. de los Reyes, *Chemistry of Materials*, **2007**, 19, 5627-5636.
- [79] C. Stinner, Z. Tang, M. Haouas, T. Weber, R. Prins, *Journal of Catalysis*, **2002**, 208, 456-466.
- [80] J. G. Tittensor, R. J. Gorte, D. M. Chapman, *Journal of Catalysis*, **1992**, 138, 714-720.
- [81] R. Ramos Pinto, P. Borges, M.A.N.D.A. Lemos, F. Lemos, J.C. Vedrine, E.G. Derouane, F. Ramoa Ribeiro, *Applied Catalysis A: General*, **2005**, 284, 39-46.
- [82] J. Scherzer, A. J. Gruia, *Hydrocracking Science and Technology*, **1996**, Taylor & Francis.

- [83] H. Beuther, O. H. Larson, A. J. Perrotta, in: B. Delmon, G. F. Froment (Eds.), *Catalyst Deactivation*, **1980**, Stud. Surf. Sci. Catal., *6*, 271-282.
- [84] C. H. Bartholomew, *Applied Catalysis A: General*, **2001**, *212*, 17-60.
- [85] S. M. Augustine, G. N. Alameddin, W. M. H. Sachtler, *Journal of Catalysis*, **1989**, *115*, 217-232.
- [86] H. Beuther, O. A. Larson, *Industrial & Engineering Chemistry Process Design and Development*, **1965**, *4*, 177-181.
- [87] P. Liu, J. A. Rodriguez, T. Asakura, J. Gomes, K. Nakamura, *The Journal of Physical Chemistry. B*, **2005**, *109*, 4575-4583.

5.7 Appendix

5.7.1 Experimental details of the kinetic tests

Table 5A-1. Amounts of catalyst introduced in the reactor, effective concentration of metal and acid sites per reaction and activation energies.

Catalyst	Catalyst, mg	Metal sites per reaction ^a , μmol	Total Brønsted acidity per reaction ^b , μmol	Metal/Brønsted Acid sites molar ratio, x 10 ²	Ea, kJ·mol ⁻¹
H-USY	34	-	11.5	0	74
Ni(5)/H-USY	36	0.22	9.7	2.2	85
Ni(10)/H-USY	38	0.48	11.1	4.3	84
Ni(15)/H-USY	40	0.96	7.6	12.8	85
Ni(25)/H-USY	45	0.96	9.0	10.6	63
Ni ₂ P(5)/H-USY	36	0.21	10.0	2.1	88
Ni ₂ P(10)/H-USY	38	0.37	6.2	5.9	102
Ni ₂ P(15)/H-USY	40	1.19	4.9	24.5	119
Ni ₂ P(25)/H-USY	45	0.57	4.8	12.0	111

^a Calculated from the amount of CO chemisorbed in Table 5-2 considering the mg of catalyst introduced in the reactor.

^b Calculated from the Brønsted acidity in Table 5-3 considering the amount of catalyst introduced in the reactor.

5.7.2 Characterization of the Ni/H-USY and Ni₂P/H-USY precursors

The X-ray diffractograms of the oxide catalyst precursors are shown in Figure 5A-1 and 5A-2. After calcination only NiO is present in the Ni-catalyst precursors, whereas reflections of crystalline phases, other than the zeolite, were not observed in the precursors of the Ni₂P-catalysts.

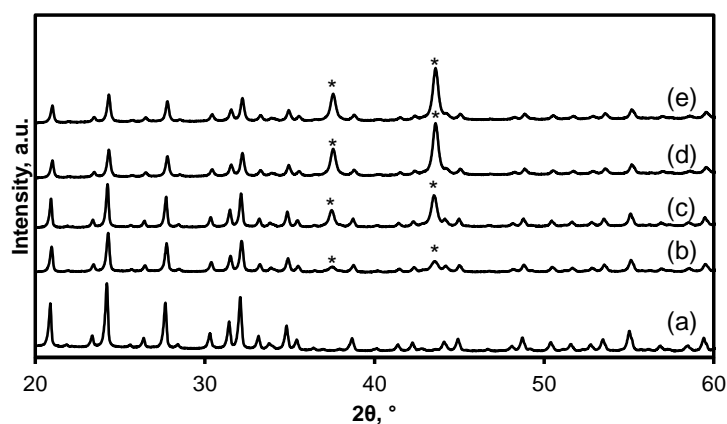


Figure 5A-1. X-Ray diffractograms of the precursors (materials before temperature programmed reduction) of bare H-USY (a) and the Ni-containing precursors: Ni(5)/H-USY (b), Ni(10)/H-USY (c), Ni(15)/H-USY (d), Ni(25)/H-USY (e). The reflections labeled with (*) are assigned to NiO. The reflections not labeled are assigned to H-USY.^[1]

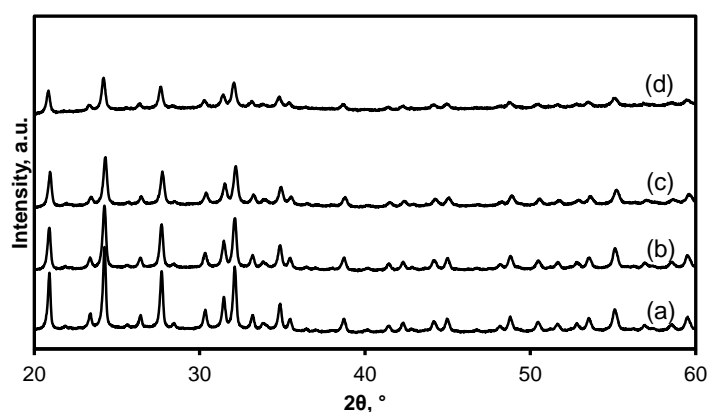


Figure 5A-2. X-Ray diffractograms of the precursors (materials before temperature programmed reduction) of the Ni₂P-based catalysts: Ni₂P(5)/H-USY (a), Ni₂P(10)/H-USY (b), Ni₂P(15)/H-USY (c), Ni₂P(25)/H-USY (d). All reflections are assigned to H-USY.^[1]

5.7.3 Study of the stability of H-USY during impregnation

In order to dissolve the precipitate formed when mixing Ni(NO₃)₂·6H₂O and (NH₄)₂HPO₄ different amounts of citric acid or concentrated nitric acid had to be added to the solution. In order to verify the impact of the acidic solutions on the crystallinity of H-USY, both acids were impregnated in the material and the crystalline structure was verified afterwards. Figure 5A-3 shows the X-ray diffractograms of the H-USY impregnated with the same amount of citric or nitric acid needed to prepare Ni₂P(25)/H-USY. The crystallinity of the impregnated zeolite decreased slightly (to a larger extent with citric acid than with nitric acid). The calcination step did not modify the material.

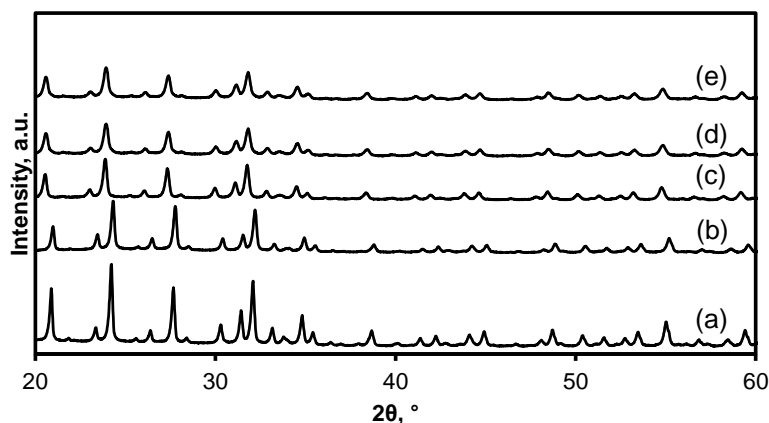


Figure 5A-3. X-Ray diffractograms of H-USY (a), H-USY treated with nitric acid and dried (b), H-USY treated with citric acid and dried (c), H-USY treated with nitric acid and calcined (d), and H-USY treated with citric acid and calcined (e). The amount of citric or nitric acid introduced during the incipient wetness impregnation corresponds to the amount used to synthesize the Ni₂P(25)/H-USY.

In stark contrast, when the H-USY was impregnated with a solution of (NH₄)₂HPO₄, the crystallinity of the zeolite was compromised even before calcination as shown in Figure 5A-4. Using an excess of (NH₄)₂HPO₄ to impregnate the H-USY resulted in completely amorphous aluminosilicates as only reflections of (NH₄)₂HPO₄ are observed. After calcination, crystalline reflections are completely absent.

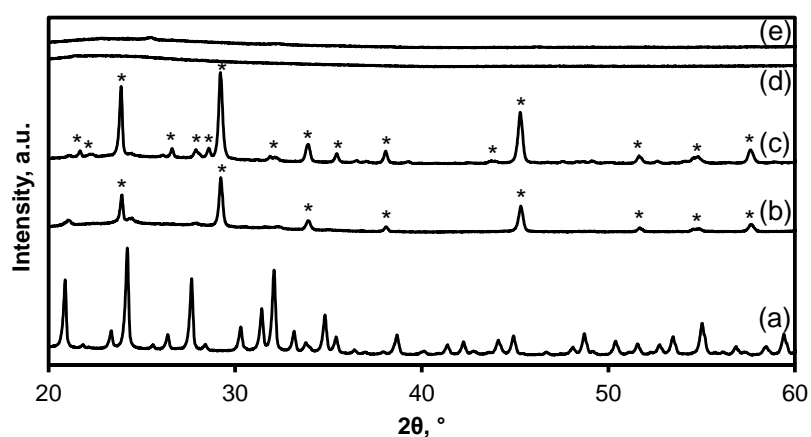


Figure 5A-4. X-ray diffractograms of H-USY (a), H-USY treated with half of the amount of (NH₄)₂HPO₄ used during the preparation of Ni₂P(25)/H-USY and dried (b), H-USY treated with the amount of (NH₄)₂HPO₄ used during the preparation of Ni₂P(25)/H-USY and dried (c), H-USY treated with half of the amount of (NH₄)₂HPO₄ used during the preparation of Ni₂P(25)/H-USY and calcined (d), and H-USY treated with the amount of (NH₄)₂HPO₄ used during the preparation of Ni₂P(25)/H-USY and calcined (e). The labeled signals with (*) correspond to (NH₄)₂HPO₄.

5.7.4 Particle size distribution on Ni(15)/H-USY and Ni₂P(15)/H-USY

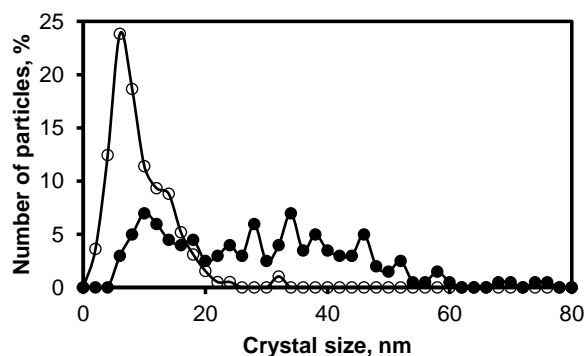


Figure 5A-5. Particle size distribution on (●) Ni(15)/H-USY and (○) Ni₂P(15)/H-USY.

5.7.5 Temperature programmed desorption of NH₃ and *n*-propylamine

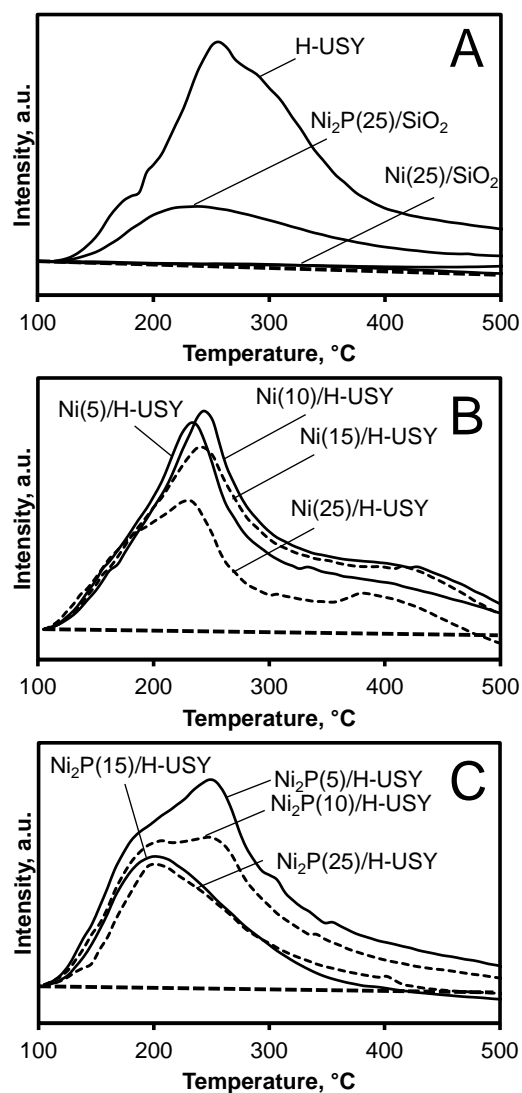


Figure 5A-6. NH₃ desorption profiles from H-USY, Ni₂P(25)/SiO₂, and Ni(25)/SiO₂ (A); Ni-based (B) and Ni₂P-based (C) catalysts.

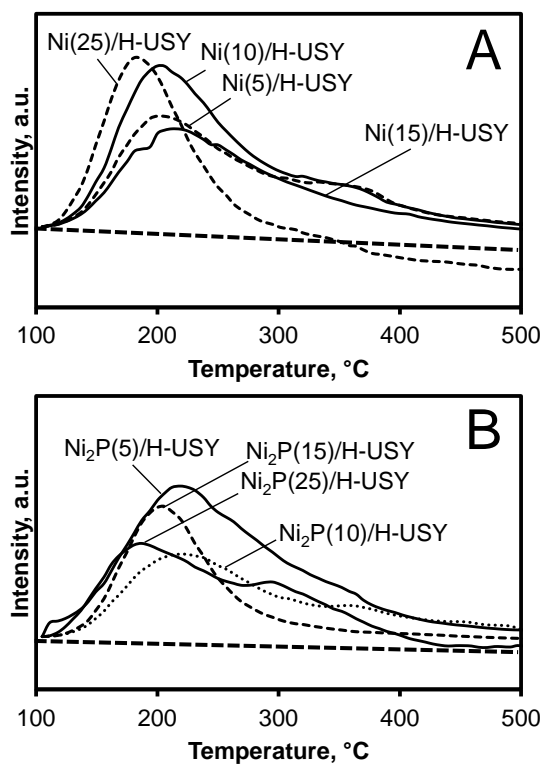


Figure 5A-7. TPD of *n*-propylamine: unreacted *n*-propylamine desorption profiles on Ni-based (A) and Ni₂P-based (B) catalysts.

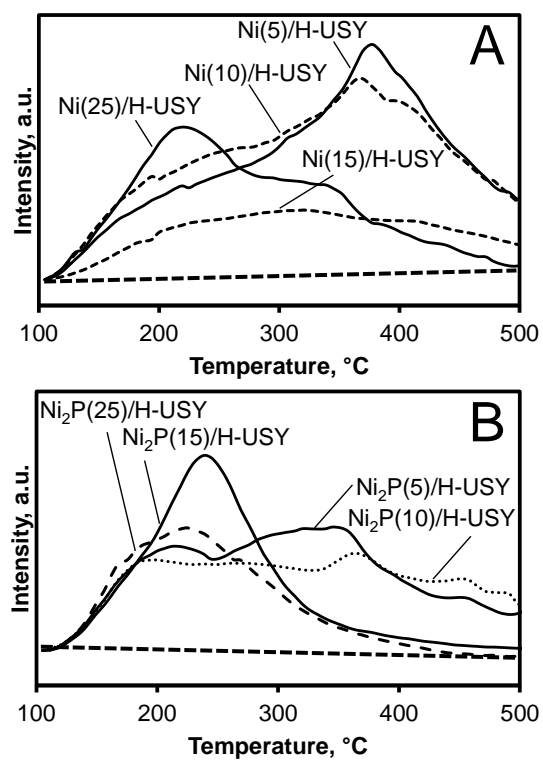


Figure 5A-8. TPD of *n*-propylamine: NH₃ desorption profiles on Ni-based (A) and Ni₂P-based (B) catalysts.

5.7.6 Characterization of Ni(25)/SiO₂ and Ni₂P(25)/SiO₂

Table 5A-2. Physicochemical properties of Ni(25)/SiO₂ and Ni₂P(25)/SiO₂

Catalyst	Metal/P, Molar ratio	CO chemisorbed, μmol·g ⁻¹	Acidity, μmol _{NH₃} ·g ⁻¹
Ni(25)/SiO ₂	-	34.1	6
Ni ₂ P(25)/SiO ₂	0.9	8.5	140

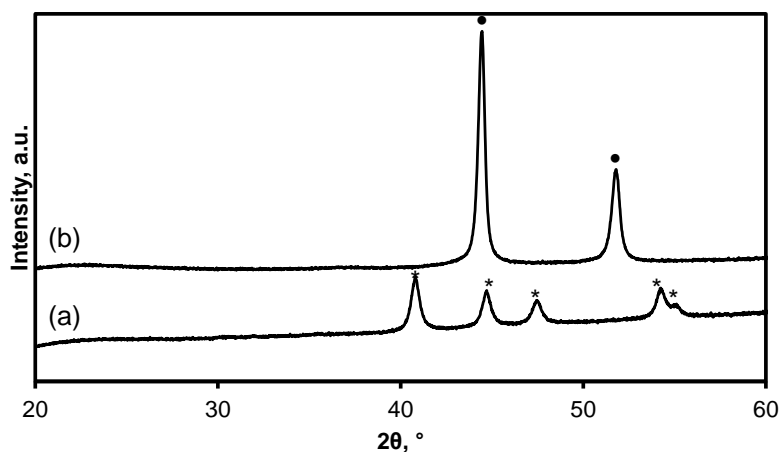


Figure 5A-9. X-ray diffractograms of (a) Ni₂P(25)/SiO₂ and (b) Ni(25)/SiO₂. The reflections labeled with (*) are assigned to Ni₂P. The reflections labeled with (●) are assigned to Ni.

5.7.7 Coke deposition on the spent catalysts

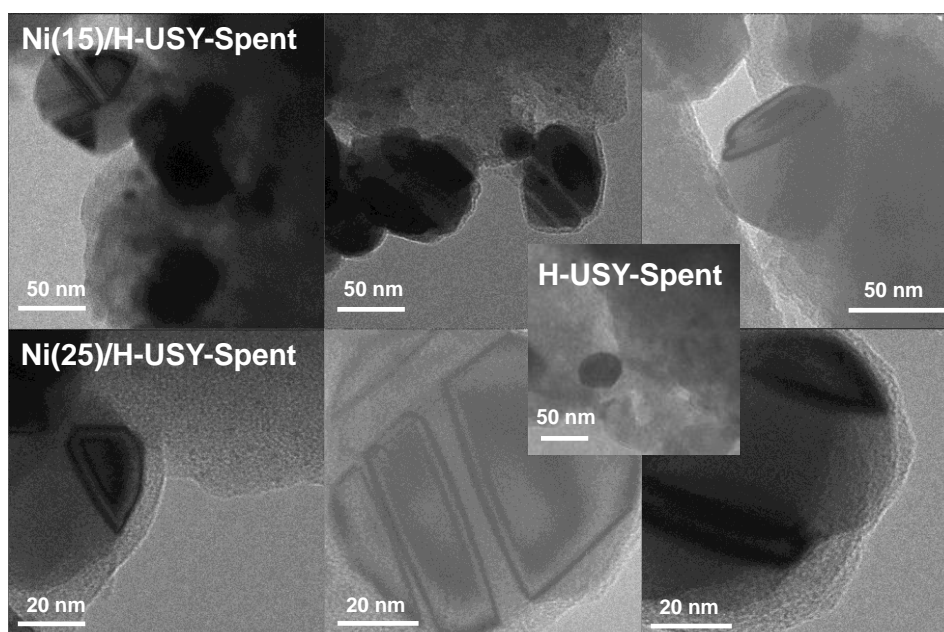


Figure 5A-10. Selected TEM micrographs of spent Ni(15)/H-USY, Ni(25)/H-USY and H-USY.

Table 5A-3. Coke deposition after the reaction.

Catalyst	wt. % C	wt. % H	C/H molar ratio
H-USY	31.1	4.0	0.6
Ni(25)/SiO ₂	21.7	2.5	0.7
Ni(5)/H-USY	21.3	2.4	0.7
Ni(10)/H-USY	16.9	1.9	0.7
Ni(15)/H-USY	28.9	4.3	0.6
Ni(25)/H-USY	19.1	1.7	1.0
Ni ₂ P(5)/H-USY	12.4	2.1	0.5
Ni ₂ P(10)/H-USY	10.4	2.3	0.4
Ni ₂ P(15)/H-USY	9.1	1.9	0.4
Ni ₂ P(25)/H-USY	2.3	1.0	0.2

5.7.8 Test of stability on Ni(25)/SiO₂ at 400 °C

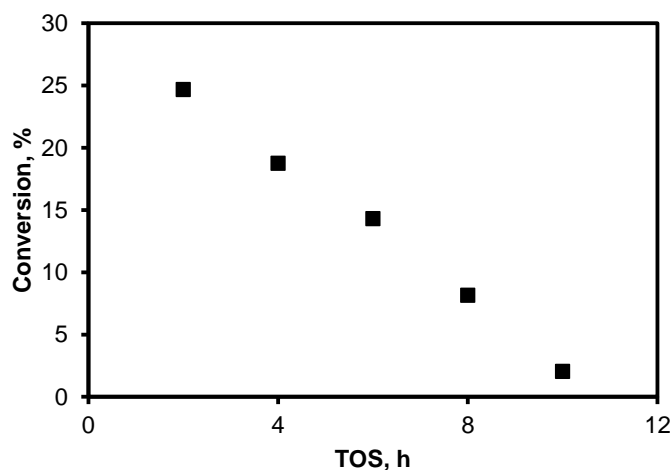


Figure 5A-11. *n*-Hexadecane conversion as a function of time on stream on Ni(25)/SiO₂ at 400 °C, 1.13 min of contact time with the H-USY and 4 MPa H₂ in a flow reactor. H₂/hexadecane molar ratio: 9, activation: 2 h at 450 °C in H₂.

5.7.9 Study of the effect of Ni to P ratio in the precursor solutions on the properties of the Ni₂P/H-USY materials

The effect of the Ni/P molar ratio was investigated in the range of 0.5-1 on Ni₂P(25)/H-USY. Table 5A-4 reports the amount of precursor used during the preparation of the Ni₂P(25)-based catalysts. The crystallinity of H-USY was compromised by the amount of phosphorous precursor used during the impregnation of the zeolite (Figure 5A-12). Indeed, Ni₂P(25)/H-USY/(1:1), where (x:y) is the molar ratio between Ni (x) and P (y), synthesized with the lowest amount of phosphorous, showed the highest crystallinity of the zeolite among the Ni₂P(25)-based materials.

In literature, the formation of the pure Ni₂P phase is obtained with a Ni/P molar ratio of 0.5 during the preparation of the precursor's solution. Ni₃P and Ni₁₂P₅ phases are obtained with an initial Ni/P molar ratio of 2 whereas a mixture of Ni₁₂P₅ and Ni₂P is obtained decreasing the Ni/P ratio to 1.6.^[2] When the Ni/P ratio is lower than 1.5 the obtainment of the Ni₂P is strongly enhanced. It was demonstrated that the formation of Ni₂P on catalysts prepared with an initial Ni/P molar ratio of 2, begins with the reaction between Ni and P during the reduction in presence of hydrogen, forming Ni₃P with the lowest P content. At higher reduction times the excess of phosphorous leads to the formation of Ni₁₂P₅, a more P-rich nickel phosphide. In general, after 2 h of reduction at 650 °C Ni₂P is formed.^[2] However, on supported catalysts the phosphorous can migrate into the support during the reduction of the material, leading to a deficiency of P available to react with Ni.^[2, 3] In these cases, it is recommended to work with an excess of initial phosphorous.

Table 5A-4. Amount of precursors used in the synthesis of the Ni₂P(25)-based catalysts.

Catalyst	Metal, wt. %	Ni(NO ₃) ₂ ·6H ₂ O, g	(NH ₄) ₂ HPO ₄ , g	Citric acid, g	Nitric acid, ml	H-USY, g	Metal/P, Molar ratio
Ni ₂ P(25)/H-USY/(1:2) ^a	25	4.90	4.45	-	1.0	3.75	1/2
Ni ₂ P(25)/H-USY/(2:3) ^a	25	4.90	3.33	1.56	-	3.75	2/3
Ni ₂ P(25)/H-USY/(1:1)	25	4.90	2.22	-	0.7	3.75	1/1

^aTwo steps of impregnation. After the first impregnation, the material was dried overnight and impregnated again.

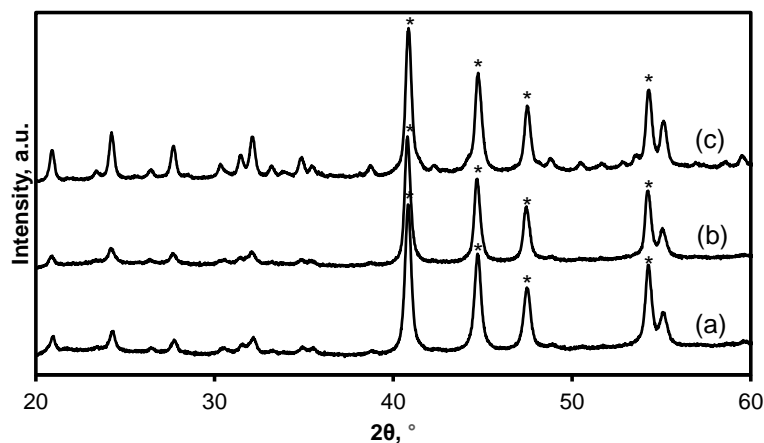


Figure 5A-12. X-ray diffractograms of Ni₂P(25)-based catalysts: (a) Ni₂P(25)/H-USY/(1:2), (b) Ni₂P(25)/H-USY/(2:3), (c) Ni₂P(25)/H-USY/(1:1). The reflections labeled with (*) are assigned to Ni₂P. The reflections not labeled are assigned to H-USY.^[1]

Figure 5A-13 shows the N₂ physisorption isotherms of the Ni₂P(25)-based materials. The N₂ adsorption isotherm of Ni₂P(25)/H-USY/(1:2), with the highest P content, was type II (IUPAC) pointing to non-porous material. The hysteresis loops at high relative pressures indicated high contribution of macroporosity derived from the destruction of the pore system

of the zeolite. Ni₂P(25)/H-USY/(2:3) showed a low microporosity, comparable to the Ni₂P(25)/H-USY/(1:2). However, on this material the hysteresis loop is less pronounced, pointing to the less macroporosity of the material. According to the description of the N₂-isotherms given above, the increase of the metal/P molar ratio during the impregnation results in a strong increase of the porosity of the catalyst. Ni₂P(25)/H-USY/(1:1) showed high contribution of microporosity as indicated by the large volume adsorbed at low relative pressures. The wide hysteresis loop observed at higher relative pressure indicates a porous solid with a broad distribution of pore sizes due to the presence of relatively large cavities connected by narrower pores. The hysteresis loop is flat below the relative pressure of 0.8, which suggests ink-bottle type mesopores, originated from a less compromised zeolite.

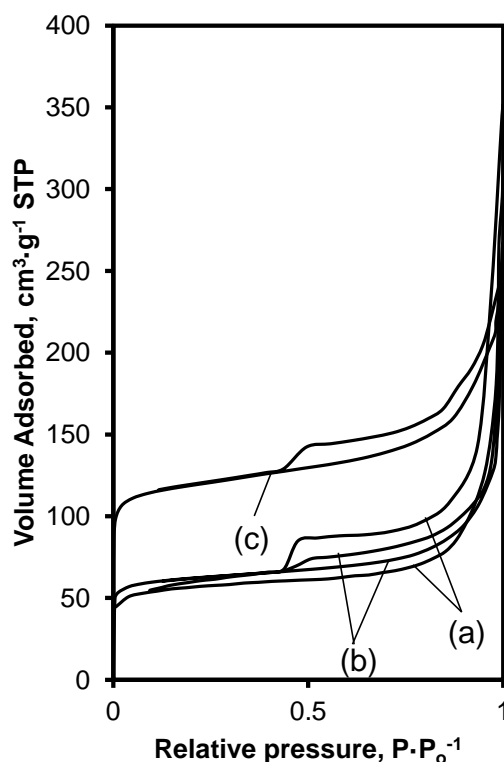


Figure 5A-13. N₂ physisorption isotherms of the Ni₂P(25)-based catalysts: Ni₂P(25)/H-USY/(1:2), (b) Ni₂P(25)/H-USY/(2:3), (c) Ni₂P(25)/H-USY/(1:1).

Reducing the phosphorus precursor avoids the collapse of the H-USY as demonstrated from the TEM images in Figure 5A-14. The crystalline structure of Ni₂P(25)/H-USY/(1:2) results totally compromised, whereas on Ni₂P(25)/H-USY/(2:3) and Ni₂P(25)/H-USY/(1:1) there are only some spots where the H-USY seems collapsed and the metal particles are agglomerated but the catalyst as a whole maintain his structure.

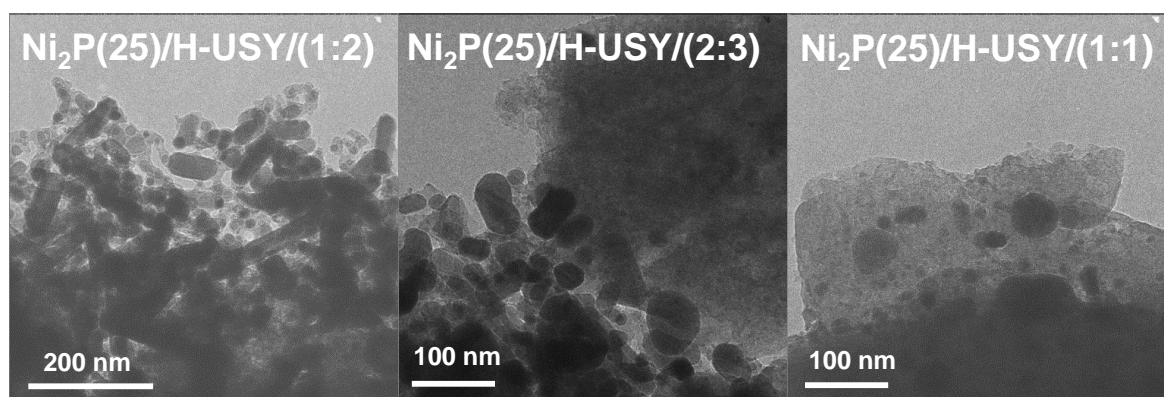


Figure 5A-14. Selected TEM micrographs of the Ni₂P(25)/H-USY/(1:2), Ni₂P(25)/H-USY/(2:3) and Ni₂P(25)/H-USY/(1:1).

On Ni₂P(25)-based materials, at the same metal loading, the effect of the crystal size on the CO uptake can be directly observed (Table 5A-5). The CO chemisorption on Ni₂P(25)/H-USY/(1:1) and Ni₂P(25)/H-USY/(2:3), having a crystal size of 12 nm, was four times higher (13.4 and 12.8 $\mu\text{mol}\cdot\text{g}^{-1}$ respectively) than the amount chemisorbed on Ni₂P(25)/H-USY/(1:2) (3.3 $\mu\text{mol}\cdot\text{g}^{-1}$), having a crystal size of 20 nm.

Table 5A-5 also shows that the decrease of the phosphorous precursor resulted in more acidic materials as indicated by the acidity of Ni₂P(25)/H-USY/(1:1) (253 $\mu\text{mol}\cdot\text{g}^{-1}$), i.e., more than two times higher than the acidity of Ni₂P(25)/H-USY/(1:2). The higher acidity of Ni₂P(25)/H-USY/(1:1) is ascribed to the more crystalline zeolite.

Table 5A-5. Physicochemical properties of the Ni₂P(25)-based catalysts.

Catalyst	Metal/P, molar ratio	BET Surface area, $\text{m}^2\cdot\text{g}^{-1}$	Mesopores surface area, $\text{m}^2\cdot\text{g}^{-1}$	Pore volume, $\text{cm}^3\cdot\text{g}^{-1}$	Particle size ^b , nm	CO uptake, $\mu\text{mol}\cdot\text{g}^{-1}$	Acidity, $\text{mmolNH}_3\cdot\text{g}^{-1}$
Ni ₂ P(25)/H-USY/(1:2)	1.05	204	43	0.19	20	3.3	0.11
Ni ₂ P(25)/H-USY/(2:3)	1.01	230	37	0.17	12	12.8	0.19
Ni ₂ P(25)/H-USY/(1:1)	1.27	438	67	0.30	12	13.4	0.25

^a Calcined at 500 °C.

^b Obtained from TEM images.

On Table 5A-6 the effect of the phosphorous precursor on the Brønsted/Lewis sites ratio can be easily highlighted. The interaction between the phosphorous precursor and the Brønsted acid sites during the impregnation of the zeolite can be proved comparing Ni₂P(25)/H-USY/(1:1) with the Ni₂P(25)/H-USY/(2:3), having the same metal loading and the same phosphide crystal size (12 nm). The former, prepared with less phosphorous precursor showed the same Brønsted/Lewis acid sites molar ratio than the bare H-USY (2.0) whereas the ratio measured on the latter, prepared with higher amount of phosphorous precursor, was half of that value (0.9).

Table 5A-6. Lewis and Brønsted acidity on Ni₂P(25)-based catalysts.

Catalyst	Brønsted Acidity, μmol/g _{cat}	Lewis Acidity, μmol/g _{cat}	Total Acidity, μmol/g _{cat}	Brønsted/Lewis acidity, molar ratio
Ni ₂ P(25)/H-USY/(1:2)	57	28	85	2.0
Ni ₂ P(25)/H-USY/(2:3)	106	117	223	0.9
Ni ₂ P(25)/H-USY/(1:1)	173	92	265	1.9

Figure 5A-15 shows NH₃ desorption profiles from Ni₂P(25)-based catalysts. The peaks related to the H-USY drastically decreases increasing the phosphorous precursor. On Ni₂P(25)/H-USY/(1:2), where the crystallinity of the zeolite is totally compromised, the desorption region related to the H-USY (above 210 °C) is almost completely suppressed, whereas only the acidity of the material mainly related to the phosphide phase remains.

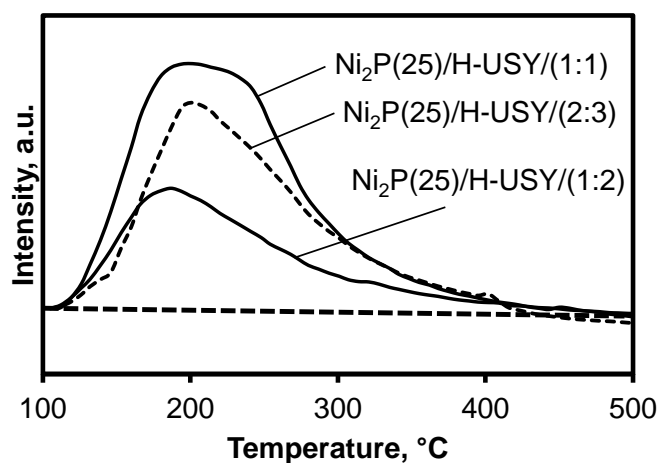
**Figure 5A-15.** NH₃ desorption profiles from Ni₂P(25)-based catalysts.

Figure 5A-16 shows the conversion of Ni₂P(25)-based catalysts at 400 °C as a function of time on stream. The total amount of catalyst tested for each reaction (in order to keep constant the amount of H-USY introduced) and the corresponding total amount of metal and acid sites and the activation energies are reported in Table 5A-7. The activity after the stabilization period followed the order (Figure 5A-17): Ni₂P(25)/H-USY/(1:2) < Ni₂P(25)/H-USY/(2:3) < Ni₂P(25)/H-USY/(1:1). The activity increased with the Brønsted acidity of the materials, whereas the product distribution was strongly correlated to the metal/acid sites ratio. Ni₂P(25)/H-USY/(2:3), with the highest metal/acid sites ratio among the Ni₂P(25) catalysts, was the one showing the highest selectivity to hydroisomerization, whereas strong overcracking was observed on Ni₂P(25)/H-USY/(1:1) increasing the reaction temperature (Figure 5A-18). The activity on Ni₂P(25)/H-USY/(1:2) was very low due to the low acidity, large Ni₂P particle size, and the low surface area.

Table 5A-7. mg of catalyst introduced in the reactor, effective concentration of metal and acid sites per reaction and activation energies for the Ni₂P(25)-based catalysts.

Catalyst	mg of catalyst	Metal sites per reaction ^a , μmol	Total Brønsted acidity per reaction ^b , μmol	Metal/Brønsted Acid sites molar ratio, x 10 ²	E _a , kJ·mol ⁻¹
Ni ₂ P(25)/H-USY/(1:2)	45	0.15	2.6	5.7	101
Ni ₂ P(25)/H-USY/(2:3)	45	0.57	4.8	12.0	111
Ni ₂ P(25)/H-USY/(1:1)	45	0.60	7.8	7.8	100

^a Calculated from the amount of CO chemisorbed in Table 5A-5 considering the mg of catalyst introduced in the reactor.

^b Calculated from the Brønsted acidity in Table 5A-6 considering the mg of catalyst introduced in the reactor.

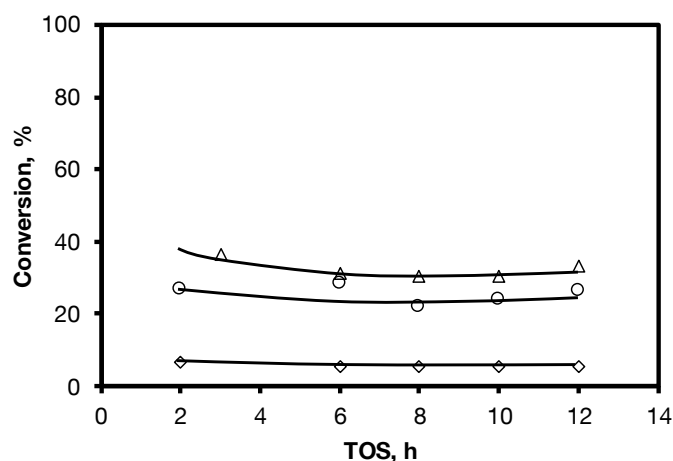


Figure 5A-16. *n*-Hexadecane conversion as a function of time on stream on Ni₂P(25)-based catalysts: (◇) Ni₂P(25)/H-USY/(1:2); (○) Ni₂P(25)/H-USY/(2:3); (Δ) Ni₂P(25)/H-USY/(1:1). 400 °C, 1.13 min of contact time with the H-USY and 4 MPa H₂ in a flow reactor. H₂/hexadecane molar ratio: 9, activation: 2 h at 450 °C in H₂.

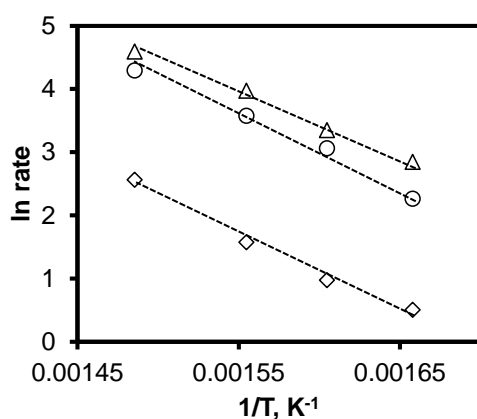


Figure 5A-17. Variation of the reaction rate for the conversion of *n*-hexadecane at varying temperature on Ni₂P(25)-based phosphide catalysts ((◇) Ni₂P(25)/H-USY(1:2); (○) Ni₂P(25)/H-USY/(2:3); (Δ) Ni₂P(25)/H-USY/(1:1)) at 1.13 min of contact time with the H-USY and 4 MPa H₂ in a flow reactor. H₂/hexadecane molar ratio: 9, activation: 2 h at 450 °C in H₂, stabilization: 16 h. The rates are calculated based on the amounts of H-USY introduced in the reactor.

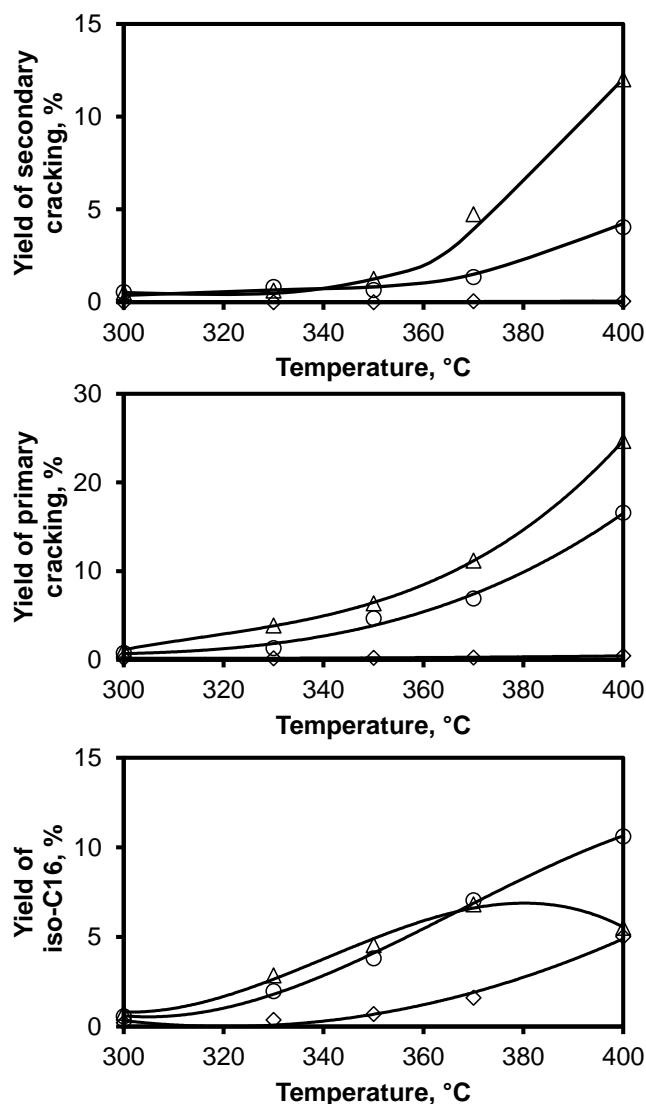


Figure 5A-18. Yields of secondary cracking, primary cracking and *iso*-C16 at varying temperatures on Ni₂P(25)-based phosphide catalysts ((\diamond) Ni₂P(25)/H-USY(1:2); (\circ) Ni₂P(25)/H-USY(2:3); (Δ) Ni₂P(25)/H-USY(1:1)) at 1.13 min of contact time with the H-USY and 4 MPa H₂ in a flow reactor. H₂/hexadecane molar ratio: 9, activation: 2 h at 450 °C in H₂, stabilization: 16 h.

The conversion of *n*-hexadecane was studied also at 370 °C and different residence times as shown in Figure 5A-19. The activity of the Ni₂P(25) catalysts between 0 and 2.06 min of contact time with the H-USY followed the trend: Ni₂P(25)/H-USY(1:2) < Ni₂P(25)/H-USY(2:3) < Ni₂P(25)/H-USY(1:1). Decreasing the metal/acid sites ratio, resulted in decreasing the mono-branched/multi-branched molar ratio at low conversion and in increasing the selectivity to cracking products (Figure 5A-20). Ni₂P(25)/H-USY(2:3), with a ratio of 0.12, showed higher selectivity to hydroisomerization than Ni₂P(25)/H-USY(1:1), where the ratio was 0.08. Ni₂P(25)/H-USY(1:2), having extremely low amount of acid sites, was exclusively

selective to *iso*-hexadecane. On the less acidic materials as Ni₂P(25)/H-USY/(1:2) and Ni₂P(25)/H-USY/(2:3), the formation of secondary cracking products was limited and at low conversion the materials showed high selectivity to hydroisomerization (Figure 5A-21). In contrast, Ni₂P(25)/H-USY/(1:1) was highly selective to secondary cracking and its hydroisomerization selectivity was the lowest.

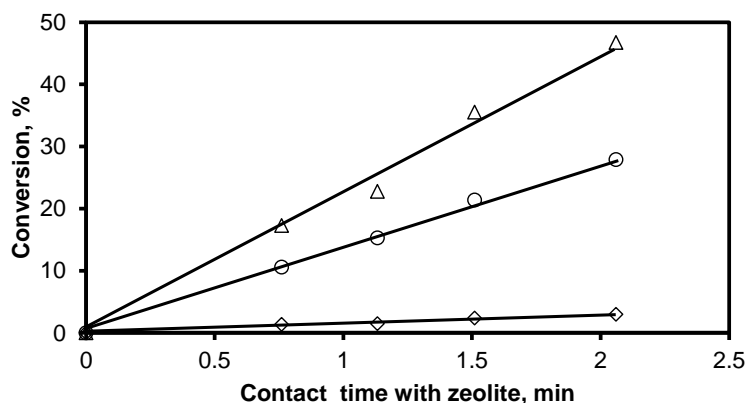


Figure 5A-19. *n*-Hexadecane conversion at varying contact times with zeolite on Ni₂P(25)-based phosphide catalysts ((\diamond) Ni₂P(25)/H-USY(1:2); (\circ) Ni₂P(25)/H-USY/(2:3); (Δ) Ni₂P(25)/H-USY/(1:1)) at 370 °C and 4 MPa H₂ in a flow reactor. H₂/hexadecane molar ratio: 9, activation: 2 h at 450 °C in H₂, stabilization: 16 h.

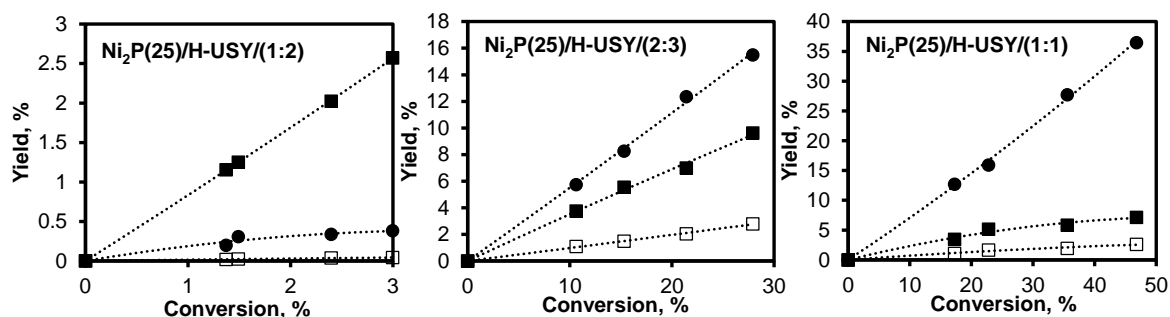


Figure 5A-20. Yield/conversion plots for the Ni₂P-based catalysts: mono-branched hexadecanes (■); multi-branched hexadecanes (□); cracking products (●). 370 °C and 4 MPa H₂ in a flow reactor. H₂/hexadecane molar ratio: 9, activation: 2 h at 450 °C in H₂, stabilization: 16 h.

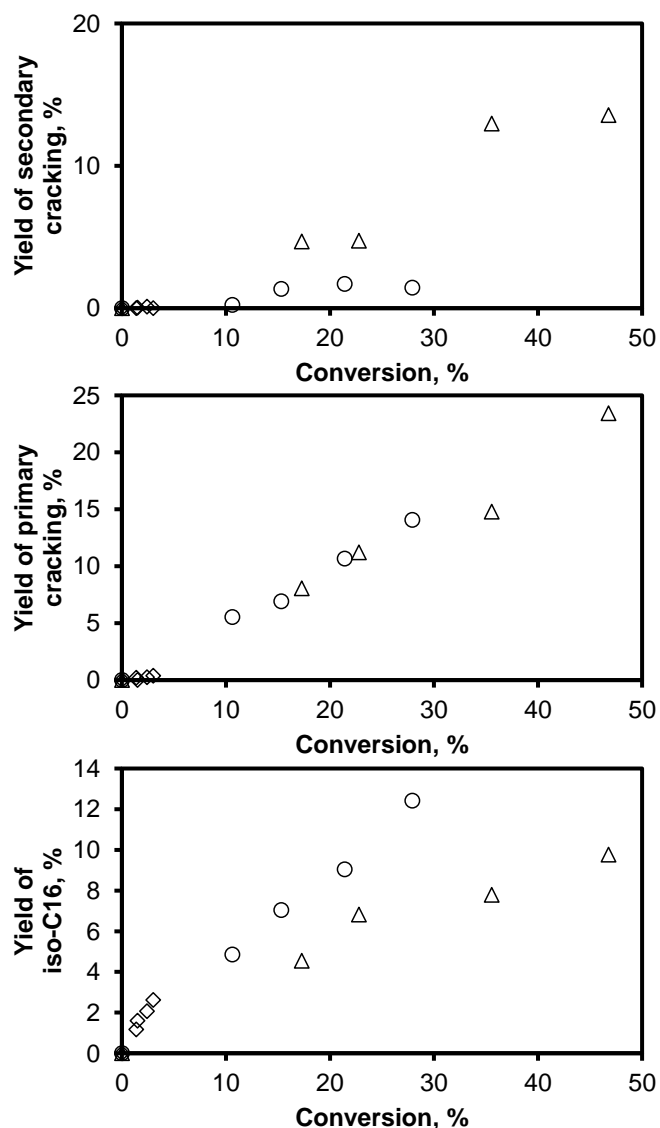


Figure 5A-21. Yields of secondary cracking, primary cracking and *iso*-hexadecane at varying conversions on Ni₂P(25) catalysts ((\diamond) Ni₂P(25)/H-USY(1:2); (\circ) Ni₂P(25)/H-USY/(2:3); (Δ) Ni₂P(25)/H-USY/(1:1)) at 370 °C and 4 MPa H₂ in a flow reactor. H₂/hexadecane molar ratio: 9, activation: 2 h at 450 °C in H₂, stabilization: 16 h.

On Ni₂P(25)/H-USY/(2:3) the product distribution at 370 °C and at 1.13 min of residence time (Figure 5A-22), showed the bell-shaped and symmetric curve typical of materials approaching the ideal hydrocracking selectivity. On Ni₂P(25)/H-USY/(1:1), with lower amount of metal/acid sites compared to the former, the curve starts to be non-symmetrical and shifted to lighter alkanes. Ni₂P(25)/H-USY/(1:2) showed only *iso*-hexadecane.

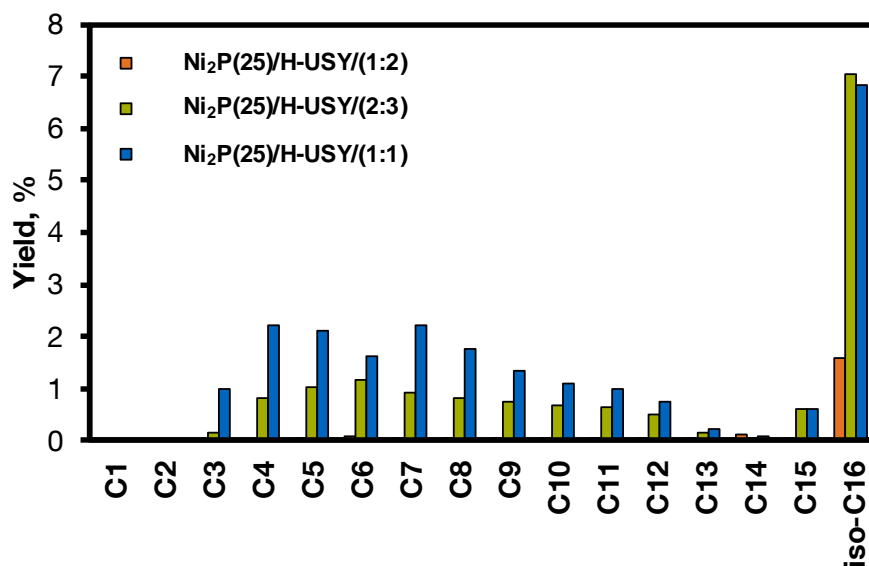


Figure 5A-22. Distribution of products at 370 °C on Ni₂P(25)-based catalysts, contact time with zeolite 1.13 min, 4 MPa H₂, H₂/hexadecane molar ratio: 9.

5.7.10 Effect of citric (CA) and nitric (NA) acid on the physicochemical properties of the Ni₂P-based catalysts

A direct comparison between Ni₂P(10)/H-USY and Ni₂P(25)/H-USY prepared with citric (CA) and nitric acid (NA) is reported in order to study the effect of the acid used during the impregnation on the physicochemical properties of the supported phosphides (Table 5A-8). The use of citric acid, as previously reported^[4,5], led to smaller particle size (Figure 5A-23 and 5A-25 and Table 5A-9) and higher amount of exposed metal sites compared to the use of nitric acid. However, the use of citric acid instead of nitric acid causes a slight decrease of the surface areas and less porosity of the catalyst (Figure 5A-24 and Table 5A-9) due to stronger interaction with the support during the synthesis of the catalyst. Therefore, the acidity of the H-USY slightly decreases with the use of citric acid (Figure 5A-26 and Table 5A-9).

Table 5A-8. Comparison between Ni₂P-based catalysts prepared with citric or nitric acid and amount of precursors used.

Catalyst	Metal, wt. %	Ni(NO ₃) ₂ ·6H ₂ O, g	(NH ₄) ₂ HPO ₄ , g	Citric acid, g	Nitric acid, ml	H-USY, g	Metal/P, Molar ratio
Ni ₂ P(10)/H-USY-NA	10	1.96	1.78	-	0.70	4.50	1/2
Ni ₂ P(10)/H-USY-CA	10	1.96	1.78	0.69	-	4.50	1/2
Ni ₂ P(25)/H-USY-NA	25	4.90	4.45	-	1.0	3.75	1/2
Ni ₂ P(25)/H-USY-CA	25	4.90	4.45	1.90	-	3.75	1/2

^a Two steps of impregnation. After the first impregnation step, the material was dried overnight and impregnated again.

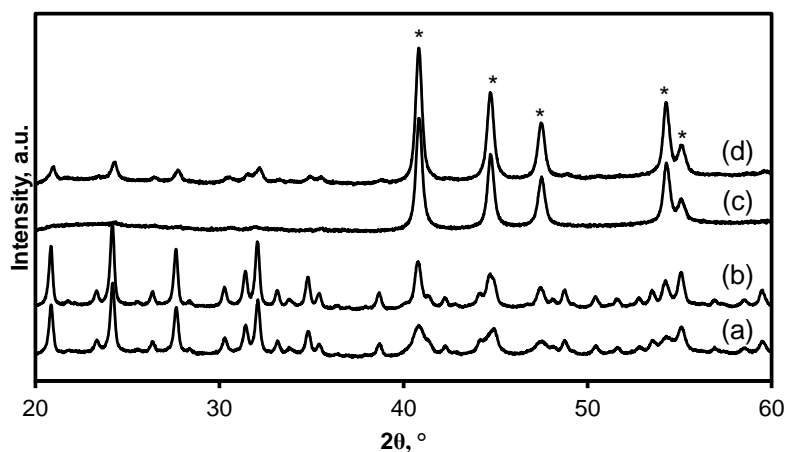


Figure 5A-23. X-Ray diffractograms of Ni₂P(10)/H-USY prepared with (a) citric acid (CA) and (b) nitric acid (NA) and Ni₂P(25)/H-USY prepared with (c) citric acid (CA) and (d) nitric acid (NA). The reflections labeled with (*) are assigned to Ni₂P. The reflections not labeled are assigned to H-USY.

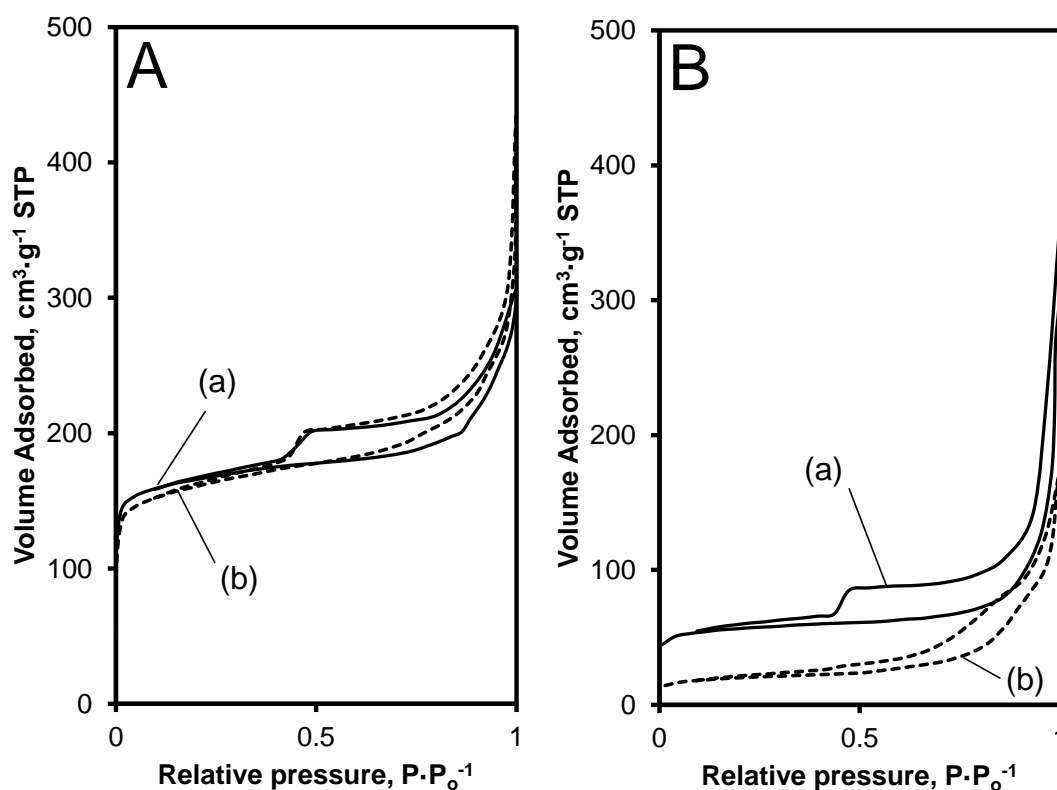


Figure 5A-24. N₂ physisorption isotherms of the (A) Ni₂P(10)/H-USY prepared with (a) nitric acid (NA) and (b) citric acid (CA) and of the (B) Ni₂P(25)/H-USY prepared with (a) nitric acid (NA) and (b) citric acid (CA).

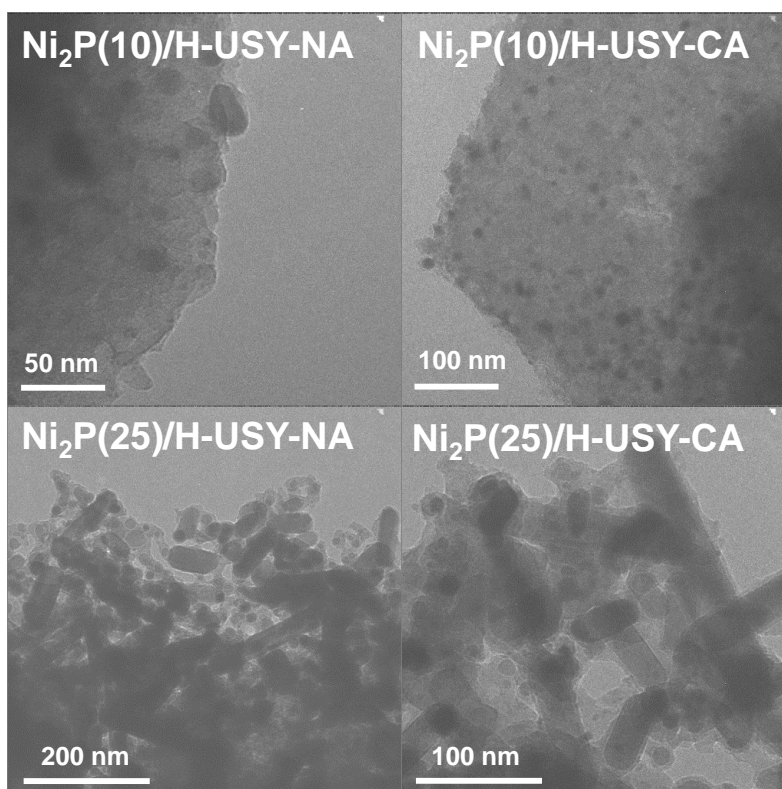


Figure 5A-25. Selected TEM micrographs of Ni₂P(10)/H-USY and Ni₂P(25)/H-USY prepared with nitric acid (NA) and citric acid (CA).

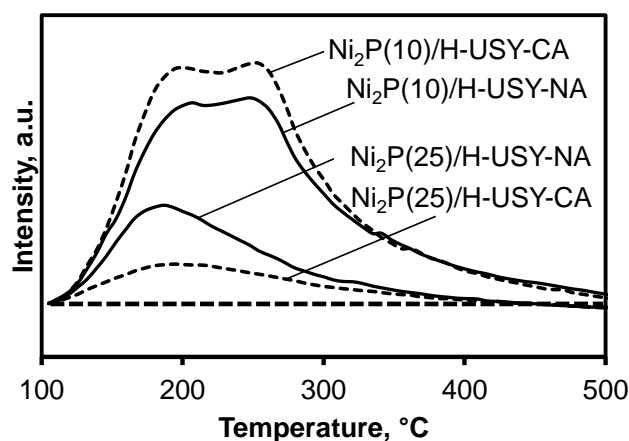


Figure 5A-26. NH₃ desorption profiles from Ni₂P(10)/H-USY and Ni₂P(25)/H-USY prepared with nitric acid (NA) and citric acid (CA).

The effect of the use of the citric acid instead of nitric acid is more marked at high metal loading. At 25 wt. % loading the amount of citric acid used to dissolve the precursors is 2.8 times higher than the amount used at 10 wt. %. Indeed, the grams of citric acid per grams of zeolite to impregnate ranges from 0.15 at 10 wt. % loading to 0.5 at 25 wt. %. Therefore, at lower metal loading the use of citric acid is beneficial leading to small phosphide particle size

with negligible interactions with the support (Figure 5A-23, 5A-24, 5A-25 and 5A-26). However, increasing the metal loading, the more citric acid used per grams of zeolite leads to a strong interaction with the support and the beneficial effect of the smaller particle size of the phosphides is suppressed by the destruction of the zeolite and the reduction of the acidity and porosity of the support. In conclusion, the use of citric acid is recommendable at Ni₂P loadings lower than 10-15 wt. % whereas at higher metal loading nitric acid represent the most appropriate choice.

Table 5A-9. Physicochemical properties of Ni₂P(10)/H-USY and Ni₂P(25)/H-USY prepared with nitric acid (NA) and citric acid (CA).

Catalyst	Metal/P, Molar ratio	BET Surface area, m ² ·g ⁻¹	Mesopores surface area, m ² ·g ⁻¹	Pore volume, cm ³ ·g ⁻¹	Particle size ^a , nm	CO chemisorbed, μmol·g ⁻¹	Acidity, mmol NH ₃ ·g ⁻¹
Ni ₂ P(10)/H-USY-NA	0.83	604	123	0.38	13	9.6	0.29
Ni ₂ P(10)/H-USY-CA	0.95	583	103	0.40	12	15.9	0.34
Ni ₂ P(25)/H-USY-NA	1.05	204	43	0.19	20	3.3	0.11
Ni ₂ P(25)/H-USY-CA	1.01	73	33	0.14	16	9.3	0.07

^a Obtained from TEM images.

5.7.11 Comparison of the yield % at 3 % conversion on H-USY, Ni-based and Ni₂P-based catalysts at 370 °C

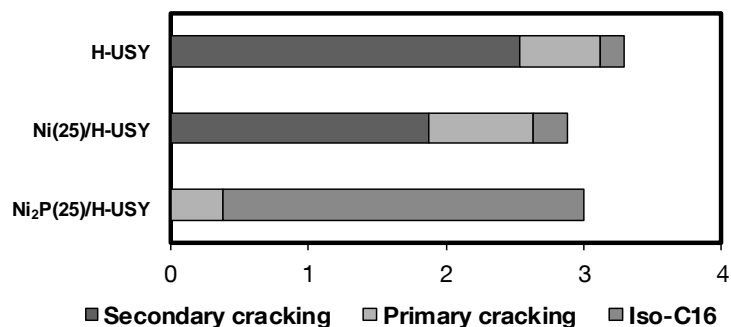


Figure 5A-27. Comparison of the yield % at 3 % conversion at 370 °C and 4 MPa on H-USY, Ni(25)/H-USY and Ni₂P(25)/H-USY.

5.7.12 References

- [1] R. Zarchin, M. Rabaev, R. Vidruk-Nehemya, M. V. Landau, M. Herskowitz, *Fuel*, **2015**, 139, 684-691.
- [2] C. Stinner, Z. Tang, M. Haouas, T. Weber, R. Prins, *Journal of Catalysis*, **2002**, 208, 456-466.

- [3] A. Montesinos-Castellanos, T. A. Zepeda, B. Pawelec, J. L. G. Fierro, J. A. de los Reyes, *Chemistry of Materials*, **2007**, *19*, 5627-5636.
- [4] M. Peroni, G. Mancino, E. Baráth, O. Y. Gutiérrez, J. A. Lercher, *Applied Catalysis B: Environmental*, **2016**, *180*, 301-311.
- [5] M. Peroni, X. Huang, I. Lee, E. Baráth, O. Y. Gutiérrez, J. A. Lercher, Deoxygenation of palmitic acid on unsupported WP, MoP, and Ni₂P, *ready for submission*.

Chapter 6

Summary and Conclusions

In the last years, the contribution of bio-oil to fuel production has been strongly encouraged due to environmental concerns. However, bio-oil containing triglycerides cannot be used in diesel engines due to its high viscosity and low volatility. In order to generate biofuel with the right properties, catalytic hydrodeoxygenation (HDO) is applied wherein fatty acids and triglycerides are converted into diesel-range hydrocarbons. The straight-chain alkanes obtained from a hydrodeoxygenation unit also need to be further processed in a hydroisomerization/hydrocracking step in order to improve the properties of the final fuel and reach the green fuel requirements. HDO and hydroisomerization/hydrocracking require a strong and stable metal function that catalyzes the (de)hydrogenation and hydrogenolysis steps. In this context, transition metal phosphides (TMP) are active for hydrodefunctionalization of biomass feedstocks, intrinsically more active than sulfides and more poison tolerant than most base or noble metals. TMP show high stability under S- and O-containing conditions. However, the intrinsic properties of such phosphides are hardly understood while their use in hydrocracking is scarcely addressed.

This dissertation reports the study of the conversion of triglycerides into green fuel on transition metal phosphides. Specifically, HDO of microalgae oil and fatty acids (model compounds) and hydroisomerization/hydrocracking of paraffins were explored on supported and unsupported TMP.

The results of this work show the changes in the trends of intrinsic activities with temperature and in the catalytic properties of the materials with the nature of the metal and the support and with metal sites concentration and concentration of acid sites. During the HDO of fatty acids, the elementary steps of the reductive oxygen elimination on the different metal phosphides were described. In the hydrocracking of paraffins, the ability of the TMP to provide the metal functionality was investigated, which allows understanding the impact of the high metal loadings on the acid concentration and strength.

Three phosphides of common base metals, i.e., WP, MoP, and Ni₂P were compared. These selected TMP are active and stable in HDO applications. Furthermore, the activity and selectivity of TMP can be tuned by the presence of Al₂O₃ as a support. Al₂O₃ promoted acid-catalyzed pathways, and influenced the phosphide functionality. Namely, the presence of Al₂O₃ increased the esterification rates due to its relative high acidity and made the supported Ni₂P phase more selective towards C-C bond cleavage than bulk Ni₂P. The performance of unsupported transition metal phosphides can be improved with a modified synthesis method that makes use of citric acid during the preparation of the catalysts. Citric acid acts as chelating

agent, preventing sintering during synthesis and counteracting the low dispersion associated to the lack of a support.

Ni₂P was found intrinsically more active than WP and MoP in the hydrodeoxygenation applications. The activity per gram of catalysts, however, was determined by the interplay between intrinsic activity and concentration of metal sites accessible to the reactant. Thus, MoP, with the highest fraction of exposed metal sites, was the most active phosphide per gram of material. The dominant route for the conversion of the fatty acid on WP and MoP was the reduction of the acid to aldehyde followed by hydrogenation to alcohol and final conversion to the alkane via consecutive dehydration and hydrogenation ($\text{R-CH}_2\text{COOH} \rightarrow \text{R-CH}_2\text{CHO} \rightarrow \text{R-CH}_2\text{CH}_2\text{OH} \rightarrow \text{R-CH}_2\text{CH}_2 \rightarrow \text{R-CH}_2\text{CH}_3$). Dehydration was the only step catalyzed by acid sites. Alcohol dehydration was much faster on WP than on MoP due to the higher concentration of acid sites of the former. The decarbonylation route via the aldehyde ($\text{R-CH}_2\text{COOH} \rightarrow \text{R-CH}_2\text{CHO} \rightarrow \text{R-CH}_3$) was an important pathway on MoP, enhanced by the low Lewis acidity, which hindered alcohol dehydration ($\text{R-CH}_2\text{CH}_2\text{OH} \rightarrow \text{R-CH}_2\text{CH}_2$) driving the reaction to dehydrogenation of the alcohol ($\text{R-CH}_2\text{CH}_2\text{OH} \rightarrow \text{R-CH}_2\text{CHO}$). Ni₂P catalyzed the hydrogenation route, the decarbonylation route via the aldehyde, and the direct C-C bond cleavage in the acid via dehydration to a ketene, followed by its decarbonylation ($\text{R-CH}_2\text{-CH}_2\text{COOH} \rightarrow \text{R-CH}_2=\text{CH}_2$).

The reduction of the fatty acid to aldehyde on all phosphides proceeds via a Langmuir-Hinshelwood mechanism, where H₂ adsorbs dissociatively and the fatty acid adsorbs without C-O bond cleavage. The product is formed with consecutive addition of adsorbed hydrogen with the second addition being the rate-determining step. Decarbonylation on Ni₂P, as expected from the stoichiometry of the reaction, does not depend on the coverage of adsorbed H.

n-Hexadecane was used as model compound of hydrocarbons obtained from the HDO of microalgae oil. TMP provided the (de)hydrogenation function during the hydrocracking of paraffins. However, Brønsted acid sites are required in order to increase the activity of the catalysts, i.e., TMP were not active for hydrogenolytic C-C cleavage. The zeolite H-USY was selected in order to obtain Brønsted acid sites minimizing diffusion limitation in its relatively large pores. H-USY led to low conversion and high selectivity to secondary cracking. Mechanically mixing the zeolite with the SiO₂-supported phosphides increased the conversion and the selectivity to primary cracking. In turn, the performance of the catalysts depended on the amount of phosphide, which provided the metal function. The activity of mechanical mixtures of TMP/SiO₂ with H-USY peaked at the phosphide/H-USY weight ratio of 0.33 with increasing phosphide content. Increasing the amount of metal phosphide, without modification

in the acid properties of the zeolite, is the key parameter for reaching ideal hydrocracking. Ideal hydrocracking was reached with increasing metal/acid sites ratios below 370 °C. The selectivity to primary cracking products also increased with the metal/acid sites molar ratio of the materials, whereas at temperature higher than 350 °C the selectivity to products of secondary cracking was favoured. At the same phosphide/H-USY weight ratio, Ni₂P-based mixtures exhibited higher concentration of metal sites and lower acidity than WP-based mixtures. Thus, Ni₂P-based phosphides showed higher selectivity to primary cracking and *iso*-C16 and their performance resembles ideal hydrocracking better than WP-based catalysts. WP-based materials, being more acidic than Ni₂P-catalysts, exhibited high selectivity to secondary cracking.

Supporting directly the phosphides on H-USY by incipient wetness impregnation doubled the active phosphide surface per gram of catalyst compared to mechanical mixtures. Therefore, the *n*-hexadecane conversion rates were higher and the product distribution resembles ideal hydrocracking better over H-USY-supported phosphides than over mechanical mixtures.

The most active Ni₂P-based catalyst prepared by incipient wetness impregnation was compared with Ni-based material for the hydrocracking of *n*-hexadecane. In particular, the effect of the metal loading and of the metal-acid balance on the stability and selectivity of the catalysts was investigated. Ni-based catalysts exhibited high selectivity to multiple C-C bond cleavage and to light alkanes (C1-C6) with marked deactivation, which was associated to the difficulty to obtain supported metal particles with high dispersion. Among the Ni-based catalysts tested in this contribution, only Ni(10)H-USY (10 wt. % Ni) was stable after the stabilization period but it was highly selective to light alkanes. In contrast, the combination of Ni₂P and H-USY provided more flexibility than Ni/H-USY in order to tune the final product distribution. Probably due to the ligand properties of phosphorous, Ni₂P particles were better dispersed on the zeolitic support and more stable than Ni catalysts. Ni₂P-based catalysts showed higher metal/acid sites ratio compared to the Ni-based counterparts. In the Ni₂P/H-USY catalysts, increasing the content of Ni₂P shifted the rate determining step from dehydrogenation on metal sites to acid-catalyzed C-C bond cleavage on the zeolite.

The total conversion rates depended linearly on the concentration of Brønsted acid sites on the material showing enough metal sites to ensure quasi-equilibrium in the (de)hydrogenation function, whereas the rate of hydroisomerization depended linearly on the concentration of metal sites. High selectivity to light alkanes was reached with metal loadings below 10 wt. % Ni₂P, especially at temperatures above 370 °C. Product distributions corresponding to ideal hydrocracking were reached with 15 wt. % Ni₂P on H-USY, which corresponded to an atomic

ratio of metal/acid sites of 0.25, at temperatures below 370 °C. Due to the interaction between the phosphorous precursor and the H-USY during the synthesis of the catalyst, at 25 wt. % of loading the structure of H-USY was compromised decreasing the activity of the catalyst. In order to avoid the deterioration of the crystallinity of the H-USY and the reduction of the number of accessible acid sites, increasing the activity of the material, small amounts of phosphorous precursor must be used during the synthesis of the Ni₂P(25)/H-USY.

This dissertation demonstrates that transition metal phosphides are suitable and stable materials to catalyze the conversion of biomass to green fuel. This opens the possibility to use this new class of materials in a one-step conversion, where a zeolitic-supported catalyst could catalyze hydrodeoxygenation and hydrocracking.

Curriculum Vitae

Name	Marco Peroni
Day and place of birth	05.09.1986 in San Benedetto del Tronto (Italy)
Citizenship	Italian
Education	
Since 07/2013	PhD at TUM München, Lehrstuhl für Technische Chemie II, Technische Universität München (Germany), at the chair of Prof. J. A. Lercher.
09/2009 – 12/2012	Master degree: Chemical Engineering - Process Engineering, University of L'Aquila (Italy). Final thesis: “ <i>Catalysts Cu/ZnO based: Synthesis, physical-chemical and catalytic characterization in the methanol production from CO₂ and H₂</i> ” (Grade: 110/110). Degree recognised by the Faculty of Chemistry of the Technische Universität München (Germany) with the grade 1.0.
09/2005 – 12/2009	Bachelor's degree: Chemical Engineering, University of L'Aquila (Italy). Final thesis: “ <i>Recovery of dead batteries by hydrometallurgical treatment: process, analysis and technical-economic feasibility</i> ” (Grade:106/110).
09/2000 – 06/2005	Secondary school degree, Industrial Technical Institute, Ascoli Piceno (Italy) – Specialization in Chemistry (Grade: 100/100).
Internships and Scholarships	
05/2012 – 09/2012	Research stay at UCL, Université Catholique de Louvain, Louvain la Neuve (Belgium), in the Laboratory of Catalysis of the Institute of Condensed Matter and Nanosciences of the UCL at the chair of Prof. P. Ruiz. (Europass mobility).
11/2011 – 05/2012	Research stay in the Laboratory of Catalysis of the University of L'Aquila (Italy) at the chair of Prof. P. Villa.
01/2011 – 07/2011	Semester abroad with Erasmus project, Universitat de Barcelona, Barcelona (Spain).
03/2003 – 04/2003	Research stay at the Faculty of Chemistry of DIT, Dublin Institute of Technology, Dublin (Ireland). (Europass mobility).
Awards	
07/2004	Stage at “Scuola Superiore di Pisa”, Pisa (Italy), selected as the best student of the “Marches” region.
11/2001	Gold School Report – Best student of the Industrial Technical Institute of the year 2000/2001.
04/2001	Olympic games of Maths – Best student in mathematics in Ascoli Piceno (Italy).

List of publications

Journal Articles

M. Peroni, G. Mancino, E. Baráth, O. Y. Gutiérrez, J. A. Lercher, “*Bulk and γ -Al₂O₃-supported Ni₂P and MoP for hydrodeoxygenation of palmitic acid*”, Applied Catalysis B: Environmental, **2016**, *180*, 301-311.

M. Peroni, X. Huang, I. Lee, E. Baráth, O. Y. Gutiérrez, J. A. Lercher, “*Deoxygenation of palmitic acid on unsupported WP, MoP, and Ni₂P*”. **Paper ready for submission.**

M. Peroni, I. Lee, O. Y. Gutiérrez, J. A. Lercher, “*Hydrocracking of Paraffins on Transition Metal Phosphides Catalysts*”, DGMK-Tagungsbericht 2016-3, ISBN 978-3-941721-66-1, **2016**, 183-190.

M. Peroni, I. Lee, O. Y. Gutiérrez, J. A. Lercher, “*Ni₂P/H-USY catalysts for hydrocracking of n-hexadecane*”. **Paper in preparation.**

Oral presentations

M. Peroni, X. Huang, I. Lee, E. Baráth, O. Y. Gutiérrez, J. A. Lercher, “*Hydrodeoxygenation on transition metal phosphides*”, 24th North American Catalysis Society Meeting (NAM24), Pittsburgh, Pennsylvania – USA, **2015**.

M. Peroni, X. Huang, I. Lee, E. Baráth, O. Y. Gutiérrez, J. A. Lercher, “*Towards efficient hydrodeoxygenation on transition metal phosphides*”, 12th European Congress on Catalysis (EuropaCatXII), Kazan – Russia, **2015**.

Poster presentations

M. Peroni, X. Huang, I. Lee, E. Baráth, O. Y. Gutiérrez, J. A. Lercher, “*Towards efficient hydrodeoxygenation on transition metal phosphides*”, 48. Jahrestreffen Deutscher Katalytiker, Weimar – Germany, **2015**.

M. K. Braun, M. Peroni, E. Baráth, O. Gutiérrez, J. A. Lercher, “*Yeast biomass as a new source of sustainable aviation biofuels and platform chemicals*”, Conference on Industrial Biotechnology (IBF 2016), Garching – Germany, **2016**.

M. Peroni, X. Huang, I. Lee, E. Baráth, O. Y. Gutiérrez, J. A. Lercher, “*Metal phosphide catalysts for the conversion of microalgae oil to biofuel*”, 3rd International Symposium on Catalysis for Clean Energy and Sustainable Chemistry (CCESC2016), Madrid – Spain, **2016**.

M. Peroni, I. Lee, O. Y. Gutiérrez, J. A. Lercher, “*Hydrocracking of Paraffins on Transition Metal Phosphide Catalysts*”, Catalysis – Novel Aspects in Petrochemistry and Refining, DGMK Conference, Berlin – Germany, **2016**.

